SYNTHESIS, MECHANISTIC STUDY AND INTERACTION OF METAL NANOPARTICLES WITH BIOLOGICALLY IMPORTANT MOLECULES

By

ABHISHEK DAS

CHEM01201404021

Bhabha Atomic Research Centre, Mumbai

A thesis submitted to the

Board of Studies in Chemical Sciences

In partial fulfillment of requirements

for the Degree of

DOCTOR OF PHILOSOPHY

of

HOMI BHABHA NATIONAL INSTITUTE

January, 2020

Homi Bhabha National Institute

Recommendations of the Viva Voce Committee

As members of the Viva Voce Committee, we certify that we have read the dissertation prepared by Shri **Abhishek Das** entitled "**Synthesis, mechanistic study and interaction of metal nanoparticles with biologically important molecules**" and recommend that it may be accepted as fulfilling the thesis requirement for the award of Degree of Doctor of Philosophy.

Chairman – **Dr. H. Pal (Ex-BARC)**	**Signature:**	**Date:** 21-11-2020
Guide / Convener – **Dr. Sudhir Kapoor (Ex-BARC)**	**Signature:**	**Date:** 21/11/2020
Examiner - **Dr. J. Bellare (IITB)**	**Signature:**	**Date:** 21-Nov-2020
Member 1- **Dr. S. Kannan (BARC)**	**Signature:**	**Date:** 21/11/2020
Member 2- **Dr. V. Sudarsan (BARC)**	**Signature:**	**Date:** 21- NOV. 2020

Final approval and acceptance of this thesis is contingent upon the candidate's submission of the final copies of the thesis to HBNI.

I/We hereby certify that I/we have read this thesis prepared under my/our direction and recommend that it may be accepted as fulfilling the thesis requirement.

Date: 21-11-2020

Place: BARC, Mumbai

Signature

Guide

STATEMENT BY AUTHOR

This dissertation has been submitted in partial fulfillment of requirements for an advanced degree at Homi Bhabha National Institute (HBNI) and is deposited in the Library to be made available to borrowers under rules of the HBNI.

Brief quotations from this dissertation are allowable without special permission, provided that accurate acknowledgement of source is made. Requests for permission for extended quotation from or reproduction of this manuscript in whole or in part may be granted by the Competent Authority of HBNI when in his or her judgment the proposed use of the material is in the interests of scholarship. In all other instances, however, permission must be obtained from the author.

Abhishek Das

Abhishek Das

DECLARATION

I, hereby declare that the investigation presented in the thesis has been carried out by me. The work is original and has not been submitted earlier as a whole or in part for a degree / diploma at this or any other Institution / University.

Abhishek Das

Abhishek Das

List of Publications arising from the thesis

a. Journals:

1) Synthesis of pH sensitive gold nanoparticles for potential application in radiosensitization;
Abhishek Das, Ridhima Chadha, Nandita Maiti, Sudhir Kapoor;
Materials Science and Engineering C, 55(2015), 34-41.

2) Adsorption and sub-nanomolar sensing of thioflavin T on colloidal gold nanoparticles, silver nanoparticles and silver-coated films studied using surface-enhanced Raman scattering;
Nandita Maiti, Ridhima Chadha, **Abhishek Das**, Sudhir Kapoor;
Spectrochim Acta A Mol Biomol Spectrosc, 149 (2015), 949-956

3) Surface selective binding of 2,5-dimercapto-1,3,4-thiadiazole (DMTD) on silver and gold nanoparticles: a Raman and DFT study;
Nandita Maiti, Ridhima Chadha, **Abhishek Das**, Sudhir Kapoor;
RSC Advances, 6 (2016), 62529-62539.

4) A study of light induced surface reactions of sildenafil citrate on hybrid AgCl/Ag nanoparticle dimers by surface enhanced Raman scattering and pulse radiolysis techniques;
Abhishek Das, Nandita Maiti, Akshay C. Dhayagude, Arup K. Pathak, Ridhima Chadha, Suman Neogy, Sudhir Kapoor;
Colloids and Surfaces A: Physicochemical and Engineering Aspects, 582 (2019), 123864.

5) In-situ reduction of gold nanoparticles in alginate film matrix for application in surface enhanced Raman scattering;
Abhishek Das, Himanshi, Ridhima Chadha, Nandita Maiti, Suman Neogy and Sudhir Kapoor
G P Globalize Research Journal of Chemistry, 3 (2019) 11-20.

6) Ultra-trace level qualitative and quantitative detection of sildenafil citrate by surface enhanced Raman scattering (SERS) based fingerprinting method;
Abhishek Das, Akshay Dhayagude, Nandita Maiti, Ridhima Chadha, Anand Ballal and Sudhir Kapoor;
Asian Journal of Physics, 28 (2019) 227-242.

b. Conference/Symposium

1) Ultra-Trace Level Detection of Sildenafil Citrate for potential Application in Quality Control of Herbal Drugs;
Abhishek Das, Nandita Maiti, Ridhima Chadha and Sudhir Kapoor;
DAE-BRNS 7th Interdisciplinary Symposium on Material Chemistry, December 4-8, 2018, Mumbai.

2) Photo-tautomerism of sildenafil citrate on silver nanoparticles: A SERS and DFT study;
Abhishek Das, Nandita Maiti, Ridhima Chadha and Sudhir Kapoor;
7th International Conference on Perspectives in Vibrational Spectroscopy (ICOPVS-2018), November 25-29, 2018, Mumbai.

Other Publications

1) γ-Radiation induced synthesis of silver nanoparticles in aqueous poly (N-vinylpyrrolidone) solution;
Akshay C.Dhayagude, **Abhishek Das**, Satyawati S.Joshi, SudhirKapoor;
Colloids and Surfaces A: Physicochemical and Engineering Aspects, 556 (2018) 148-156.

2) Understanding the reaction mechanism of the reactivity of free radicals with graphene oxide;
RidhimaChadha, **Abhishek Das**, NanditaMaiti, SudhirKapoor;
Surfaces and Interfaces, 9 (2017) 201-205.

3) Effect of anion and alkyl chain length on the structure and interactions of N-alkyl pyridinium ionic liquids;
MangeshPotangale, **Abhishek Das**, SudhirKapoor, ShraeddhaTiwari;
Journal of Molecular Liquids, 240 (2017) 694-707.

4) Role of PVA in synthesis of nano Co_3O_4 decorated graphene oxide;
Surekha S. Jogdand, **Abhishek Das**, AkshayDhayagude, Sudhir Kapoor, Satyawati S. Joshi;
Polym. Adv. Technol., 26 (2015) 1114– 1122.

5) Synthesis of silver nanoparticles: Effects of anionic ligands on formation and catalytic activity;
RidhimaChadha, **Abhishek Das**, NanditaMaiti, SudhirKapoor;
Materials Chemistry and Physics, 148 (2014) 1124-1130.

Abhishek Das
(Abhishek Das)

Dedicated to Maa

ACKNOWLEDGEMENTS

I am very grateful to all who have assisted, supported and inspired me, either actively or passively, during as well as before, the doctoral programme.

Firstly, I would like to thank my guide, Dr. Sudhir Kapoor, who has infused in me the basics of nanochemistry, slowly over the years. It was a great learning experience.

I would like to extend my gratitude to the members of the Nanochemistry Group, Dr. Nandita Maiti, for extending her expertise in understanding Raman spectroscopy and associated techniques to me and also Smt. Ridhima Chadha, for helping me understand the intricacies of synthesis of nanomaterials. Again, the experimental assistance provided by Dr. Akshay Dhayagude and Shri. Rajeshwar Sharma, is highly appreciated.

I am thankful to all the members of the doctoral committees for critically assessing the annual reports and providing essential inputs which have helped in improve the quality of work.

All the work in this thesis were supported by the present as well as previous Heads of Radiation & Photochemistry Division, Chemistry Group, BARC.

It gives me immense pleasure to acknowledge the efforts of LINAC section, RPCD, for the technical support during Pulse Radiolysis experiments. Moreover, I am also grateful to all my collaborators, Dr. Goda Jayant Sastri (ACTREC, Kharghar) and Shri. Nitin Kakade (RP&AD). I am also thankful to Smt. Ashmita Sharma for Gas chromatography experiments.

The company provided by the colleagues cum friends, Dr. Juby Kuttan, Shri Krishankant Singh, Shri. Amit Kanjilal, Dr. Sugosh Prabhu, Shri. Mohsin Jafar, Dr. Goutam Chakraborty and others, for encouragement and constant support.

Last but not the least, I am thankful to my wife Smt. Sudeshna Ghosh for being the pillar of support throughout the doctoral programme.

Contents

Synopsis

The word 'Nanomaterials' is synonymous with innovation which is the need of the hour. Any material when reduced to nanometric dimension, shows drastically different characteristics in comparison to the bulk which is mainly due to some fundamental phenomenon associated with increase in surface to volume ratio[1], discretization of energy levels[2], collective oscillation of surface electrons[3], etc. All these fundamental phenomena alter the optical[4], mechanical[5], thermal[6] or electrical properties[7] of the materials. This idea formed the crux of a new branch of science known as nanotechnology which basically deals with synthesis of nanomaterials with desired properties and their implementation for societal benefits. Size and shape of nanomaterials[1] are the two most important physical parameters which control the nanomaterial properties. Synthesis of nanomaterials requires control of chemical reaction which is done in two steps: firstly, by identification of the factors affecting the size and shape of the nanomaterials and secondly by varying reaction conditions to achieve desirable size and shape. Synthetic approach for nanomaterials[8] can be done broadly classified into two categories: Top-down and Bottom-up[9]. Two-down method involves breaking down of bulk to smallest possible size and shape whereas bottom-up approach relies on building of nanomaterials from atoms. The work presented in this thesis involves bottom-up approaches as chemical synthesis methods are all bottom-up. Application of nanomaterials in the field of medicine[10], photovoltaics[11], sensing[12], etc. which cater to the societal need has motivated researchers from all over the world to discover innovative methods for synthesis of nanomaterials. Nanomaterials can be broadly classified into two categories: inorganic[13] and organic[14]. As name suggests, organic nanomaterials are basically made up of organic compounds whereas inorganic nanomaterials consists of inorganic materials such as oxides[15], halides[16], metals[17], etc. Metallic nanomaterials are very difficult to synthesize as in nanometric dimension, higher surface to volume ratio enhances their propensity to oxidize unless a strong capping agent has been used to protect its chemical oxidation state. Noble metals[18] are in this regard very interesting as they lack in

tendency to oxidize. The synthesis of noble metal nanoparticles has been a topic of interest due to a number of factors which is discussed in this thesis in detail.

Noble metal nanoparticles (NMP) have been investigated in this work for potential application in the field of sensing[19] and radiosensitization[20]. NMPs show a unique optical property known as surface plasmon[21] which enhances the electric field in the vicinity of the nanoparticles which leads to enhancement of Raman signal[22] of molecules adsorbed on the nanoparticles surface. This phenomenon is known as surface enhanced Raman scattering which has been utilized for detection of biologically important molecules in this work. Moreover, high Z of NMPs enhances the effect of radiation by secondary processes such as emission of photoelectrons, secondary electron and auger electrons[20]. This idea has been implemented to carry out studies related to radiosensitization.

The thesis shall contain 7 chapters which are briefly discussed below:

Chapter 1: Introduction

This chapter discusses the fundamental properties of noble metal nanoparticles which are important for their application in the field of sensing and radiosensitization.

Chapter 2: Material, Methods and instrumentation

This chapter discusses the methods that have been implemented for the synthesis of gold and silver nanoparticles for carrying out various studies in this work. The instrumental techniques which vital for various characterizations of the plasmonic nanoparticles as well as their applications, have been discussed.

Chapter 3: Synthesis and characterization of pH sensitive gold nanoparticles for application in radiosensitization

Extracellular fluid of cancer tissues is deemed acidic owing to anaerobic respiration due to poorly developed vascular system leading to hypoxia. Targeting of cancer tissues is obtained by making vectors sensitive to pH gradient in a tissue. The surface characteristics of gold nanoparticles govern interparticle interaction of the particles. pH sensitive GNPs can be synthesized by using a pH sensitive reducing agent as well as stabilizer for its application as a prospective vector for cancer cell targeting. L-tryptophan, an amino acid, is a mild reducing agent. Chloroauric acid was reduced by l-tryptophan in buffered aqueous medium to form pH

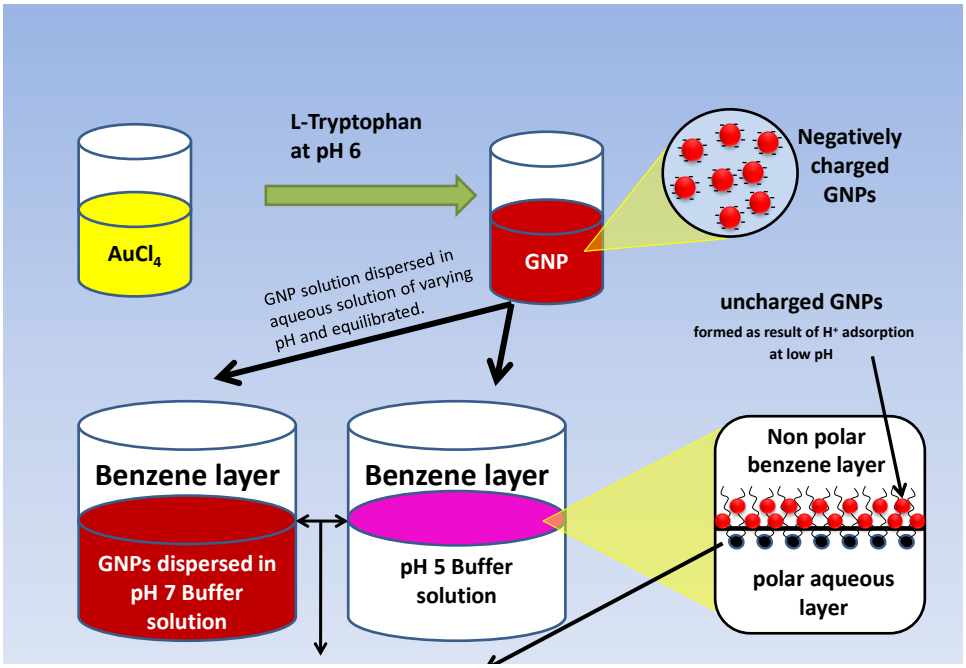

Figure 1: *A schematic diagram representing the synthesis of gold nanoparticles by tryptophan and its implementation in pH sensitive accumulation at cellular interface mimicking cancer cell.*

sensitive GNPs. Oxidized l-tryptophan moieties were found to show attachment to GNPs through indolyl nitrogen as observed by infrared studies. Evidence of decarboxylation of l-tryptophan was observed in gas chromatogram. Phosphatidyl choline, an amphiphile, was used to simulate cell membrane, dispersed between polar and non-polar liquid liquid interface. At pH lower than 5, synthesized GNPs were found to accumulate at the interface. This showed the pH

sensitive property of GNPs suitable for radio-sensitization of cancer cells. Moreover, GNPs synthesized by tryptophan reduction method were subjected to survival (MTT) assay in cancer cell and normal cell lines. The assay shows that GNPs are non-toxic to the cells and respond to radiosensitization.

Chapter 4: Synthesis and characterization of gold / silver nanoparticles loaded polymeric film for sensing and dosimetric applications.

Hand held Raman spectrometers have found application in forensic as well as in quality control in industries. Stable and economic SERS substrate are in demand. Here, we have prepared stable SERS substrate by in-situ reduction of gold ions in a biocompatible polymeric matrix. Alginate

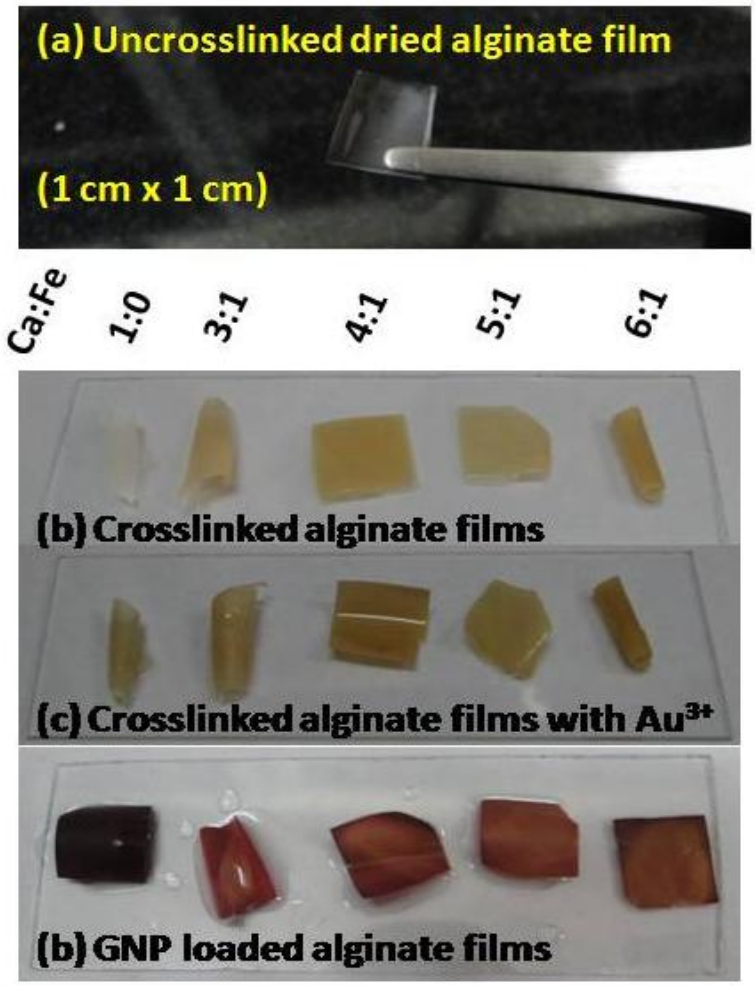

Figure 2: *Photograph of (a) uncross-linked alginate film, (b) cross-linked alginate films, (c)* Au^{3+} *loaded cross-linked film and (d) GNP loaded alginate film.*

was chosen as the polymer of choice as cross-linking step is very simple. 2% sodium alginate

solution was casted in a standard 7 cm dia petri-dish and air dried. Dried films were peeled off and cut into pieces of size 1 cm x 1 cm and cross-linked in Ca-Fe (1:5) aqueous solution. After the cross-linking step, films were submerged in chloroauric acid solution for 2 hrs., till the absorption of gold ions into the polymer matrix is complete. Gold ion loaded films were then reduced by 0.05 M glucose solution at 60°C for 6 minutes to form red colored GNP loaded films. GNP loaded films were then etched in 0.1 M HCl solution for 45s. These films were then tested for their efficacy as SERS substrate. Crystal violet (CV) was chosen as a model dye. Different low concentration (10^{-4} M and below) of CV was then dropped on the films and Raman signal was recorded. It was found that the GNP loaded films could detect as low as 10^{-8} M of CV. It was also found that the films had a shelf life of more than six months. Detection of adulterants, insecticides and pesticides are of future interest to establish these films as a universal SERS substrate.

Silver nanoparticles (AgNPs) were synthesized by reducing $AgNO_3$ by alginate solution (1%) at alkaline pH and 65°C. Atomic force microscopy image microscope image reveal that the particles are spherical in shape with size ~10 nm. The synthesized AgNPs were further added to 2.25 % alginate solution such that the final Ag concentration is 4 mM. This

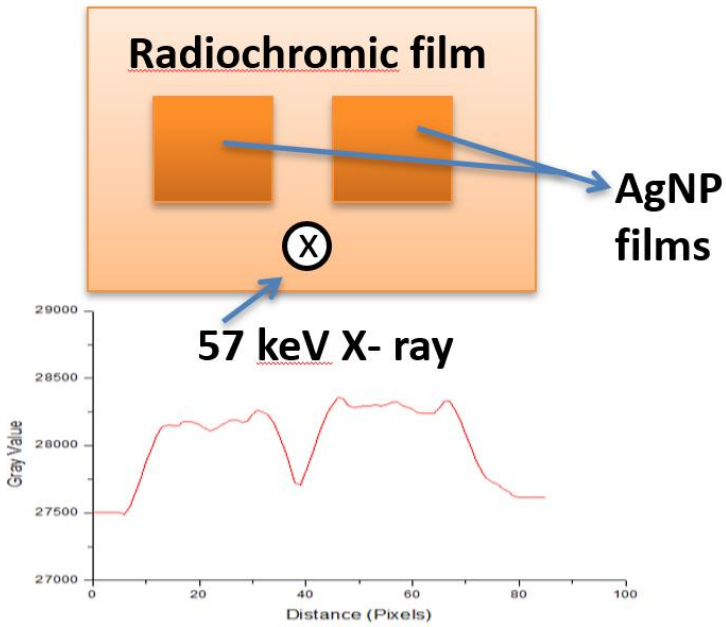

Figure 3: *Schematic representation and dose enhancement observed on AgNP loaded alginate film superimposed on radiochromic films*

solution was casted into films by drying. Dried films were cross-linked by $Ca(NO_3)_2$ solution. Silver films were used for detection of crystal violet (fungicide) and Rhodamine 6G (dye). Detection limit of crystal violet and Rhodamine 6G were found to be 10^{-8} and 10^{-10} M, respectively, by SERS.

AgNP loaded polymeric films were also studied for dosimetric study using radiochromic films. They show a maximum dose enhancement of 29% which is important for potential use of the above films in treatment of superficial cancer by radiation therapy.

Chapter 5: Synthesis and characterization of AgNPs and AgCl/AgNPs for detection of sildenafil citrate

Sildenafil citrate is a widely used PDE-5 inhibitor vasodilator drug commercially available as Viagra®. PDE-5 inhibitor drugs possess some side-effects when administered through conventional oral therapy. These side-effects can be reduced if the drug is targeted to a specific organ via a drug delivery vector. For this purpose, understanding of binding of SC to noble

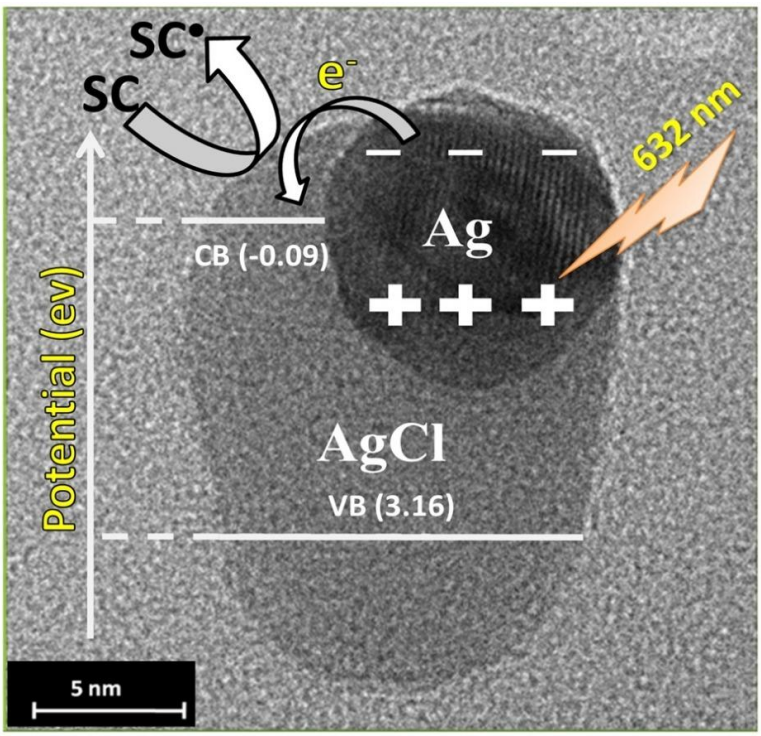

Figure 4:*Schematic representation of light induced protonation of sildenafil citrate adsorbed on hybrid AgCl/AgNP dimer.*

metal nanoparticles, potential drug delivery vectors, is important. Silver nanoparticles were synthesized by citrate reduction method. Silver nanoparticles synthesized by citrate reduction method, were employed to detect trace concentration of sildenafil citrate (SC). Limit of quantitation was found to be 10^{-9} M whereas limit of detection was found to be 10^{-10} M. Conditions for sensing were optimized by studying the effect of medium pH, time of equilibration and concentration of SC.

Ag/AgCl nanoparticle dimers (NPD) were formed by the reaction of AgNPs with 0.03 M HCl in presence of SC. It was observed that upon reducing the concentration of SC, extent of chlorination increased. Formation of Ag/AgCl NPD was studied using UV-Vis spectroscopy, transmission electron microscopy (TEM) and selected area electron diffraction (SAED). It was found that AgCl played an important role in charge transfer reaction of SC at the surface of the nanoparticles leading to appearance of new peaks in SERS spectra.

Chapter 6: Study of interaction of plasmonic nanoparticles with biologically important molecules by surface enhanced Raman scattering

This chapter deals with SERS study of various molecules of biological importance adsorbed on plasmonic nanoparticles. Structural information with respect to their orientation and conformation were extracted by analysis of SERS spectra.

Gold and silver nanoparticles were used for sensing of Thioflavin T (ThT) using SERS. It was observed that at concentrations lower than 10^{-7} M, ThT binds to GNPs and SNPs through S-atom with torsional angle between benzothiazole and dimethyl aminobenzene being 90°.

Different tautomers of 2,5-Dimercapto-1,3,4- dithiazole were investigated by computational methods to ascertain conformation of DMDT at varying pH. SERS spectra revealed selective binding of DMDT to Ag and Au surface via N and S atom respectively.

Chapter 7: Summary and Future scope

This chapter summarizes all the work presented in the thesis and brings forward the possible outcomes from the work presented in the thesis.

References

1. G. Guisbiers, S. Mejia-Rosales and F. Leonard Deepak, 2012, *Journal of Nanomaterials*, **2012**, 2.
2. D. Sumanth Kumar, B. Jai Kumar and H. M. Mahesh, 2018, Synthesis of Inorganic Nanomaterials, Woodhead Publishingp. 59-88.
3. V. Amendola, R. Pilot, M. Frasconi, O. M. Maragò and M. A. Iatì, 2017, *Journal of Physics: Condensed Matter*, **29**, 203002.
4. B. Zhang, 2018, Physical Fundamentals of Nanomaterials, William Andrew Publishing(Boston) p. 291-335.
5. D. Guo, G. Xie and J. Luo, 2013, *Journal of Physics D: Applied Physics*, **47**, 013001.
6. T. Savage and A. M. Rao, 2004, Thermal Conductivity: Theory, Properties, and Applications, Springer US(Boston, MA) p. 261-284.
7. G. Y. Yurkov, A. S. Fionov, Y. A. Koksharov, V. V. Koleso and S. P. Gubin, 2007, *Inorganic Materials*, **43**, 834.
8. C. Dhand, N. Dwivedi, X. J. Loh, A. N. Jie Ying, N. K. Verma, R. W. Beuerman, R. Lakshminarayanan and S. Ramakrishna, 2015, *RSC Advances*, **5**, 105003.
9. Y. Wang and Y. Xia, 2004, *Nano Letters*, **4**, 2047.
10. O. V. Salata, 2004, *Journal of Nanobiotechnology*, **2**, 3.
11. G. Chen, J. Seo, C. Yang and P. N. Prasad, 2013, *Chemical Society Reviews*, **42**, 8304.
12. W. Zeng, H. Wang and Z. Li, 2016, *Journal of Nanotechnology*, **2016**, 2.
13. W. Paul and C. P. Sharma, 2010, Biointegration of Medical Implant Materials, Woodhead Publishingp. 204-235.

14. H. Dong and W. Hu, 2013, Springer Handbook of Nanomaterials, Springer Berlin Heidelberg(Berlin, Heidelberg) p. 905-940.

15. J. A. Rodríguez and M. Fernández-García.

16. L. Cui, T. Jiao, Q. Zhang, J. Zhou and Q. Peng, 2015, *Nanomaterials and Nanotechnology*, **5**, 20.

17. V. V. Mody, R. Siwale, A. Singh and H. R. Mody, 2010, *J Pharm Bioallied Sci*, **2**, 282.

18. Z. Zhang and P.-C. Lin, 2018, Emerging Applications of Nanoparticles and Architecture Nanostructures, Elsevierp. 177-233.

19. H. Malekzad, P. S. Zangabad, H. Mirshekari, M. Karimi and M. R. Hamblin, 2017, *Nanotechnol Rev*, **6**, 301.

20. X.-Y. Su, P.-D. Liu, H. Wu and N. Gu, 2014, *Cancer Biol Med*, **11**, 86.

21. H. Aghlara, R. Rostami, A. Maghoul and A. SalmanOgli, 2015, *Optik*, **126**, 417.

22. Y. Hernández and B. C. Galarreta, 2019, Nanomaterials for Magnetic and Optical Hyperthermia Applications, Elsevierp. 83-109.

List of Figures

List of Schemes

List of Tables

Homi Bhabha National Institute

Ph. D. PROGRAMME

Name of Candidate:	Abhishek Das
Name of the Constituent Institution:	Bhabha Atomic Research centre, Mumbai
Enrollment Number:	CHEM01201404021
Title of the Thesis:	Synthesis, mechanistic study and interaction of metal nanoparticles with biologically important molecules

Thesis Highlights

- **Synthesis of pH sensitive gold nanoparticles for application in radiosensitization**

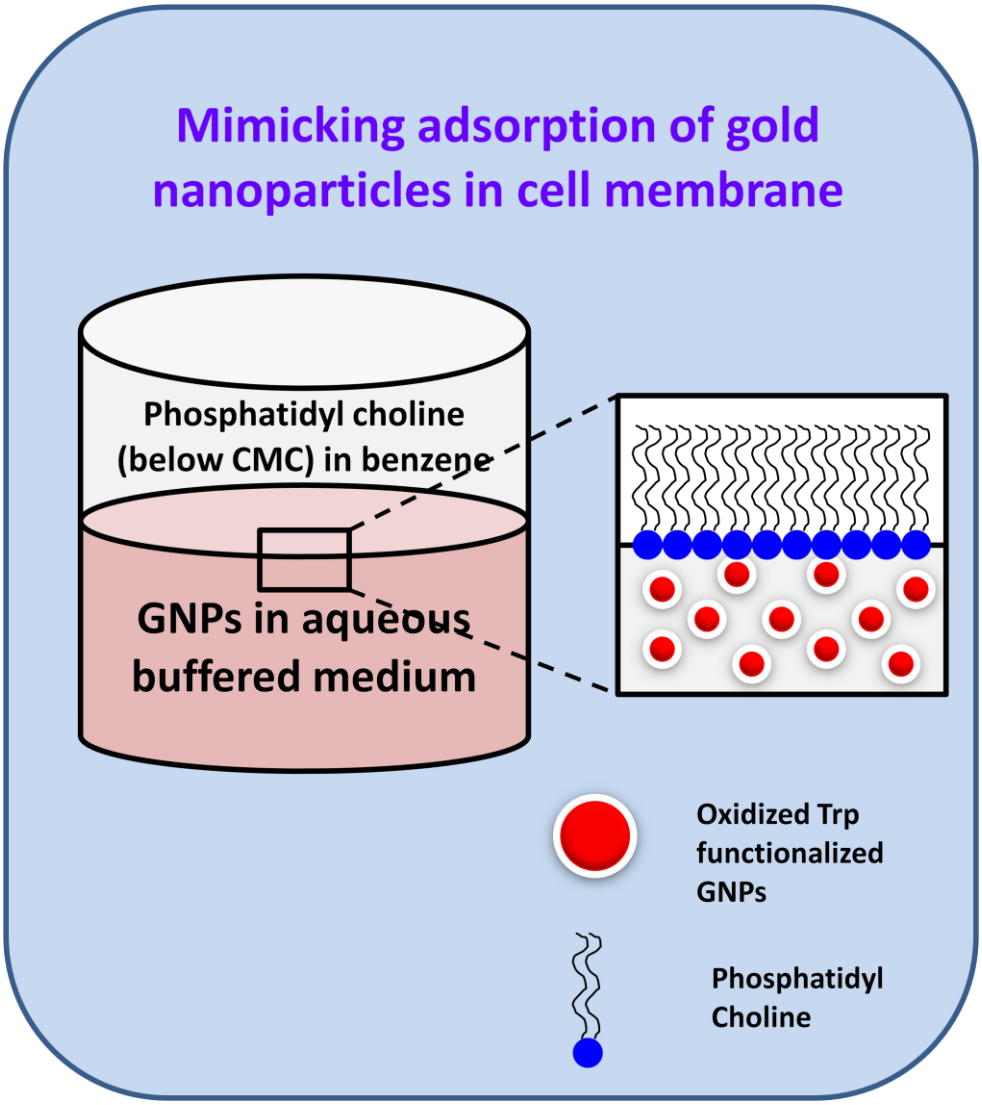

❖ **Synthesis of plasmonic nanoparticles loaded films for sensing and radiosensitization application**

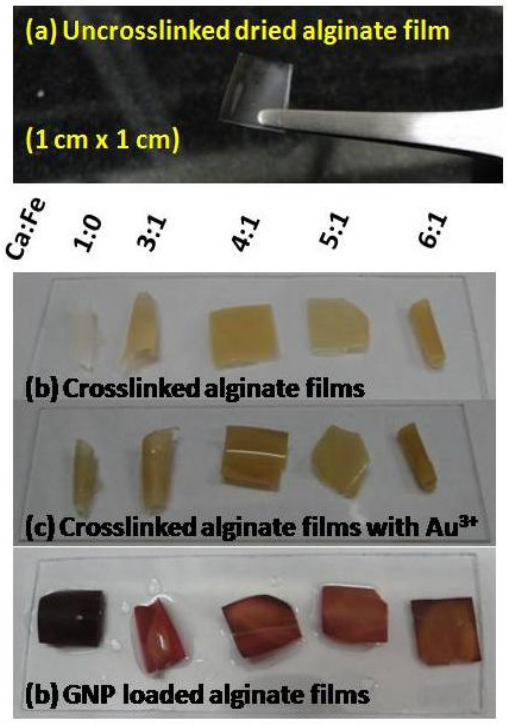

❖ **Synthesis of AgCl/Ag nanoparticles for study of surface reactions of sildenafil citrate**

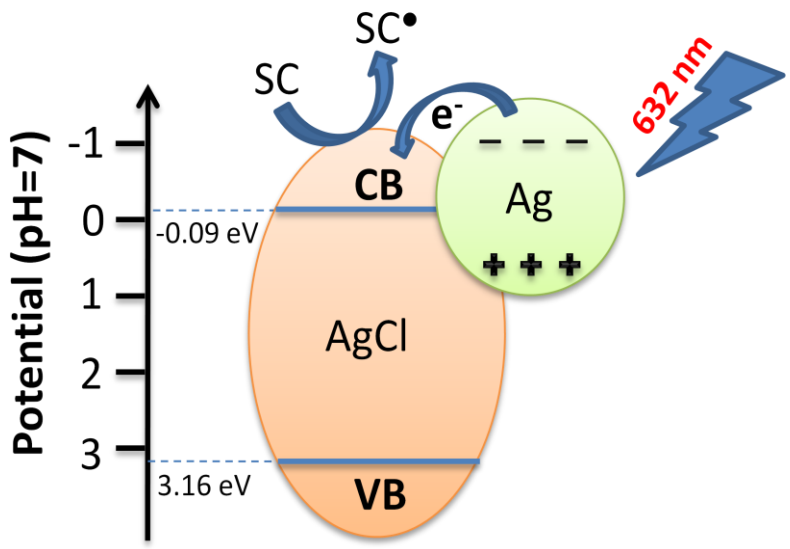

1

Introduction

Material science is a branch of science which deals with the discovery, synthesis, characterization and application of materials for the benefit of mankind. Based on the source of origin, materials can be broadly classified into two types: organic and inorganic. Materials are being developed all over the world to meet certain technological requirements. For example, it has been observed that increasing chain length of N-alkyl pyridinium ionic liquids can alter the microscopic arrangement which can influence its solubilization efficiency[1]. Materials were earlier characterized based on their chemical composition only, which meant that material with one chemical composition can have only a fixed set of properties which is irrespective of the size. The above understanding was proven inadequate with the discovery of a new set of materials, known as 'nanomaterials (NMs)'.Richard Adolf Zsigmondy won the Nobel Prize in 1925 for his noted works on colloids[2]. By definition, colloids are materials which do not settle and cannot be separated using filtration or centrifugation. Colloids were, in-fact, discovered even before they were understood. Lycurgus cups[3] are one of the earliest example of application of nanotechnology to manufacturing of glass cups. Cups are dated in the fourth century A.D. and were found in the Roman empire. Most interesting feature of the cups are that they are dichroic in reflected light they appear greenish yellow whereas in transmitted light they appear ruby red. Traces of colloidal silver and gold which were added while manufacturing, were found to be responsible for greenish yellow colour in reflected light and ruby red in transmitted light, respectively.

In principle, NMs are materials which must have one of the dimensions confined to 1-100 nm. There is no universally accepted single definition. Environmental Protection Agency (EPA)suggests that, "NMs can exhibit unique properties dissimilar than the equivalent chemical compound in a larger dimension."[4] In order to get familiarized and understand different types of NMs, we need to classify NMs based on composition, dimensions and origin.

1.1. Classification of nanomaterials based on composition

NMs can be classified into four categories based on composition:

1.1.1. Carbon based NMs

Carbon is the most versatile element found on earth due to its omnipresence. It exists in various allotropic forms which have completely different characteristics due to different arrangement of adjacent carbons. Diamond and graphite are two such examples. Graphite is made up of sp^2hybridized planar carbon sheets stacked one upon each other, with high electrical conductivity and low thermal conductivity. On the other hand, diamond is a 3D network of sp^3 hybridized carbon atoms with low electrical conductivity and high thermal conductivity[5].Fullerene (C_n) is the third allotropic form of carbon after graphite and diamond[6].C_n consists of sp^2 hybridized carbon atoms in closed caged geometry. Fullerenes behave as electron deficient alkenes which readily react with electron rich species. This reactivity arises from the strained structure which has the tendency to relieve the strain by undergoing addition reaction[6].Fullerenes are currently being used in various applications in the field of photovoltaics[7] and pharmaceuticals[8].One or few sp^2 hybridized planar sheets are referred to as graphene. Graphene is a widely used crystalline form of carbon with exceptional electrical, mechanical, and chemical properties[9]. Upon universal recognition of possible application of graphene, its discoverers Andre Geim and Konstantin Novoselov

from the University of Manchester, England were awarded Noble Prize in 2010[10]. Graphene based nanocomposites find their application in photovoltaics[10], supercapacitors[11], etc. Carbon nanotubes (CNTs) is another carbon based nanomaterial which is widely used in sensing[12], aerospace engineering[13], supercapacitors[14], etc. CNTs are single or multi-layered folded sp^2 carbon sheets which has high mechanical strength and excellent electrical conductivity, for extensive nanotechnological applications.

1.1.2. Inorganic NMs

This class of NMs mostly includes metal and metal oxide nanomaterials. Metals have extensive metallic bonding which originates from bunching of MO's to give rise to two different band: valence band and conductional band.[15]Metals are characterized by overlapping conduction and valence band, which means that electrons in the valence shell are free to travel throughout the metal. A work function is required to knock-off metals from its surface which is analogous to ionization potential in elements[16]. When a metal is reduced in dimension such that the electron is confined within a limited space, various newer properties emerge. The study of confined electrons in a metallic or metal-like nano-dimensional system is referred to as plasmonics[17], which we is discussed later. Semiconductor materials also have band structure but there exists a gap between valence and conduction band, known as fermi gap.[18] Interestingly, metal chalogenides[18] as well as halides[19] are also found to be semiconductor materials apart from intrinsic semiconductor materials such as silicon, germanium, etc. All the above materials, show unique as well as tunable optical properties and comprises a major part of photonic[20] materials. Confinement of electrons in the valence band and discretization of energy levels in semiconductor nanomaterials give rise to unique optical[21], electrical and thermal properties[22].

1.1.3. Organic based nanoparticles

Organic based nanoparticles find its origin in self assembled organic molecules which constitutes liposomes[23], vesicles[24], dendrimer[25], micelles[26] and polymeric[27] nanomaterials. All the above nano-structures are formed due to self-assembly of organic molecules which involves non-covalent interactions[28]. Organic nanoparticles are mostly used as a drug carrier[25]. Interestingly, organic nanomaterials are often used for trans-dermal therapy due to their high biocompatibility and permeability[29].

1.1.4. Nanocomposites

This class of NMs are mostly combination of two or more of the above types of materials. The nanocomposites are found to show synergistic enhancement[30] in properties of materials. Nanocomposites are generally tailor-made NMs used to serve a definite purpose. For instance, silver/silver chloride hybrid nanocomposites finds its probable application in photocatalysis where silver nanoparticle serves as a photosensitizer for silver chloride semiconductor photocatalyst[31].

Another classification of NMs can be done based on dimensions. Nanomaterials show unique properties owing to increased surface to volume ratio[32]. For a given material, surface to volume ratio, S/V is given by,

$$\frac{S}{V} = \frac{4\pi r^2}{\frac{4}{3}\pi r^3} = \frac{3}{r} \qquad (1.1)$$

where S/V is surface to volume ratio and r is the radius of the nanoparticle, respectively.

Surface to volume ratio is inversely proportional to the radius of the particle. As the particle size reaches nanometric dimension, percentage of atoms or molecules present on the surface increases. There is a fundamental difference between the atoms present on the surface and bulk. In bulk, atoms or molecules experience isotropic environment unlike that on the

surface. In nanoparticles, increased surface area leads to increased surface energy. This surface energy is quenched either by agglomeration or by capping agents. Besides size, shape of nanoparticles plays an important role in determining their chemical and physical characteristics.

1.2. Classification of nanomaterials based on dimensional property

Different types of nanomaterials based on dimensions are as follows:

1.2.1. 0D NMs: NMs where the motion of electron is dimensionless, i.e., confined to a very small space is known as 0-D NMs. Examples of 0D NM includes quantum dots, silver and gold nanoparticles.

1.2.2. 1D NMs: NMs where electrons are free to move in any one direction are referred to as 1D NMs. Examples of 1D NMs includes carbon nanotubes and nanowires.

1.2.3. 2D NMs: Nano flakes or plates can be considered as2D NMs. Graphene is one such example.

1.2.4. 3D NMs: Nanostructures which show electron motion in all directions, are 3D NMs. They are associations of 1D or 2D NMs.

In this work, inorganic 0D nanoparticles are investigated in detail. It would be important to understand the extent of advancement that has occurred around inorganic nanomaterials.

1.3. Inorganic nanomaterials and their types

Inorganic nanomaterials mostly consist of metal, metal chalcogenides and metal halides nanoparticles. Metal nanoparticles are most extensively exploited nanomaterial because of their unique optical properties, inert nature and biocompatibility. Semiconductor nanoparticles have also been extensively exploited for easy tunability of band gap as well as optical properties.

1.3.1. Metal nanoparticles

Existence of metals in their elemental form depends on its standard reduction potential. Standard reduction potential ($E^0_{M^{n+}/M}$) of redox half-cell (M^{n+}/M) in its standard state is defined as the electromotive force of the cell when it connected to standard hydrogen electrode (SHE)[33]. Standard reduction potential of SHE is generally taken as 0.00 V by convention. Electromotive force of a cell is given by,

$$\mathrm{E}^0_{cell} = \mathrm{E}^0_{cathode} - \mathrm{E}^0_{anode} \qquad (1.2)$$

where E^0_{cell} is the electromotive force of the cell, $\mathrm{E}^0_{cathode}$ is the standard reduction potential of cathode half-cell and E^0_{anode} is the standard reduction potential of cathode half-cell. For any spontaneous reaction, E^0_{cell} must be greater than zero. Reduction and oxidation take place at cathode and anode, respectively. Moreover, reagent undergoing oxidation is a good reducing agent and vice versa. SHE can be both in anode as well as cathode depending on the activity of the redox couple under inspection. Metal which can reduce acidic proton to hydrogen gas is a stronger reducing agent than SHE. E^0 of such metals is always negative. Another interpretation is that these metals do not favour reduction as E^0 stands for "Standard reduction potential". Similarly, those metals which cannot reduce acidic proton, have positive E^0 value. These metals tend to remain in elemental state. Examples of metals with negative E^0 value are sodium, potassium, calcium, magnesium, iron, aluminium, etc, whereas those with positive E^0 values are gold, silver, copper and platinum. Metals with positive E^0 values are less reactive and less prone to corrosion, which has earned them the title of noble metals. Most of the metal nanoparticles consists of noble metals. Surveying the literature, it can be observed that very few metals other than noble metals are stable in colloidal state. Aluminium nanoparticles are highly reactive and are often prepared by non-

aqueous physical synthetic routes[34]. Aluminium nanoparticles are used as rocket propellant. Manganese[35], cobalt[36] and iron[37] nanoparticles are also synthesized with great difficulty using very strong reducing agents for their unusually strong magnetic property. The quantum of work done in the field of noble metal nanoparticles is comparatively much larger in terms of tunability of properties as well as application than other non-noble metals.

Noble metals such as gold[38], silver[39], platinum[40] and copper[41] show surface plasmon resonance in nanometric dimension. Noble metal nanoparticles (NMNPs) have shown potential for catalytic[42-48], sensing[49-56] and biomedical[57-62] applications. Gold and silver nanoparticles have been discussed later in detail.

1.3.2. Metal chalcogenide and metal halide nanoparticles

Metal oxides, sulphides, selenides, etc. constitutes metal chalcogenides. Iron oxide nanoparticles finds application in biomedicine[63] as they are biocompatible and potential non-toxicity[64] to humans. Magnetic property of iron oxide nanoparticles can be exploited for real-time magnetic resonance imaging[65]. Cadmium sulphide[66] and cadmium selenide[67] are well known semi-conductor material. In nanometric dimensions quantum dots of cadmium sulphide as well as selenides show discretization of bands which results in increasing the band gap of semiconductor materials[68]. Metal halides such as silver chloride[69] are reported to be semi-conductors of class I-VII compounds. In this work, we have carried out some studies with silver chloride which is discussed in later chapters.

1.4. Noble metal nanoparticles and associated phenomena

Noble metal nanoparticles show unique optical property know as surface plasmon resonance (SPR) opens up a new multidisciplinary branch of science, popularly known as '*Plasmonics*'. All metal nanoparticles which show SPR are called as plasmonic

nanoparticles. It is essential to understand the phenomena associated with generation of SPR in order to understand noble metal nanoparticles.

1.4.1. Plasmonics

Surface plasmon resonance is an electromagnetic phenomenon arising from interaction of incident light with free electrons at the metal-dielectric interface which results in emergence of two-dimensional longitudinal electromagnetic wave of free electrons. Energy of photons is transferred to the free electron only at a specific wavelength when the momentum of photons matches that of the oscillating free electrons[70]. These collectively oscillating free electrons are confined to the surface of the metal and are collectively known as surface plasmon (SP).The SPs excited are localized at the interface as a result are considered as surface waves that propagate along the interface and decay exponentially with distance normal to the interface. There are basically two types of SPs, propagating and localized. In propagating SPR (PSPR), plasmons propagate upto micron or tens of micron distances and decays perpendicular to the surface. Decay lengths are very high, of the order of half the wavelength of incident light. On the other hand in case of localized surface plasmons, nanoparticles much smaller than the incident light experience uniform electric field as a result free electrons oscillate synchronously with the oscillating electric field of the electromagnetic wave. This leads to a plasmon that oscillates locally around the nanoparticle with frequency known as the localized surface plasmon resonance (LSPR). As the propagation length of PSPR and LSPR are different, the sensitivity to surrounding dielectric environment is different. PSPR responds sensitively to changes in bulk dielectric environment where as LSPR responds to changes in local dielectric environment such as molecular adsorption layer. Thus PSPR is sensitive to large biomolecules and LSPR sensors can detect small molecules. Again, the interaction of individual electric field of LSPR of two or more nanoparticles give rise to surface enhanced Raman scattering (SERS).

1.4.1.1. Localized surface plasmon resonance (LSPR)

When size of metal nanoparticles is restricted to sub wavelength dimensions, the plasmons cannot propagate beyond the physical boundary of the nanoparticles. Hence, they become localized. Most interesting feature of such a phenomenon is concentration of light in a region smaller than the wavelength of light. Enhance electric field associated with LSPR acts as a local source of excitation for vicinal molecular layer, i.e., local dielectric environment.

Let us consider a metallic sphere of radius R embedded in a medium of dielectric constant ε_d. Since the electric field is uniform at any instant of time around the metallic sphere, it is safe to assume $R<<\lambda$. The solution for Laplace's equation for the static potential inside a sphere can be given as[71, 72]:

$$\phi\,(r,\theta,\varphi) = \sum_{l=0}^{\infty}\sum_{m=-1}^{l} a_{lm}\, r^{l} Y_{lm}\,(\theta,\varphi)\,, \qquad 0 \le r \le R \tag{1.3}$$

where r,θ,φ are the radial, polar and azimuthal coordinates accordingly; $Y_{lm}\,(\theta,\varphi)$is the spherical harmonic function. Outside the sphere, the solution is:

$$\phi\,(r,\theta,\varphi) = \sum_{l=0}^{\infty}\sum_{m=-1}^{l} b_{lm}\,\frac{1}{r^{l+1}} Y_{lm}\,(\theta,\varphi), \qquad r \ge R \tag{1.4}$$

The solution of the equations 3 and 4, vanish at the center of the sphere and infinity respectively. The continuity condition at the surface for the potential and its derivative $\varepsilon\partial\varphi/\partial r$ leads to the following dispersion relation:

$$\frac{\varepsilon_m}{\varepsilon_d} + \frac{l+1}{l} = 0 \tag{1.5}$$

where ε_m is the dielectric constant of the medium.

Using Drude form for metal dispersion, we get:

$$\omega_l = \omega_p \left[\frac{l}{\varepsilon_d(l+1)+l}\right]^{1/2} \quad (1.6)$$

where l is a positive integer. For lowest order mode, $l = 1$ denotes the dipole mode which is the most significant mode for small sphere. On the other hand for large spheres, $\rightarrow \infty$, is the most significant mode, where the resonance frequency becomes $\omega_\infty = \omega_p\sqrt{(\varepsilon_d + 1)}$ which is the SP frequency for semi-infinite metal-dielectric interface.

For the dipolar case, the electromagnetic field outside the sphere is given as:

$$E_{out}(x,y,z) = E_0\hat{z} - \left[\frac{\varepsilon_m - \varepsilon_d}{\varepsilon_m + 2\varepsilon_d}\right].a^3E_0.\left[\frac{\hat{z}}{r^3} - \frac{3z}{r^5}(x\hat{x} + y\hat{y} + z\widehat{z})\right] \quad (1.7)$$

where E_0 is the applied magnetic field polarized in z direction. The electromagnetic field displaces the free electron cloud and produces a positive charge near the particle surface. This resonance associated to the above oscillations is called the localized SPR (LSPR). The term “surface” is used as the oscillations are caused by the polarization of the particle surface, and also because the generated electric field is larger near the particle surface and decays with distance normal to the surface. The frequency of the collective oscillations is dependent upon factors such as the electron concentration, electron effective mass, the particle shape and size, interaction between particles, and the influence of the environment. For the elementary description of the nanoparticles plasmon resonance it is sufficient to use the usual dipole approximation as within nanometric size regime only dipolar mode is active.

Within the dipole approximation the absorption and scattering of light by a small particle are determined by the electrostatic polarizability of the particle α_0, which can be calculated using themetal optical permittivity$\varepsilon_m(\omega)$, the medium dielectric constant ε_d, and the particle geometricaldimensions[73]:

$$\alpha_0 = \frac{3}{4}\frac{V}{\pi}\left[\frac{\varepsilon_m - \varepsilon_d}{\varepsilon_m + 2\varepsilon_d}\right] = a^3\left[\frac{\varepsilon_m - \varepsilon_d}{\varepsilon_m + 2\varepsilon_d}\right] \quad (1.8)$$

Extinction cross-section may be considered as a sum of absorbed and scattered radiation which is accounted as:

$$C_{ext} = C_{abs} + C_{sca} = \frac{12\pi k}{a^3}\frac{\varepsilon_d \mathrm{Im}(\varepsilon_m)}{|\varepsilon_m - \varepsilon_d|^2}.|\alpha|^2 + \frac{8\pi}{3}k^4\alpha^2 \cong 4\pi k\,\mathrm{Im}(\alpha) \quad (1.9)$$

where $k = \frac{2\pi\sqrt{\varepsilon_d}}{\lambda}$.

The above expression clearly shows that maximum polarizability condition is achieved when $(\varepsilon_m + 2\varepsilon_d) \to 0$.

Thus, the resonance condition is established when

$$\varepsilon_m = -2\varepsilon_d \quad (1.10)$$

Dielectric constants of most of the solvents are positive. For instance, dielectric constant of water is 80. This means that two charges when separated in water, each experience 1/80th of the coulombic force as they would experience in vacuum. Thus, dielectric constant may be understood as a property of a material which quantifies the tendency of the material to resist changes associated with an electric field vector. Positive dielectric constant means that it highly resists change. Higher the value higher is the resistance. Negative dielectric constant means it is completely non-resistive. Rather higher negative value indicates enhanced effect of electric field vector on the material. For the above LSPR condition to hold, metals must exhibit negative dielectric constant values in nanometric dimensions.

The physical significance of negative dielectric constants in noble metals in visible region means that in presence of electric field vector of electromagnetic radiation, electric field on the surface is enhanced due to formation of plasma in the electron gas of the metal surface. In a typical schematic representation of polarization of electron gas of metal nanoparticles,

electron cloud is displaced synchronously with electric field vector of electromagnetic radiation which is shown in fig. 1.1.

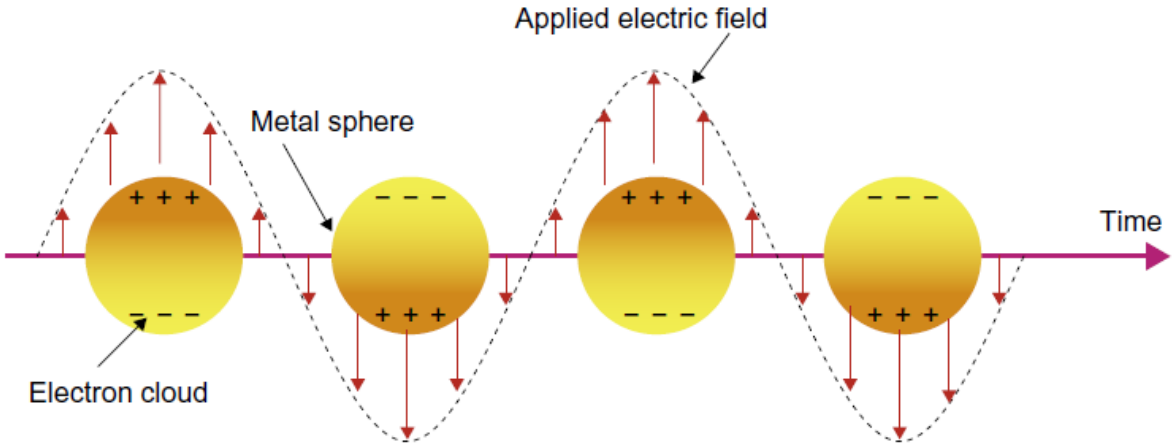

Figure 1.1. *Displacement of electron cloud on metal nanoparticles upon excitation by electromagnetic radiation.*

1.4.1.2. Plasmon in anisotropic nanoparticles

It is well known that charge density on a metallic surface is inversely proportional to the radius of curvature[74]. In an anisotropic nanoparticle, assuming it to be a nanorod, electron density is minimum at the equatorial region where as maximum at the ends of the axis. The above is explained schematically in 1.2. Moreover, this difference in electron density increases with increasing aspect ratio, i.e., the ratio of major vs. minor axis. Electronic oscillation along axis of the nanorod is more polarizable which means that ε_d corresponding to longitudinal oscillation is more negative than that of transverse oscillation. In order to meet the resonance condition mentioned in eq.10, ε_m must increase in case of longitudinal oscillation. It is known that dielectric constant generally decreases with decreasing wavelength as lesser number of modes of polarization is available for propagation of electromagnetic radiation[75]. Thus, lowerε_d for longitudinal vibration balances ε_m at a higher wavelength whereas ε_d for transverse vibration remains closer to plasma frequency of the

metal. With increasing aspect ratio, the difference between SPR of longitudinal and transverse mode increases. Mulvaney et. al. has shown that the longitudinal and transverse SPR of gold nanorods (GNRs) evolve with change in aspect ratio[76].

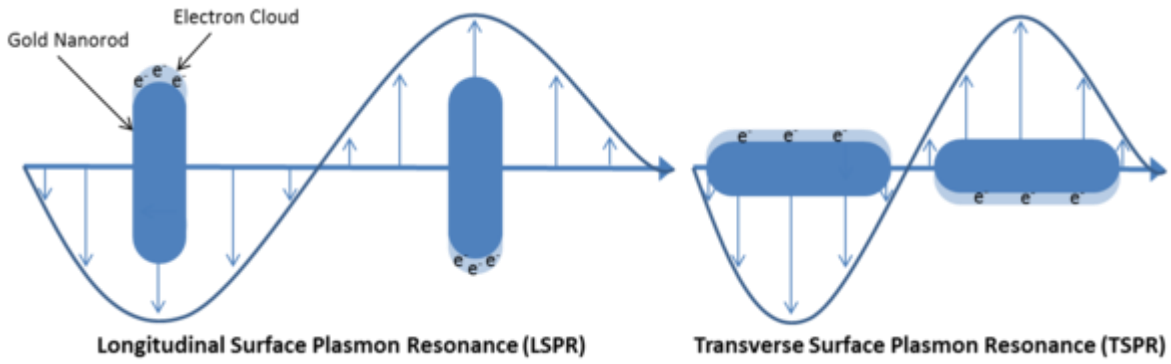

Figure 1.2. *Displacement of electron cloud on metal nanorods parallel and perpendicular to major axis in gold nanorods upon excitation by electromagnetic radiation.*

1.4.1.3. Effect of size on surface plasmon resonance

As the size of plasmonic nanoparticles is increased, the SPR is found show red-shift along with broadened peak feature. The dipolar approximation of surface plasmon is based on the idea that as the particle is much smaller than the wavelength of incident light. As the size increases, the surface electrons begin experiencing non-uniform electric field. As a result, higher order modes of vibration appear in the absorption spectra of plasmonic nanoparticles of larger sizes. With increasing contribution of low energy higher order modes of oscillation, SPR of plasmon nanoparticles show apparent red-shift along with peak broadening[77].

1.4.1.4. Plasmonic coupling

Plasmonic nanoparticles such as gold and silver nanoparticles show near field in the vicinity of the surface of the nanoparticle. This near field tend to decay with distance normal to the surface[78]. Every electron could on the plasmonic nanoparticles has its own polarizability,

α_m. Electric field vector, E_0 of an electromagnetic radiation generates an oscillating dipole, P_m on the plasmonic nanoparticle which is given as

$$\vec{P}_m = \hat{\alpha}_m \vec{E}_0 \tag{1.11}$$

Another plasmonic nanoparticle at a distance, r from the surface of the above nanoparticle shall experience cumulative electric field due to incident electromagnetic radiation as well as near field of the adjacent nanoparticles. Near field of a plasmon experienced at a distance, r from the surface is given by

$$\vec{E} = \frac{\vec{P}}{r^3} \tag{1.12}$$

Cumulative field experienced by the other plasmonic particle generates an oscillating dipole in the particle given by

$$\vec{P_i} = \hat{\alpha}_m \left(E_0 + \frac{\hat{\alpha}_m E_0}{r^3}\right) = \hat{\alpha}_m E_0 \left(1 + \frac{\hat{\alpha}_m}{r^3}\right) \tag{1.13}$$

Likewise, the first particle also experiences enhanced excitation field. After n^{th} times enhancement or amplification, the enhanced oscillating dipole is given by

$$\vec{P_i} = \hat{\alpha}_m E_0 + \frac{\hat{\alpha}_m E_0}{r^3} \left(1 + \hat{\alpha}_m + \hat{\alpha}_m^2 + \cdots + \hat{\alpha}_m^n\right) \tag{1.14}$$

The enhancement of interparticle plasmonic coupling[79] is limited by dielectric constant of the surrounding medium, ε_m. Higher near field reduces $\varepsilon_d$which is compensated by ε_m at red-shifted wavelength to fulfil the SPR resonance condition. The extent of red-shift in SPR of gold or silver nanoparticles is a measure of plasmon coupling in self assemblies. This red-shift in SPR band serves as the basis of agglomeration based sensing of analytes or adsorbates[79]. The above enhanced electric field is also expressed in far-field as *surface enhanced Raman scattering* (SERS).

1.4.1.5. Surface enhanced Raman scattering (SERS)

Light can be scattered on incidence with matter with or without loss or gain of energy. An electromagnetic radiation consists of two mutually perpendicular transverse fields, electric and magnetic[80]. Electric field distorts the electron cloud in any atomic or molecular orbital. When the extent of distortion is such that the shape of the transformed orbital matches geometrically with the higher energy excited state, electronic excitation takes place. In such a case, we observe colour and this absorption can be studied by UV-vis spectroscopy[81]. But when the electric field mildly polarizes the electron cloud to form a transformed orbital such that no electronic transition occur, this transformed orbital is called virtual state, which immediately releases the absorbed energy. This phenomenon is known as scattering. When the wavelength of radiation released from the virtual state is same as that of absorbed radiation, then the phenomenon is called Rayleigh scattering[82]. But if there is a change in wavelength of the scattered radiation with respect to that of the incident radiation, it is called Raman scattering[83]. The vibrational energy levels are present within an electronic energy level. Hence Raman lines contain information about the vibrational state of the molecule, which is shown in fig. 1.3.

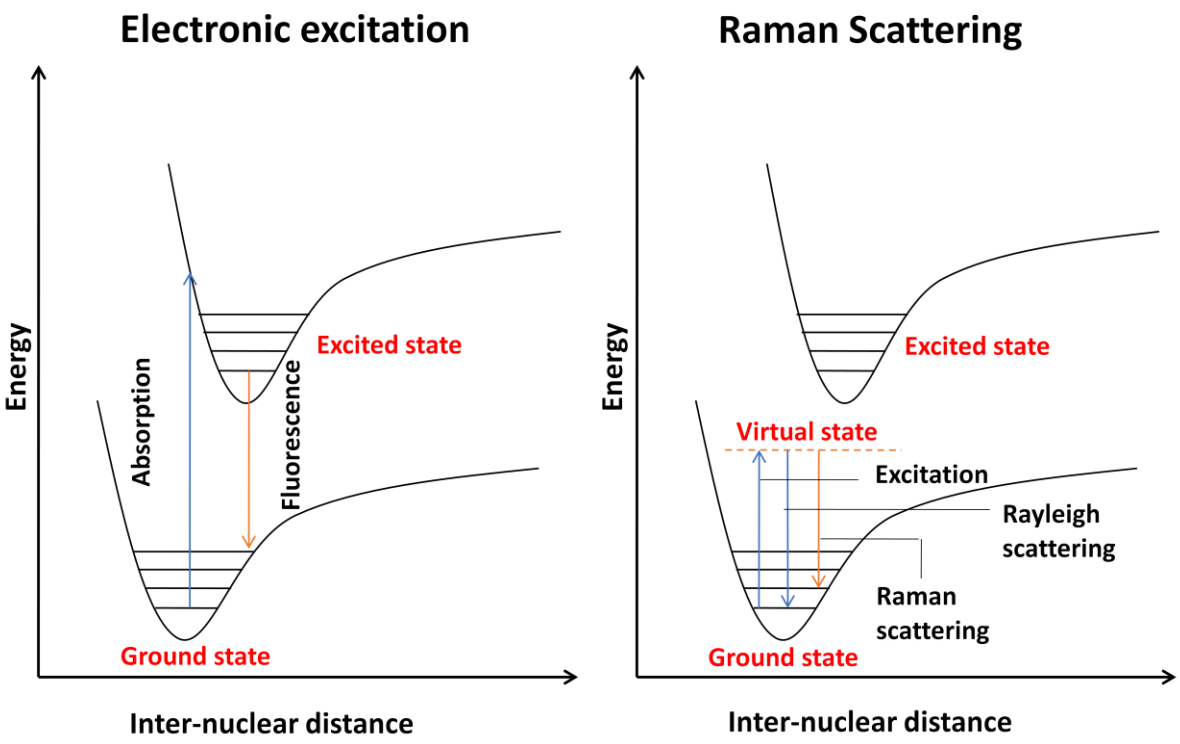

Figure 1.3. *A schematic representation electronic transition and Raman scattering.*

Raman spectroscopy is a technique complementary to infrared absorption spectroscopy[84] which has an absorption cross-section of about ~10^{-24} cm^2. On the contrary, Raman spectroscopy[83] is a scattering technique with a scattering cross-section of ~10^{-30} cm^2. This low scattering cross-section makes Raman technique suitable only to solid samples or solution upto 10^{-2} M concentration. In order to study vibrational features of molecule present at a much lower concentration for the purpose of detection by fingerprinting, Raman technique is modified with the help of plasmon[85]. In the earlier section, we have discussed that light upon incidence on a noble metal nanoparticles incite 'lossy quasi-particles' called plasmons[86]. The plasmon can also be taken as a source of alternating electric field resonant with the incident radiation. Any molecules, adsorbed on the surface of gold or silver nanoparticles are polarized by the plasmon in the vicinity, to form a virtual state which releases energy back to plasmons, which further interact with the incoming electromagnetic radiation and scatters the light with vibrational information embedded with it. This

phenomenon of extracting vibrational information of trace concentration of molecules adsorbed on noble metal nanoparticles is called surface enhanced Raman scattering (SERS). However, understanding the vibrational spectroscopy is essential to interpret SERS signals.

1.4.1.5.1. Vibrational spectroscopy

In order to understand SERS, it is essential to know the motivation behind exploration of vibrational spectra of a molecule. A molecule consists of many bonds. When each and every bond of the molecule is stabilized, the molecule is said to exist in its ground state. Every bond has its unique potential energy which varies with inter-nuclear distance as shown in fig. 1.3. Out of all the bonds, the chemical bonds where lone pair or π-bonding is involved, the energy gap between excited state and ground state is often found to be in the range of visible region. Upon excitation with electromagnetic radiation comparable to the above energy gap, the electronic transition occurs. Every bond has its associated discrete vibrational levels as shown in fig. 1.2. Vibrational levels of any bond can be mapped either using absorption technique as in infrared spectroscopy or using scattering technique as in Raman spectroscopy. Vibrational spectrum of any molecule is its unique feature which is often referred as chemical fingerprint.

Any molecule with N number of atoms has 3N degrees of freedom. For any non-linear molecule, there are 3N-6 vibrations where as for a linear molecule there are 3N-5 vibrations[87, 88].

Typical modes of vibrations are as follows:

(a) Stretching: Bond length between two atoms increase and decreases periodically with respectto an equilibrium bond distance with an vibrational frequency, ω_{osc} given by:

$$\omega_{osc} = \frac{1}{2\pi}\sqrt{\frac{k}{\mu}} \qquad (1.15)$$

where k is the force constant of the bond and μ is the reduced mass of the two atoms.

Typically the vibrational energy of a chemical bond is typically measured in wave numbers (cm^{-1}). Bond containing heavier atoms as well as with higher bond orders appear at higher wave numbers.

(b) Symmetric stretching (three atom systems): Synchronous stretching of two bonds is generally known as symmetric stretching. Net change in dipole moment is zero in case of two adjacent bonds with 180° angle. In all other cases, net change in dipole moment is vectorial addition of dipole moment at any moment.

(c) Asymmetric stretching (three atom systems): Asynchronous stretching of two bonds is generally known as asymmetric stretching, where one bond expands and the other compresses at the same time. Net change in dipole moment is non-zero in case of two adjacent bonds with 180° angle.

(d) Scissoring(three atom systems): The bond angle between three consecutive atoms in a molecule varies from minimum to maximum value during bending motion.

*(e) Wagging:*Two bonds of a tetravalent atom move out of plane synchronously as well as in same direction, with respect to the molecular plane in wagging.

(f)Twisting: Two bonds of a tetravalent atom move out of plane synchronously but in opposite direction, with respect to the molecular plane in twisting.

(g) Rocking: Two bonds of a tetravalent atom move in-plane synchronously in same direction in rocking.

There are other complex modes which are variations of the modes mentioned above (fig. 1.4).

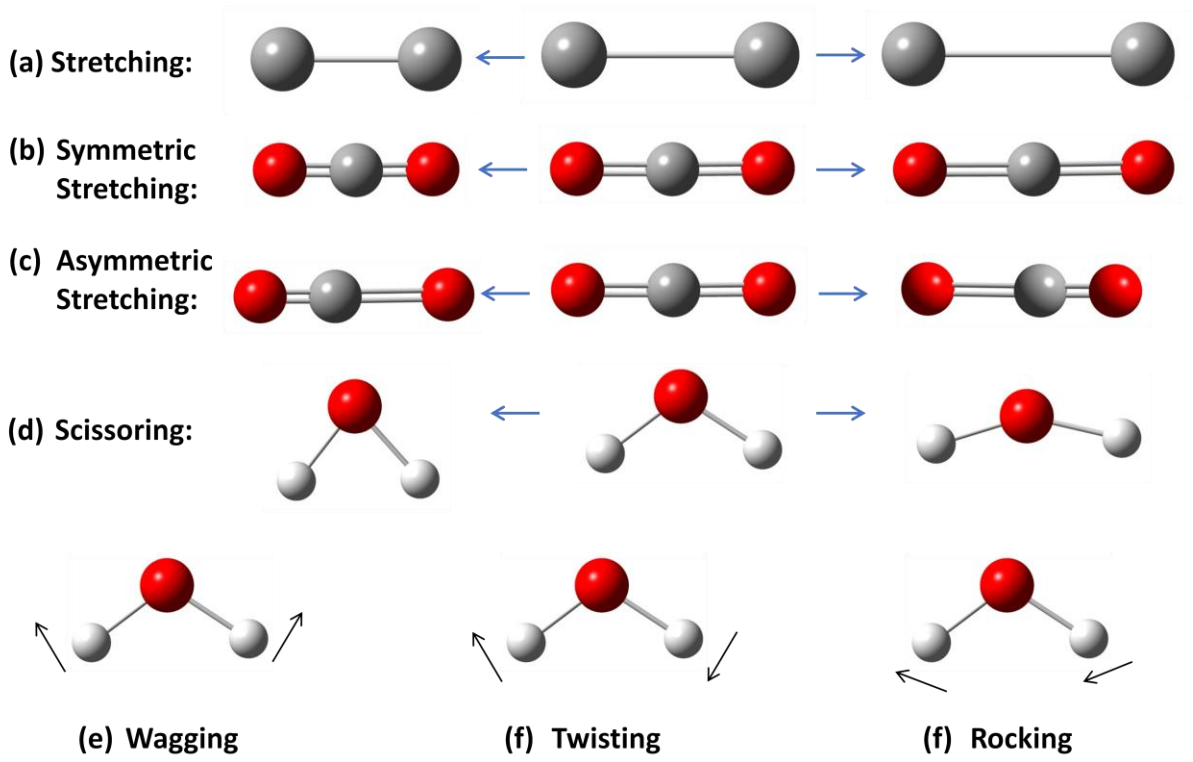

Figure 1.4. *A schematic representation of different modes of molecular vibrations.*

1.4.1.5.1.1. Infrared spectroscopy

Electromagnetic radiation in the infrared region is absorbed by vibrating bonds upon resonance. Thus, absorption of energy, E, that matches the vibration frequency, υ, would trigger molecular vibration because of the change in the dipole moment[89].Asymmetric modes of vibrations are more prone to show net change in dipole moment upon vibration. Moreover, bending needs less energy compared to stretching and hence is more feasible, as the net change in dipole moment is comparatively less in bending than that in stretching.

There are different IR zones, namely, the far-IR (FIR, 400–10 cm^{-1}), the mid-IR (MIR, 4000–400 cm^{-1}) and the near-IR (NIR, 14,000–4000 cm^{-1}) zones. It is the mid-IR region where most compounds would have a signature absorption/emission in this region. Based on

the types of vibrational bands observed, the MIR region can be further divided into the *fingerprint region* (400–1400 cm^{-1}) and the *functional groups' region* (1400–4000 cm^{-1})[87].

1.4.1.5.1.2. Raman spectroscopy

Electromagnetic radiation in the visible region is polarizes the electron cloud around the bonds in a molecule which radiates upon non-absorption to show Rayleigh and Stokes/anti-Stokes scattered radiation.

Absorption, fluorescence, phosphorescence and stimulated emission deal with electronic transitions between two or more electronic states. Scattering is altogether a different phenomenon which involves the simultaneous (instantaneous) absorption of an incident photon and emission of another photon. The emitted photon is called the scattered photon. Scattering processes can further be categorized into two main groups:

In elastic scattering, the incident and scattered photons possess the same energy but may have different direction or polarization. For molecules, this process is called Rayleigh scattering. Rayleigh scattering does not reveal much about the electronic energy levels of the molecule and at the end of the scattering the molecule remains unaffected. Elastic scattering is for larger objects, and in particular for nano-particles (metallic or not); it is then usually called Mie scattering.

In inelastic scattering, the scattered photon is at a different energy from that of the incident photon (fig. 1.3). The energy difference corresponds to an accompanying transition between two states in the molecule. One of the most important forms of inelastic scattering in molecules is Raman scattering, which involves transitions between the vibrational/rotational levels.

A molecule in a static electric field, E, experiences distortion in the electric cloud, which results in separation of charges. As a result, an induced dipole, μ is generated. The magnitude and direction of μ depends upon the polarizability of electron cloud on any bond.

$$\mu = \alpha E \tag{1.16}$$

The polarizability of any bond can be described to some extent with the help of polarizability ellipsoid. Polarizability ellipsoid of hydrogen bond in different directions is shown in fig. 1.5.

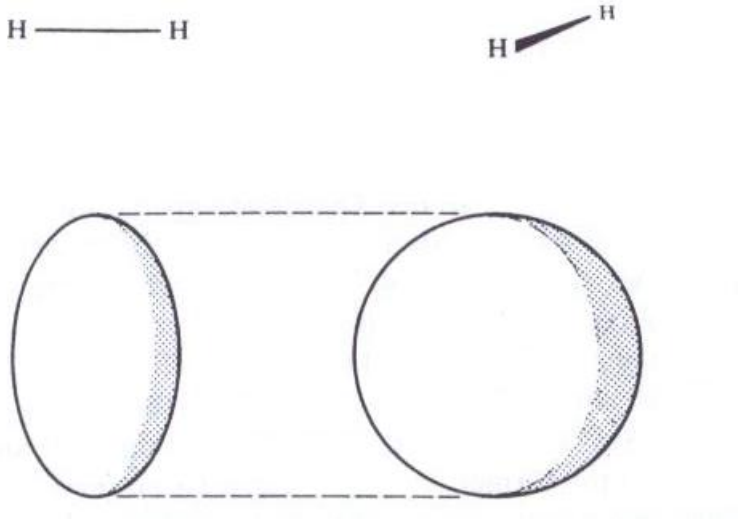

Figure 1.5. *Hydrogen molecule and its associated polarizability as observed in two dimensions at right angles.*

The distance of any point on the surface of the polarizability ellipsoid from its centre is the measure of polarizability of the associated bond at that point. One can seen upon three-dimensional visualization, that the polarizability ellipsoid in the above case is like a flattened sphere, whose minor axis is in line with the principal axis of the molecule.

Any molecular bond undergoes internal motion such as rotation and vibration. Internal vibration motion tends to change the polarizability periodically. In case of stretching, a

periodic vibration with frequency ν_{vib}, changes the polarizability, with respect to time. The instantaneous polarizability is given by,

$$\alpha = \alpha_0 + \beta \sin 2\pi \nu_{vib} t \quad (1.17)$$

Moreover, when a molecule encounters an incident electromagnetic radiation, it experiences oscillating electric field, E where in electric field varies with respect to time at any particular point, which is given by

$$E = E_0 \sin 2\pi\nu t \quad (1.18)$$

where E_0 and ν are the amplitude and frequency of the electromagnetic radiation, respectively.

Upon substitution of the values of α (eq. 17) and E (eq. 18), in eq. 16, the instantaneous induced dipole moment bears a signature of time, which is given by

$$\mu = (\alpha_0 + \beta \sin 2\pi \nu_{vib} t) E_0 \sin 2\pi\nu t \quad (1.19)$$

Upon expanding eq. 18, using the trigonometric relation,

$$\sin A \sin B = \frac{1}{2}\{\cos(A - B) - \cos(A + B)\} \quad (1.20)$$

we get,

$$\mu = \alpha_0 E_0 \sin 2\pi\nu t + \frac{1}{2}\beta E_0\{\cos 2\pi(\nu - \nu_{vib})t - \cos 2\pi(\nu + \nu_{vib})t\} \quad (1.21)$$

and thus the oscillating dipole has frequency components $\nu \pm \nu_{vib}$ as well as exciting frequency ν.

It can be noted from eq. 21, that if vibration does not alter the polarizability, i.e. $\beta = 0$, the oscillating dipole has the frequency same as the incident radiation.$\nu - \nu_{vib}$ and $\nu + \nu_{vib}$

corresponds to the stokes and anti-stokes lines associated with Raman scattering, repectively.

Thus, for any chemical bond to show Raman signal, it is important to have a change in polarizability upon vibration which is reflected by change in either magnitude or in direction of the polarizability ellipsoid. In order to understand the impact of change in polarizability, let us consider the following cases:

Case 1: Linear molecule molecules such as CO_2 shows change in polarizability in symmetric vibrational modes which is shown in fig. 1.6.

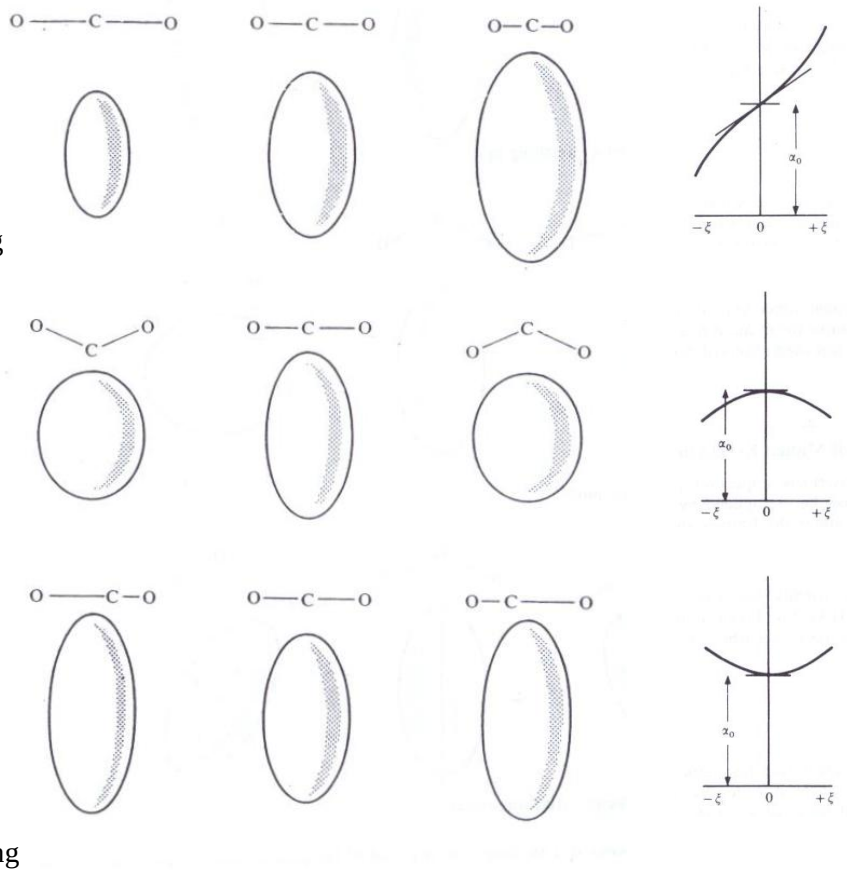

(a) Symmetric stretching

(b) Symmetric bending

(c) Asymmetric stretching

Figure 1.6. *Schematic representation of vibrational modes of CO_2 and their associated change in polarizability ellipsoid presented along with change in polarizability with displacement across the equilibrium state, ξ.*

It can be seen in fig. 1.6., that only symmetric stretching mode is showing a change in polarizability across the equilibrium state. It can also be said that the strength of Raman signal is proportional to the magnitude of $\frac{d\alpha_0}{d\xi}$.

Case 2: Non-linear molecule molecules such as H_2O shows change in polarizability in symmetric vibrational modes which is shown in fig. 1.7.

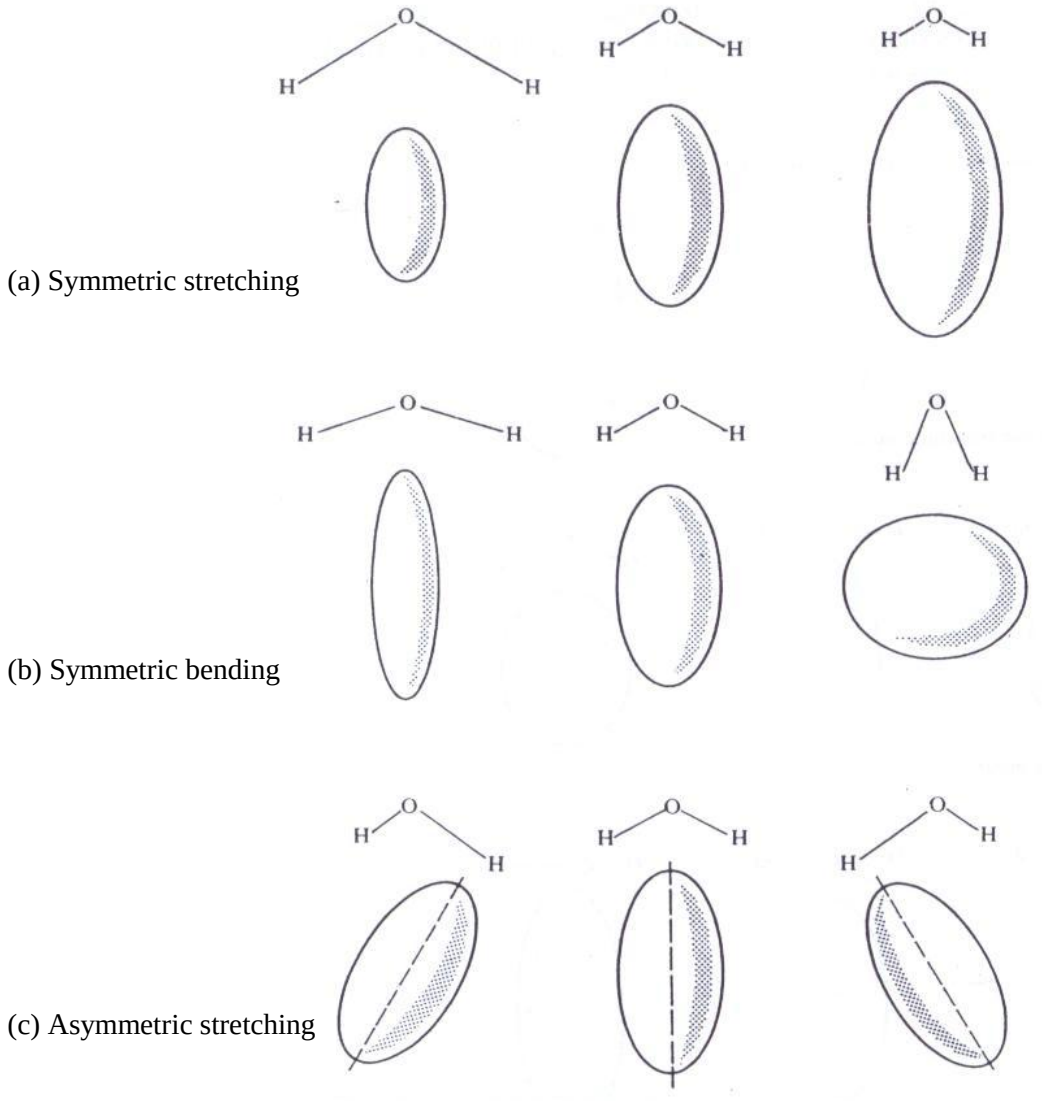

Figure 1.7. *Schematic representation of vibrational modes of H_2O and their associated change in polarizability ellipsoid.*

In case of H_2O, in all the three vibrational mode, there is an observed change in polarizability in terms of either magnitude or direction. In case of asymmetric stretching of water, the observable change in polarizability is weak.

From the above two cases, it can be generalized that *symmetric molecules show intense Raman signals.* Again, in molecules such as CO_2 which has a centre of symmetry, shows mutually exclusive Raman and IR active modes.

1.4.1.5.2. Types of SERS substrates

Solution based SERS substrates: Gold and silver nanoparticle solutions are most common forms of SERS substrate as chemical reduction is the most accessible form of synthesis methodology. Weakly bound reducing agents such as sodium citrate[90, 91], sodium borohydride[92, 93], ascorbic acid[94, 95], are mostly used for synthesis of SERS substrate solutions. Very low detection limit can be achieved in case of sensing of analytes using SERS substrate solutions as the noble metal nanoparticles are sensitive to very slight change in dielectric environment over the surface of metal nanoparticle. Reusability and colloidal stability of the substrate are drawbacks which has led to their limited use for R&D purposes[96].

Solid SERS substrate: Metal nanoparticles deposited on solid supports are often used for SERS sensing. The methods used for fabrication of substrates includes electron-beam lithography[97], electrodeposition[98], chemical deposition[99], etc. The substrates are often reported to be reusable and have high shelf life[100]. The substrates find application in onsite sensing of analytes yet the sensitivity achieved in case of solid supported SERS substrate is not as good as SERS substrate solution due to limited freedom for inter-particle interaction. The hot-spots developed in case of solid substrates are preformed and the addition of analytes only changes the dielectric environment over nanoparticle surface.

1.4.1.5.3. Advantages of SERS for societal applications over other techniques

Molecular sensing is often used for detection of hazardous chemicals such as pesticides[101], industrial effluents[102], pathogens[103], food adulterants[104], dopant drugs[105], etc. for bio-medical, diagnostic, environmental monitoring and quality control applications. Techniques used for sensing of the above-mentioned analytes are mass spectrometry, fluorimetry, gas chromatography, etc. The above techniques have ultra-trace level detection limits. The above techniques cannot qualitatively confirm the presence in presence of complex sample matrix as they lack fingerprinting ability. On the other hand, Raman spectroscopy is a powerful tool showcasing finger printing ability in presence of complex matrix. Vibrational signature of a molecule is a characteristic feature of any molecule. Upon pin-pointing the marker Raman bands, the analytes can be qualitatively and quantitatively detected. Unlike standard sensing techniques, every SERS sensing methodology requires unique sample processing. This gives SERS sensing leverage over other analytical tools.

1.4.1.5.4. Application of SERS

SERS spectra of any analyte adsorbed on the surface of plasmonic nanoparticles provides information about the chemical characteristics of the analyte such as concentration[106], surface selectivity[107] and surface orientation[108]. Determination of concentration can be carried out using SERS technique[109]. Molecules with affinity to adsorb over silver or gold nanoparticles can be detected as the LSPR polarizes the molecules in the vicinity. Higher concentration of molecules tends to show low SERS signal as the molecular vibrations are suppressed in multi-layer systems. Upon reducing the analyte concentration to monolayer, maximum SERS intensity is obtained. Further lowering the concentration, reduces SERS signal due to sub monolayer formation. A calibration curve can be obtained from monolayer system to sub monolayer system for quantitative analysis of analytes. SERS intensity of the

strongest peak in the spectra is plotted with respect to concentration to obtain the calibration curve. Apart from quantitative analysis, peak positions in SERS spectra are characteristic of the molecule which forms the basis of qualitative analysis using SERS[110]. Molecules with hard basic groups tend to show stronger affinity toward hard acid metal surfaces such silver whereas soft basic groups show affinity towards soft surfaces such as gold. For instance, N-atoms show stronger affinity for silver whereas S-atom tends to adsorb on gold nanoparticle surface[111]. Moreover, SERS spectrum provides additional information about the groups attached to the metal nanoparticle surface. Groups attached to metal surface will show red-shifted peaks in SERS spectra in comparison with the Raman spectra of the free molecule in solution. This information is vital to understand in case of drug delivery, where active sites of the drug molecule are required to be free to form further bonds with the target. Orientation of molecules is another vital information provided by SERS technique. LSPR intensity is perpendicular to the surface of the metal nanoparticles. Polarizability ellipsoid of the bond under inspection must show a change in polarizability parallel to the LSPR oscillation in order to exhibit strong SERS intensity. This forms the basis of surface selection rules associated with SERS technique[112]. Upon analysis of relative intensity of the peaks and comparing it with the Raman spectra of free molecule, the orientation of the molecule on the surface of plasmonic nanoparticles can be ascertained. This information is also vital from catalysis[113] and drug delivery[114] point-of-view.

1.4.1.5.5. Development of SERS substrates

In this thesis, SERS substrates were developed for detection of a variety of materials such as thioflavin T (ThT), 2,5-dimercapto-1,3,4-thiadiazole (DMTD), crystal violet (CV) and rhodamine 6G (R6G). ThT, an important marker for amyloid fibrils, was detected using SERS for posthumous diagnostic purpose. DMDT is bidentate ligand which has both N and S groups for binding to noble metal surfaces. Surface selectivity of DMDT was studies

using SERS technique over silver and gold nanoparticles. Novel solid SERS substrate was synthesized by *in-situ* and *ex-situ* reduction of noble metal nanoparticles in bio-polymeric matrix. Silver and gold nanoparticles embedded polymeric SERS substrates were found to show trace level SERS sensing of CV and R6G. These solid SERS substrates are aimed for development of universal SERS substrate to replace energy extensive SERS substrate fabricated using chemical vapour deposition techniques.

Plasmonic nanoparticles, especially gold and silver nanoparticles show other applications in biomedical field owing to their inert nature. They have been often used as vectors for drug delivery[115, 116]. Moreover, apart from drug delivery, gold and silver nanoparticles are reported to show radiosensitization ability for radiotherapy.

1.4.2. Noble metal nanoparticles mediated radiosensitization

Gold nanoparticles are high Z elements with a high X-ray absorption cross-section. Absorption of gamma or X-rays by noble metal nanoparticles can lead to a number of process by which absorbed energy can be concentrated as well as deposited in the vicinity to kill. It is essential to understand the types of interaction matter can have with gamma or X-rays, in order to understand the mechanism of radiosensitization by noble metal nanoparticles.

1.4.2.1. Interaction of matter with gamma or X-rays

Gamma rays originate from the de-excitation of an excited nucleus of a radionuclide after radioactive decay whereas X-rays are produced when a metal atom excited by impinging of energised electrons undergoes de-excitation. Radioactive emission of gamma is a stochastic nuclear phenomenon whereas X-ray emission is stopped as soon as source of energised electron is shut down. But by nature, both X-rays and gamma rays are massless, chargeless electromagnetic radiation. X-rays possess energy in the range of 100 eV to 200 keV,

whereas gamma energies are from few hundred keV to MeV. Three major possible interaction mechanisms for gamma rays or X-rays with matter are: photoelectric absorption, Compton scattering, and pair production.

1.4.2.1.1. Photoelectric absorption

In the photoelectric absorption process[117, 118], a photon undergoes an interaction with an absorber atom in which the photon completely absorbed. Subsequently, an energetic photoelectron is ejected by the atom from one of its bound shells. The interaction is with the atom as a whole and cannot take place with free electrons. This interaction is unlike photoelectric emission process where incident visible light knocks of valence shell electron. For gamma or X-rays of sufficient energy, the most probable origin of the photoelectron is the most tightly bound or K shell of the atom. The photoelectron appears with an energy given by

$$E_{e^-} = h\nu - E_b \qquad (1.22)$$

where $h\nu$ and E_b are energy of incident photon and binding energy of ejected photoelectron. For X-rays and gamma rays used for therapeutic purposes, photoelectron is the major contributor for dissipation of absorbed energy in cancer tissue[119]. Ejected photoelectron may also lead to subsequent ejection of a secondary electron[120] from a neighbouring atom.

Moreover, in addition to the photoelectron, the interaction also ionizes the absorber atom with a vacancy in one of its inner shells. This vacancy is quickly filled either through capture of a free electron from the medium or by rearrangement of electrons from the outer shells of the atom which leads to emission of X-ray photons characteristic of the element. In some of the cases, an Auger electron is emitted to carry away the atomic excitation energy. Auger electron is emitted upon de-excitation of ionized absorbed atom in photoelectric

absorption process occurs by emission of a weakly bound outer shell electron. Auger electrons[121] are also important for dissipation of energy in case of radiotherapy of cancer cells.

The photoelectric process is the predominant mode of interaction for gamma rays or X-rays of relatively low energy. The process is also enhanced for absorber materials of high atomic number Z. A rough estimation of the probability of photoelectric absorption per atom is given by

$$\tau \propto \frac{Z^n}{E_\gamma^{3.5}} \qquad (1.23)$$

where E_γ is the energy of incident gamma or X-ray photon. The exponent *n* varies between 4 to 5, in the case of low energy gamma or X-rays.

1.4.2.1.2. Compton scattering

Unlike photoelectric absorption process, Compton scattering is associated with inelastic interaction of gamma or X-ray with loosely bound electrons of an atom. Gamma energies of the range of 100 keV and above show Compton scattering predominantly. In this process, the incident gamma-ray photon is deflected through an angle θ with respect to its original direction. The photon transfers a portion of its energy to the electron (assumed to be initially at rest), which is then known as a *recoil electron*, as shown in fig. 1.8. Because all angles of scattering are possible, the energy transferred to the electron can vary from zero to a large fraction of the gamma-ray energy.

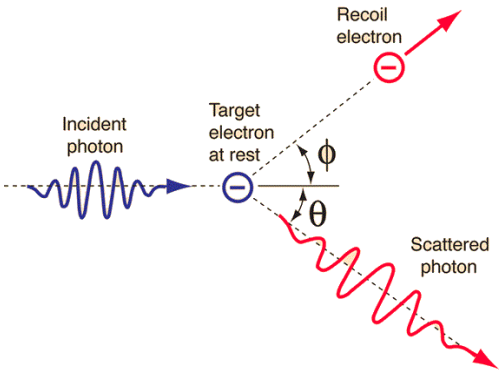

Figure 1.8. *Schematic representation of the phenomenon of Compton scattering*

The energy of scattered photon, $h\nu'$ is related to the energy of incident photon, $h\nu$ by the following relation:

$$h\nu' = \frac{h\nu}{1+\frac{h\nu}{m_0c^2}(1-\cos\theta)} \tag{1.24}$$

where m_0c^2 is the rest mass energy of the electron (0.512 MeV). The probability of Compton scattering per atom of the absorber depends on the number density of electrons, as a result, it increases linearly with Z. The angular distribution of scattered gamma rays[117] is predicted by the *Klein-Nishina formula*[122] for the differential scattering cross section $\frac{d\sigma}{d\Omega}$:

$$\frac{d\sigma}{d\Omega} = Zr_0^2\left(\frac{1}{1+\alpha(1-\cos\theta)}\right)\left(\frac{1+\cos^2\theta}{2}\right)\left(1+\frac{\alpha^2(1-\cos\theta)^2}{(1+\cos^2\theta)[1+\alpha(1-\cos\theta)]}\right) \tag{1.25}$$

where $\alpha = \frac{h\nu}{m_0c^2}$ and r_0 is the classical electron radius. In case of backscattering of photon, maximum energy is transferred to recoil electron. This recoil electron carries out maximum damage to the cancer cells in case of radiotherapy[123].

Elastic interaction of gamma rays or X-rays with matter, no energy transfer occurs between photon and matter, which is known as *coherent scattering*.

1.4.2.1.3. Pair production

Pair production is the least probable mode of interaction required for radiotherapy using gamma or X-ray as a minimum of 1.02 MeV photon energy is required. In practice, such high energy gamma rays are not used as at high energy, the probability of other interactions such as photoelectric absorption and Compton scattering is reduced drastically. In this interaction which occurs in the coulomb field of a nucleus, the gamma-ray photon is replaced by an electron-positron pair upon interaction with the target nucleus. All the excess energy carried in by the photon above the 1.02 MeV required to create the pair goes into kinetic energy shared by the positron and the electron. Because the positron will subsequently annihilate after slowing down in the absorbing medium, two annihilation photons are normally produced as secondary products of the interaction which further generate photo or auger or secondary electrons.

1.4.2.2. Radiotherapy

Cancer is defined as uncontrolled growth or abnormal proliferation of cells with loss of physiological functions[124]. The genes undergo mutation such that the physiological function is lost, the cells behave erratically and forms a burden to the tissue. Cancer can be of two types: benign or malignant. Benign cancer is localized form of abnormal tissue growth wherein overall physiological function is not disrupted yet due to increased size, the benign tissue requires excision. Malignant cancer is a physiological state where the cancer cells migrate and induces abnormal growth in other locations in human body. The physiological study of cancerous tissue under microscope can reveal the origin of cancerous tissue. This process is popularly known as biopsy. In order to understand the motivation behind radiotherapy, a short precise knowledge of biochemical phenomenon behind development as well as killing of cancer cell is vital.

1.4.2.2.1. Biochemistry associated with cancer

Cellular growth is a phenomenon associated with DNA materials of chromosomes present in the nucleus of a cell. Cell of non-reproductive organs undergo cell division by mitosis. The DNA is passed onto the daughter cells after mitosis. In normal cells, the characteristics of the parent cell are retained in the daughter cells. Genetic code of DNA is expressed in the cell by means of DNA transcription wherein mRNA (messenger RNA) carry genetic information to the ribosomes for synthesis of proteins specific to a cell. In presence of external perturbing factors known as mutagens, the DNA strands undergo modification, as a result, the genetic code is modified erratically. This results in synthesis of proteins which are not required by the cell to run physiological function. This disrupted DNA is further passed onto daughter cells which further become unwanted by the tissue. Every tissue has a DNA repair mechanism[125] by which every moment a cell undergoes repair from the damage caused by the mutagens. When the extent of damage by mutagens supersedes the extent of repair in tissues, cancerous cells begins to proliferate.

Disruption of cancerous cells can be induced by specific chemicals as well as radiation. Chemically induced disruption of cancerous cells is known as chemotherapy whereas radiation induced killing of cancer cell is known as radiotherapy.

1.4.2.2.2. Comparison of biochemical processes associated with chemotherapy and radiotherapy

Cisplatin is a well-known chemotherapeutic drug which is known to disrupt the helical structure of DNA. The helical structure of DNA is due to the presence of chiral carbon in the deoxyribose moiety of nucleic acids. Chloride groups present in cis-platin binds irreversibly upon hydrolysis to adjacent nitrogenous bases of DNA. As a result, scissoring

of DNA strands occur. This disrupts further cellular proliferation. A schematic representation of DNA damage by cisplatin is shown in fig. 1.9.

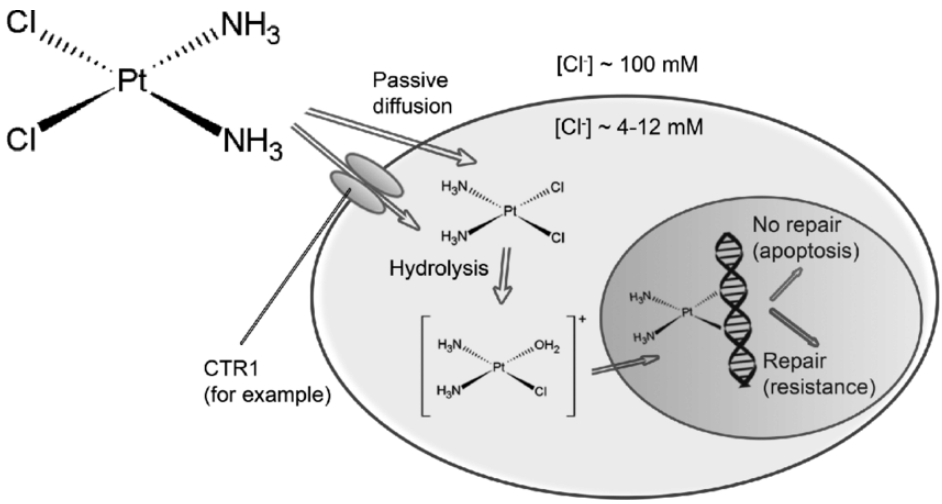

Figure 1.9. *A schematic representation cis-platin induced DNA damage.*

Radiation induced damage is altogether a different phenomenon as it is non-selectively to cancer cells. Chemotherapy disrupts cell division in actively dividing cells whereas radiotherapy can only by physically confined to cancerous tissue.

Ionising radiations, such as alpha, beta and gamma radiations, deposit high amount of energy in the vicinity of DNA. The secondary electrons generated in the cellular matrix can directly damage the DNA strand. It can also indirectly break water molecules to yield hydroxyl radical which damages the chemical structure of DNA. This disrupts the proliferation as the chemical integrity of DNA is compromised. A schematic representation of radiation induced DNA damage is shown in fig. 1.10.

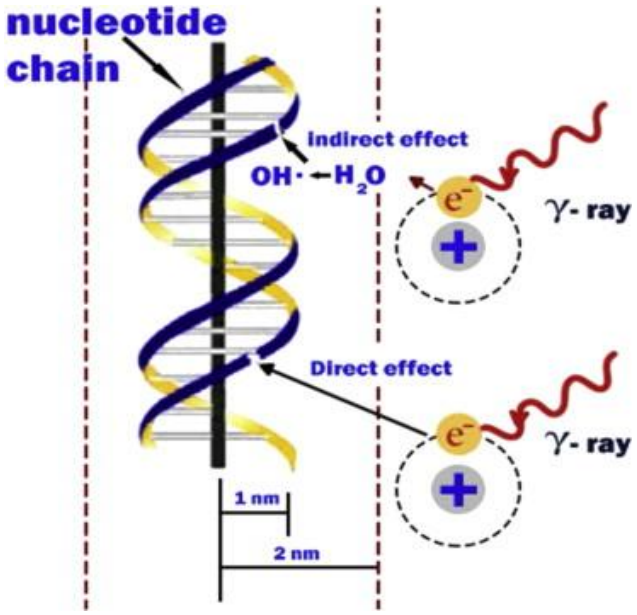

Figure 1.10. *Radiation induced damage of DNA strands*

1.4.2.2.3. Hypoxia and associated radiation resistance by cancer cells

The mechanism of cell damage by radiation is a complex process involving a number of steps. Energy received by the cancer cells are dissipated in the cellular matrix by secondary and auger electrons. These electrons carry out radiolysis of water to form various transient species such as $H^{\bullet}$, $OH^{\bullet}$ and $\boldsymbol{e_{aq}^{-}}$. $OH^{\bullet}$ radical damages DNA strands by abstraction of a proton. In cellular system, hydrogen atom generated due to radiolysis of water can further recombine with the damaged DNA strand to repair the system. Thus, the damage becomes reversible.

Oxygen plays a very important role in fixation of DNA damage. $\boldsymbol{e_{aq}^{-}}$ reacts with free dissolved oxygen to form superoxide radical $\boldsymbol{O_2^{-}}$. The damage done by $\boldsymbol{O_2^{-}}$ is irreparable and irreversible. Thus, it is important to have sufficient oxygen concentration in cell for effective damage by ionizing radiation. A schematic representation of the phenomenon of DNA damage fixation by oxygen is given in fig. 1.11.

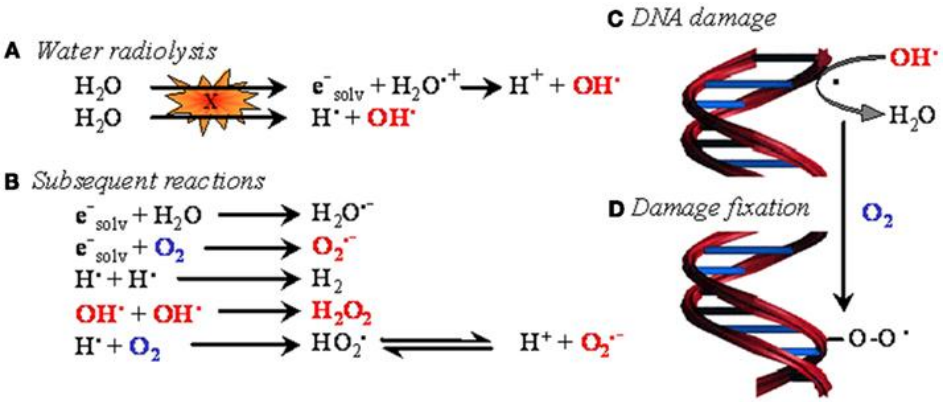

Figure 1.11. *A schematic representation of the DNA damage fixation by oxygen.*

Tumour or cancer cells, on the other hand, show hypoxia in the tumour centres. Uninhibited growth of cancer cells in a tumour puts undue burden on the vasculature, as the fast dividing cells have high oxygen demand. Tumour cells have poorly developed vasculature which is inadequate in catering oxygen demand of the tumour. This leads to hypoxia in tumour tissue wherein oxygen concentration reduces from periphery to centre. This tumour upon undergoing radiotherapy, tends to repair itself. This problem led the researcher to search for analogous phenomenon that could replace the need of oxygen in the hypoxic cells. Use of radiosensitizers is the solution to the above problem.

1.4.2.2.4. Radiosensitizers

Radiosensitizers are chemical agents that sensitize or enhance the response of the tumor cells to radiation[126]. These chemical agents promote fixation of the free radicals produced by radiation damage at the molecular level. The mechanism of action of radiosensitizers is similar to the oxygen effect, in which biochemical reactions in the damaged molecules prevent repair of the radiation induced cellular damage. $OH^{\bullet}$ radical captured by the radiosensitizers make the molecules incapable of repair. Radiosensitizers such as nitro-imidazoles were used to overcome diffusion limited hypoxia. Electron affinity of radiosensitizers play a vital role in radiosensitization of hypoxic cells[127]. Metronidazole and

its analogues such as nimorazoles and misonidazoles are found to show high radiosensitization efficiency. Metronidazoles are NO_2 functionalized molecules that take reacts with e_{aq}^- to form reactive transient species R-$NO_2^{\bullet-}$ which has the ability to fix radiation damage similar to oxygen. The mechanism of radiosensitization of noble metal nanoparticles is different from that of chemical radiosensitizers.

1.4.2.2.5. Noble metal nanoparticles as radiosensitizers

Gold nanoparticles are known to be chemically inert in a cellular system, as a result they are deemed highly biocompatible for bio-medical applications[128]. In a cellular environment, gold nanoparticles are known to show radiosensitization under gamma or X-ray radiation by production of reactive oxygen species (ROS) and associated oxidative stress which leads to induction of DNA damage and disrupts cell cycle. Gold is a high Z element. We have earlier noted that Z value plays an important role in extent of photoelectric absorption as well as Compton scattering. Under irradiation, gold nanoparticles in a cellular environment, absorbs more energy than the surrounding cellular matrix. This absorbed energy is dissipated in the surrounding in the form of secondary and Auger electrons. Electron transfer occurs from the surface of gold nanoparticles to O_2 molecules in the cellular environment. This leads to formation of ROS which increases the oxidative stress in the cell. In hypoxic cells, in absence of oxygen, low energy secondary and Auger electrons induce direct DNA damage[129].

For application of gold nanoparticles for radiosensitization, it is important that targeting of cancer cells is achieved by functionalization of gold nanoparticle surface with hypoxia selective groups. This may lead to reduction of radiation induced damage in the peripheral normal cells in comparison to the cancer cells.

1.4.2.2.6. Development of hypoxia selective gold nanoparticles for potential radiosensitization applications

In this thesis, the work involving synthesis of pH sensitive gold nanoparticles is discussed. pH sensitivity is the modality chosen for the targeting of cancer cells. Hypoxic cells tend to show anaerobic respiration which leads to accumulation of lactic acid which is an end-product of glycolysis[130].Warburg effect hints towards enhanced uptake of glucose in cancerous cells due to high energy demand under proliferation conditions. Glucose capped gold nanoparticles have also been studied in this work to enhance cellular uptake of gold nanoparticles in cancer cells. The work related to study of efficiency of gold nanoparticles in cancer cells is under progress.

Silver nanoparticles are also reported to show radiosensitization[130]. As a spin-off, silver nanoparticle embedded alginate films were found to show enhanced dose under X-ray radiation which was recorded using EBT3-GAFchromic films. The silver nanoparticles loaded polymeric films are yet to be tested for radiosensitization efficiency in cancer cells. These films holds potential for application for radiosensitization of superficial cancer such as skin[131] and uveal[132] cancer.

2

Material, Methods and Instrumentation

The discussions in this chapter revolves around the materials used as metal precursors, reducing agents, stabilizing agent, adsorbants, etc., the synthetic methods and the instrumentation techniques used for the characterization as well as application of the synthesized products.

2.1. Materials

Chemicals in its pure form were used for the synthesis as well as application purposes in all the work that are discussed in this thesis. There are two types of nanoparticle synthetic approach, top-down and bottom-up[133]. In top-down approach, bulk materials is converted into nanomaterials by application physical methods[134] whereas in bottom-up method, chemicals means are used to grow nanoparticles from atoms[135]. Gold and silver metal precursors are in the form of metal salts and complexes were used for bottom-up synthesis of noble metal nanoparticles. Reducing agents were used based on the application[136]. Reducing agents affected the rate of the reactions[137]. Oxidized reducing agents or excess reducing agents sometimes served as the stabilizing agent[138].

2.1.1. Metal precursors

Chloroauric acid ($HAuCl_4$) and its sodium and potassium salts are used as metal precursors[139]. $HAuCl_4$as well as its salt are strong electrolytes. $HAuCl_4$is used as a metal precursor when the reaction is required to be carried out in acidic pH where as in case

synthesis of metal nanoparticles in basic pH, sodium and potassium salts of $HAuCl_4$are used. Standard electrode potential of $AuCl_4^-$, given by reduction half-cell reaction,

$$AuCl_4^- + 3e^- \rightarrow Au^0 + 4Cl^- \quad (2.1)$$

is reported to be 0.994 V[140]. $AuCl_4^-$ imparts yellow color to the solution due to strong ligand to metal charge transfer.

Silver nitrate ($AgNO_3$) is the main precursor used for the synthesis of silver nanoparticles. $AgNO_3$ is a soluble strong electrolyte. In some cases, when silver nanoparticles are required to be synthesized using ionizing radiation, silver perchlorate ($AgClO_4$) is preferably used as nitrate ions also react with hydrate electron (e_{aq}^-). Standard reduction potential of Ag^+/Ag half-cell is 0.7996 V.

2.1.2. Reducing agents

A reducing agent undergoes oxidation to reduce the other component. A compound must have standard reduction potential lower than that of Au or Ag in order to be a reducing agent for synthesis of gold or silver nanoparticles, respectively[141]. Different organic and inorganic compounds such as amino acids, carbohydrates, carboxylic, nitrile functionalized biopolymers, alkali metal hydrides, organic solvents, etc. are used as reducing agents for the synthesis of metal nanoparticles.

2.1.2.1. Amino acids

Amino acids are the building blocks of proteins essentially consisting of an amine and a carboxylic group. It has been observed in general that the amine group participate in complexation of metal whereas the carboxylic group undergoes decarboxylation[142]. It has been reported that silver and gold nanoparticles are synthesized using amino acids such as tyrosine, tryptophan, etc. [143-145]. Amino acids are generally used by researchers to

synthesized bio-compatible nanoparticles for in-vitro applications[146]. Zwitterionic property of amino acids provide a precise control over reaction pH for synthesis of monodispersed metal nanoparticles. In acidic as well as zwitterionic form, amine group is protonated which restricts the complexation of metal ion. This disrupts the stabilization of metal nanoparticles post synthesis. Thus it has been observed that amino acid mediated synthesis of metal nanoparticles is best carried out in basic range.

2.1.2.2. Reducing sugars

Sugars containing aldehyde groups are known as reducing sugar due to their ability to form silver mirror by Tollen's reaction.[147]Silver and gold nanoparticles have been often reported to be synthesized using monosaccharides as well as polysaccharides.[148, 149] The advantage of using reducing sugars is that the capping formed on the surface of nanoparticles would be biocompatible as sugars and its oxidized products are ubiquitous in living organisms. Moreover, it has been reported that carboxylate group is present on the surface of nanoparticles due oxidation of aldehyde to carboxylic acid group. [150] The presence of carboxylate group on the surface of nanoparticles imparts a negative charge to the surface of the nanoparticle which is aiding in stabilization of the nanoparticles as well as assists in adsorption of cationic adsorbates.

2.1.2.3. Biopolymers

Biopolymers such as chitosan,[151] chitin,[152] alginate,[153] etc., are known to reduce noble metal ions such as silver and gold due to availability of large number of functional group in their structure. Moreover, a capping of biopolymer provides stability to nanoparticles solution by steric hindrance. Biopolymer capped metal nanoparticles were also found to be biocompatible for medical application.[154]

2.1.2.4. Metal hydrides

Metal hydrides such as sodium borohydride,[155] lithium aluminium hydride,[156] etc., are know to play an important role in reduction of synthetic chemistry as hydride ions, released upon dissolution of the above salts in water, facilitate reduction of organic compounds or metal ions, due high reduction potency of hydride ions.

2.1.2.5. Natural acids

Natural acids such as citric acid,[157] ascorbic acids,[158] etc., are potent reducing agents for noble metal ions. Natural acid reducing agents are slow reducing agents due to high activation energy. They are often used in tandem with fast reducing agents to facilitate slow growth of nanoparticles, which increases the possibility of formation of anisotropic nanoparticles.[159]

2.2. Synthetic method

2.2.1. Chemical reduction method

Synthesis of metal nanoparticles by reduction of metal ions in aqueous or non-aqueous medium using several reducing agents has been done and method is described in the respective chapters. In chemical reduction method the initial nuclei formation is induced by the reducing agent.[160] The nuclei formation is followed by a growth phase. The growth can result into aggregation in the absence of a stabilizer so to passivate the surface stabilizers are used. The reducing agent also acts as a stabilizing agent to avoid aggregation of the synthesized nanoparticles in few cases.

2.3. Instrumentation

2.3.1. UV-vis absorption spectroscopy

Absorption measurements were carried out on a Jasco-650 spectrophotometer. The spectra were recorded at room temperature using either 0.3 cm or 1 cm quartz cuvette. The absorption of the incident radiation by bonding/non-bonding electron represents a high

energy (~100 kcal mole^{-1}) transition[161]. This corresponds to a high frequency, i.e. low wavelength, absorption band which is observed at 200-800 nm in the UV and Visible range of detection. In solution, electronic absorption spectra are found with broad, generally unresolved bands.

For a solution of an absorbing substance, an absorptivity ratio at a monochromatic wavelength is defined as:

$$\frac{Intensity\ \ of\ incident\ \ light\ (I_0)}{Intensity\ \ of\ transmitted\ \ light\ (I)} \qquad (2.2)$$

and this is logarithmically related to concentration and optical path-length by the Lambert Beers law[162]:

$$Absorbance\ (A) = \log_{10}\frac{I_0}{I} = \varepsilon cl \qquad (2.3)$$

where, c (mol dm^{-3}) is the concentration of solute and l (cm) is the distance travelled between parallel optical faces of a suitable cell, and ε is called the molar absorption coefficient or molar absorptivity.

The absorption of UV-Visible radiation corresponds to the excitation of outer electrons. There are three types of electronic transition which can be considered:

2.3.1.1. Transition involving π, σ and n electrons

Absorption of ultraviolet and visible radiation in organic molecules is restricted to certain functional groups (chromophores) that contain valence electrons of low excitation energy. The spectrum of a molecule containing these chromophores is complex due to the superimposition of rotational and vibrational transitions on the electronic transition giving rise to a combination of overlapping lines. The possible electronic transitions of π, σ and n electrons are shown in fig. 2.1. Of the six transitions outlined, only the two lowest energy

ones ($n \rightarrow \pi^*$ and $\pi \rightarrow \pi^*$) can be monitored by the UV-visible spectroscopy as the absorption peaks for these transitions fall in an experimentally convenient region of the spectrum (200-800 nm). As a rule, energetically favored electron promotion will be from the highest occupied molecular orbital (HOMO) to the lowest unoccupied molecular orbital (LUMO), and the resulting species is called an excited state.

Molar absorptivities from the $n \rightarrow \pi^*$ transition are relatively low, and range from 10 to 100 dm^3 mol^{-1} cm^{-1}. The $\pi \rightarrow \pi^*$ transitions normally give molar absorptivities between 1000 and 10,000 dm^3 mol^{-1} cm^{-1}. The solvent in which the absorbing species is dissolved also has an effect on the spectrum of the species. The Peak resulting from $n \rightarrow \pi^*$ the transition are shifted to shorter wavelengths (blue shift) with the increasing solvent polarity. This arises from an increased solvation of the lone pair, which lowers the energy of the n orbital. However, the reverse is observed for the $\pi \rightarrow \pi^*$ transition i.e. the peak is shifted to higher wavelength. This is caused by attractive polarization forces between the solvent and the absorber which lower the energy levels of both the excited and the unexcited states. This effect is greater for the excited state, and so the energy difference between the excited and unexcited states is slightly reduced resulting to red shift. This effect also influences $n \rightarrow \pi^*$, but is over shadowed by the blue shift resulting from the solvation of lone pairs.

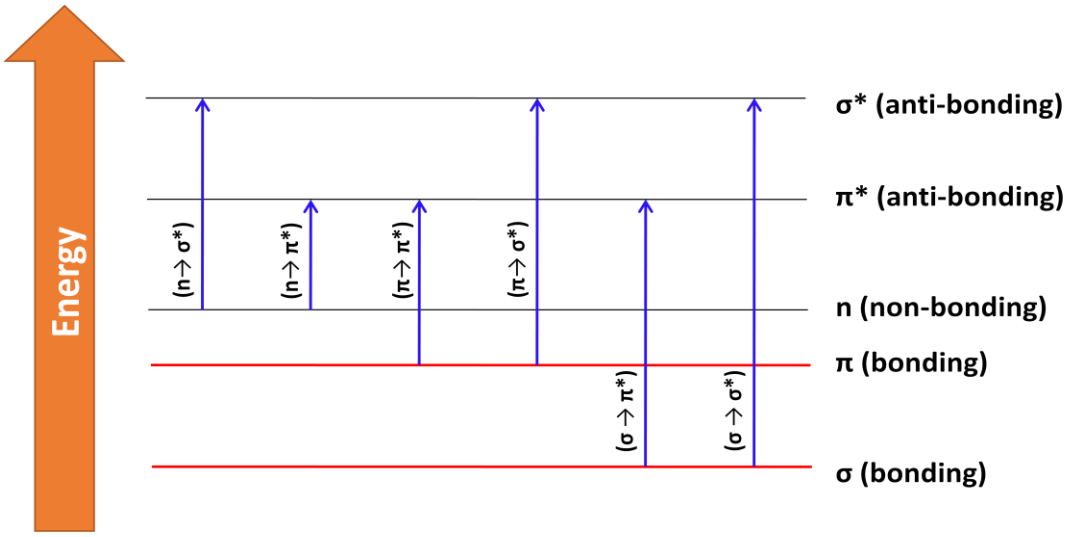

Figure 2.1. *A schematic representation of the electronic transitions of π, σ and n electrons*

2.3.1.2. Transition involving charge transfer electrons

Many inorganic species show charge transfer absorption and are called charge transfer complexes.[163] For a complex to demonstrate charge-transfer behavior, one of its components must have electron donating properties and another component must be able to accept electrons. Absorption of radiation then involves the transfer of an electron from the donor to an orbital associated with the acceptor. Molar absorptivity resulting due to the charge transition is large (greater than 10,000 dm^3 mol^{-1} cm^{-1}).

2.3.1.3. Transitions involving d and f electrons

In metal-ligand complexes, energy splitting of d or f-orbitals takes place. An electron from lower ground state to upper excited state may takes place, following the selection rules for electronic transition.[164]

2.3.2. Raman spectroscopy

Raman spectra were recorded at room temperature using the 514 nm line from the Argon ion laser (35-LAP-431-230, Melles Griot), 532 nm line, from a diode pumped solid state

Nd^{3+}:YAG laser (Cobolt Samba 0532-01-0500-500) M/s Cobolt AB, Sweden and 633 nm line, from a He-Ne laser. The laser power used to record the Raman spectrum was ~ 10 mW, and the spot size on the sample was ~ 50μ. For the Raman measurements, the sample solutions were taken in a standard 1x1cm^2 cuvette and the Raman scattered light was collected at 90° scattering geometry and detected using a CCD (Synapse, Horiba Jobin Yvon) based monochromator (Triax550, Horiba Jobin Yvon, France) together with a notch filter, covering a spectral range of 200-1700 cm^{-1}. Some of the experiments where microscopy was required, i.e., in solid samples, Horiba LABRAM HR MicroRaman Setup was used and the Raman signal was collected by backscattering.

Raman spectroscopy named after Sir C. V. Raman is a spectroscopic technique used to study vibrational, rotational, and other low-frequency modes in a system. Raman spectroscopy is based on inelastic scattering of monochromatic light, usually from a laser source. Inelastic scattering means that the frequency of photons in the monochromatic light changes upon interaction with a sample.

2.3.2.1. Origin of the Raman signal

The Raman effect is based on molecular deformations in an electric field E determined by the molecular polarizability, α. The laser beam can be considered as an oscillating electromagnetic wave with the electrical vector, E. Upon interaction with the sample it induces electric dipole moment, $P = \alpha E$ which deforms molecules. Because of periodical deformation, molecules start vibrating with characteristic frequency, υ_m.

Amplitude of vibration is called nuclear displacement. In other words, monochromatic laser light with frequency υ_0 excites molecules and transforms them into oscillating dipoles. Such oscillating dipoles emit light of three different frequencies as shown in fig. 2.2.

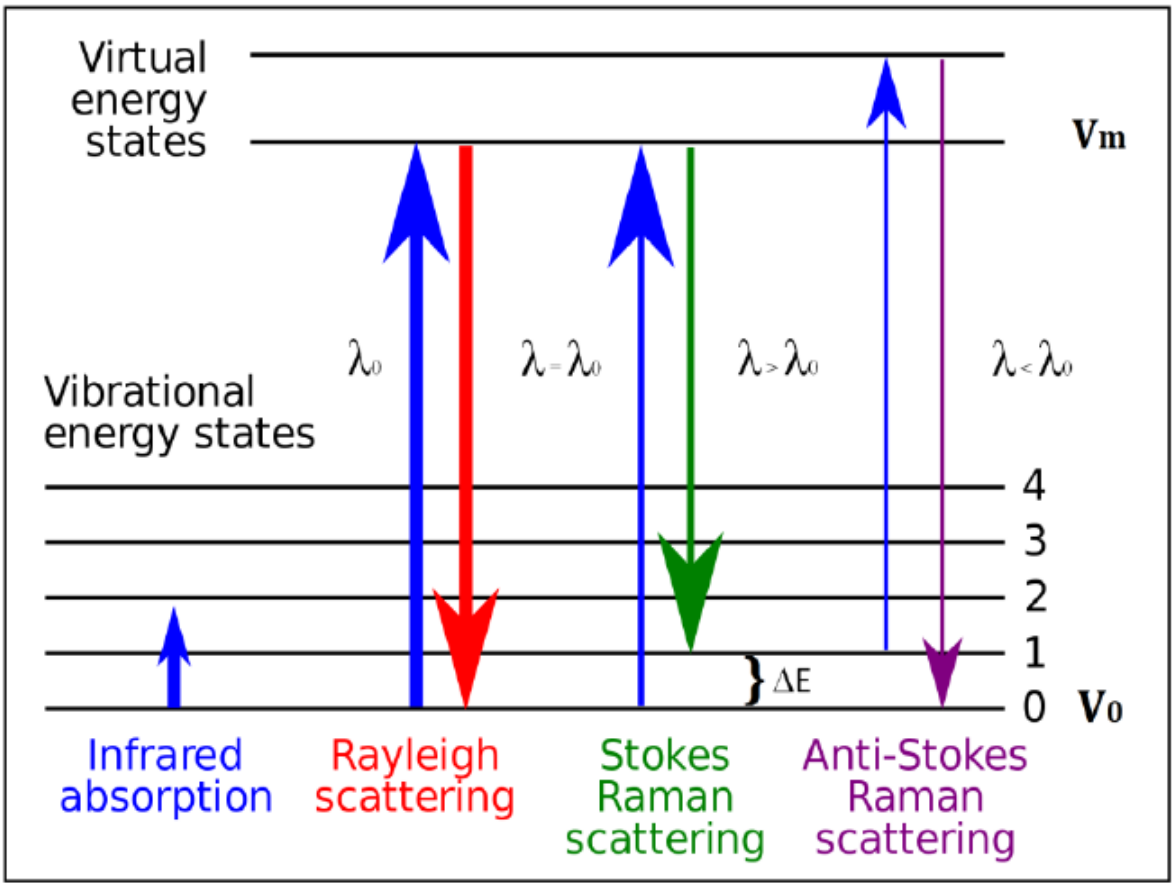

Figure 2.2. *Energy level diagram showing the states involved in the Raman signal*

The different light frequencies emitted are:

2.3.2.1.1. Rayleigh scattering:

A molecule with no Raman-active modes absorbs a photon with the frequency υ0. The excited molecule returns back to the same basic vibrational state and emits light with the same frequency υ_0 as an excitation source. This type if interaction is called an elastic "**Rayleigh scattering**".

2.3.2.1.2. Stokes Scattering:

A photon with frequency υ0 is absorbed by the Raman-active molecule which at the time of interaction is in the basic vibrational state. Part of the photon's energy is transferred to the Raman-active mode with frequency υ_m and the resulting frequency of the scattered light is reduced to $\upsilon_0 - \upsilon_m$. This Raman frequency is called Stokes frequency, or just "**Stokes**".

2.3.2.1.3. Anti-Stokes Scattering:

A photon with frequency υ_0 is absorbed by a Raman-active molecule, which, at the time of interaction, is already in the excited vibrational state. Excessive energy of the excited Raman active mode is released, the molecule returns to the basic vibrational state and the resulting frequency of the scattered light goes up to $\upsilon_0 + \upsilon_m$. This Raman frequency is called Anti-Stokes frequency, or just "**Anti-Stokes**".

About 99.999% of all incident photons in the spontaneous Raman undergo elastic Rayleigh scattering. This type of signal is useless for practical purposes of molecular characterization. Only about 0.001% of the total incident photons produces inelastic Raman signal with the frequencies, $\upsilon_0 \pm \upsilon_m$. Spontaneous Raman scattering is very weak and special measures should be taken to distinguish it from the predominant Rayleigh scattering. Instruments such as notch filters, tunable filters, laser stop apertures, double and triple spectrometric systems are used to reduce Rayleigh scattering and obtain high-quality Raman spectra.

2.3.2.2. Instrumentation

Raman system typically consists of four major components:

1. Excitation source (Laser).
2. Sample illumination system and light collection optics.
3. Wavelength selector (Filter or Spectrophotometer).
4. Detector (Photodiode array, CCD or PMT).

Many different ways of sample preparation, sample illumination or scattered light detection were invented to enhance intensity of Raman signal. Some of them are,

1) Simulated Raman (SR)

2) Coherent Anti-Stokes Raman (CARS)

3) Resonance Raman (RR)

4) Surface Enhanced Raman Scattering (SERS)

5) Surface Enhanced Resonance Raman Scattering (SERRS)

2.3.2.3. Surface Enhanced Raman Scattering

Raman signal from molecules adsorbed on certain metal surfaces can be 5-6 orders of magnitude stronger then the Raman signal from same molecules in the bulk volume. The intensity of the Raman signal is proportional to the square of the electric dipole moment $P = \alpha E$, there are two possible reasons-the enhancement of polarizability, α, and the enhancement of electrical field, E.

The enhancement of polarizability may occur because of a charge-transfer effect or chemical bond formation between metal surface and molecules under observation. This is a so-called chemical enhancement. The enhancement of electric field takes into account interaction of the laser beam with irregularities on the metal surface such as metal micro-particles or roughness profile. It is believed that laser light excites conduction electrons at the metal surface leading to a surface plasma resonance and strong enhancement of the electric field E. It is also called electromagnetic enhancement.

In all cases choice of appropriate surface substrate is very important. The most popular and universal substrates used for SERS are electrochemically etched silver electrodes as well as silver and gold colloids with average particle size below 20 nm. In the present work noble metal colloids are used as the substrate and the interaction between the substrate and the adsorbed molecule of interest was studied. Results were supported with theoretical calculations.

SERS spectra were recorded at room temperature using the 514 nm line, from a Ar+ ion laser (35-LAP-431-230, Melles Griot). In order to record the excitation wavelength-

dependent SERS spectra, 488 nm (Ar^+ ion), 532 nm (diode-pumped solid state Nd^{3+}:YAG) and 633 nm (He-Ne) laser lines were used. The sample solutions were taken in a standard 1 x 1 cm^2 cuvette or on glass slides and the Raman scattered light was collected at 180° scattering geometry or with a 50X LWD (long working distance) objective and detected using a CCD (Synapse, Horiba Jobin Yvon) based monochromator (LabRAM HR800, Horiba Jobin Yvon, France) together with an edge filter, covering a spectral range of 200-1800 cm-1. The spot size on the sample was ~ 0.5 mm in diameter, and the laser power at the sampling position was 8 mW, 10.2 mW, 50 mW and 12.7 mW for the excitation wavelengths of 488, 514, 532 and 633 nm, respectively. The power density on the sample was 8.16, 10.40, 51.0 and 12.95 W/cm^2 for 488, 514, 532 and 633 nm, respectively. The Raman band of a silicon wafer at 520.7 cm^{-1} was used to calibrate the spectrometer, and the accuracy of the spectral measurement was estimated to be better than 1 cm^{-1}. The block diagram of Raman setup is shown in fig. 2.3.

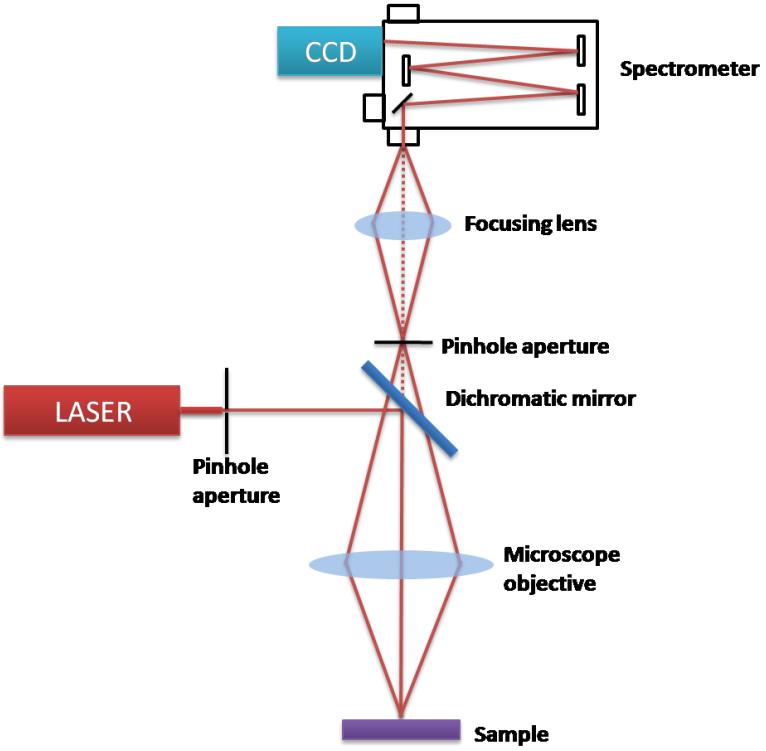

Figure 2.3. *Block diagram of Raman system*

2.3.3. Electron microscopy

In electron microscopy, a beam of highly energetic electrons is used to examine objects on a very fine scale, which gives information about topography, morphology, composition and crystallographic information about the arrangement of atoms in a material.[165] Electron microscopes were developed due to the limitations of optical Microscopes, which are limited by the physics of light to 500x or 1000x magnification and a resolution of 0.2 micrometers. In the early 1930's this theoretical limit had been reached and there was a scientific desire to see the fine details of the interior structures of organic cells (nucleus, mitochondria, etc.). This required 10,000x plus magnification which was just not possible using optical Microscopes. The wavelength of an electron is given by the following expression developed by de Broglie,

$$\lambda\, ln\, \text{Å} = 12.26/\sqrt{V} \qquad (2.4)$$

where, V is the acceleration voltage of the microscope (High Tension), Å is the wavelength in Angstroms (10^{-10} meter). This wavelength is 100000 x smaller than the wavelength of visible light. Therefore, the electron microscope has a possibility of showing much smaller details. In practice, we are obtaining information of distances up to 0.1nm, where in an optical microscope the resolution is limited to 100nm. Electrons are easily obtainable, since they are emitted from very hot metal surfaces (conventional guns) or can be pulled out of materials at excessive high field strengths (field emission). Moving electrons behave as waves, so electrons obey all the optical laws of diffraction, which is only due to the wave-like behavior of electrons.

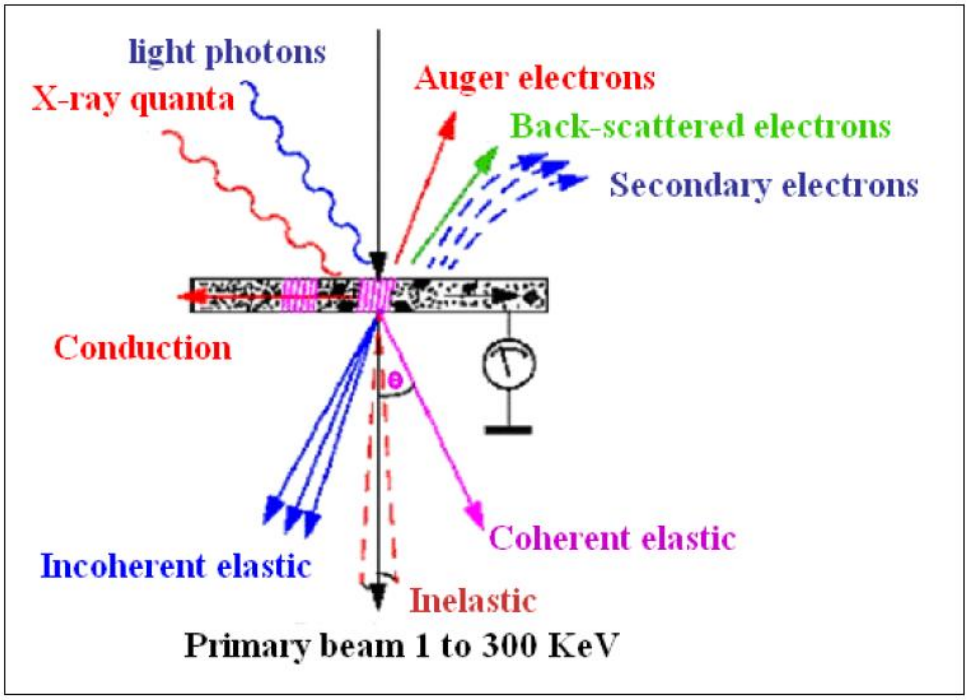

Figure 2.4. *Various types of radiations generated during electron specimen interactions*

Electron Microscopes (EMs) function exactly as their optical counterparts except that they use a focused beam of electrons instead of light to obtain image of the specimen and gain information of its structure and composition. A stream of electrons is accelerated toward the specimen using a positive electrical potential. This stream is confined and focused using metal apertures and magnetic lenses into a thin monochromatic beam onto the sample using a magnetic lens. The energetic electrons in the microscope strike the sample and various reactions can occur as shown in fig. 2.4. The reactions noted on the top side of the diagram are utilized when examining thick or bulk specimens (SEM) while the reactions on the bottom side are those examined in thin or foil specimens (TEM).

2.3.3.1. Interaction of electrons with atoms

The focused electron beam in EM interacts elastically and inelastically with the specimen generating various types of radiation. The principal electron signals are secondary electrons, backscattered electrons, auger electrons and characteristic X-rays, *etc*. Backscattered electrons are caused by an incident electron colliding with an atom in the specimen which is

nearly normal to the incident's path. The incident electron is then scattered backward at 180 degrees. The production of backscattered electrons varies directly with the specimen's atomic number. This causes higher atomic number elements to appear brighter than lower atomic number elements. This interaction is utilized to differentiate parts of the specimen that have different average atomic number. Secondary electrons are caused by ionization of the electron in the specimen atom. An incident electron imparts some of its energy to a lower energy electron (usually in the K-shell). This causes a slight energy loss and path change in the incident electron. This ionized electron then leaves the atom with a very small kinetic energy (5eV) and is then termed a secondary electron. Each incident electron can produce several secondary electrons. Production of secondary electrons is very topography related. Auger Electrons are produced by the de-energization of the specimen atom after a secondary electron is produced. Since a lower (usually K-shell) electron is emitted from the atom during the secondary electron process an inner (lower energy) shell now has a vacancy. A higher energy electron from the same atom can fall to a lower energy, filling the vacancy. This creates an energy surplus in the atom, which can be corrected by emitting an outer (lower energy) electron called Auger electron. The latter has a characteristic energy, unique to each element from which it is emitted. These electrons are collected and sorted according to their energy to give compositional information about the specimen.

2.3.3.2. Transmission Electron Microscopy (TEM)

The size and shape of nanoparticles were determined by using a Zeiss-Carl, Libra-120 TEM instrument. Specimen for TEM analysis was prepared on Lacey Formvar/carbon-coated 200 mesh copper grid from Ted-Pella. The 20 μL droplet of the solution was put on the grid and put on filter paper to remove excessive solution. The TEM image was taken by air-drying of the nanoparticles. Particle sizes were measured from the TEM micrographs and calculated by taking average of at least 100 particles.

The Transmission Electron Microscope (TEM) was the first type of Electron Microscope to be developed and is patterned exactly on the Light Transmission Microscope except that a focused beam of electrons is used instead of light.[166] It was developed by Max Knoll and Ernst Ruska in Germany in 1931. Fig. 2.5 illustrates the components of a transmission electron micrograph. The virtual Source at the top represents the electron gun for producing a stream of monochromatic electrons. This stream is focused to a small, thin, coherent beam by the use of condenser lenses 1 and 2. The beam is restricted by the condenser aperture for knocking out high angle electrons. The beam of electrons then strikes the sample and part of it is transmitted. This transmitted portion is focused by the objective lens into an image.

The image is passed down the column through the intermediate and projector lenses, being enlarged all the way. The microscope column is maintained at very high levels of vacuum to prevent scattering of electrons by the atmosphere. The image strikes the phosphor image screen and light is generated. The specimen thickness in the range of 50-100 nm is required for sample to be transparent to the electrons. An image can be obtained by using the transmitted or diffracted beam. In the former case the image is known as bright field image having mass thickness contrast due to variations in the density of the elements present in different parts of the specimen whereas the latter is known as the dark field image having diffraction contrast. The latter arises because of the variation in the intensity of the diffracted beam from region to region due to change in the orientation of atomic planes. In conventional TEM, an image is obtained by using only one beam whereas in phase contrast or HRTEM, using two or more beams, which are allowed to interfere, images are formed.

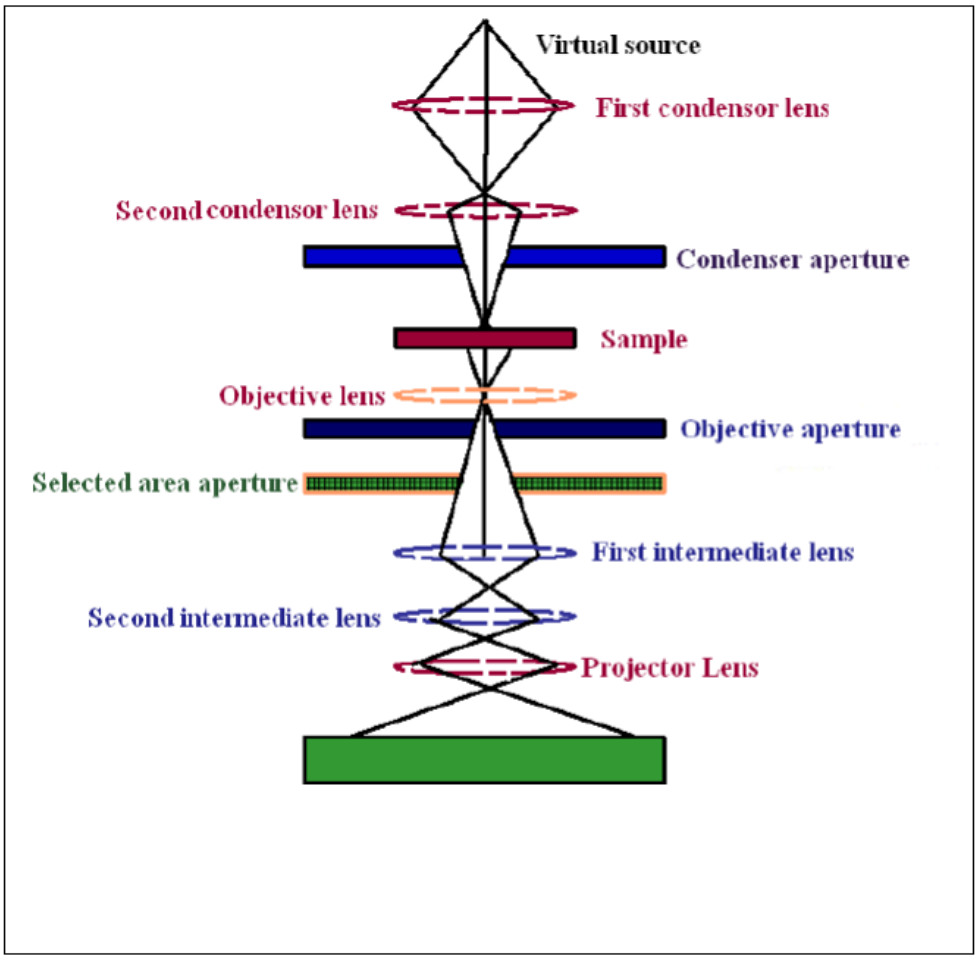

Figure 2.5. *Block diagram for imaging and various components of TEM*

2.3.4. Pulse radiolysis

Pulse radiolysis technique is a sophisticated time-resolved technique used to identify, characterize and elucidate the reaction mechanism of the highly reactive intermediates involved in various free radical reactions occurring at short time scales. These fast physico–chemical processes can be monitored by various experimental techniques. One of the most popular amongst them is the one based on spectrophotometric methods. In the present work, pulse radiolysis technique, using short electron pulses for generating and characterizing the free radical and reactive intermediates is used.

2.3.4.1. Principle of pulse radiolysis

In pulse radiolysis a pulse of high intensity electrons is given to a system to achieve a non-equilibrium situation in which significant concentrations of transient species is produced in a short time interval and these transient species are monitored by following the changes in their characteristic properties such as optical absorption,[167] electrical conductivity,[168] electron spin resonance[169] and diffusion current at a suitably polarized electrode i.e. polarography.[169] In pulse radiolysis there are two basic requirements. First is, it should produce very short (i.e. short in relation to the life time of the species under observation) pulses of radiation of sufficiently high energy to produce an adequate concentration of chemical species and of suitable penetration characteristics to ensure homogeneous distribution of the species formed within the irradiated sample. Second is a means of observing the chemical changes induced by radiation either optically or by other means.

The basic arrangement of pulse radiolysis set up is as shown in the following fig. 2.6. Sample solutions are irradiated with the help of 7 MeV electron pulse from a linear electron accelerator (section 2.3.7.2). Sample solutions are taken in a suprasil quartz cuvette and are kept at a distances of 12 cm from the electron beam window, where the beam diameter is 1 cm. Transient changes in the absorbance of the solution caused by the electron beam pulse are monitored with the help of a collimated light beam from a pulsed 450 W Xenon arc lamp. The accelerator, the sample cell and the monitoring light source are housed in a shielded cave with 1.5 M thick concrete wall and roof.

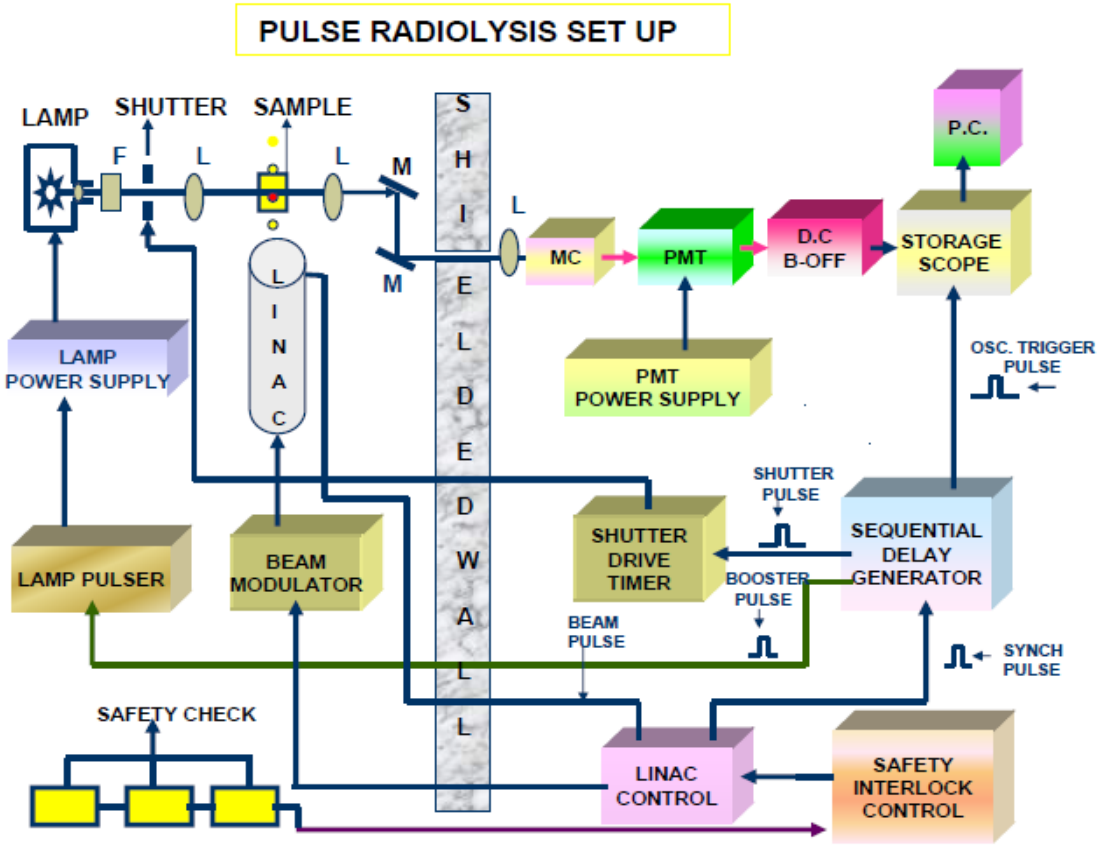

Figure 2.6. *Schematic of the pulse radiolysis set up (L: Lens, F: Filter, M: Mirror)*

The monitoring light beam, after passing through the sample cell is directed to the detection equipment through a tunnel in the wall by making use of fused silica lenses and mirrors coated with aluminum on the front surface. The light beam is finally focused on the entrance slit of a monochromator, on the exit slit of which a photomultiplier is fixed. Photomultiplier signal is fed into a storage oscilloscope from which traces are recorded on X-Y recorder or transferred to a computer. Details of the linear accelerator and kinetic spectrophotometer are given in the following sections.

2.3.4.2. Linear Electron Accelerator (LINAC)

An accelerator is the main component of the pulse radiolysis technique. Its function is to impart high energy to ions, mostly electron in radiation chemistry, and then direct them

through the experimental medium. The most commonly used pulsed sources are linear electron accelerators, Van de Graff accelerators and Febetrons.[167, 170, 171] In the present set up of pulse radiolysis technique, linear electron accelerator (fig. 2.7) has been used as the source of 7 MeV energy electron pulses (Obtained from Forward Industries, U.K., formerly known as Radiation Dynamics and Viritech Ltd).[172]

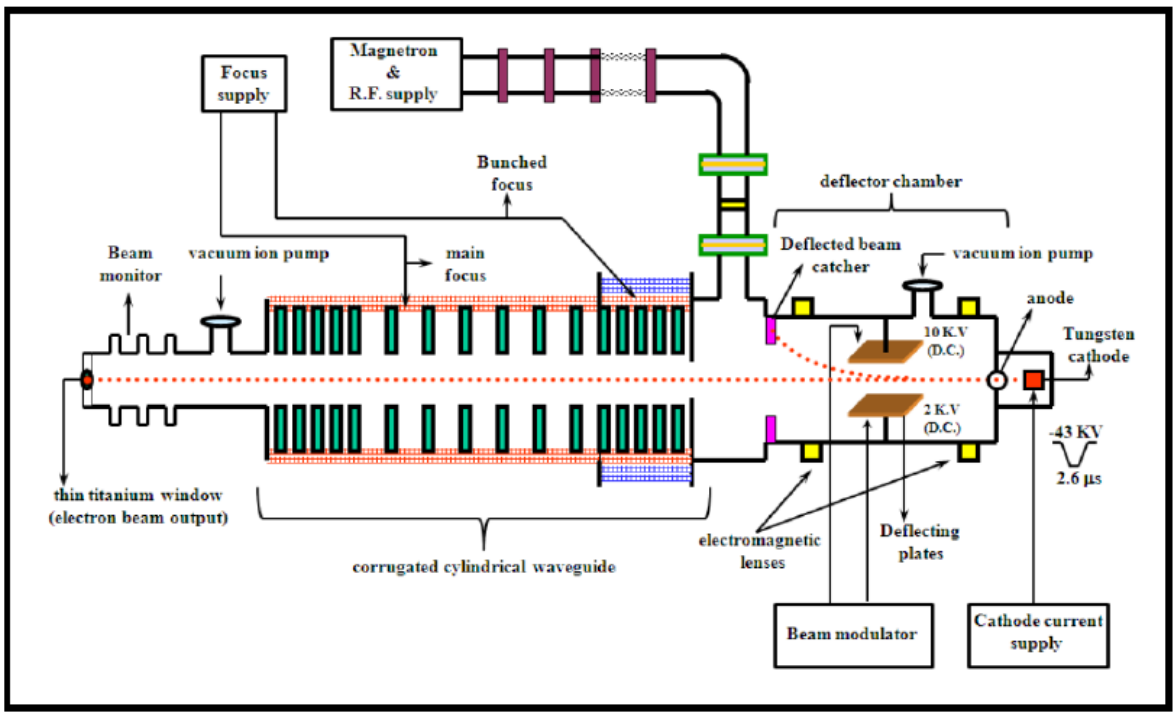

Figure 2.7. *Schematic of Linear Electron Accelerator (LINAC)*

In the electron gun the tungsten electrode in the form of a pellet is continuously heated by electrons emitted from the filament of the gun kept at -6 KV (DC) with respect to the cathode. Then the cathode is switched for 2 µs duration at an amplitude of -43 KV with respect to the anode, thus generating 2 µs pulses of electrons of energy 43 KeV which are focused by electromagnetic lenses into a deflector chamber and then into a corrugated cylindrical waveguide. Synchronously a travelling RF field in 2 µs pulse widths produced by a 3 GHz, 1.8 MW peak power magnetron is fed to the waveguide. The electrons produced in the electron gun assembly, entering in correct phase of the RF field, are accelerated in vacuum (10-8 mbar) to 7 MeV by the time it reaches the other end of the

waveguide. Accelerated electrons are focused by electromagnetic coils to produce a well-defined uniform beam of 2 mm diameter which comes out of the waveguide through a thin titanium window. It is feasible to get electrons of pulse widths varying from 5 ns to 2 μs time duration and peak currents ranging from 1000 to 70 mA. To get nanosecond electron beam pulses, a deflector chamber comprising of two parallel copper plates are incorporated between the electron gun and corrugated waveguide. The upper plate is kept at +10 KV (DC) voltage and the lower plate is biased at 2 KV (DC), so that -43 KeV electrons emitted from the electron gun are kept deflected and collected by a water-cooled beam catcher. During the deflection period of 2 μs the beam modulator delivers a pre-selected nanosecond pulse which pulls down the potential of the upper plate from +10 KV to that of the lower plate. Thus both plates become equi-potential for a short duration and electrons enter the corrugated waveguide for the acceleration. The first pulse from the pulse generator of the accelerator is used to trigger a sequential delay pulse generator (SDPG), which then sequentially actuates an electromechanical shutter control unit, a xenon arc lamp power supply with pulser unit to boost the analyzing light intensity for monitoring the fast events and triggering of the oscilloscope. Finally the electron beam is fired from LINAC on to the sample solution.

2.3.4.3. Kinetic Spectrophotometer

In the present set up the monitoring as well as characterization of the transient species formed on pulse radiolysis is done by the absorption technique. It consists of (i) analyzing light source, (ii) optical components like electromechanical shutter, light filters, lenses and mirrors, monochromator and photomultiplier or photodiode detector and (iii) data acquisition system consisting of oscilloscope, computer and printer.

2.3.4.3.1. Analyzing light source

For monitoring weak absorption signals lasting for very short duration, the light source should be intense and stable to give sufficient signal to noise (S/N) ratio. It should have effective output range covering as wide spectral range as possible. Continuous light sources are not suitable for monitoring fast events because of their low intensity. Hence pulsed light sources are used, here light intensity is enhanced 10- 200 times the steady level depending on the wavelength region for short time duration. In the present pulse radiolysis set up a 450 W Xenon arc lamp (OSRAM model XBO 450) is used. The arc lamp is operated by a regulated DC power supply which is switched initially at 100 V DC with a 20 kV pulse. Then onwards the lamp operates on a steady 25 A and 18 V supply. The steady arc lamp is electrically pulsed for only for 3 ms by the pulser power supply, during which current supply to the lamp is boosted to 400 A. This pulsing boosts the light output by 20-70 times depending on the optical region of detection. Normally the light intensity is steady for around 100-150 μs, during which the transient absorption measurement are done accurately. The second pulse from the SDPG activates the pulser unit of this arc lamp to boost the analyzing light intensity (fig. 2.7). When an event is to be monitored after 100 μs from the electron pulse, the analyzing lamp is used in the continuous mode without boosting.

2.3.4.3.2. Electromechanical shutter

In order to minimize the photodecomposition of the sample solution and also to protect the photomultiplier tube (PMT) from fatigue due to continuous illumination from the light sources, an electromechanically shutter is placed between the lamp and the sample holder (fig. 2.7) In the present set up, an electromechanical shutter from JML optical industries INC., Rochester, New York; operated by shutter drive timer is used. The shutter is opened just prior to the boosting of the analyzing light and remains open until all the other events *viz.* boosting of light, arrival of the electron pulse and transient events are over. Normally

the shutter opening time is set at 80 ms. Shutter control unit is actuated first, by the SDPG (fig. 2.7).

2.3.4.3.3. Sample cuvette

A square (1 cm x 1 cm) quartz cell is placed on a aluminum cell holder such that its geometry is the same every time it is removed or replaced and the collimated light beam from the arc lamp passes through it such that it is at a right angle to the electron beam falling on the cell. Precautions are taken to align the optics in such a way that the electron beam and light beam cross each other inside the cell exactly at right angles and the light beam passes entirely through the cell contents.

2.3.4.3.4. Monochromator

Analyzing light beam after passing through the sample cell is focused on the entrance slit of a high intensity grating monochromator (Kratos Model GM 252, with Grating Model No GMA 252-20) which can be used in the 180-800 nm range, with dispersion of 3 nm per mm. Slit width of this monochromator can be continuously varied from 0.01 to 6.0 mm.

2.3.4.3.5. Detector

At the exit slit of the monochromator a photomultiplier tube (PMT) (Hamamatsu model R-955) is fixed. It has a uniform spectral response in the 180-900 nm regions. A 5-stage PMT biasing circuit suitable for nanosecond recording was used. The negative high voltage required for PMT cathode is obtained from a regulated 0-3000 V, 3 mA DC power supply (ECIL Model HV 4800 D). The PMT output current is converted to voltage signal by a load resistor connected across its anode and ground. With a load resistor 500 ohms, the overall rise time of detection is 75 ns. Thus, only the events of duration much longer than this time period can be studied by using the detector.

2.3.4.3.6. Back off device

There is a constant DC output of PMT (I_0) due to the incident light before the arrival of the electron pulse. Thus for monitoring small absorption changes over a background of large monitoring pulse on an oscilloscope, this background light level should be compensated for which a back-off device is required. An automatic DC compensation unit is used for this purpose to record digitally and display I_0 after the electron pulse. DC compensation is possible up to 1999 mV though generally the working negative DC level is maintained between 800-1000 mV.

2.3.4.3.7. Transient digitization

The output voltage from PMT is fed into the vertical amplifier of the oscilloscope (Larsen and Toubro 4072, 100 MHz or Tektronix TDS 220, 100 MHz). The time base of the storage scope is triggered externally by a signal (derived from the accelerator) synchronous with the electron beam pulse. For recording 100 ns time scale events, a delay sweep facility available on the scope is used. Due to its limitations, the SDPG in this case cannot adjust the pre-trigger in ns time scale.

2.3.4.4. Transient Absorption Measurements

The PMT output voltage V developed across a suitable anode resistor is directly proportional to the anode current which in turn, at fixed values of the photocathode potential, is directly proportional to the intensity of the monochromatic light incident on the photocathode. When, as a result of action of electron pulse on the sample solution in the cell, transient species formed capable of absorbing light at a given wavelength are produced, the intensity of light transmitted through the cell is given as:

$$I = I_0 e^{-\varepsilon c l} \qquad (2.5)$$

where, I_0 is the intensity of light transmitted just prior to electron pulse, c is the molar concentration of the species formed in the sample, ε is the molar extinction coefficient and l

the length of the light-path through the cell contents. Because of the proportionality between V and I, the PMT output voltage just after and prior to pulsing are related as

$$V = V_0 e^{-\varepsilon c l} \tag{2.6}$$

As the concentration of the transient species produced by the electron pulse will change with time due to various chemical processes, I and hence V will be time-dependent. It is this time-dependence of V that is monitored with an appropriate digital oscilloscope and subsequently processed to get the kinetic information. The quantity $\varepsilon.c.l$ called the optical density or absorbance is also time-dependent. From the experimental quantities, V and the absorbance (A) of the transient species at any given time can be calculated using the following equation:

$$A = \log \frac{V_0}{V} \tag{2.7}$$

At any instant of time after pulse, a plot of the absorbance vs. wavelength reflects the absorption spectrum of the species present in the system at that instant of time.

2.3.4.5. Dosimetry for Pulse Radiolysis

Dosimetry for pulse radiolysis differs from the dosimetry of the conventional steady-state radiolysis (γ-radiations of ^{60}Co) as pulse radiolysis involves high dose rate. In pulse radiolysis experiments thiocyanate dosimeter is commonly used to measure the absorbed dose per pulse. It is an aerated aqueous 0.01 M potassium thiocyanate solution. Upon irradiation with the electron pulse, e_{aq}^- and H atom are scavenged by the dissolved oxygen and $OH^\bullet$ radical oxidizes SCN^- ions to produce $(SCN)_2^{\bullet -}$ radical according to the following reactions 2.8 and 2.9.

$$SCN^- + OH^\bullet \rightarrow SCN^\bullet + OH^- \tag{2.8}$$

$$SCN^- + SCN^\bullet \rightleftarrows (SCN)_2^{\bullet -} \tag{2.9}$$

The species $(SCN)_2^{\bullet-}$ formed has strong absorption in the visible region. The radiation dose is estimated from the maximum absorbance of $(SCN)_2^{\bullet-}$ radical at 475 nm. G value for this species is reported to be 3.3 per 100 eV of the absorbed dose and the extinction coefficient (ε) of this radical is reported to be 7600 dm^3 mol^{-1} cm^{-1} at 475nm. G value is doubled in N_2O saturated solution. From the measured absorbance, the absorbed dose per pulse (D) is computed from the following equation:

$$D = \frac{\Delta OD}{G.\varepsilon.l} \times N \times 1.602 \times 10^{-19}\ Gy \qquad (2.10)$$

Where, N is the Avogadro number. Substituting the value for $G.\varepsilon$ for $(SCN)_2^{\bullet-}$ at 475 nm, the above expression (2.10) can be written in simplified way as:

$$D = \Delta OD \times 385\ Gy \qquad (2.11)$$

Generally, the maximum dose obtained from a 50 ns pulse is 16 Gy and that for a 2 μs pulses is about 120 Gy. For estimation of the extinction coefficient of the transient species studied, experiments were carried out at lower doses.

2.3.5. Atomic force Microscopy (AFM)

Atomic force microscopy (AFM) is a technique where the surface morphology is mapped by a cantilever with a tip of atomic dimensions. The interaction of the tip with the surface is crucial for the mapping. When the tip comes closer to the surface, the close-range attractive forces come into play which causes deflection of the tip, whereas upon going further closer to the surface, the tip experiences repulsion which also causes deflection of the tip. A laser beam is focused on the cantilever and its reflection is detected in a position sensitive photodiode detector. The deflection of the tip is measured by the extent of deflection in the position of laser spot on the photodiode.[173] In fig. 2.8, a schematic representation of the working principle of AFM is shown. A piezo-electric driver positions the tip at a fixed

distance from the sample, depending on the feedback from the photodiode. There are two modes of operation of AFM, namely contact and non-contact. In contact mode, the tip is kept at a fixed distance from the sample. The deflections are registered on the tip as it goes away or comes closer to the surface, due to varying force on the tip. These deflections are used to map the surface. In non-contact mode, the tip is oscillated in its natural frequency. Upon coming closer to the sample surface, the frequency of the tip is changed due to interaction. The photodiode then signals the piezo-electric driver to move away from the surface to restore its natural frequency of oscillation. The deflections observed in photodiode w.r.t to the surface in X-Y plane is plotted in a 3D space to obtain AFM image.

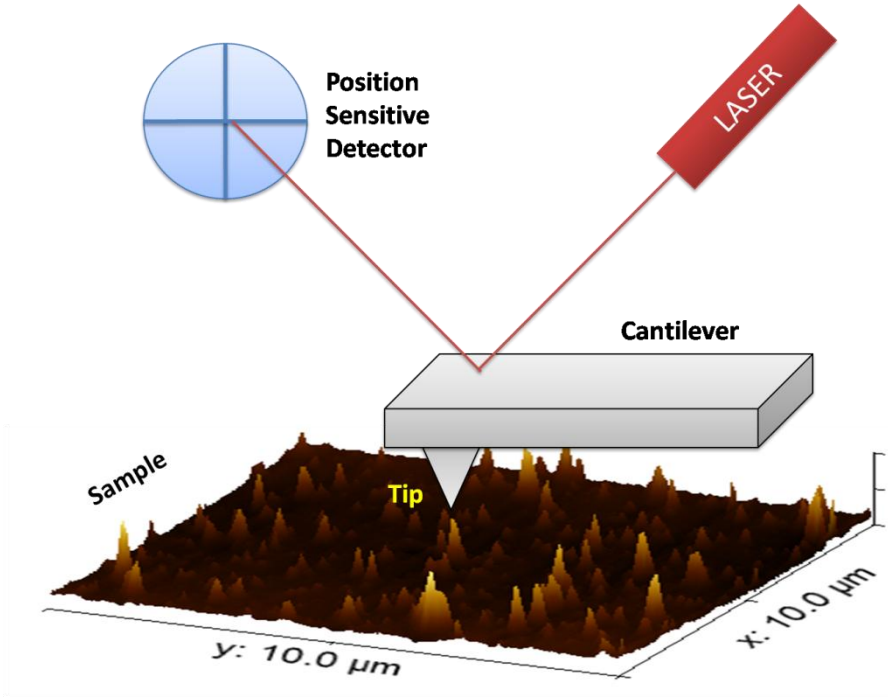

Figure 2.8. *Schematic representation of components of atomic force microscope (AFM).*

In this work, AFM from A.P.E. Research, Italy, model no. A-100 has been used.

3

Synthesis and characterization of pH sensitive gold nanoparticles for application in radiosensitization

6.1. Background

As it was discussed in earlier chapters, nanotechnology has tremendous popularity among recent works as it has opened up a large number of opportunities for finding new materials with tunable properties. Nanomaterials are often used in diagnostics, sensing and catalytic applications owing to their unique and interesting properties.[174-180]

It is known that spatial movement of electrons in the orbitals is the source of the characteristic optical property in metal nanoparticles, which has been earlier discussed in section 1.3.1. This motion is quantum mechanical in nature. The LSPR imparts size dependent characteristic color to the nanoparticles.[181]

Understanding of thermodynamics of nanoparticles[182]is very important for stabilization of the nanoparticles in the dispersing medium. In the nanometric dimension, surface energy is much higher than the bulk. As a result, the particles tend to agglomerate in order to reduce available work energy of the system or the Gibbs free energy. The critical criterions which govern the agglomeration or aggregation of nanoparticles are surface change density,[183]electrical double layer thickness[184]and ionic strength.[185]Double layer thickness of any colloidal system in polar solvent is largely dependent upon surface charge density[186]which depends upon pH of the surrounding medium as well as the chemical nature of the adsorbed species.[187] Higher ionic strength also reduces the double layer thickness.

Higher double layer thickness leads to lower interaction among the nanoparticles which lowers the tendency of agglomeration in the colloidal system.

Gold nanoparticles (GNPs)are an important subject of investigation for researchers who are focused in designing probes and vehicles for bio-nano-technological applications[188].The size of nanoparticles (<100nm) is comparable to those of the various important biomolecules involved in physicochemical cycle of the cell. As a result effective interaction of nanoparticles with the essential macro biomolecules[189] affects the physicochemical pathways. Thus, synthesis of new materials which holds potential to enter the physico-chemical cycle due to their analogous dimensional property has become an important topic of investigation among researchers as this phenomenon may accelerate or decelerate the process. Moreover, properties such as biocompatibility, rich surface chemistry andunique optical properties have made GNPs a good tool for imaging, diagnosis, therapy, bio-sensing and drug delivery[190]. Synthesis of GNPs involves a lot of optimization to obtain a desired property which has been discussed in chapter 2.

As discussed in section 1.3.2., radiosensitization property is also another application oriented aspect of GNPs apart from surface plasmon. Gold atoms have a high absorption cross-section for high energy radiation such as X-ray or gamma rays owing to its high Z.[191, 192]More over GNPs also show auger electrons production on irradiation with high energy photons along with a major emission of photoelectrons.[193]In order to cure cancer, irradiation of affected tumor cells by high energy photons is performed to kill the cancerous cells is performed which is known as radiotherapy. But upon irradiation the normal peripheral cells also get killed as a collateral damage. In order to reduce the death of normal cell in comparison to cancer cells, GNPs are used as radio-sensitizers which are often specifically transported to the cancer cells. Upon irradiation, the GNPs produce low range photoelectrons that deposit all their energy in the vicinity, which leads toincrease in the

mortality of target to non-target cells in the cancer patient's body.[194]In order to attain such a result, selective transport of GNPs to the target cells is required. Tumor or cancer cells are formed as a result of abnormal cell growth in the body (see section 1.3.2.2.1.). Due to rapid unorganised growth of cancerous tissue, the vascular system, i.e., the blood vessels are not well-developed in the tumor. This leads to gradual decrease oxygen concentration gradient across the radial cross-section of the tumor, from outer layer to the core. The drop in oxygen level in the core of the tumor is so alarming that the cells are no longer able to perform aerobic respiration. Thus, the inner core cancerous cells carries out anaerobic respiration and produces lactic acid and two molecules of ATP per molecule of glucose as a product. This lactic acid is distributed between intra and extracellular region[195] at equilibrium. The above processes lead to drop in pH in the vicinity of tumor cells. As a result, a gradient of decreasing pH is formed between normal cells and tumor cells. It is also reported that pH reduction can also be due to dissociation of ATP.[196, 197]In order to attain specificity of targeting GNPs towards cancer cells for effective application in radiotherapy, GNPs are required to be made responsive towards varying pH by functionalization of the gold surface with pH sensitivegroups.[198]One such strategy can be to design such a functionalization on the GNPs that upon reduction of pH, as it occurs in cancerous cells in comparison to normal cells, the surface charge on GNPs is reduced. This may lead to controlled and slow adsorption of GNPs at the cellular interface which is analogous to the interface of polar and non-polar medium[199].It is known that like dissolves like. A polar medium can solubilize a charged species such as a charged GNP. Upon neutralization of the surface charge on the GNP, the polar medium is no longer able to solubilize it. The best way to stabilize the GNP would be either agglomeration or disposal of the GNP to the nearest non-polar zone. This in a system containing two liquids, one polar and another non- polar, such a scenario is possible. The interface of polar to non-polar liquid experiences a transition in polarity. Thus,

it is probable that the GNP is transported to the interface and get stabilized in the non-polar medium. Similar phenomenon is often observed in case of selective extraction of GNPs from aqueous medium to non-polar medium by an extractant.[200]Cell membranes in biological systems can also be considered as an interface between polar aqueous vascular system lined by outer hydrophilic part of cell membranes and inner hydrophobic lipids layer. In this work, a similar biomimetic interface has been used to study the accumulation of synthesized GNPs.

Citrate method[201] of preparation is one of the most popular method for preparation of GNPs which the procedure requires high temperature in order to attain activation energy. The GNPs obtained by the above method are not pH sensitive as the citrate capping is labile. Another useful method to prepare GNPs involves reduction by borohydride[202] which is also not pH sensitive. Again two-phase method of synthesis of GNPsproduces uniform sized GNPs.[203] But the by-product or the reagents involved in these techniques make the GNPs unsuitable for biological applications. In order to synthesize biocompatible GNPs with pH sensitive properties it is wise to look for organic compounds that participate in various physic-chemical redox reactions[204].Thus,use of such a compound would serve the purpose as both its oxidized and reduced form are accepted in the body.[205, 206] This idea has often the researchers towards using biomolecules for synthesis of GNPs.

In this chapter, the synthesis of spherical GNPs by reduction of chloroauric acid by l-tryptophan (Trp), an essential amino acid, is discussed. Surface functionalization of the pH sensitive GNPs was attained by the adsorption of oxidized Trp product on the surface of GNPs. The pH of the aqueous medium containing dispersed GNPs was varied to control the surface charge, in order to study the extent of agglomeration of nanoparticles at different pH as well as the extent of accumulation of nanoparticles at polar – non polar liquid-liquid interface.

6.2. Experimental

3.2.1. Materials

Gold chloride hydrate (Sigma- Aldrich), l-tryptophan (Fluka AG), sodium dodecyl sulphate (Sigma, USA), sodium acetate (Polypharm, India),glacial acetic acid (SDFCL), phosphatidyl choline (Phospholipon 90G) and benzene (Spectrochem, India)were used as received. All the experiments were performed in Millipore purified water.

3.2.2. Synthesis and characterization of gold nanoparticles

Synthesis of GNPs was carried out by the reduction of chloroauric acid by Trp in aqueous medium at room temperature. Reaction conditions were controlled by addition of stabilizer sodium dodecyl sulphate (SDS) and buffer solutions. The synthesized GNPs were characterized by UV-Vis absorption spectroscopy (JASCO V-650 spectrophotometer), infrared spectroscopy (Shimadzu IRAffinity-1, FTIR) and transmission electron microscopy (Ziess, Libra 12). Proposed reaction mechanism was confirmed by gas chromatography (Shimadzu GC 2014). The interaction of Trp and GNPs was studied by steady-state fluorescence spectroscopy (F-4500, Hitachi) whereas inter-particle interaction was studied by measurement of degree of accumulation of GNPs at polar non-polar liquid-liquid interface using UV-vis absorption spectrometry.

3.3. Results and discussion

3.3.1. Study of synthesis of GNPs using UV-Visible absorption spectroscopy

UV-Vis absorption spectroscopy[207] is one of the most reliable yet fundamental technique which is often used to predict the shape and size of GNPs. Moreover a quantitative measurement of concentration of GNPs within experimental, technical and instrumentation limits can also be obtained using UV-vis absorption spectroscopy. UV-Vis spectroscopy is

widely used for characterization and agglomeration studies of GNPs.0.5mL of 10 mM chloroauric acid ($HAuCl_4$)solution to 2 mL millipore water in a 5 ml volumetric flask. To this 1mL of 5 mM Trp solution was added and the total volume was made up to 5 ml. The formation of GNPs was indicated by the visual changes in the color of the solution from yellow to light pink to violet within 1 h which was also confirmed by UV-Vis spectroscopy (fig. 3.1.a) by the observation of LSPR of the GNPs at 570 nm. The appearance of LSPR at a slightly higher wavelength than 520 nm, is an indication of unstable GNPs which are prone to aggregation. The gold sol started precipitating after 40 min. The pH of the solution when measured after GNP formation was 4.0.

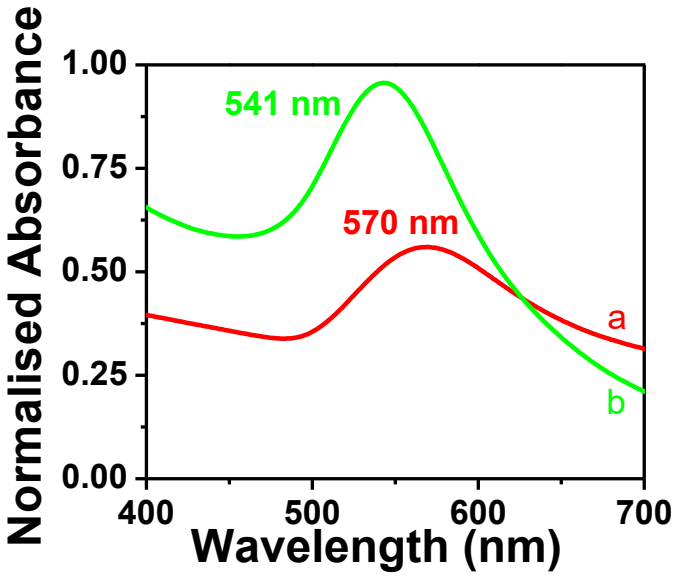

Figure 3.1. *UV-vis absorption spectrum of GNPssynthesised in aqueous medium by the reaction of 1 mMHAuCl₄ with 1 mM Trp (a) in absence of any stabilizer (b) in presence of 1mM SDS.*

In another experiment, 0.5mL of 10mM chloroauric acid solution and 0.5mL of 10 mM SDS solution was added to 2mLmillipore water in a 5 ml volumetric flask, followed by addition of 1mL of 5 mM Trp solution. The final volume was made upto 5 ml immediately. The color of the solution changed from yellow to pink to orange to wine red in 1 h. After 5

minutes of addition of Trp solution to the solution of chloroauric acid and SDS, the solution turned light pink. After 20 minutes that a sudden change of color occurred from light pink to deep wine-red color. UV-vis absorption spectrum of the resulting GNP solution which is wine red in color, exhibited a LSPR at 541 nm (fig. 3.1.b). The above prepared GNPs precipitated in about2-3 days.

The above results indicate that the oxidized Trp is unable to stabilize GNPs at ambient pH of the reaction mixture. Again, Trp along with SDS, which is a widely used stabilizer, fails in stabilizing GNPs at the ambient pH. This led to the investigation of the reason behind the precipitation of GNPs. DLVO theory[208]explains the theoretical basis of stabilization of nanoparticles on the basis of two opposing forces namely, repulsive coulombic force acquired by the nanoparticles because of the surface charge associated with the adsorption charged chemical species on nanoparticles surface and attractive Van der Waal's force. The surface charge on the GNPs can be varied with a certain limit by altering the pH of the medium. This idea implemented in the following experiment.

The reduction of $HAuCl_4$ was carried out in a buffered medium. In a buffered medium, due to the presence of weak acid and its associated salt which is a strong electrolyte, small change in pH due to addition of acid or base externally is negated and the pH of the system is maintained. Thus, all the solutions made in this experiment were prepared in buffered medium such that the final buffer strength of each solution was 10mM.In order to study the effect of pH on the formation of GNPs, initially a pH window of 3 to 7 was chosen. Five reaction sets were prepared at varying pH from 3 to 7 by using acetate buffer. Acetate buffer was chosen based on its characteristic low ionic strength and compatible pH range corresponding to physiological pH. Final concentration of $HAuCl_4$ and Trp in each reaction set was 1mM. All UV-Vis absorption spectra required for the experiment were measured in a 0.3 cm pathlength cuvettewhich is shown in fig. 3.2.

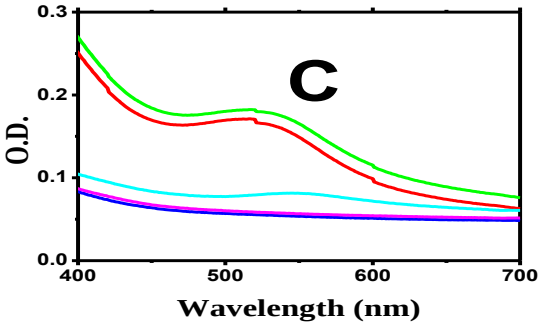
C
O.D.
Wavelength (nm)
0.0
0.1
0.2
0.3
400
500
600
700

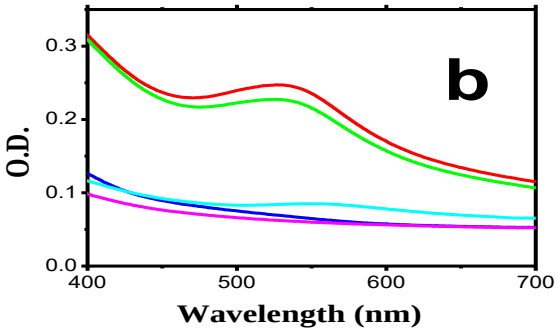
b
O.D.
Wavelength (nm)
0.0
0.1
0.2
0.3
400
500
600
700

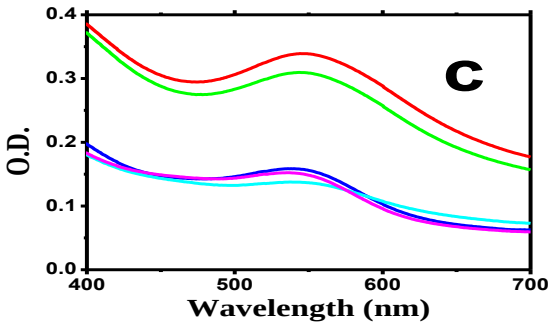
c
O.D.
Wavelength (nm)
0.0
0.1
0.2
0.3
0.4
400
500
600
700

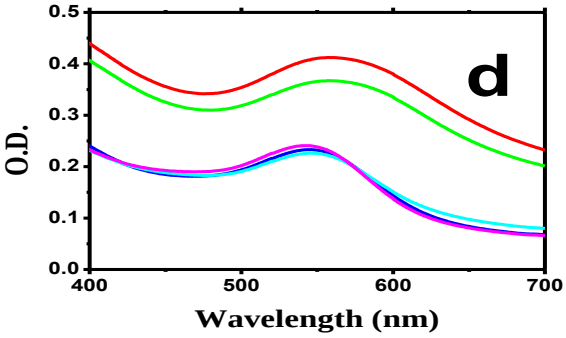
d
O.D.
Wavelength (nm)
0.0
0.1
0.2
0.3
0.4
0.5
400
500
600
700


pH 3
pH 4
pH 5
pH 6
pH 7


pH 3
pH 4
pH 5
pH 6
pH 7

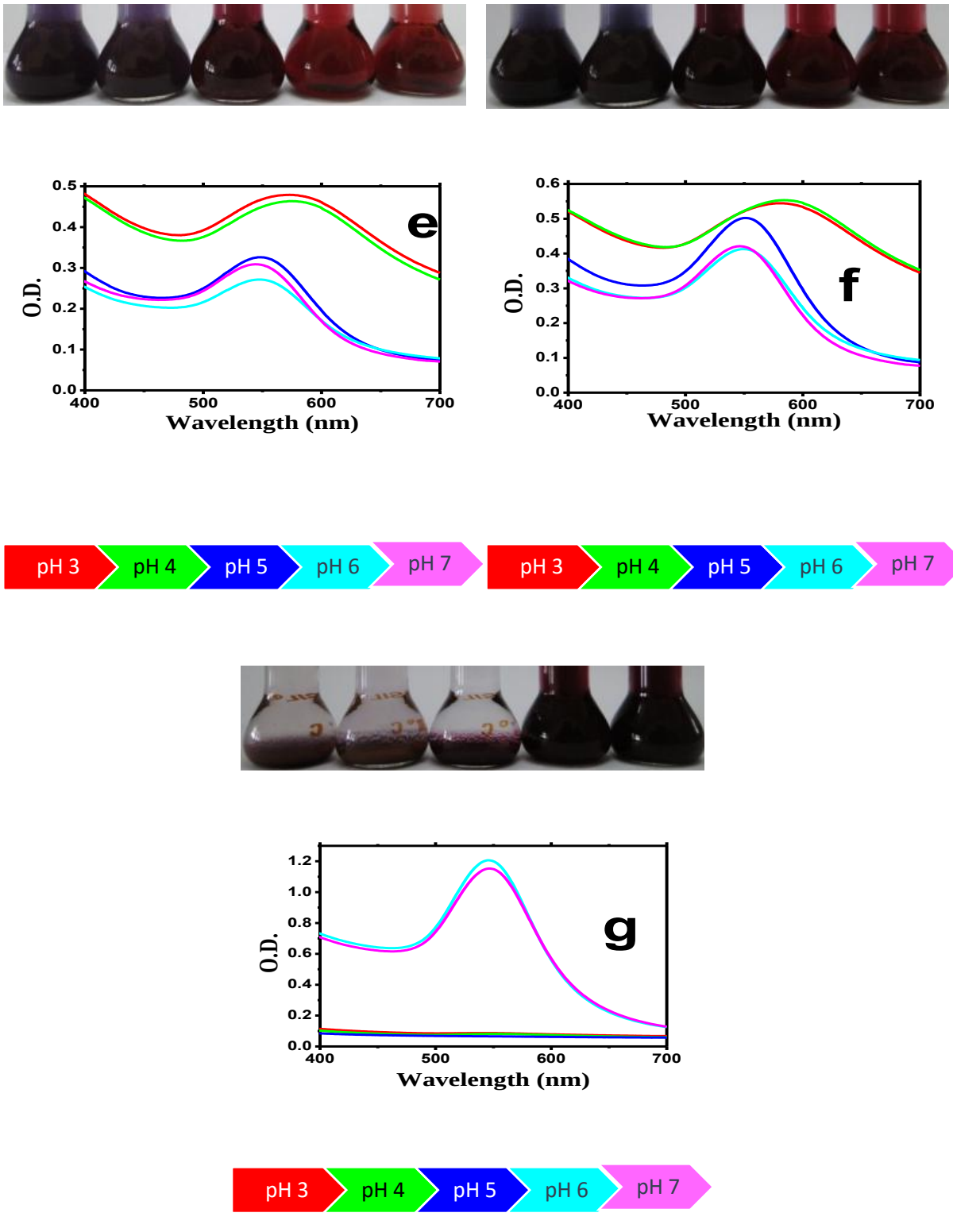

Figure 3.2. *Photographs and UV-vis absorbance spectrum of GNPssynthesised by the reaction of 1mM $HAuCl_4$ with 1mM Trp in aqueous medium at varying pH range of 3 to 7*

after (a) 1 minute, (b) 5 minutes, (c) 25 minutes, (d) 30 minutes, (e) 35 minutes , (f) 45 minutes and (g) 1 day of the onset of the reaction.

Addition of water to make up the volume in a 5 ml volumetric flask just after addition of Trp to $HAuCl_4$, marked the onset of the reaction. At pH 3 and 4, the solution turned pinkish just within 1 minute of the reaction. A steady increase inintensity was observed with time in the above case as shown in fig. 3.2.a.The plasmon band appeared at around 580nm for both the solution sets. In both cases, since the initiation of the reaction, the solution was turbid visually. The observation points towards the propensity of the GNPs towards instability and precipitation. After about 40 min, the GNPs started precipitating. At pH 5, the color of the solution turned to pale yellow colour (fig. 3.2.b), followed by yellow and then slowly turned into wine red colour after 25 minutes (fig. 3.2.c). The LSPR at pH 5, appeared at 550 nm after 25 minutes. The deviation of LSPR is not as much in the case of pH 3 and 4.At pH 6 and 7, pale yellow color appeared in the solution only after 5 minutes(fig. 3.2.b), followed by the appearance of slight pink color after 25 minutes (fig. 3.2.c) but became prominent only after 30 minutes(fig. 3.2.d) from the onset of the reaction.It was observed that the color of solutions in all the sets intensified between 35 min to 45 min which is shown in fig. 3.2.e and f.Thus, the rate of reaction as observed visually as well as by increase in intensity of LSRP at λ_{max} in the UV-vis absorption spectrum, was found to be dependent upon the pH of the medium. After 1 day, all the GNPsexcept those formed at pH 6 and 7 (fig. 3.2.g), were found to have precipitated. Thus, the stability of the colloids was found to be dependent on pH of the medium.In order to eliminate any influence of Au(III) blank or Trp black on the pH dependent absorption spectrum of GNPs, $HAuCl_4$ and Trp solutions were studied independently at the above reaction condition by UV-vis absorption spectroscopy. Chloroauric acid blank or Au(III) blank solution was prepared at different pH (fig. 3.3.a). Similarly, Trp blank solution was prepared at different pH (fig. 3.3.b). In Au(III) blank

solution (fig. 3.3.a), it was observed that the ligand to metal (L-M) charge transfer band of $HAuCl_4$ shifted its position with change in pH[209] which is also reported by other groups due to partial replacement of chloride ions by hydroxyl ions at higher pH. In Trp blank solution, only the peak intensity of π→ π* band and n→ π* band varied with change in pH (fig. 3.3.b).

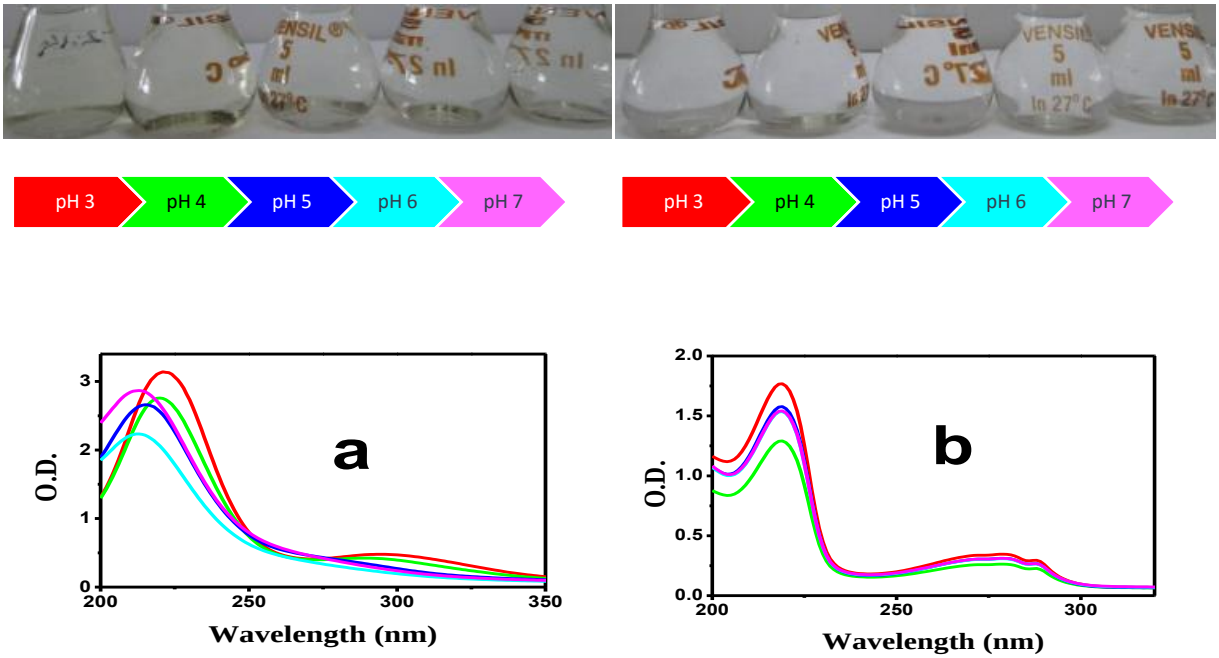

Figure 3.3. *Photographs and UV- vis absorption spectrum of solution of (a) 1 mM Trp in and (b) 1 mM $HAuCl_4$ in aqueous medium at varying pH range of 3 to 7.*

Trp has pK_1 and pK_2at 2.83 and 9.39 respectively with isoelectric point at 5.89. Isoelectric point is defined as the pH at which any molecule exhibits overall charge neutrality. It was observed in fig. 3.2. that the rate of formation of reaction sets at pH 3 and 4 showed a striking difference from that of reaction sets 5, 6 and 7. Red color appears in the reaction sets at pH 3 and 4 within 1 minutes of onset of the reaction (fig. 3.2.a). Appearance of red color is the indication of formation of GNPs which has been discussed earlier. After 20 minutes, the above solutions were found to turn slightly hazy and turbid (fig. 3.4.).

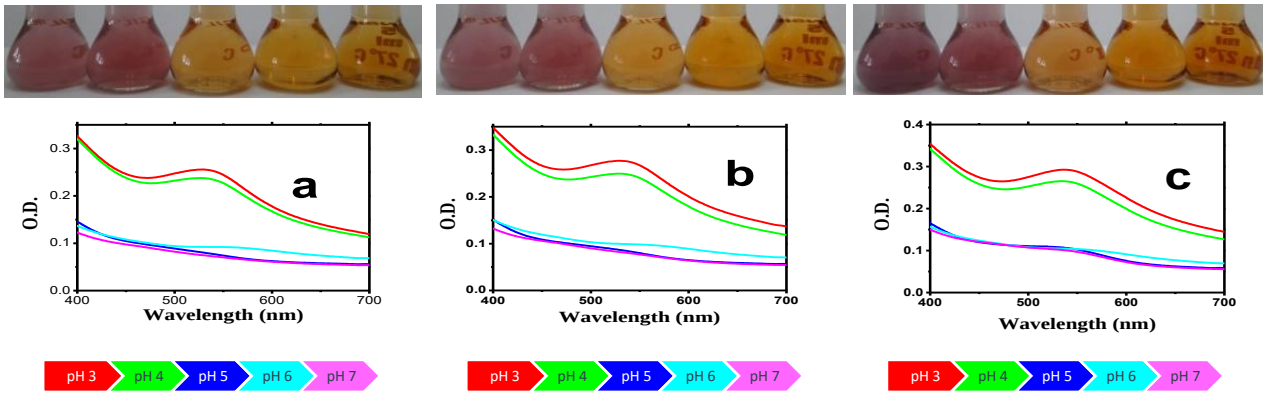

Figure 3.4. *Photographs and UV- vis absorption spectrum of GNPs synthesised by the reaction of 1mM $HAuCl_4$ with 1mM Trp in aqueous medium at varying pH range of 3 to 7 after (a) 10 minutes, (b) 15 minutes and (c) 20 minutes.*

After 25 minutes of the onset of the reaction, color of the solutions started to turn violet with increase in visible turbidity (fig. 3.2.c). The GNPs formed at pH 3 and 4 were found to precipitate after 1 day (fig. 3.2.g). In reaction sets at pH 5, 6 and 7, the color of the solutions turned pale yellow after 5 minutes (fig. 3.2.b). Out of the above solution sets, the color of the reaction set at pH 5 turned red by 25minutes (fig. 3.2.c). The color of the reaction sets at pH 6 and 7 turned red after 30 min(fig. 3.2.d). Reaction set at pH 5 was found to precipitate after a day (fig. 3.2.g) whereas reaction sets at pH 6 and 7 were found to retain color after a day. It was validated experimentally that Trp is unable to reduce $HAuCl_4$ below pH 3 and above pH 9.

It is known that,

$$rate\ of\ product\ formation = k\ [reactant]^n \qquad (3.1)$$

where n is the order of the reaction and k is the rate constant[210].Since, the concentration of $HAuCl_4$ and that of Trp is kept same in all the sets, such asynchronous change of color in

the solutions during synthesis of GNPs at varying pH can be due to pH dependent change in the structure or complex formation. Moreover, the precipitation of the GNPs solution may be due to the reduction of negative surface charge due to adsorption of H^+ ion at lower pH.[183, 187]

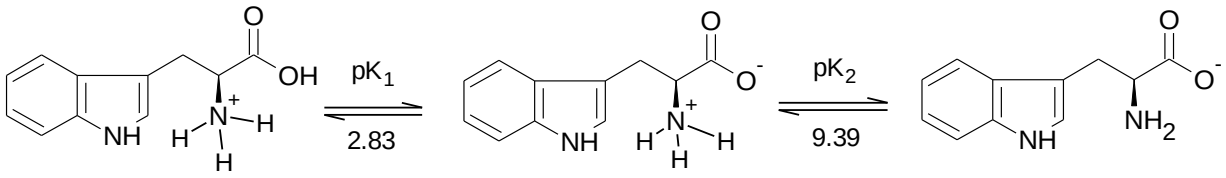

a b c

Figure 3.5. *Structure of Trp at varying pH (a) acidic form, (b) zwitterionic form and (c) basic form.*

In fig.3.5., the different forms of Trp are shown. Trp exhibits three different structure at various pH ranges. Below pH 2.83, Trp exists in its acidic form which has two acidic protons (fig. 3.5.a). Moreover, the lone pair on NH_2 is blocked. Above pH 2.83, zwitterionic form containing both NH_3^+ and $COO^-$of Trp (fig. 3.5.b) begins to appear. At the isoelectric point, i.e., pH 5.89, Trp completely exists in its zwitterionic form. Above isoelectric point, the alkaline form of Trp begins to appear (fig. 3.5.c) and above pH 9.39, it exists completely in basic form. At pH 3 and 4, Trp exists as a mixture of the acidic and the zwitterionic form of Trp (fig. 3.5.a and b) where amine group is protonated, which is unable to form complex with Au (III) ion. As a result, GNPs are formed directly. This may be the reason behind the instability of GNPs prepared at pH 3 and 4. In the later sections, it has been shown that Infrared study provides the evidence of direct binding of Trp to GNPs through amine group

and gas chromatographic study shows that Trp reduces $HAuCl_4$ via decarboxylation step as predicted by Zaheer et al[211].

At pH 6 and 7, Trp exists as a mixture of zwitterionic form and basic form (fig. 3.5.b and c). In its basic form, the amine group of Trp is free to donate its lone pair for the formation of a complex between Au (III) and Trp, which explains the formation of initial yellow color of the reaction solution as in reaction sets at pH 6 and 7 as shown in fig. 3.2.b. After the formation of GNPs, the amine group of oxidized Trp species attaches to the GNPs and stabilizes the GNPs in aqueous solution at the pH of the buffer. At pH 5, Trp exist more in the zwitterionic form. Thus, in this case, yellow color disappears faster (fig. 3.2.c) due weaker complexation with Au(III) than that in the case of pH 6 & 7 (fig. 3.2.e). Again, inthe presence of protonated amine group, oxidized Trp does not attach itself to the GNPs leading to agglomeration with time at pH 5.

The above discussion clearly indicates that the formation of stable GNPs by reduction of $HAuCl_4$ by Trp, occurs only in presence of a mixture of both zwitterionic and basic form. The basic form of Trp is responsible for the formation of yellow color complex (fig. 3.2.d and e) which slowly under goes reduction to GNPs whereas the zwitterionic form of Trp takes active part in reduction via decarboxylation. From the above experiments, it was evident that the GNPs formed at pH 6 were most stable.

In order to do further studies associated with the pH sensitive property of GNPs, the GNPs solution prepared at pH 6 was centrifuged at 10000 rpm for 5 min and the supernatant was decanted. The red coloured residue was washed with millipore water to remove unreacted reagents, followed by re-centrifugation and decantation. This step was repeated thrice so as to achieve maximum removal of reactants, buffer and other by-products. The residue, thus obtained was then dispersed in fresh acetate buffer solutions of strength 10 mM made in

millipore water by sonication in a sonicator bath for 3 minutes. The concentration of GNPs in the redispersed solution was three times ofthat in the GNPs solution obtained at pH 6 as mentioned above. This redispersed stock solution was further utilized for other experiments.Upon25 times dilution of the above solutionin buffer medium,it was observed that the GNPs at pH 5, 6 and 7 were stable but those with pH 3 and 4 had precipitated after one daywhich is shown in fig. 3.6.

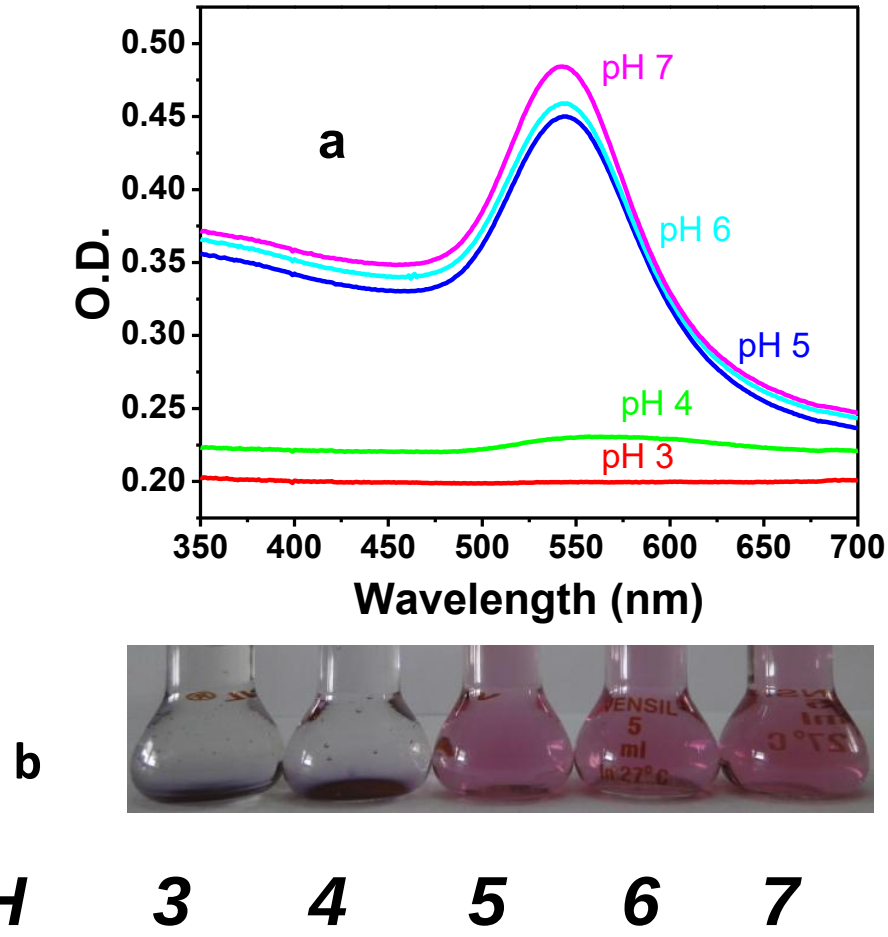

Figure 3.6. *(a) UV-vis absorption spectrum and (b) photograph of redispersed GNPs solution in buffered medium with pH varying in the range of 3 to 7, recorded after 1 day of redispersion.*

Redispersed solution of GNPs was prepared in pH 6, since at this pH the buffer capacity of acetate buffer found to be the highest.This experiment was not carried out at pH higher than 7, since the buffer capacity detoriates drastically on drifting away from the pK_a value of the acetate buffer used. However, the redispersed GNPs were found to be stable in phosphate buffer solution of pH higher than 7. This aggregation and subsequent precipitation of GNPs may be attributed to the adsorption of H^+ ions on the GNPs surface at pH lower than 5 which leads to neutralization of the surface charge of GNPs. The formation of stable GNPs in the pH range of 6 to 7 may be due to anchoring of the oxidised Trp species via the amine group on the GNP surface.

3.3.2. Study of functional groups on GNPs using infrared spectroscopy

The presence of oxidised Trp species on the surface of GNPs was confirmed by the study of vibrational spectra of Trp and oxidized Trp stabilized GNPs by Fourier Transform Infrared (FTIR) technique.Upon comparison of the observed peaks in Trp[212]with that in the oxidised species indicates that, $NH_2(\nu_{sym})$ at 3400 cm^{-1} is suppressed, aromatic CH (ν_{sym}) from 3003 to 2353 cm^{-1} is also suppressed and COO^- peaks at 1571 and 1408 cm^{-1} are retained, which is shown in fig. 3.7.

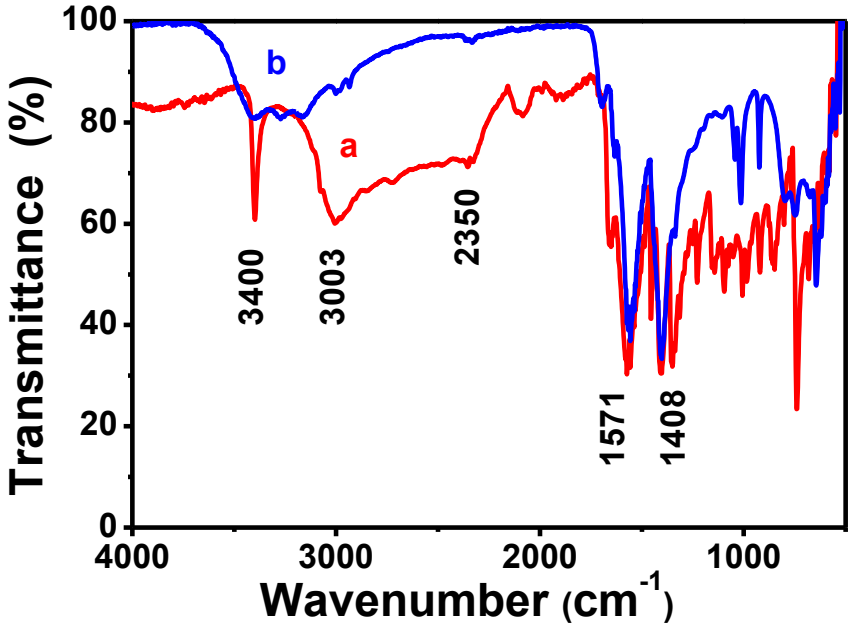

Figure 3.7. *Infrared spectrum of (a) Trp and (b) oxidised Trp stabilized GNPs dried after redispersion in pH 6.*

Theseobservations points out that oxidised Trp moeity undergoes drastic structural change in its aromatic skeleton along with disappearance of N-H bonds of NH_2 group from its structureand COO^- groups are present on the GNPs which is imparting negative polarity to the surface at higher pH. Earlier it was predicted that NH_2 may have participated in complexation and COOH may have undergone decarboxylation. The above observations from FTIR studies completely contrsdicts our earlier predictions. Presence of COO^- groups on the GNPs surface is also reported in literature in case ofGNPs synthesised by glutamic acid reduction.[213] This points out that not all COO^- undergo elimination and NH_2 group may lead to partial polymerization of Trp[205] on the surface of GNPs. Thus, the infrared spectroscopy of Trp blank and oxidised Trp stabilized GNPs has releaved a great deal about the structural change of tryptophan moeity at the surface og GNPs and the stability of GNPs at pH 6 and above.

3.3.3. Study of interaction of Trp with GNPs using steady-state fluorescence spectroscopy

The interaction of Trp with the GNPs was further confirmed by study of quenching of steady state fluorescence of Trp by the addition of GNPs solution synthesized at pH 6, to a solution of Trp. To 3 mL of 10^{-4} M Trp, incremental volumes of GNPs, prepared at pH 6, was added and its steady-state fluorescence spectrum recorded from 300 to 450 nm after excitation at 290 nm. The characteristic fluorescence of Trp is observed at 355 nm upon being excited at 290 nm, which was found to diminish with incremental addition of oxidized Trp stabilized GNPs, is shown in fig 3.8.

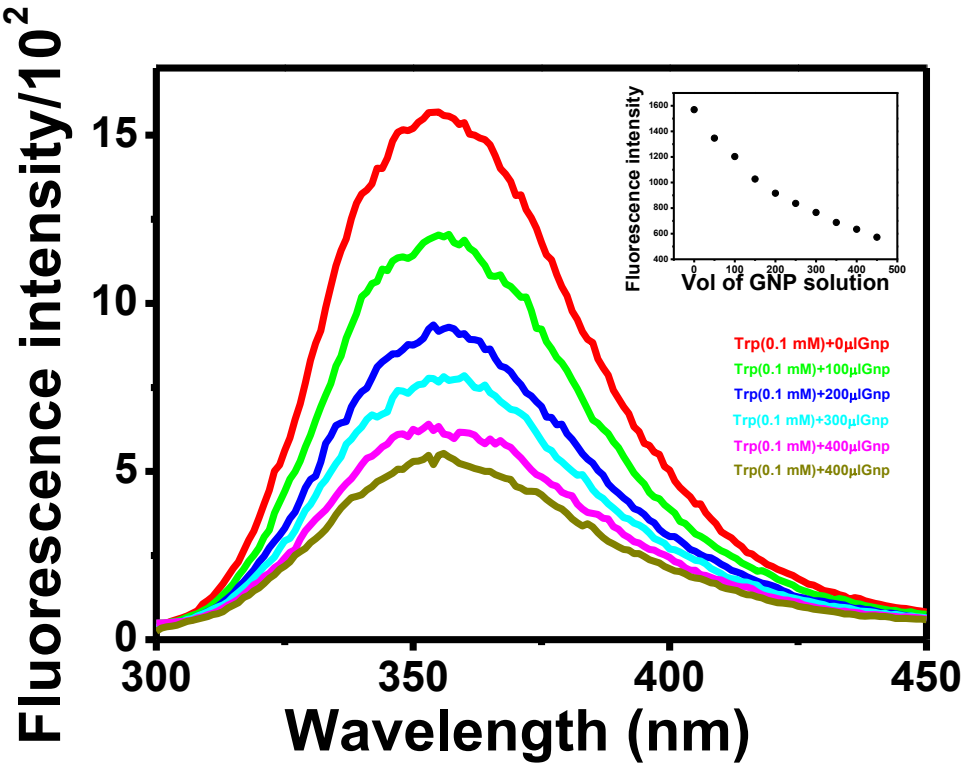

Figure 3.8. *Fluorescence spectrum of 0.1 mM Trp excited at 290 nm with incremental addition of oxidized Trp stabilized GNPs. Fluorescence intensity at 355 nm vs. volume of GNP solution added (Inset).*

This shows that the GNPs interact with Trp molecules and quenches fluorescence shown by Trp. This further proves the statement that Trp molecules adhere to GNPs in such a manner that results in effective decay of excited state of the aromatic moiety by non-radiative processes.[214]

UV-visible absorption spectroscopic measurements were carried out in order to ascertain the oxidation of Trp by $HAuCl_4$ (fig.3.9.). Comparison of the UV-vis absorption spectrum of 10^{-3} Moxidised Trp with that of the unoxidised Trp showed that the n→ π* peak shifted from 271 to 254 nm and the valley between n→ π* and π → π* peak shifted from 239 nm to 234 nm. Again the UV-vis absorption spectrum of the neat Trp showed a sharp peak at 275 nm due to n→ π* transition. However, the above UV-vis absorption spectrum showed drastic change after the addition of $HAuCl_4$, which is in line with the work reported by Iosin et. al.[205]It is reported that due to the strong electron donating nature of the nitrogen atom of the indole moeity[214] of Trp,Au^{3+} to Au^0can be reduced by Trp.

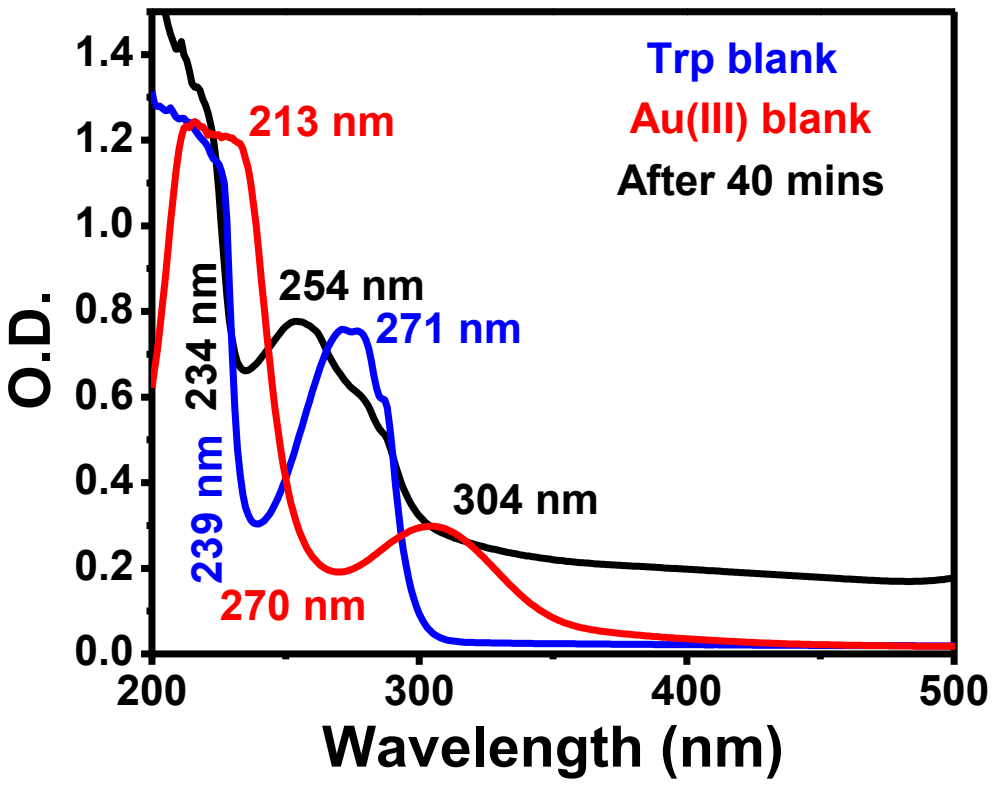

Figure 3.9. *UV- Vis absorption spectrum of (a) l-tryptophan blank solution, (b) chloroauric acid blank solution and (c) oxidised tryptophan formed after 40 min of reaction between chloroauric acid and l-tryptophan.*

3.3.4. Study of morphology of GNPs using transmission electron microscopy

TEM image of the oxidised Trpstabilized GNPs syhtesized at pH 6showed that the GNPs are highly monodispersed and spherical, as shown in fig. 3.10. The average diameter of the GNPs was found to ~40 ± 1 nm.

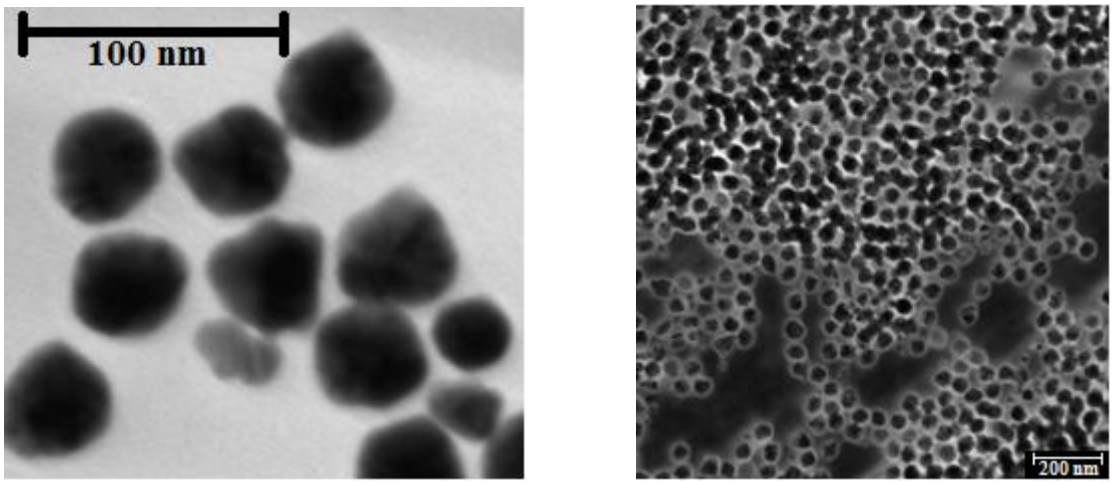

(a) (b)

Figure 3.10. *Transmission electron micrograph of oxidisedTrp stabilized GNPs with an average size of 40nm (a) at higher magnification (b) at lower magnification.*

3.3.5. Validation of reaction mechansim by gas chromatograpy

In order to provide more evidence related to the reaction of Trp with $HAuCl_4$, gas chromatography experiments were carried out. The reduction reaction of $HAuCl_4$ by Trp in buffered medium at pH 6 was used for the study of evolved gases to study the reaction mechanism. A 5 mL volumetric flask was taken, whereas the concentration of buffer solution at pH 6 was maintained at 10mM. To it $HAuCl_4$ was added. Then the volumetric flask was corked and Trp solution was injected under air tight condition. The final concentration of Au(III) and Trp in solution was 1mM. After 40 min, 2mL of supernatant gas was sampled out for analysis of CO_2 by gas chromatography. Another reaction set, devoid of $HAuCl_4$ was taken as blank in GC measurements. As the equilibrium parameters were not determined, yield of carbon dioxide was not calculated. But nevertheless, the GC results showed that the oxidation of Trp proceeds via a decarboxylation mechanism, which is shown in fig. 3.11.

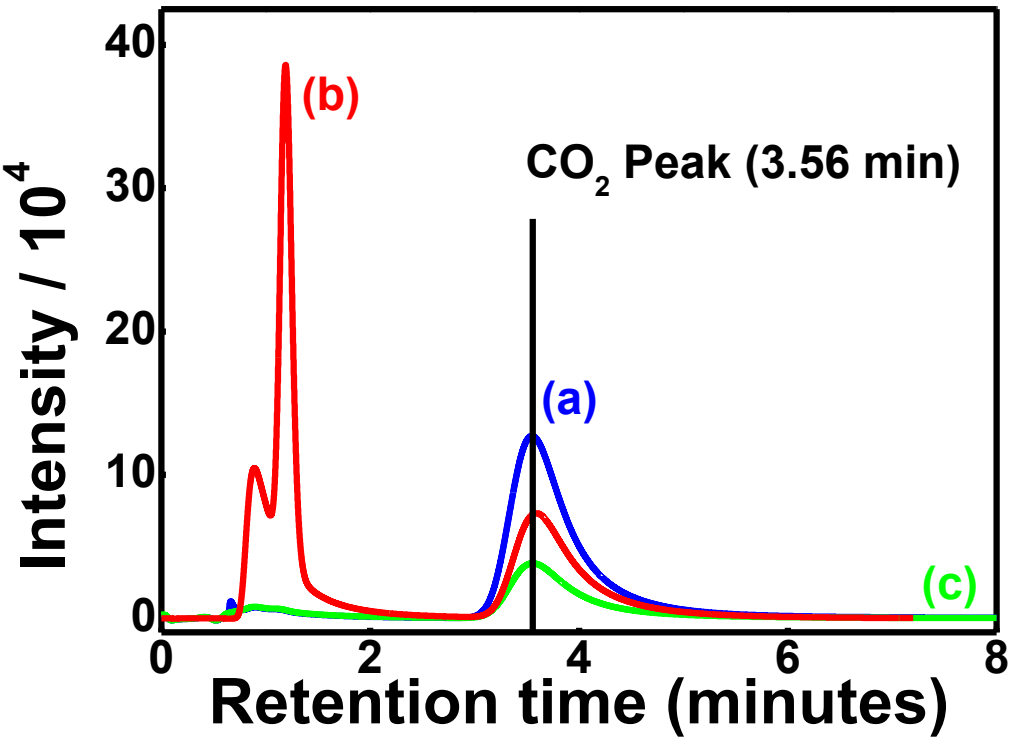

Figure 3.11. *Gas chromatograph for the reaction between 1 mM Trp and 1 mM $HAuCl_4$ in acetate buffer solution at pH 6of concentration of 10 mM performed in corked volumetric flask (sample)of volume 5 mL. 2 mL of supernatant gaseous phase (aliquot) is extracted by a pressure syringe from sample (a), standard (b) and blank (c) was used for GC measurement and their relative intensities were compared for detection as well as quantitative estimation.*

Quantitative estimation revealed that 635 ppm (v/v) of CO_2 was liberated during the reaction. As the solution sets were not N_2 bubbled, it can be assumed that the solutions were CO_2 saturated. Gas chromatographic study has revealed that during the reaction between Trp and $HAuCl_4$, CO_2 gas gets evolved.Thus,the GNPs synthesized in this work proceeds via the mechanism proposed by Zaheer et al.[211]

3.3.6. Study of response of GNPs in simulated extra-cellular environment

As the synthesis of GNPs in this study involved usage of zwitterionic molecule Trp, pH dependent variation in the stability of synthesized GNPs was observed (fig. 3.2.g). It was also found that the re-dispersed GNPs precipitated below pH 6 (fig. 3.6.) which pointed out towards the pH-sensitive behavior of the oxidized Trp products adsorbed on the GNPs surface. In order to study the possibility of utilization of this property for extraction GNPs from aqueous solution toan interface, another experiment was performed. Five solution sets of 3 mL each containing 25 times diluted re-dispersed GNPs in buffer solutions of pH 3, 4, 5, 6 and 7were taken and to all the solutions, 2mL of benzene was added. After this, the solutions were shaken till they became completely turbid. Then each solution set was allowed to settle until both the phases were completely separated. The above process of shaking and resettling was repeated thrice for each set. 1mL of the lower aqueous phase was then extracted from each set without disturbing the other phase to record the UV-Vis absorption spectrum to determine the concentration of GNPs, remaining in the aqueous phase.

It was observed that the color of the lower aqueous layer slowly became less intense and GNPs accumulated at the water- benzene interface. It is reported that GNPs must be well stabilized by a surfactant to be able to be extracted into the organic phase.[203] But if the surface charge[183]onthe nanoparticles is reduced, the nanoparticles tend to agglomerate due to increased inter-particle interaction promoted by reduced double layer thickness. Upon reducing pH of the aqueous layer, surface charge density of the GNPs is reduced due to neutralization of surface charge by H^+ ion and the nanoparticles precipitate with time as shown in fig. 3.6. The observed accumulation of the GNPs at the interface at low pH is to be noted as an interesting phenomenon. This could be due to the increase in the available surface area between polar and non-polar phase while shaking. The GNPs with low surface

charge at lower pH were stabilized by accumulating at water-benzene interface. The solution sets at pH 3 to 7 showed steadily decreasing accumulation with increasing pH, as shown in fig.3.12, which is evident from the absorption spectrum of aqueous layer showing an increasing trend in optical density at λ_{max} with increasing pH.

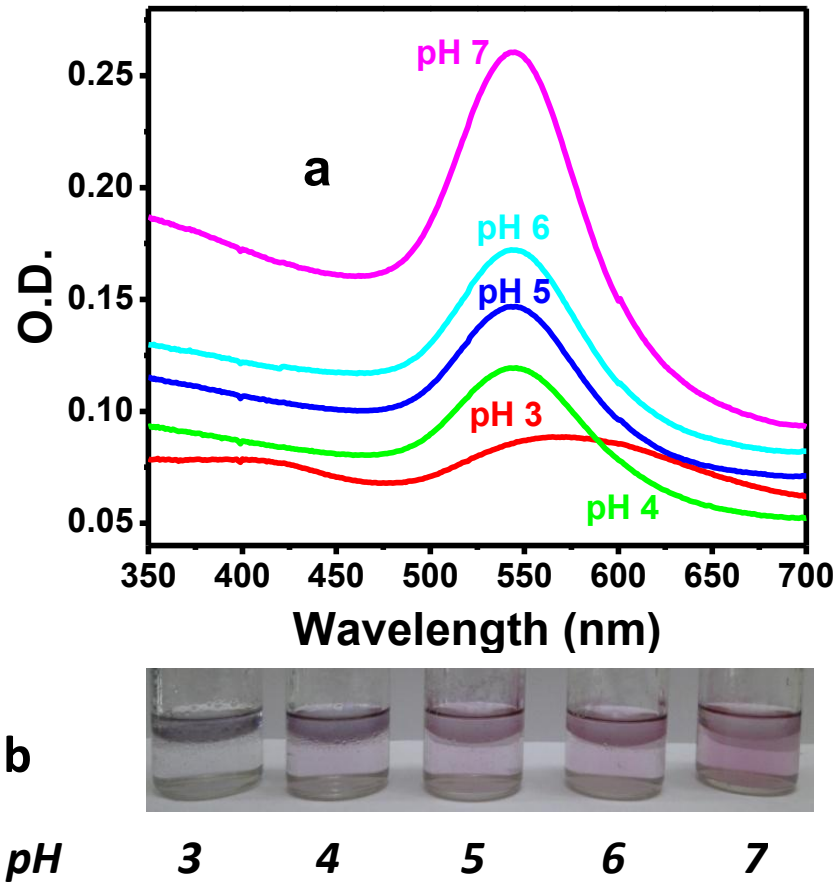

Figure 3.12. *Absorbance spectrum and (b) photograph of aqueous phase containing redispersed GNPs in different buffered medium with pH varying from 3 to 7, recorded after equilibrating for three times.*

The comparison of the extent of accumulation of the GNPs at the interface to that of precipitation at varying pH (fig. 3.6.) as shown in fig. 3.13., it was found that the interface accumulation process is much faster compared to the precipitation as the former process depends only on the surface charge on the nanoparticles at equilibrium condition. But the

precipitation process is slower as it depends both on surface charge and rate of agglomeration.[184]Assuming the double layer thickness to be constant in GNPs as buffer strength is kept constant, the reduction of the surface charge GNPs increases collisional interaction between the particles leading to increased rate of agglomeration. At lower pH 3 and 4, H^+ ion neutralizes the negatively charged surface of GNPs leading to higher rate of agglomeration and so the nanoparticles agglomerate and precipitate. At pH 5 and above, rate of agglomeration of GNPs is not as much as that in pH 3 and 4, so very little precipitation is observed.

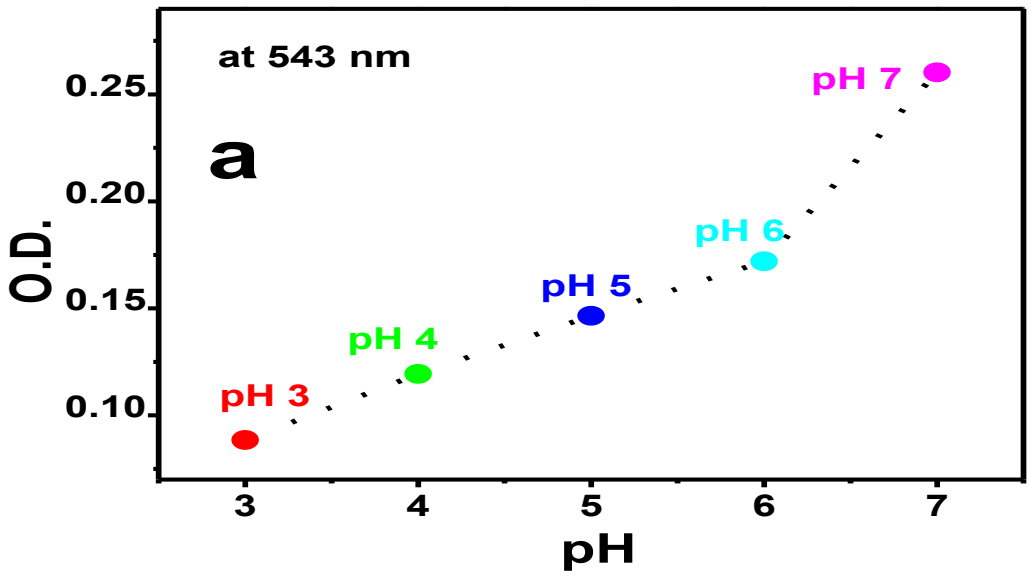

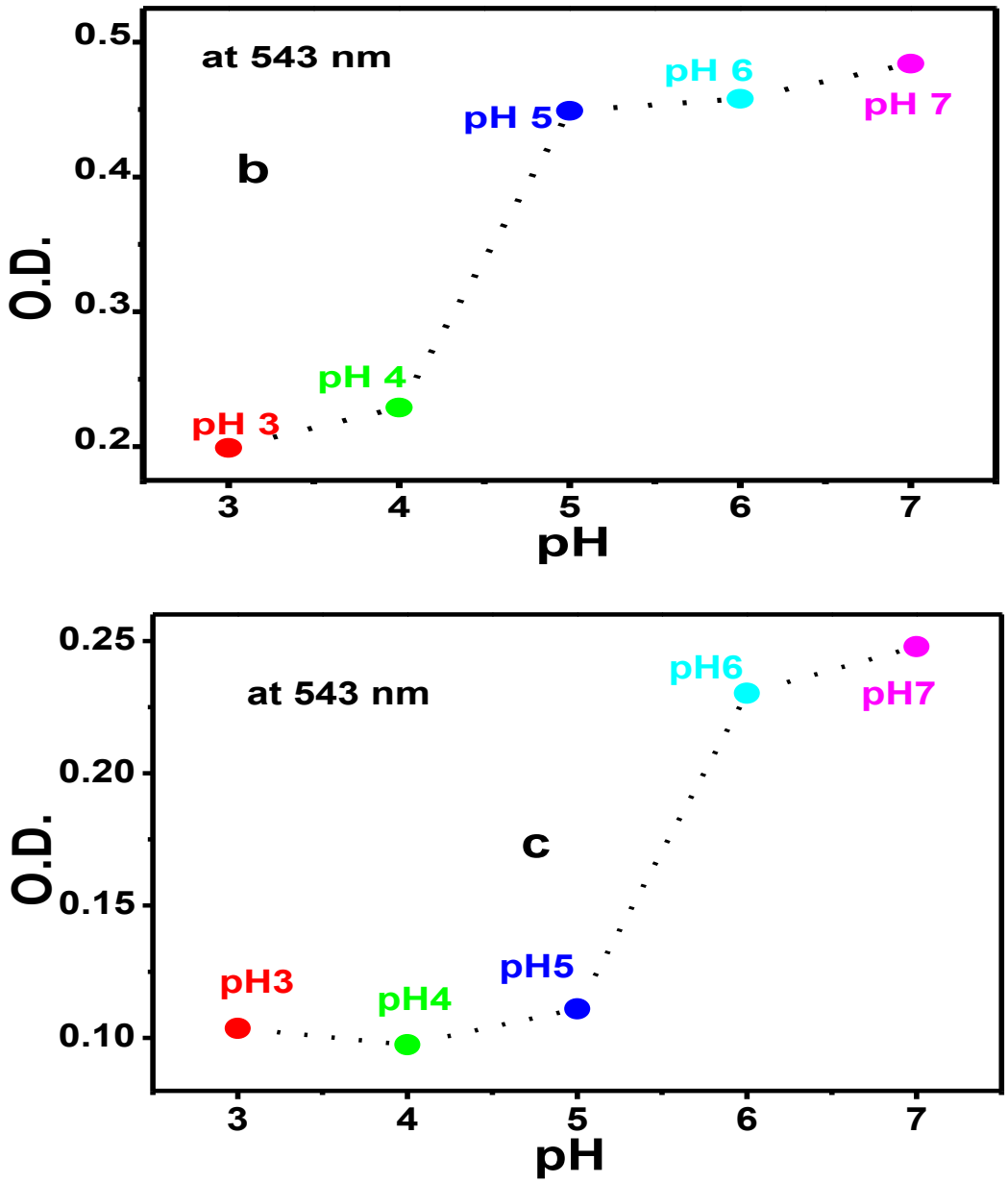

Figure 3.13. *Absorbance at 543 nm (bottom) of (a) redispersed GNPs solution in buffered medium atvarying pH from 3 to 7, recorded after 1 day, (b) aqueous phase containing redispersed GNPs in different buffered medium with pH varying from 3 to 7, recorded after equilibrating for three times with benzene layer and (c) aqueous phase containing redispersed GNPs in different buffered medium with pH varying from 3 to 7, recorded after equilibrating for three times with benzene layer containing phosphatidyl choline.*

Earlier studies on cancer, by J.R. Griffiths,[197]showed that extracellular fluids of tumours have lower acidity due to diffusion of lactic acid, produced in the tumour cells, to the periphery across the plasma membrane. Due to the presence of intermediate lipid layer in plasma membranes, transport of lactate ion is barred. As a result, the extracellular fluid in the tumours are found to be slightly acidic in comparison to normal tissue. Moreover, plasma membrane can be considered as an interface between polar extracellular fluid and the non polar, outer lipid layer of plasma membrane. In the above experiment, it was demonstrated thatthe accumulation of GNPs at polar- non polar liquid liquid interface increases with decreasing pH. Thus, oxidised Trp stabilized GNPs can act as a potential vehicle for targeting tumour cells due to its pH sensitive property. Moreover, the accumulation of GNPs in tumour cells can be used for radiosensitization.

Natural cell membranes are made up of phospholipid bilayer.[215] Phosphatidyl choline vesicles are often used to simulate cell membrane conditions.[216, 217] Therefore, in order to further substantiate the above observation,regarding the accumulation of GNPs at the polar-non polar liquid-liquid interface, phosphatidyl choline is used to construct an interfacial film at water-benzene interface just above CMC.[218] Phosphatidyl choline dispersed in benzene just above CMC,formeda saturated surface film which is analogous to the interface between extracellular and intracellular fluid in human vascular system. It was observed that GNPs accumulated differently at the polar non polar interface containing phosphatidyl choline as shown in fig. 3.14.

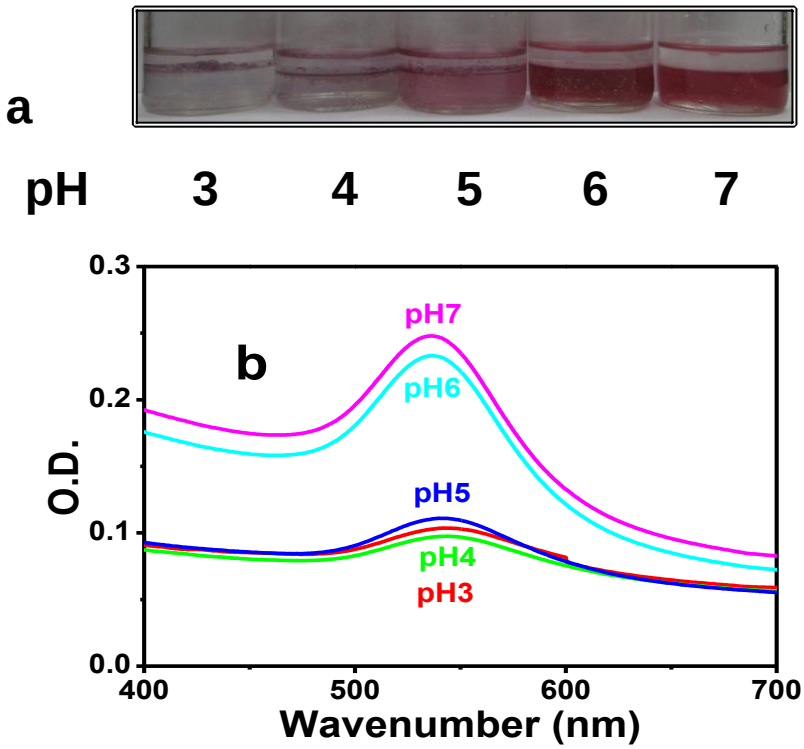

Figure 3.14. *Photograph of the solution sets containing an interfacial film of phosphatidyl choline formed between benzene and buffered aqueous phase containing GNPs with pH varying from 3 to 7. (b) Absorption spectrum of aqueous phase containing redispersed GNPs in different buffered medium with pH varying from 3 to 7, recorded after stirring for 20 min.*

The GNPs dispersed in buffered aqueous systems at pH varying from 3-7, showed a different trend in extent of interfacial accumulation of GNPs as shown in fig. 3.13.c unlike that shown in fig. 3.13.b.In this experiment, redispersed GNPs were diluted 10 times and all UV-visible measurements were carried out in a 0.3 cm pathlength cuvette. Here it was assumed that GNPs accumulate in between the non-polar portions of phosphatidyl choline present in the benzene phase and not in between the zwitterionin polar head groups, similar to the findings of Tatur et. al.[219]

Trp exists in our bodies in form of peptides as well as plasma free amino acid.[220]But according to the theory of absorption of proteins, absorption of proteins in our alimentary canal takes place in two forms- (a) as free amino acids and (b) as oligopeptides.[221]Recent

studies have shown that Trp and its metabolites 5-hydroxytryptamine or serotonin is present in blood in micro molar (μM) concentrations.[220, 222, 223]Thus, Trp can be used for the synthesis of biocompatible GNPs fit for in-vivo applications.

3.3.7. Study of radiosensitization efficiency of GNPs in gliomas cell lines

GNPs synthesized by reduction of Au^{3+} ions by tryptophan at pH 6 were used for the purpose of studying radiosensitization efficiency in cancer cell lines. Cytotoxicity study by Sulforhodamine B colorimetric assay method was done in human malignant glioblastoma (U-251MG), human cervical cancer (SiHa) and human transformed keratinocyte (HaCaT) cell lines as reported elsewhere.[224] It was found that GNPs were ton-toxic in the concentration of 10^{-3} M of Au. GI50 (Growth inhibition 50%) was found to be $2x10^{-7}$, $3x10^{-9}$ and $1x10^{-26}$ M for U-251MG, SiHa and HaCaT cell lines, respectively for a known drug, Adriamycin (Doxorubicin). Under the same conditions, the above cell lines did not show any reduction in growth, indicating non-cytotoxicity by the GNPs. Moreover, MTT assay[225] was performed in presence and in absence of ^{60}Co-γ irradiation in glioma cell line, U-87MG. It was observed that GNPs show a reduction in survival fraction of U-87MG to a maximum 5 %, in presence of 2 Gy radiation, as shown in fig. 3.15.

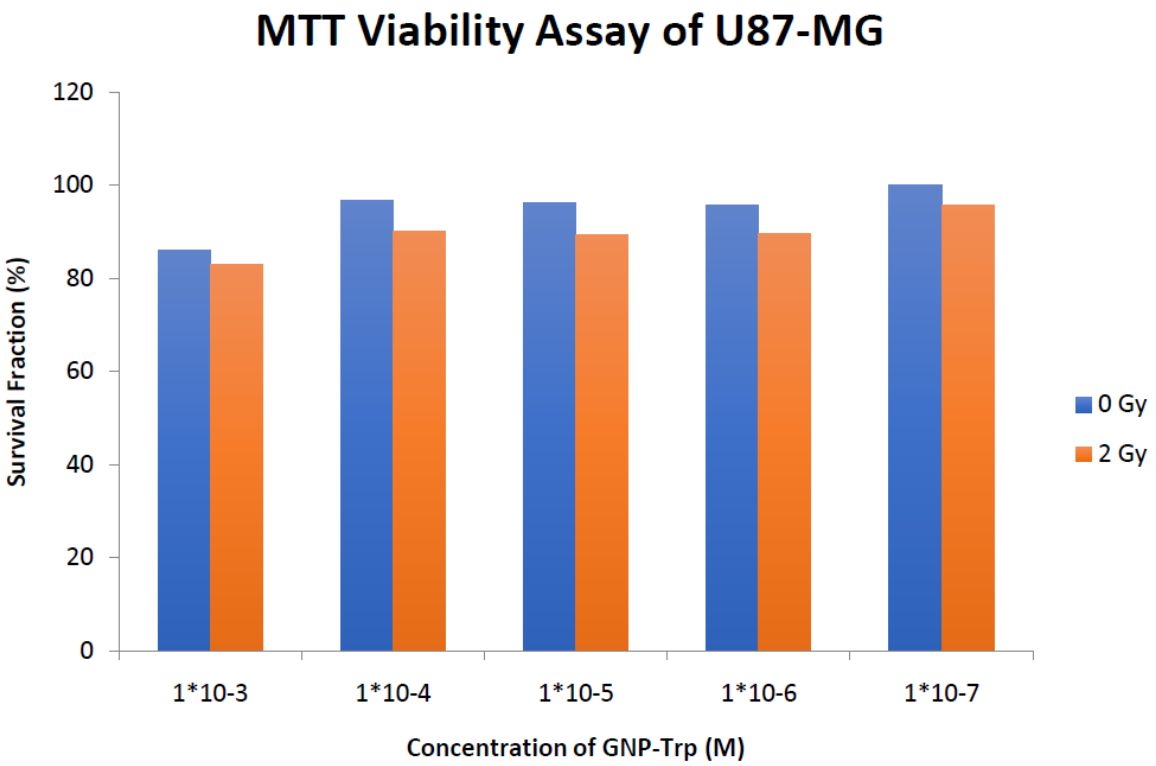

Figure 3.15. *MTT viability assay of U87-MG in absence (blue) and in absence of 2 Gy dose of ^{60}Co-γ radiation (red) after addition of varying concentration of GNPs in U-87MG cell lines.*

The observation of slight radiosensitization effect by GNPs in presence of ^{60}Co-γ radiation may be due to low absorption cross-section for photoelectric absorption of photon and subsequent emission at energies of the gamma rays (1.1732 and 1.3325 MeV). The phenomenon of radiosensitization was further explored in chapter 4 with silver nanoparticles in presence of low energy ionizing radiations.

3.4. Conclusion

Trp is used to reduce Au^{3+} to Au^{0} via pH dependent decarboxylation pathway. GNPs that are synthesized at pH 6 are most stable with negative surface charge, imparted by COO^{-} group attached to the adsorbed oxidized Trp species. pH plays a very important role not only

in the synthesis of GNPs but also in controlling the colloidal stability and surface charge of GNPs. The novelty of the synthesis is the non-requirement of surfactants to stabilize the colloidal system as the oxidized product of the reducing agent acts as a stabilizer. Lowering of pH leads to reduction of the surface charge on GNPs which eventually accumulates at the polar- non polar liquid-liquid interface. This phenomenon suggests that the GNPs can be regarded as a potential radio-sensitizer that would accumulate at the intra-cellular and extra-cellular fluid interface of acidic hypoxic cancerous cells. Moreover, in-vitro assays of radiosensitization efficiency of GNPs in gliomas showed slight reduction in survival fraction indicating the viability of GNPs for further radiosensitization studies.

4

Synthesis and characterization of gold / silver nanoparticles loaded polymeric film for sensing and dosimetric applications

4.1. In-situ synthesis of gold nanoparticles loaded polymeric films

4.1.1. Background

Gold nanoparticle (GNP) substrates are widely used for trace level detection of organic molecules by surface enhanced Raman scattering (SERS) technique[226, 227]. Noble metal nanoparticles exhibit unique optical property where free electrons present on the surface of the nanoparticle oscillate collectively[38] upon excitation by an electromagnetic radiation of a specific wavelength which is dependent on the size[228], shape[229] and dielectric constant[230] of the material. The above resonance condition is called surface plasmon resonance. The surface plasmon creates a near field[231] in proximity to the surface of the nanoparticle. When two or more noble metal nanoparticles come closer to each other, the near field of each nanoparticle interact or couple giving rise to a resultant enhanced electric field at the junction of the particles[232]. The above junction is often referred as hot-spot[233]. Any molecule in the vicinity of the above hot-spot is most likely to experience enhanced electric field which may polarize its electron cloud. The molecule may ultimately stabilize by scattering back the absorbed energy. The changes in the near field of the coupled plasmon are recorded in far-field in the form of UV-vis optical absorption[234] and SERS[235]. Designing of substrates made up of GNPs or silver nanoparticles (AgNPs) which would absorb analytes in its hot-spots to show SERS signal at low concentration has been the aim of researchers working in

the field of SERS sensing[236]. SERS substrates can be either in the form of solution as well as solid. Both have their own advantages and disadvantages. Noble metal nanoparticles in solution are very sensitive to addition of analytes, as it often induces agglomeration [237, 238] leading to generation of hot-spots. As a result, very low concentrations of analyte can be detected in solutions containing noble metal nanoparticles. Most commonly known GNPs and AgNPs can be prepared in solution by citrate[239] and borohydride[240] method. Most noted drawback of these solutions is that the solutions tend to agglomerate if the temperature and pH conditions are not maintained[241]. Solid substrates on the other hand are generally synthesized by electrochemical deposition [242, 243] of noble metals on rough surfaces or by chemical vapor deposition[244]. The above substrates can be stored for long time without any changes as well as can be carried to outdoors for on-site detection using hand-held Raman spectrometer[245]. The detection limits of the solid substrates are observed to be comparatively higher than their solutions counter-parts as the metal nanoparticles are immobilized on a solid matrix which reduces the control over agglomeration of particles upon adsorption of analytes. Thus, it can be said that solution based SERS substrates are suited for low concentration detection whereas solid SERS substrates are suited for on-site detection[246].

Recently, SERS substrates were developed by immobilizing GNPs in a filter paper[247].Silver nanoparticles can also be coated on the surface of glass for SERS sensing[238]. But such a coating requires sophisticated handling as scratch on the surface can remove the layer of silver nanoparticles. The aim of this work was to synthesize GNPs in a solid matrix where plasmonic nanoparticles are not dislodged from the matrix. Polymeric matrixes were one of the most important choices. Very few reports are available where polymeric films are used to immobilize GNPs for application in SERS sensing[248]. The polymer used in this study is sodium alginate. Sodium alginate is a biopolymer obtained from brown algae. Alginic acid

is a biopolymer consisting of alternating units of α-L-guluronic acid (G) and β-D-mannuronic acid (M)[249]. Sodium replaces the acidic proton in the carboxylic groups of the alginic acid and makes the biopolymer highly soluble in water. Cross-linking of alginate polymer is one of the simplest methods of cross-linking. Addition of sodium alginate solution drop-wise in Ca^{2+} or Ba^{2+} solution leads to cross-linking of alginate as bivalent metal ion binds to two adjacent carboxylic groups present on the skeleton of the polymer. The above cross-linked structure is well explained by "egg-box model", where cavities are created for sorption of metal ions by residual carboxylic groups[250]. Alginate biocomposites can be obtained in the form of beads[251] or films[252] depending on the application. GNPs were also synthesized in alginate anisotropic structures for sensing applications[253]. There are reports where mixtures of bivalent calcium ion and trivalent ferric ions have been used to cross-link alginate[254]. Ferric ions strongly bind alginate and have one free valency which can be used for extraction of anions[255]. In this work, monovalent tetrachloroaurate ions were added to cross-linked alginate films for adsorption via replacement of Ca^{2+} or Fe^{3+}ions or both. The Au^{3+} ions loaded in the films by sorption were further reduced by glucose to synthesize GNPs *in-situ*. The GNP loaded films were then used for detection of crystal violet (CV), a dye and a fungicide, using SERS.

4.1.2. Experimental Section

4.1.2.1. General Materials and Methods:

Gold (III) chloride hydrate (99.995% trace metal basis), sodium alginate (synthetic), crystal violet (90.0%), poly-vinyl pyrollidone (PVP, avg mol wt 40,000), n-hexane (95%), calcium nitrate (99%), ferric chloride (97%) and D-glucose (99.5%) were obtained from Sigma-Aldrich and were used as received. Hydrochloric acid (30%) was obtained from Merck. All the experiments were performed in Millipore purified water.

4.1.2.2. Synthesis of GNP loaded alginate films:

2% (w/v) sodium alginate solution and 8% (w/v) PVP solution were mixed in the ratio of 9:1 by volume at 25ºC. 20 ml of the above mixture was stirred for half an hour followed by addition of 1 ml n-hexane while stirring vigorously. The above mixture was spread on a perfectly flat petri-dish with an internal diameter of 9 cm and air-dried to form a robust transparent film. Dried film was removed later from the petri-dish using a pair of forceps. The above water-soluble film was cut into pieces of dimension: 1 cm x 1 cm. All the cut films were washed in acetone and air-dried in order to remove any organic impurities. The above films were added to cross-linking solution consisting of 0.1M Ca^{2+} and 0.1M Fe^{3+} ions in various ratio by volume while stirring for 2 hours. The each of the above water insoluble cross-linked films were dipped in 1 ml of $3x10^{-3}$ M $HAuCl_4$ solution for 1 day. Au^{3+} containing cross-linked alginate films were immersed in 5 ml of 0.05 M D-glucose solution in a 10 ml volumetric flask and heated in a boiling water bath for *in-situ* reduction of Au^{3+} to GNPs. Red coloured GNP loaded alginate films were further used for SERS detection of CV.

4.1.2.3. Instrumentation details:

The absorption spectra of the solutions, used in this work, were recorded using UV-vis absorption spectrophotometer (JASCO V-650). The Raman spectra of solid CV and SERS spectra of the solutions were recorded using 632 nm laser line from a He-Ne laser. The sample solutions were taken in a standard 1×1 cm^2 quartz cuvette and the Raman scattered light was collected at 180° scattering geometry and detected using a CCD (Synapse) based monochromator (LabRAM HR800, Horiba JobinYvon, France) together with an edge filter. The spot size on the sample was ~0.5 mm in diameter, and the laser power at the sampling position was 10 mW for the excitation wavelengths of 632 nm. The Raman band of a silicon

wafer at 520 cm^{-1} was used to calibrate the spectrometer, and the accuracy of the spectral measurement was estimated to be better than 1 cm^{-1}. Transmission electron microscope (TEM) images and selective area electron diffraction (SAED) patterns for the samples were taken on JEOL 1200 EX Microscope operated at an accelerating voltage of 200 kV. Fourier transform infrared (FT-IR) spectra were recorded using Shimadzu FT-IR instrument.

4.1.3. Results and Discussion:

Robust water-soluble alginate (Alg) films were immersed in cross-linking solution after washing in extrapure acetone. This washing is acetone is necessary to remove organic impurities present on the surface. Solubility of sodium alginate in acetone is much lower than that in water. Five washed Alg films were dipped in 20 ml of cross-linking solutions comprising of mixture of 0.1 M $Ca(NO_3)_2$ and 0.1 M $FeCl_3$ in the ratio of 1:0, 3:1, 4:1, 5:1 and 6:1. The above cross-linked films were further immersed in 1 ml of $3x10^{-3}$ M Au^{3+} solution to study the extent of absorption of Au^{3+} by the films by recording the UV-vis absorption spectra at regular interval for 1 day. The absorption maximum of $AuCl_4^-$ appears at ~ 310 nm for $3x10^{-3}$ M $HAuCl_4$. As the concentration of Au^{3+} was decreased, the absorption maximum was found to be blue shifted. This may be due to the overlap of more intense 220 nm peak and less intense 310 nm peak of $HAuCl_4$. UV-visible absorption spectra of a series of different concentrations are shown in fig. 4.1.a. Calibration curve for quantitative detection of concentration of $HAuCl_4$ can be obtained by plotting absorbance vs. concentration at a specific wavelength. Fitting of the above curve were fitted with least square fit method[256]. The coefficient of determination (R^2) for each fit at different wavelength predicts the accuracy of the method (fig. 4.1.b)[256]. From fig. 4.1.b, it can be seen that R^2 is lower in the range 300 to 345 nm due to overlap of 220 nm peak. At 350 nm, the R^2 value is 0.99973, which indicates that determination of concentration of $HAuCl_4$ can be carried out with minimal error at this wavelength. The absorbance of the supernatant in the

above cases at 350 nm vs. time is shown in fig. 4.1.c. More than 60% decrease in absorbance was observed in case of the cross-linking solution containing Ca^{2+} and Fe^{3+} in the molar ratio of 1:0 and 5:1. Based on the above observation, films cross-linked with 0.1 M $Ca(NO_3)_2$were considered for further experiments and the film was assigned name 'Ca-Alg' film. Similarly, films cross-linked with 0.1 M $Ca(NO_3)_2$ and 0.1 M $FeCl_3$ in the ratio 5:1, were considered for further experiments and called 'Ca-Fe-Alg' film.

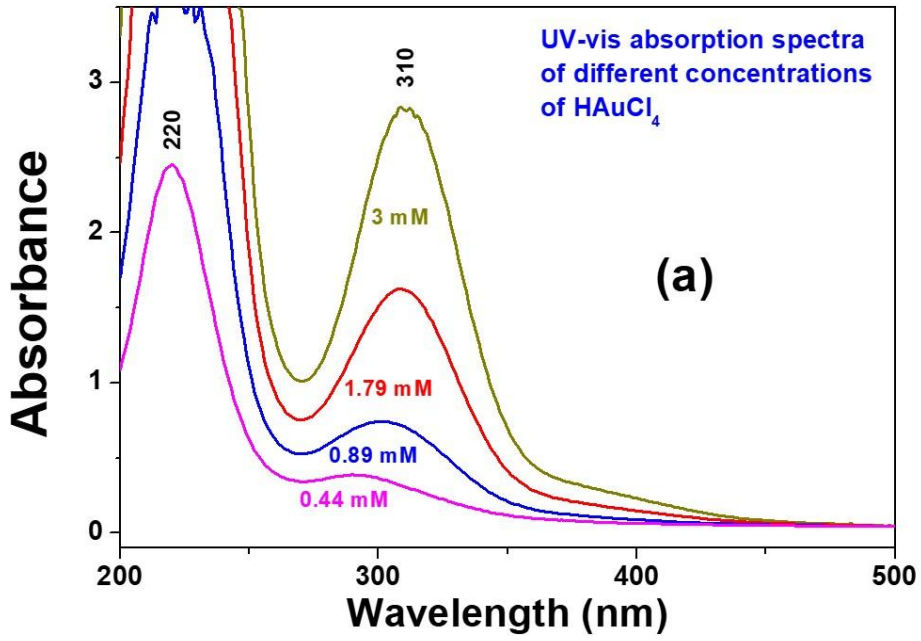

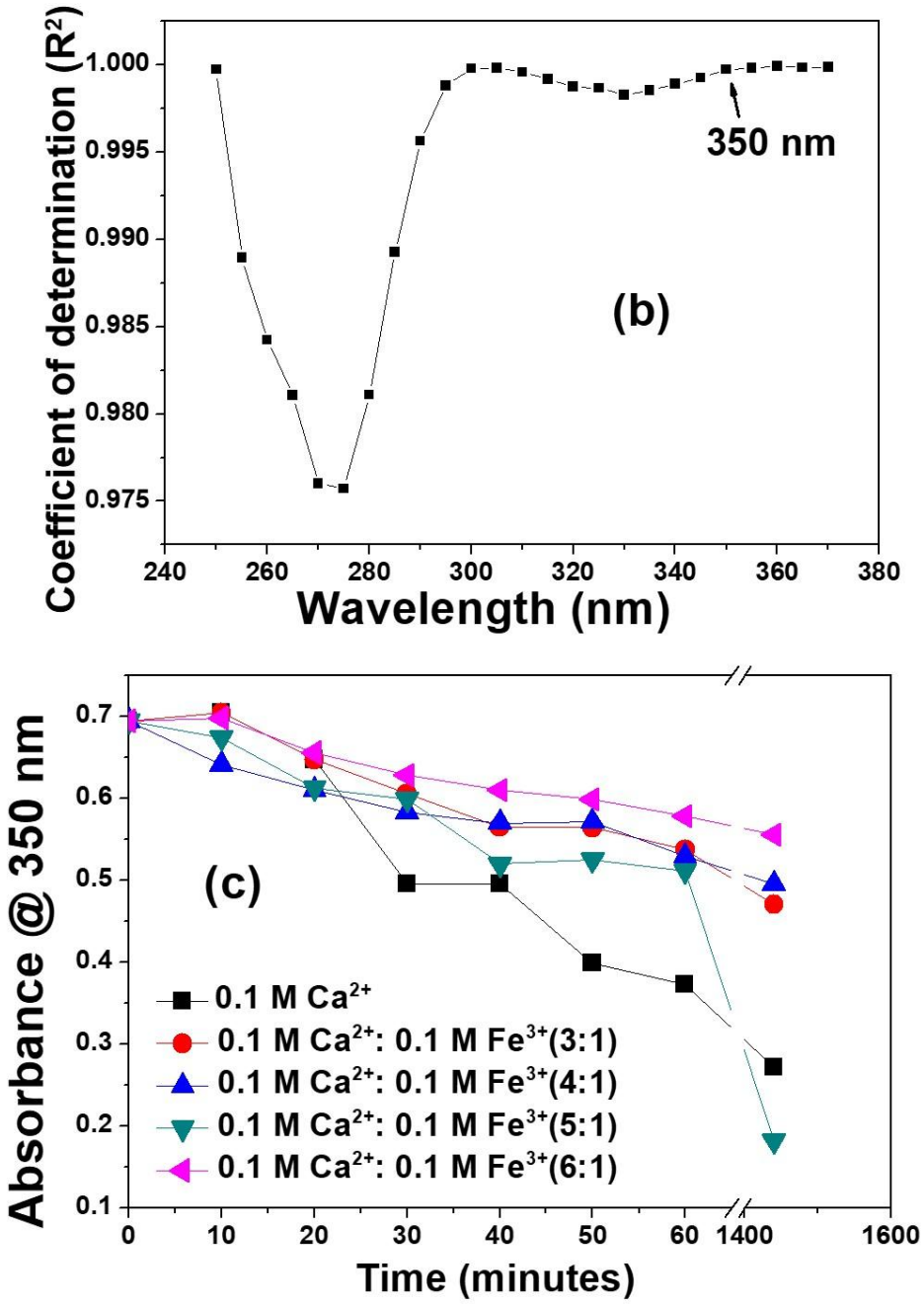

Figure 4 .1. *UV-vis absorption spectra of different concentrations of $HAuCl_4$,, (b) Coefficient of determination (R^2) for varying wavelength obtained from fitting of absorbance vs. concentration of $HAuCl_4$ solutions at fixed wavelength, and (c) Absorbance of the supernatant of the cross-linked films with Ca^{2+} to Fe^{3+} content (molar ratio) of 1:0, 3:1, 4:1, 5:1 and 6:1 immersed in a solution of $3x10^{-3}$ M Au^{3+} recorded at regular intervals.*

The images of the transparent film, cross-linked film, Au^{3+} loaded cross-linked film and GNP loaded cross linked films are shown in fig. 4.2. It can be seen that cross-linking of the film only in Ca^{2+} turns transparent film into translucent white colour, whereas in presence of Fe^{3+}, the film turns light yellow (fig. 4.2.b). Absorption of Au^{3+} imparts a yellowish tinge to all the cross-linked films (fig. 4.2.c). Further *in-situ* reduction of Au^{3+} absorbed in the films by D-glucose turns the films reddish due to formation of GNPs as shown in fig. 4.2.d. The extent of cross-linking of alginate matrix of the films depends upon the charge density of the cross-linking ion. Surface charge density of Fe^{3+} is higher than that of Ca^{2+}. Brus et al. has demonstrated that cross-linked alginate polymer with higher surface charge density on cross-linking cation show higher extent of chemical exchange due to carboxylic groups[257]. Thus, Fe^{3+} may contribute more towards increasing the adsorption of $AuCl_4^-$ by chemical exchange, in comparison to Ca^{2+}.

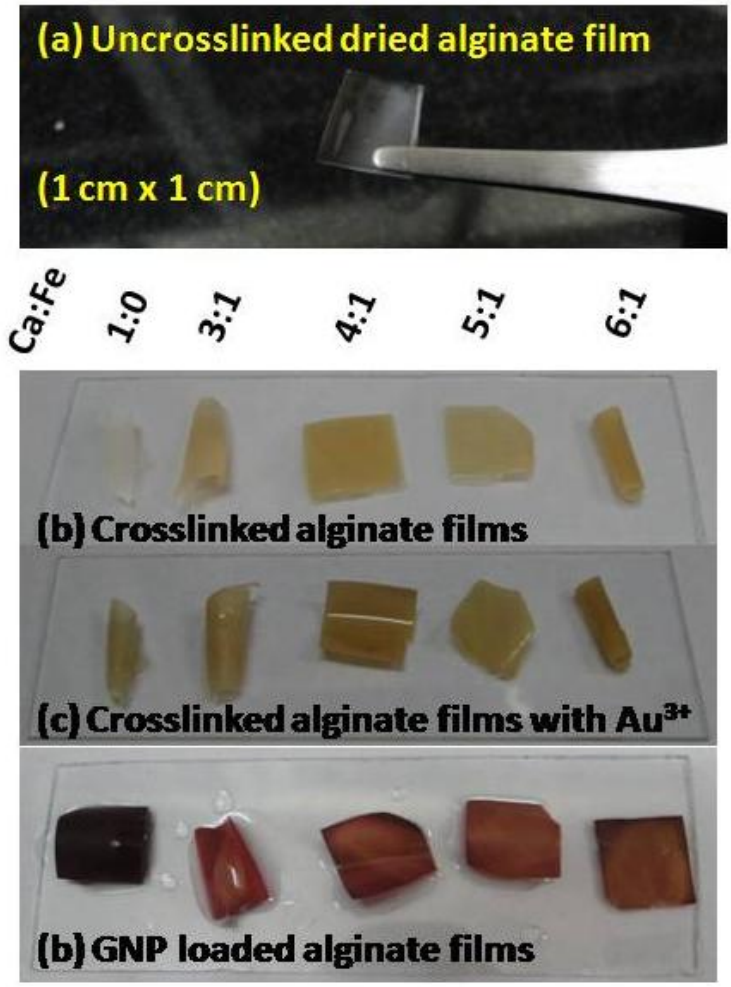

Figure 4 .2. *Photograph of (a) uncross-linked dried transparent alginate film, (b) cross-linked alginate films, (c) Au^{3+} loaded cross-linked alginate films, and (d) GNP loaded alginate films.*

GNPs loaded Ca-Alg and Ca-Fe-Alg are designated as Au/Ca-Alg and Au/Ca-Fe-Alg films respectively. The extent of GNPs lost in Au/Ca-Alg and Au/Ca-Fe-Alg films were further measured by recording the supernatant of the reduction reaction by glucose in boiling water bath for 3 minutes as shown in fig. 4.3. In case of Au/Ca-Alg and Au/Ca-Fe-Alg films, leached out GNPs showed LSPR at 526 nm and 550 nm respectively, as shown in fig. 4.3. Moreover, the absorbance of GNPs in case of Au/Ca-Alg films were found to be lower than that of Au/Ca-Fe-Alg films indicating that extent of retention of GNPs is better in case of

the former. The LSPR of Au/Ca-Fe-Alg films appeared at a higher wavelength than that of Au/Ca-Alg films.

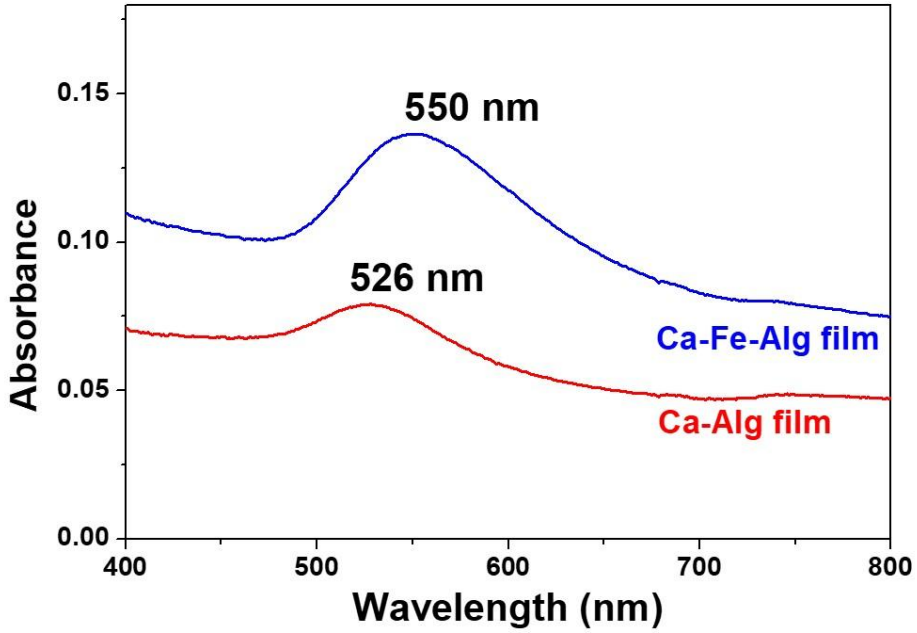

Figure 4 .3. *UV-vis absorption spectra of leached GNPs during reduction of* Au^{3+} *in Ca-Alg and Ca-Fe-Alg films by 0.05 M glucose for 3 minutes in boiling water bath.*

The above supernatant solutions, whose UV-vis absorption spectrum is shown in fig. 4.3, were used for recording TEM image as shown in fig. 4.4. It can be seen in fig. 4.4.a, that particles of size ~10 nm are clustered together. Around the particles a dark shadow is also observed which may be due to the capping of alginate. The selected area electron diffraction (SAED) pattern shown in the inset of fig. 4.4.a shows that the pattern corresponding to Au(0)[258]. Sharp diffraction pattern indicate that the particles are fairly crystalline. In fig. 4.4.b, a cluster of particles of size ~5 nm is observed. The particles are in close proximity to one another compared to particles observed in fig. 4.4.a. This suggests that in case of Au/Ca-Fe-Alg (fig. 4.4.b), there is a possibility of plasmon coupling which may show lead to observation of SPR band at higher wavelength. The above inference is supported by the UV-vis absorption spectra of Au/Ca-Fe-Alg as shown in fig. 4.3. The presence of strong

plasmon coupling also suggests that the hotspots generated in Au/Ca-Fe-Alg film may be useful for SERS based sensing[259].

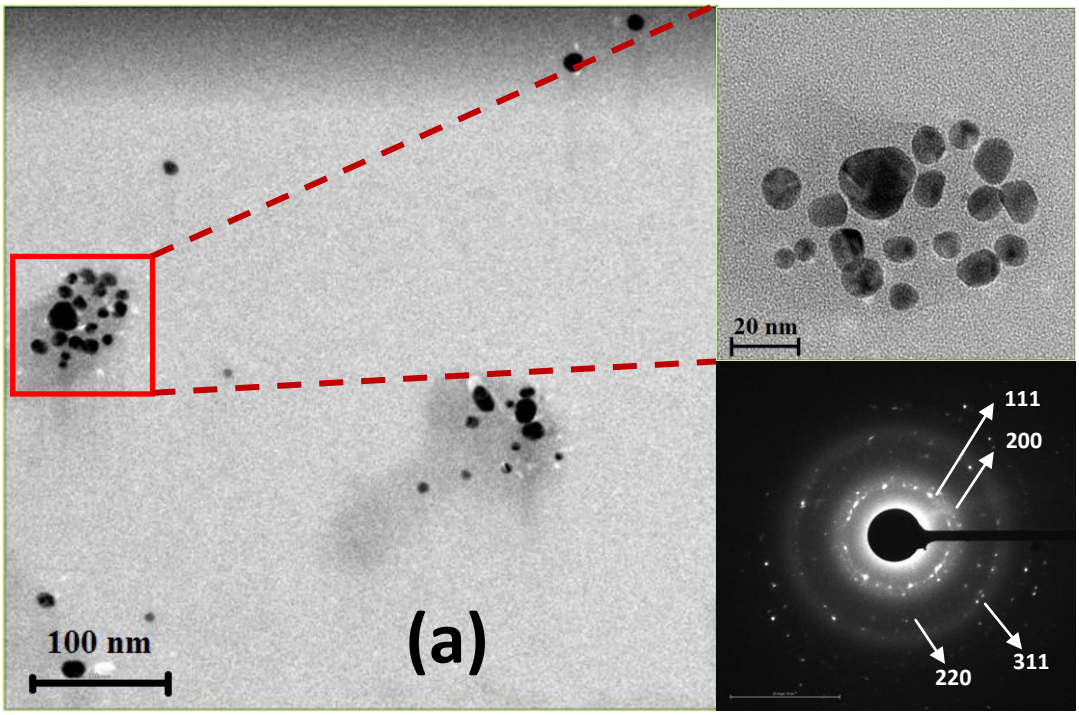

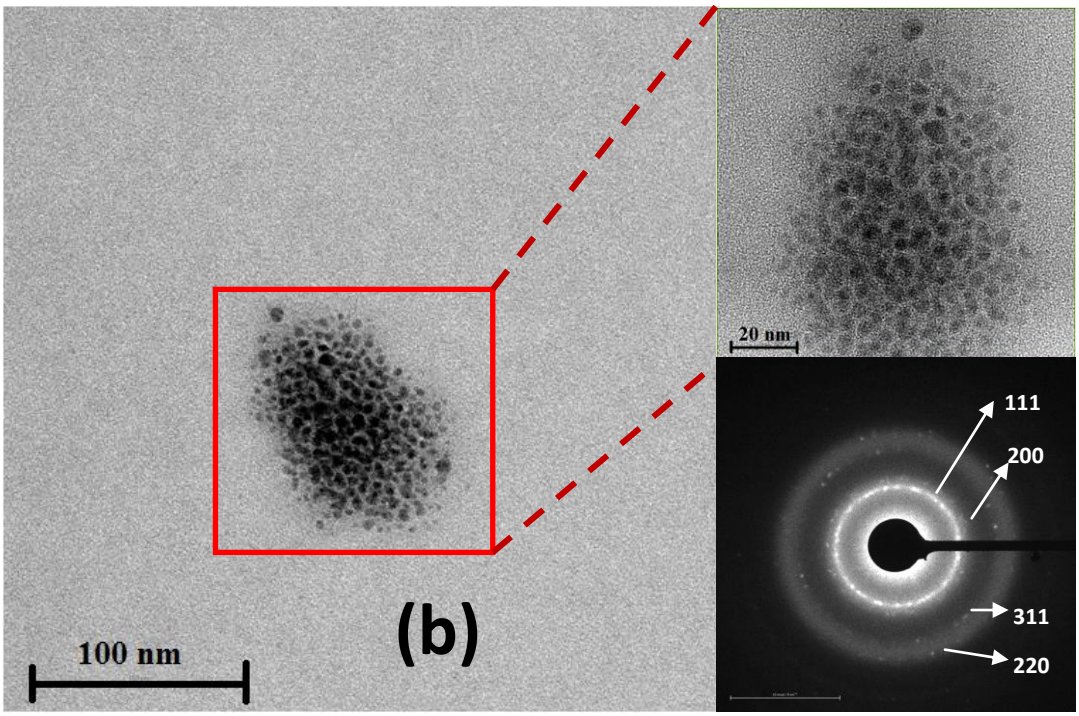

Figure 4 .4. *Transmission electron microscopy (TEM) image of (a) Au/Ca-Alg and (b) Au/Ca-Fe-Alg nanocomposite extracted from the supernatant obtained during reduction of* Au^{3+} *loaded Ca-Alg and Ca-Fe-Alg films by glucose.*

In order to study the interaction of GNPs with alginate, vibrational spectra of Au/Ca-Fe-Alg films was compared with that of sodium alginate. FT-IR spectra of Au/Ca-Fe-Alg films and sodium alginate shown in fig. 4.5, showed no appreciable difference in the vibrational bands of the two samples mentioned above, which indicates that incorporation of GNPs in the alginate matrix does not alter chemical structure of alginate[260]. The above observation further clarifies that the nature of interaction of alginate and GNPs is not chemical in nature. Thus, the GNPs loaded in the alginate films can be used for adsorption of other molecules for sensing applications.

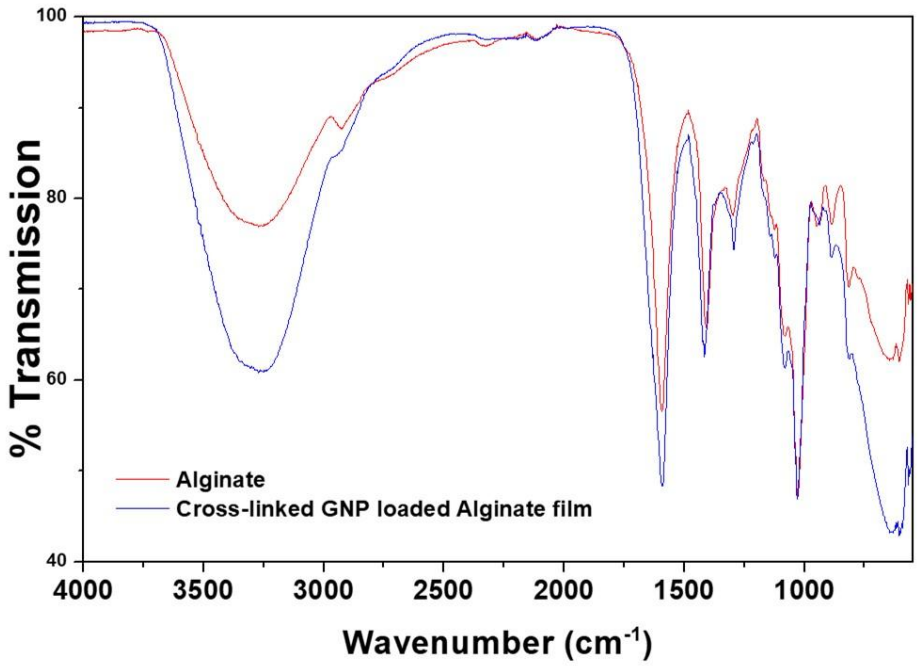

Figure 4 .5. *FT-IR spectra of sodium alginate and GNP loaded cross-linked alginate films*

Au/Ca-Alg and Au/Ca-Fe-Alg films were used to record SERS spectra of CV. For the above purpose, 10µl of 10^{-5} M CV was drop casted on the films. None of the films showed SERS spectra. This may be due to loss of GNPs from the surface of the films during reduction of Au^{3+} adsorbed in the films by 0.05 M glucose for 3 minutes. As a result, GNPs are present beneath the layers of cross-linked alginate. The above observation was also encountered by Mele E. et al.,[253] where GNPs were not found on the surface of the anisotropic alginate biocomposites. In order to remove a layer of alginate, the films were immersed in 0.2 M HCl for a fixed interval of time. Au/Ca-Alg films showed no SERS signal whereas Au/Ca-Fe-Alg film showed SERS signal. The SERS signal was found to increase with increasing etching time up to 3 minutes and then decreased was observed as shown in fig. 4.6. The above observation indicates that etching up to 3 minutes exposes GNPs present beneath the layer of cross-linked alginate (fig. 4.6.a, b and c). Further etching might have released GNPs from the pores of the alginate films, which had led to lowering of the SERS intensity as shown in fig. 4.6.d and e. Thus, acid-etched Au/Ca-Fe-Alg films were observed to be the best substrates for SERS.

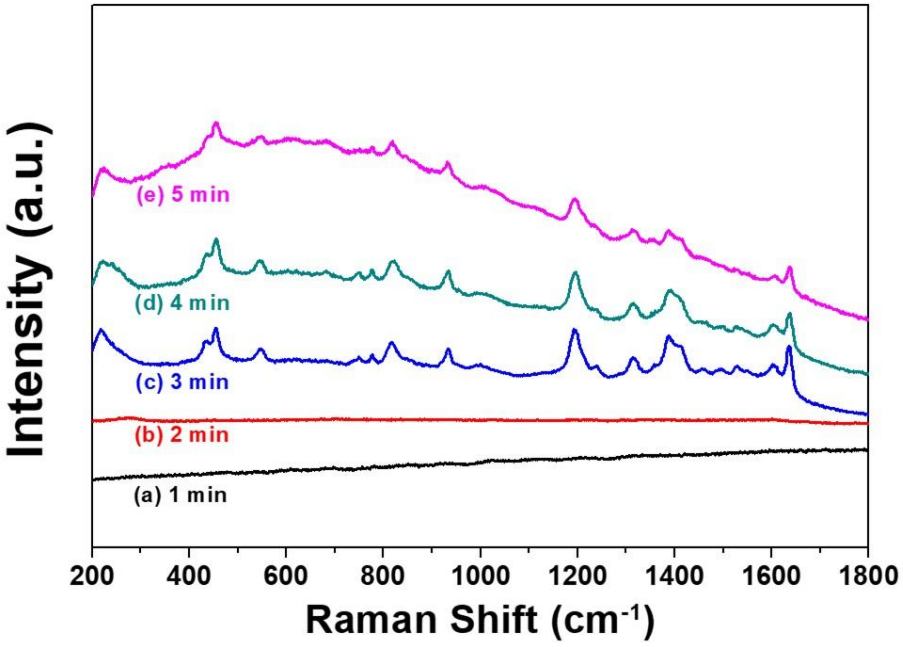

Figure 4 .6. *SERS spectra of 10µl of 10^{-6} M SC drop casted on Ca-Fe-Alg films etched for (a) 1 min, (b) 2 min, (c) 3 min, (d) 4 min and (e) 5 min.*

Raman spectrum of CV is well studied in literature[261]. Raman spectra of CV in solid form as well as in aqueous solution, recorded at 632 nm excitation, is shown in fig. 4.7.a and b, respectively. Raman spectrum of aqueous solution of 10^{-4} M CV (fig. 4.7.b) shows vibrational bands at 441, 602, 670, 765, 803, 913, 1171, 1299, 1389 and 1614 cm^{-1} which correspond to 435, 605, 628, 767, 803, 915, 1170, 1299, 1390 and 1582 cm^{-1} peaks of CV as observed by Canamares et al.[261] Raman spectrum of solid CV (fig. 4.7.a) also shows a good match with the reported values.[261]

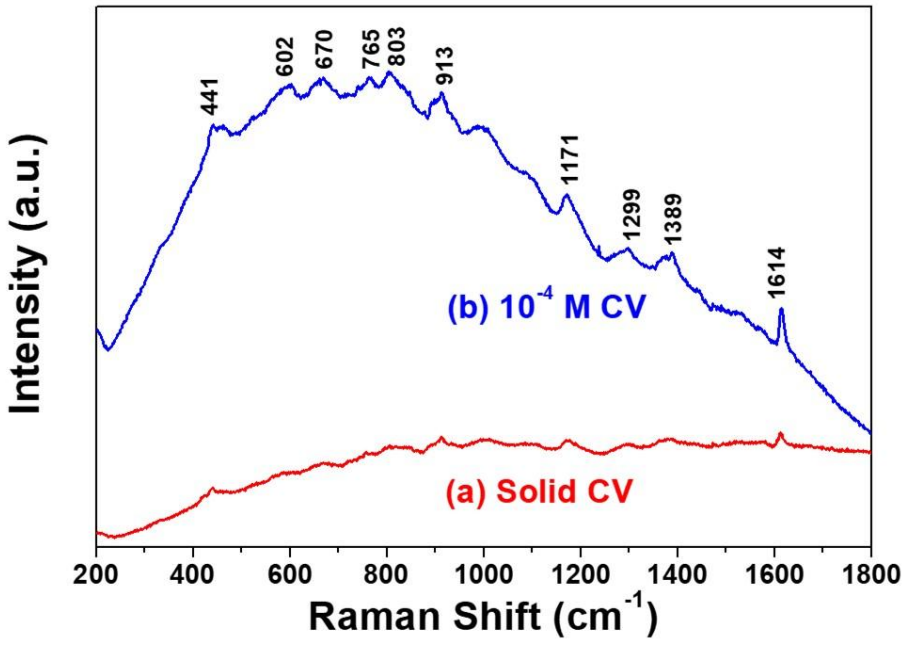

Figure 4 .7. *Raman spectra of (a) solid CV and (b) 10^{-4} M CV at 632 nm excitation recorded for 1s and 10s respectively.*

For SERS based detection of CV, acid-etched Au/Ca-Fe-Alg films were used as substrate. 10 µl of varying concentrations of CV were added to each etched Au/Ca-Fe-Alg films prior to recording of SERS signal for 1 second under 632 nm excitation. In fig. 4.8, SERS signal

of varying concentration of CV on Au/Ca-Fe-Alg films is shown. SERS spectrum of 10^{-6} M CV adsorbed on etched Au/Ca-Fe-Alg film excited at 632 nm showed vibrational bands corresponding to that of CV reported earlier.[261] Strong bands were observed at 455, 470, 1205, 1399 and 1651 cm^{-1} which correspond to C-C-C bending, C-N-C bending, C-C-C asymmetric stretching, ring/methyl bending and benzene 8a mode[261], respectively. Other medium intensity bands were observed at 791, 831, 944 and 1618 cm^{-1} which corresponded to 10a, 17b, 17a and 8b modes of benzene[261], respectively. Weaker bands at 556, 591, 636, 697, 760, 791, 867, 966, 1252, 1369, 1420, 1473, 1510 and 1566 cm^{-1}were also observed.

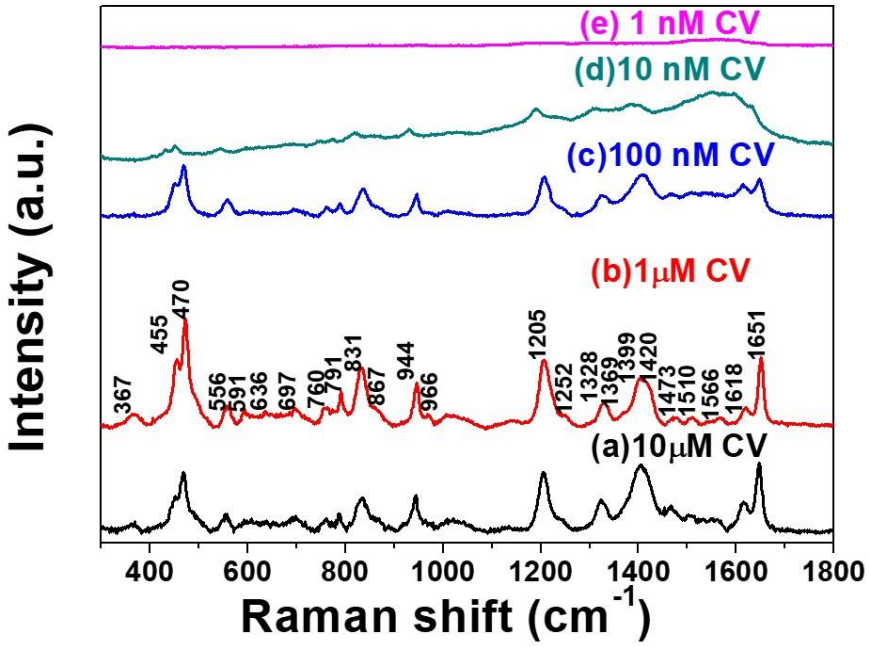

Figure 4 .8. *SERS spectra of (a) 10μM, (b) 1 μM, (c) 100 nM, (d) 10 nM and 1 nM CV drop casted on acid-etched Au/Ca-Fe-Alg films excited at 632 nm.*

In order to establish a method to determine concentration of CV detected by SERS using etched Au/Ca-Fe-Alg film, SERS intensity at 455, 470, 1205, 1399 and 1651 cm^{-1} which corresponds to strong peaks, were plotted with respect to varying concentration of CV as shown in fig. 4.9. It can be seen that the SERS intensity of peaks at 455, 470, 1205 and 1651 cm^{-1} first increases and then decreases. The increase of SERS intensity may be attributed to

monolayer adsorption of CV at a concentration of 10^{-6} M. In fig. 4.8, similar observation was made. It was observed that upon lowering the concentration of CV from 10^{-5} to 10^{-6} M SERS intensity slightly increased (fig. 4.8.a and b). Upon further lowering the concentration of CV to 10^{-7} M and lower, SERS signal was found to decrease owing to sub-monolayer occupation of CV on the surface of GNPs (fig. 4.8.c, d and e).

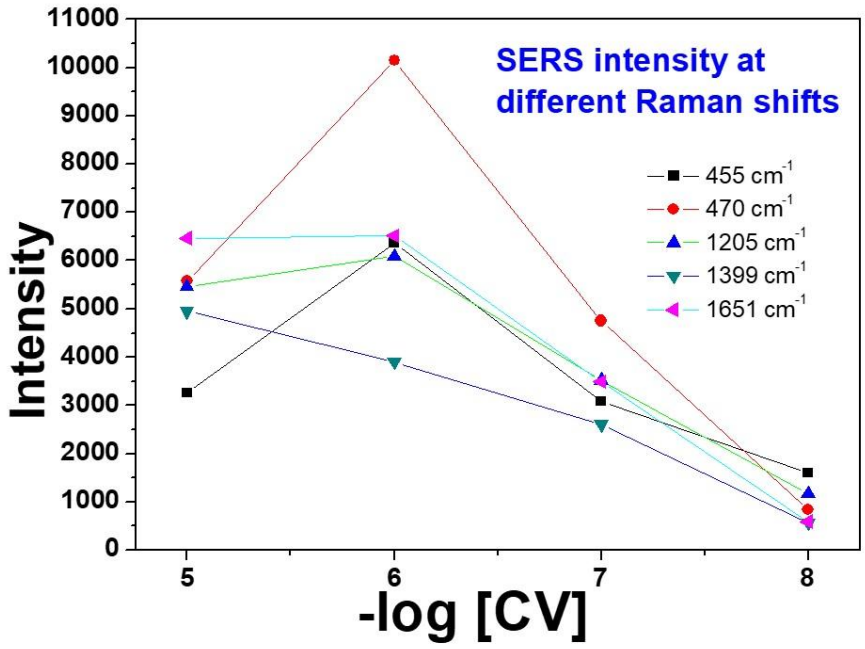

Figure 4 .9. *SERS intensity of different concentrations of CV adsorbed on etched Au/Ca-Fe-Alg films at (a) 455, (b) 470, (c) 1205, (d) 1399 and 1651 cm^{-1}.*

Since fig. 4.9 do not show a linear trend, a suitable calibration curve cannot be obtained. Thus, this method can only qualitatively detect CV in aqueous solution up to a concentration of 10^{-8} M or 10 nM.

4.2. Synthesis of alginate capped silver nanoparticles for loading in alginate film

4.2.1. Background

The premise of using gold nanoparticles loaded alginate films as a SERS substrate has already been discussed in section 4.1.1. The possibility of use of silver nanoparticles in place of gold nanoparticles is promising considering the low cost of silver in comparison to gold. Moreover, in-situ synthesis of silver nanoparticles in alginate films is not feasible. The method of loading of Au^{3+} ions into alginate matrix cross-linked with Ca^{2+} and Fe^{3+} ions, was based on the fact that alginate polymer has multidentate COO^{-} groups which bind to bivalent and trivalent cations for crosslinking. Silver ion is a monovalent cation which would weaken the structural integrity of Ca^{2+} or Fe^{3+}ion-crosslinked alginate film leading to its dissolution. It is advisable to dope AgNPs in alginate matrix and then cast dried to form films, which can be further cross-linked by Ca^{2+} and Fe^{3+}ions. It was observed that AgNPs made by citrate or borohydride tend to aggregate. In order to disperse AgNPs in alginate solution, AgNPs were required to be synthesized using chemically compatible capping agent. Thus, sodium alginate was the obvious choice.

In this work, AgNPs were reduced by sodium alginate in aqueous medium. The synthesized AgNPs were further dispersed in alginate solution and cast dried for fabrication of soluble AgNPs loaded alginate film. The dried films were cross-linked using calcium ions to form stable films which were further used to SERS sensing and dosimetric applications studied using EBT3 Gafchromic films (Radiochromic films).

4.2.2. Experimental Section

4.2.2.1. General Materials and Methods:

Sodium alginate, silver nitrate ($AgNO_3$, 99.0%), polyvinylpyrrolidone (PVP, 40, 000 M.W.) and calcium nitrate ($CaNO_3$, 99.0%) were purchased from Merck. All the experiments were performed in Millipore purified water.

Dosimetric studies were performed using Gafchromic EBT3 film (International Specialty Products, Wayne, NJ) which comprises of a radiation sensitive active layer of 28 μm thickness, with one 125 μm matte-polyester layer for mechanical adhesion of the radiation sensitive layer.

4.2.2.2. Synthesis of AgNP loaded alginate films:

Alginate capped silver nanoparticles (AgNP) were synthesized through reduction of 20 mM silver nitrate solution by 1% (w/v) sodium alginate solution at 60°C under alkaline conditions (pH 10).[262] Thereafter, 20 mM Ag nanoparticle stock was cooled to room temperature before carrying out further experiments. 2 ml of 20 mM Ag nanoparticle stock solution was added to a mixture of 7 ml 2.25% sodium alginate solution and 1 ml 8% PVP solution while stirring. After 30 minutes of continuous stirring, the homogenous viscous solution of Ag nanoparticles in alginate matrix was poured into a glass Petri dish of 7 cm internal diameter and dried under IR lamp. During the process of drying, the petri dish was shaken gently to homogenize the solution. Ag nanoparticles loaded alginate (AgNP-Alg) film was peeled of using a pair of forceps after complete drying. Twenty pieces of AgNP-Alg films of dimension 1 cm x 1 cm, were dipped in to 20 ml of 0.2 M $CaNO_3$ solution while stirring slowly for cross-linking. Cross-linked AgNP-Alg films were washed with water and were stored in water for further experiments.

4.2.2.3. Instrumentation details:

Instruments used for UV-vis absorption spectroscopy, Raman and SERS studies are same as mentioned in section 4.1.2.3. In addition to the above, in this work, SERS spectra were recorded using the 514 nm line from an Ar^+ ion laser (35-LAP-431-230, Melles Griot). The spot size on the sample was approximately 0.5 mm in diameter, and the laser power at the sampling position was 10 mW for the excitation wavelengths of 514 nm. Atomic force microscopy (AFM), model no. A-100, A.P.E. Research Italy, was used for determination of size of alginate capped AgNPs by contact mode. Thickness of the film was measured using precision thickness gauge (Hanatek Instruments, UK). The 6 and 10 MV X-rays with flattening filter (WFF) and flattening filter free (FFF) beams from TrueBeam medical electron linear accelerator (Varian Medical System, Inc., Palo Alto CA) were used for dosimetric study using EBT3 Gafchromic films in this work. All irradiations were performed with ISO wide spectrum series namely W80, W110, W150 and W200 with mean energy of 57 keV, 79 keV, 104 keV and 137 keV respectively.

4.2.3. Results and discussion:

4.2.3.1. UV-vis absorption study

The progress of synthesis of AgNPs in alginate matrix is studied using UV-vis absorption technique. The surface plasmon peak appearing at ~400 nm is indicative of formation of silver NPs.[263] After dissolution of sodium alginate at 60°C, $AgNO_3$ solution is added to obtain 20 mM final concentration of Ag^+ ions. Aliquots of 50 µl were taken from the reaction mixture and volume was made up to 1 ml. The UV-vis absorption spectrum of the above solution was recorded in a 3 mm path length cuvette with respect to time to monitor the progress of reaction which is shown in fig. 4.10.

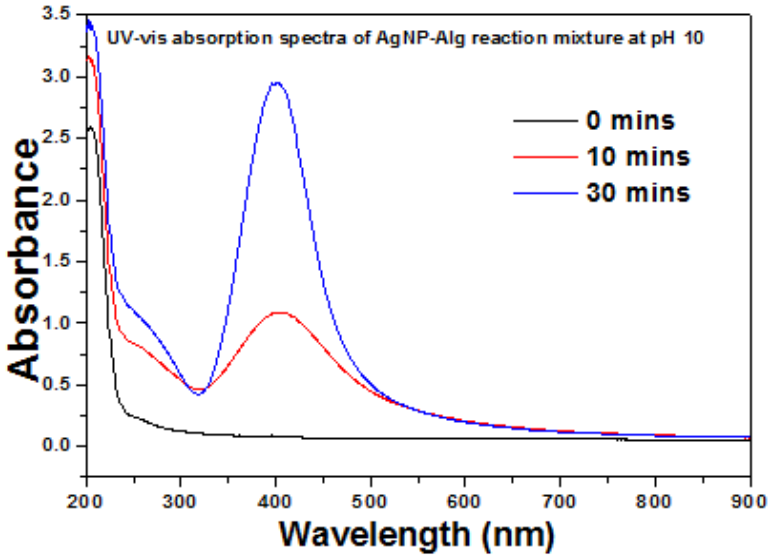

Figure 4 .10. *UV-vis absorption spectra of AgNP-Alg reaction mixture to monitor the progress of reaction with respect to time at pH 10 recorded in 3 mm quartz cuvette.*

UV-vis absorption spectrum of uncross-linked dried AgNPs loaded alginate (AgNPs-Alg) film of dimension 1cm x 1cm was dissolved in 2.5 ml water was recorded in a 3 mm cuvette as shown in fig. 4.11. In fig. 4.11, it can be clearly seen that the position of plasmon peak of AgNPs has not shifted. This indicates that no significant inter particle association has taken place in AgNPs-Alg films.

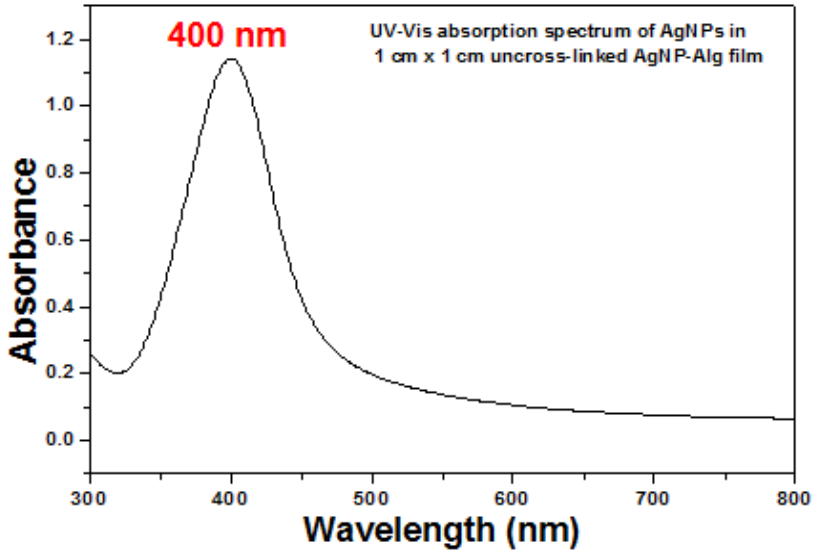

Figure 4 .11. *UV-vis absorption spectrum of AgNPs in 1 cm x 1 cm uncross-linked AgNP-Alg film*

4.2.3.2. Morphology of AgNPs and thickness of AgNPs-Alg films

A layer of the synthesized alginate capped AgNPs was formed on silicon wafer surface by spin coating. The AgNP size distribution analysis using AFM was shown in figure 4.12. The average size of the AgNPs deposited in polymer film was found to be 10 nm (within ± 1 nm variation).

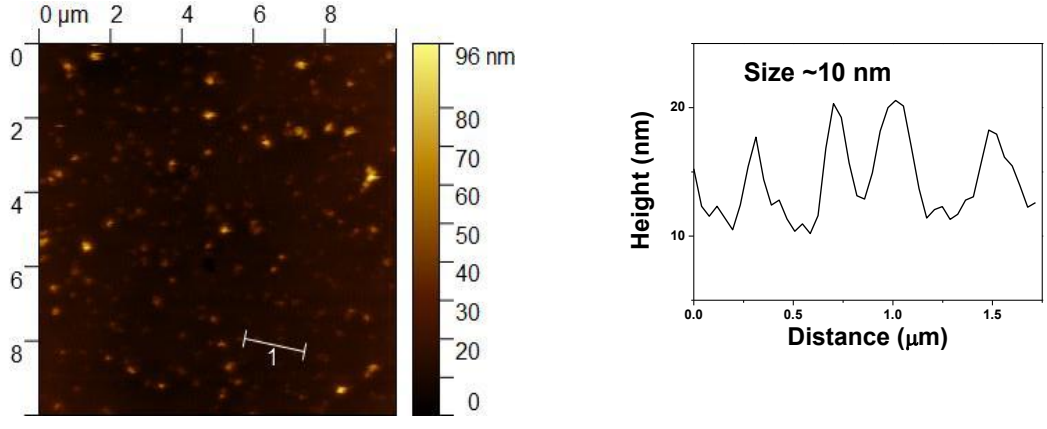

(a) **(b)**

Figure 4 .12. *(a) AFM image of the alginate capped AgNPs. The height profile of the selected region 1 is shown in (b).*

The thickness of the dried cross-linked AgNP-Alg film was 170 ± 07 µm.

4.2.3.3. SERS based sensing by AgNPs-Alg films

Varying concentration of two model dyes, crystal violet (CV) and rhodamine 6G (R6G) was drop casted on AgNPs-Alg film. SERS spectra of dye loaded films were recorded at 514 nm excitation as shown in fig. 4.13.

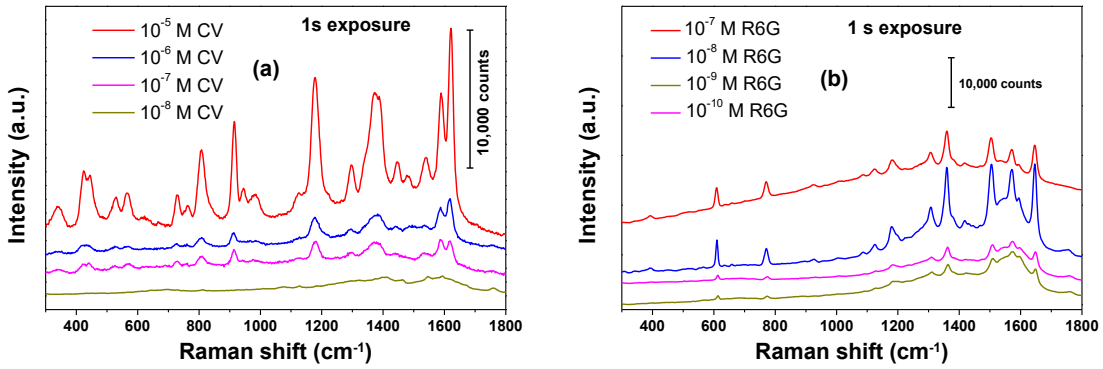

Figure 4 .13. *SERS spectra of different concentrations of (a) CV and (b) R6G dye loaded on AgNPs-Alg film excited at 514 nm*

The SERS spectra of CV[261] and R6G[264] corresponded to the reported SERS spectra. The detection limit as obtained case of sensing of CV is 10^{-8} M which is comparable to the results obtained from Au/Ca-Fe-Alg films shown in fig. 4.8. In case of detection of R6G, a detection limit of 10^{-10} M (sub-nanomolar) was obtained, which may be attributed to higher Raman scattering cross-section of R6G in comparison to CV. Moreover, in fig. 4.13, intensity peaks were observed for 10^{-8} concentration of R6G, which may be due to monolayer coverage of adsorbate.[238]

4.2.3.4. X-ray dose-enhancement by AgNPs-Alg films

Silver nanoparticles have been recently reported as a potential radiosensitizer.[265] The mechanism of radiosensitization by nanoparticles of high Z elements has been discussed in previous chapters. The prospect of using AgNPs-Alg film for radiosensitization is quite

promising considering the cost of silver as well as the ease of synthesis in comparison to the Au/Ca-Fe-Alg film. In order to measure the dose enhancement, by AgNPs-Alg film, radiochromic films named EBT3 Gafchromic films were used as dosimeters. It is known that upon exposure to ionizing radiation, EBT3 three films show linear change in colour which can be detected by flatbed color scanners (Epson Expression 10000XL, EPSON UK). At first, the EBT3 films were exposed to different amount of dose ranging from 0 cGy to 500 cGy. The corresponding colour changes in irradiated EBT3 films were recorded to plot the calibration curve of intensity vs. dose. AgNPs-Alg films were then placed on EBT3 films in close contact, at a distance of 100 cm, facing the X-ray source mentioned in section 4.2.2.3. A schematic representation of the above arrangement is shown in fig. 4.14.

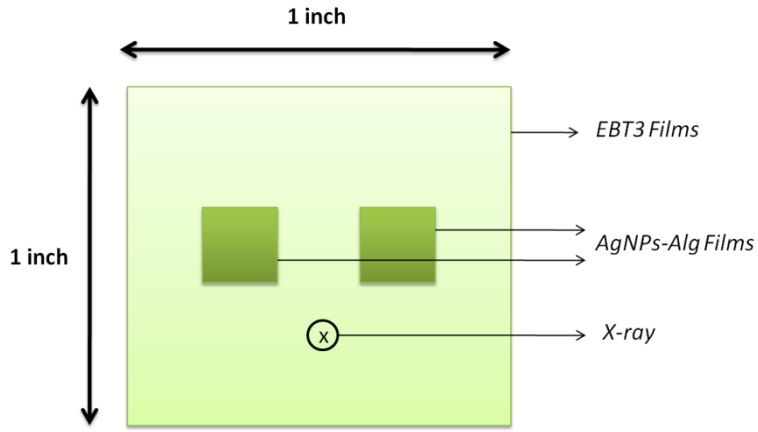

Figure 4 .14. *A schematic representation of the arrangement of AgNPs-Alg films on EBT3 films facing the X-ray source.*

Upon exposure to X-rays various extent of dose enhancement was observed depending on the energy of X-ray used. Maximum dose enhancement was observed for X-ray energy of 57 keV. Dose enhancements of 29, 23, 14 and 3% was observed for 57, 79, 104 and 137 keV X-ray, respectively. It can be seen that with increasing X-ray photon energy, the dose enhancement decreased, indicating lower interaction of X-ray with AgNPs leading to lower extent of photoelectron emission giving rise to lesser effect on the radiation sensitive layer of EBT3 films. In section 1.4.2.1.1., we have discussed the dependent of photoelectric

absorption as well as emission with energy of gamma or X-rays. Thus, the above results, indicate that the interaction of X-ray with AgNPs is mainly photoelectric in nature.

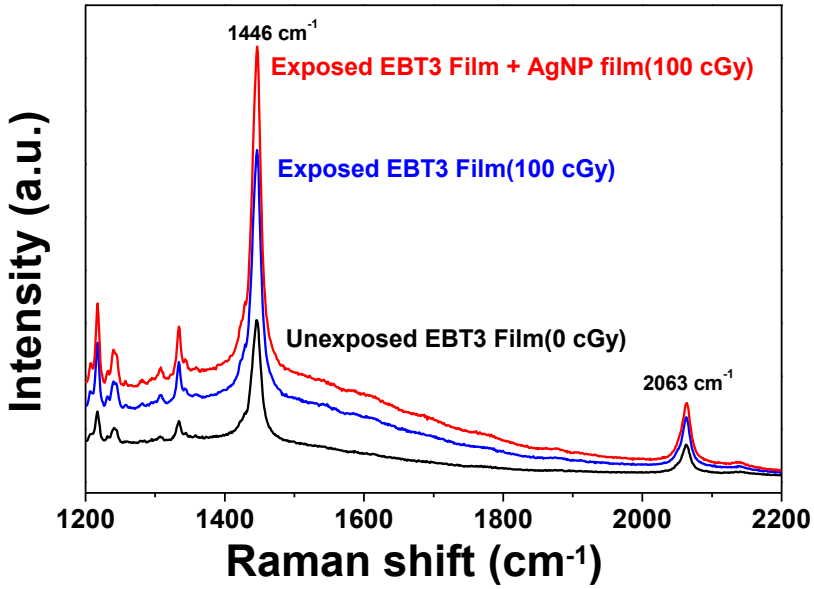

Figure 4 .15. *Raman spectra of EBT3 films excited at 632 nm.*

Unlaminated radiochromic films were exposed to a dose of 100cGy of 57 KeV X-ray in absence and in presence of AgNPs-Alg films. Raman spectrum of unexposed unlaminated radiochromic films showed signature peaks corresponding to C=C stretch and C≡C stretch at 1446 and 2063 cm^{-1} respectively.[266, 267] Raman spectra of the above films revealed that the presence of silver nanoparticles lead to enhancement in peak intensities at 1446 and 2063 cm^{-1} respectively, occurring due to polymerization of diacetylene monomers.

4.3. Conclusion

In this work, two types of synthesis of noble metal nanoparticles alginate films were discussed. Gold nanoparticles (GNPs) could be reduced in-situ where as silver nanoparticles AgNPs were externally reduced and introduced into the alginate films. Lowest concentration of CV that was detected by this method is 10 nM or ~4 ppb. CV is reported to be toxic as well as carcinogenic above a dose of 1 ppb.[268] Both the films were found to show excellent

SERS based sensing which makes both Au/Ca-Fe-Alg and AgNPs-Alg films as a potential substrate for SERS detection. AgNPs-Alg films were further used for studying dosimetric enhancement using EBT3 films for potential application in radiosensitization.

5

Synthesis and characterization of AgNPs and AgCl/AgNPs for detection of sildenafil citrate

In this chapter, we have discussed about two types of synthesis of silver nanoparticles and their application in detection of a drug molecule, sildenafil citrate (SC). Both types of nanoparticles can be used for detection of SC by SERS, yet the informations obtained from both the methods are majorly different, which has been discussed in this chapter.

5.1. Detection of sildenafil citrate by AgNPs

5.1.1. Background

Herbal medicines[269]played an important role in human health before manufactured medicines came in the market. Plant extracts, which are often used as food preservatives[270], dietary supplement[271, 272] or herbal medicines[273-275] in different countries, are a mixture of various organic compounds.[276] Characterization of each component of a plant extract to evaluate its medicinal value for the purpose of quality control is tedious and time consuming. Quality control of herbal medicines[277] is difficult owing to challenges encountered due to lack of substantial research data, expertise and appropriate control mechanism[278] is reported by World Health Organization (WHO)[279]. Moreover, herbal medicines are available as over-the-counter (OTC) drugs and they are considered to be bereft of any side-effects.

In reality, the case is a little different. Herbal medicines available to treat erectile dysfunction (ED) claim to contain natural ingredients such as Panax ginseng[280],Tribulus terrestris[281],Yohimbine[282], etc. Apart from the above ingredients, these medicines are

reported to contain very low concentration of synthetically manufactured sildenafil citrate (SC)[283] and its analogues[284], which are widely used to treat ED[285] and pulmonary hypertension[286].People suffering from ED often resort to these OTC drugs, on being unable to be vocal about the problem to the physician[287], because of the social stigma[288] associated with this problem. In such a case, quality checkof the above OTC drugs is imperative to assess the health risks involved with these drugs by available analytical techniques.

SC is a selective phosphodiesterase type 5(PDE-5) inhibitor[285]. PDE-5 binds specifically to cyclic guanosine monophosphate (GMP) and disrupts nitric oxide[289] release which is essential for vasodilation in smooth muscles for penile erection. SC is the first synthetic effective cure for ED. 1n 1998, FDA approved its usage under the brand name Viagra. This drug was prescribed to more than 130 million patients worldwide. Post marketing, many of the side effects of the drugs were reported. Fatal cardiovascular events due to myocardial infarction in patients under organic nitrate medication upon consumption of SC were reported[290].

Several analytical techniques such as high pressure liquid chromatograpy (HPLC)[291, 292], mass spectrometry[291],voltametry[293],spectrofluorimetry[294], etc. are reported for detection of SC in herbal OTC drugs with detection limit as low as 50pg/ml[292]. Applicability of any technique can be judged on the basis of its detection time and detection limit[295].

Surface enhanced Raman scattering (SERS) is a fingerprinting technique [296]where Raman spectrum of a molecule present in trace concentration can be recorded. Molecules adsorbed on the surface of plasmonic nanoparticles experience near field [231] due to plasmonic oscillation upon excitation at resonance condition. When near field of two or more plasmonic nanoparticles interact due to agglomeration, an enhanced localized electric field is generated at the confluence. This junction with enhanced localized electric field is called

hot-spot [259]. This enhanced electric field generated upon excitation of the agglomerated assembly of plasmonic nanoparticles at the resonance frequency polarizes the molecules adsorbed on the surface of the nanoparticles, which is eventually expressed as SERS spectrum in far-field[297]. In this work, we have brought forward a surface enhanced Raman scattering based methodology, which is, for detection of SC in aqueous medium with low detection limit, low detection time and high selectivity.

5.1.2. Instrumentation details

Jasco V-650 UV-visible spectrophotometer was used for acquiring the absorption spectra of experimental solutions. Raman and SERS spectra were recorded using the 514 nm line from an Ar^+ ion laser (35-LAP-431-230, Melles Griot). The Raman spectrum of solid SC was recorded using the 514 nm laser line. A sample of solid SC, in powder form, was taken on a glass slide and Raman scattering light was collected at back scattering geometry with a 50X LWD (long working distance) objective. For the SERS spectra, the sample solutions were taken in a standard 1×1 cm^2 quartz cuvette and the Raman scattered light was collected at 180° scattering geometry and detected using a CCD (Synapse) based monochromator (LabRAM HR800, Horiba Jobin Yvon, France) together with an edge filter. The spot size on the sample was ~0.5 mm in diameter, and the laser power at the sampling position was 10mW for the excitation wavelengths of 514 nm. The Raman band of a silicon wafer at 520 cm^{-1} was used to calibrate the spectrometer, and the accuracy of the spectral measurement was estimated to be better than 1 cm^{-1}. Transmission electron microscopy images (TEM) of nanoparticles were acquired by using a Ziess, Libra 12 instrument.

5.1.3. Experimental Section

5.1.3.1. Chemicals

Silver nitrate ($AgNO_3$, 99.9999%), sildenafil citrate (≥98%) and sodium citrate tribasic dihydrate (≥98%) were obtained from Sigma-Aldrich and were used as received. All the experiments were performed in Millipore purified water.

5.1.3.2. Method of synthesis of AgNPs

Silver nanoparticles (AgNPs) were synthesized by reduction of aqueous solution of $AgNO_3$ by sodium citrate [298], similar to modified Turkevich method[299-301] for synthesis of gold nanoparticles. In brief, 100 ml of 1 mM $AgNO_3$ solution was heated near to its boiling point and then 2 ml of 1 % (w/v) sodium citrate solution was added to it. The above mixture was stirred and further boiled for 5 minutes till a greenish yellow solution was obtained. The final volume of the mixture was made upto 100 ml in a volumetric flask and was allowed to cool. This aqueous stock solution of AgNPswas used to perform further experiments. UV-visible absorption spectrum of the above solution was recorded.

An aqueous stock solution of 10^{-3} M of SC was prepared. Systematic dilution of the stock solution of SC was done to obtain solutions of different concentrations, the lowest being 10^{-10} M. Different concentrations of SC solution were added to AgNPs solution and then UV-visible absorption and SERS measurements were performed. Effect of pH on the SERS spectra was studied on 10^{-6} M SC in AgNPs solution by systematic addition of HCl or NaOH to optimize maximum SERS intensity condition. HCl or NaOH was added to the experimental mixture only after specific concentration of SC has been added to the AgNPs solution in all experiments.SERS spectra were also recorded at varying time interval after addition of SC to AgNPs solution to ascertain minimum time interval for maximum intensity of SERS spectra. After optimization of pH and time interval, concentration

dependent study of SERS of SC on AgNPs was performed to obtain detection limit of the methodology.

TEM image of AgNPs stock solution and 10^{-6} M SC on AgNPs solution was recorded to check the agglomeration in AgNPs upon addition of SC.

5.1.4. Results and Discussion

5.1.4.1. UV-Visible spectrophotometry:

AgNPs were synthesized by reduction of $AgNO_3$ by sodium citrate at near boiling temperature in aqueous medium. The synthesized AgNPs showed absorption maxima at 430 nm (surface plasmon band) as shown in fig. 5.1.a. pH of the AgNPs stock solution was found to be ~6.5.Sodium citrate reduces $AgNO_3$ as well as stabilizes AgNPs by adsorption of citrate ion on the surface.[299-301] No change in absorption spectra was obtained upon addition of 10^{-5} M or 6.670µg/ml of SC to AgNPs solution. Upon changing the pH of the solution from 6.5 to 2.0 by addition of HCl, a distinct shift in plasmon peak was observed, which is shown in fig.5.1.b. Similar shift in absorption spectra was observed upon addition of 10^{-6} M or 0.667µg/ml of SC to AgNPs solution and subsequent lowering of pH from 6.5 to 2.0, is shown in fig. 5.1.c.Upon changing the pH of blank AgNPs solution from 6.5 to 2.0, plasmon peak almost disappeared which is shown in fig. 5.1.d. Carboxylate (COO^-) groups of citrate ion, present on the AgNP surface, get protonated upon lowering the pH of AgNPs stock solution to 2.0[302]and the negative charge on AgNPs[298]is reduced, which leads to agglomeration of AgNPs. pKa values of SC are reported to be 7.10 and 9.84[303, 304] corresponding to tertiary amide of piperazine moiety and secondary amide of pyrimidinone moiety, which indicates that SC exist as a positively charged moiety below pH 7.10. SC gets adsorbed on the surface of AgNPs by ionic interaction with citrate ions at pH 2.0, thereby preventing complete agglomeration of AgNPs as shown in fig 5.1.d. Extent of

agglomeration in AgNPs progresses as the concentration of SC is reduced from 10^{-5} M to 10^{-6} M, which is evident from shift in plasmon band from 482 to 489 nm and also from appearance of a shoulder at 634 nm, as shown in fig. 5.1.b and c.[305]This clearly indicates that agglomeration is brought about by increased ionic strength of the solution due to addition of 10^{-2} M HCl in order to attain pH 2. As a result, at low concentration of SC, i.e., 10^{-6} M, a shoulder appears in fig. 5.1.c due to plasmon coupling [306].

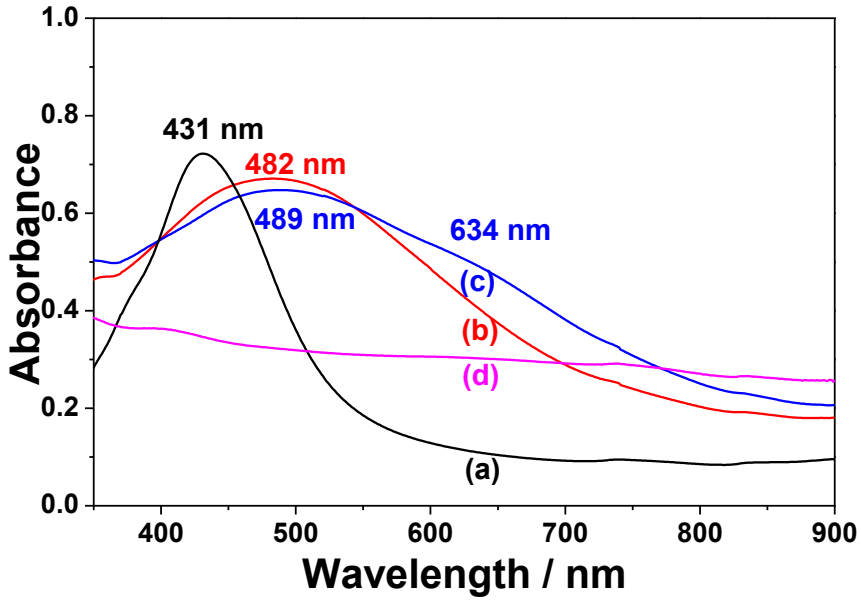

Figure 5.1. *UV-Vis absorption spectra of (a) AgNPs solution at pH 6.5, (b) 10^{-5} M SC on AgNPs solution at pH 2.0, (c) 10^{-6} M SC on AgNPs solution at pH 2.0 and (d) AgNPs solution at pH 2.0.*

TEM image of as synthesized AgNPs and AgNPs in presence of 10^{-6} M SC was recorded to confirm agglomeration in AgNPs upon lowering the pH from 6.5 to 2.0, which is shown in fig. 5.2.a and b.

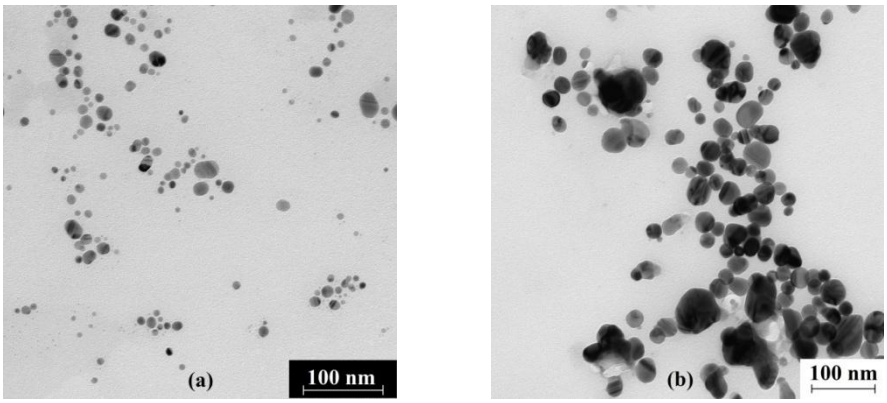

Figure 5.2. *Transmission electron microscopy (TEM) image of (a) AgNPs solution at pH 6.5 and (b) 10^{-6} M SC on AgNPs solution at pH 2.0.*

5.1.4.2. Comparative study of the experimetal and theoretical Raman spectra of SC:

Density functional theory (DFT) calculations with B3LYP functionality and 6-31G* basis set were carried out to optimize structural geometry with minimum energy and to compute the theoretical Raman spectrum of SC, as shown in fig. 5.3.a. Raman spectrum of solid SC was recorded at 514 nm excitation, as shown in fig. 5.3.b. Peaks in the solid SC Raman spectrum were assigned to the corresponding vibrational modes in the SC molecule by consideringthe theoretical Raman spectrum as a reference. The vibrational assignments are given in table 5.1.

Table 5.1. *Assignment of vibrational modes of SC by comparison of peaks of experimental and theoretical Raman of SC (fig. 5.3).*

Calculated Raman shift / cm^{-1}	**Experimental Raman shift / cm^{-1}**	**Experimental SERS / cm^{-1}**	**Modes of vibration**
1582	1580	1578	*C=C stretching (ring III)*
1562	1565	1557	*C=N stretching*

			(ring II)
1525	1529	1525	*C=C stretching (ring I and II)*
1479	1486	1483	*ring breathing (ring I and II)*
1402	1404	1397	*ring distortion (ring I and II)*

SC molecule consists of a substituted pyrazolo-pyrimidinone ring (ring I and II), a substituted phenyl ring (ring III) and a methylated piperizine ring (ring IV) connected to each other. Bond structure and geometry optimized structure of SC is given in scheme 5.1.a and b respectively. The strong Raman bands at 1580, 1565, 1529, 1486, 1404 and 1238 cm^{-1} are assigned to phenyl C=C stretch (str), C5=N4 str, C8=C9 str, ring I breathing, phenyl ring distortion (dis) and phenyl ring breathing. All the above 6 bands are characteristic bands for fingerprinting among which 1580 cm^{-1} band is the strongest in intensity[307]. All the analytical quantification can be done using 1580 cm^{-1} as the reference band. Raman bands below 1100 cm^{-1}, which corresponded to breathing vibrations of ring I, II and III, were not considered for fingerprinting as their intensity was found to be low.

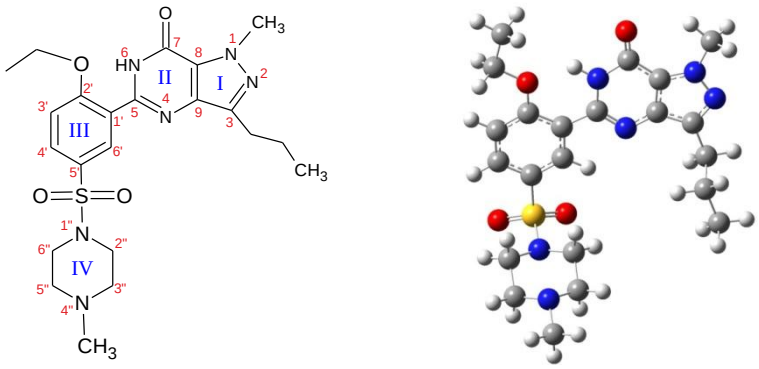

(a) **(b)**

Scheme 5.1. *(a) Bonding structure and (b) geometry optimized structure of SC. Color scheme for carbon, nitrogen, oxygen, sulphur and hydrogen is grey, blue, red, yellow and white, respectively.*

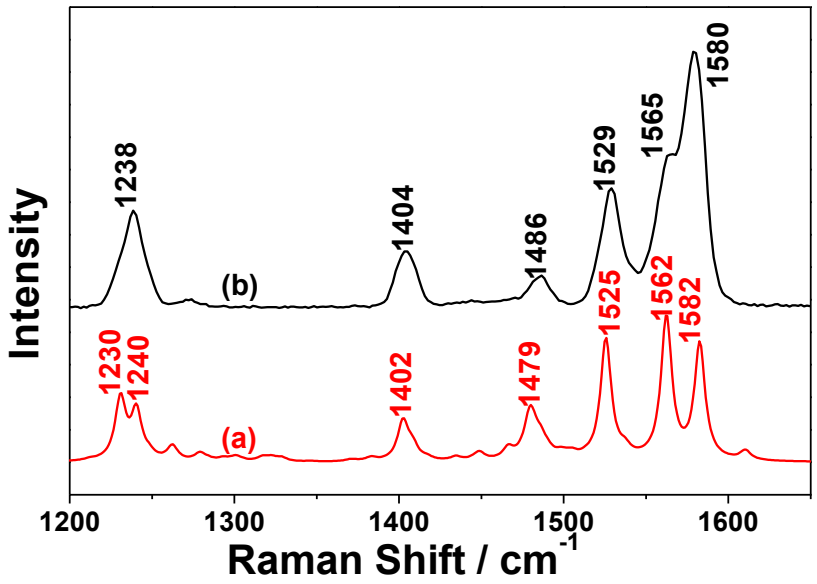

Figure 5.3. *Theoretical Raman spectrum of SC and (b) experimental Raman spectrum of solid SC recorded at 514 nm excitation.*

5.1.4.3. Surface enhanced Raman scattering study of SC:

In order to investigate the maximum intensity condition for measurement of SERS spectra, pH of the solution of 10^{-6} M SC in AgNPs solution was varied from 10.0 to 2.0, by addition of HCl or NaOH, prior to recording of SERS spectra. It is quite evident from fig. 5.4. that SERS intensity of the above solutions improve as the pH is lowered from 10.0 to 2.0. The reason for the above phenomenon is explained earlier (*vide supra*). In order to obtain most intense spectra, all the further SERS experiments were carried out at pH 2.0.

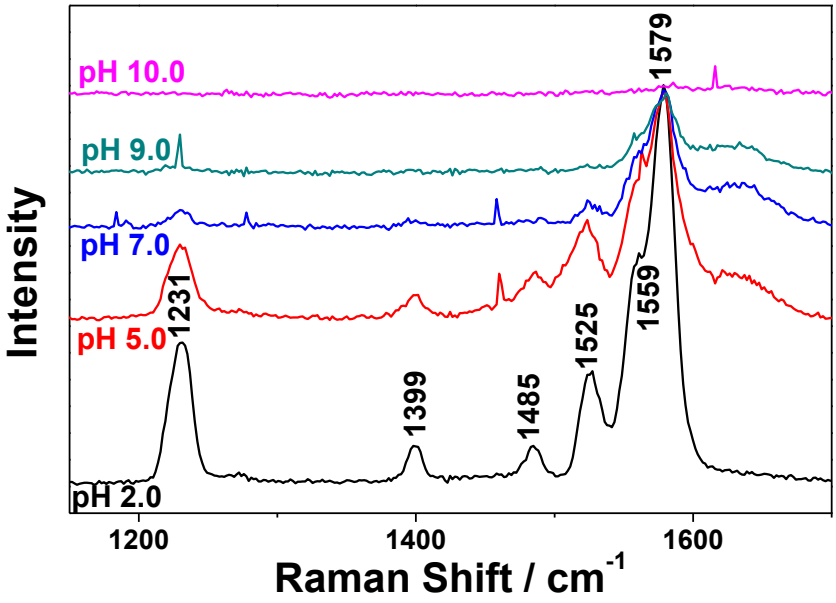

Figure 5.4. *SERS spectra of 10^{-6} M SC in AgNPs solution at pH 2.0, 5.0, 7.0, 9.0 and 10.0.*

Upon addition of 10^{-6} M SC to AgNPs solution, SERS spectra were recorded at different time intervals starting from the time of addition of HCl to bring down pH to 2.0, which is shown in fig. 5.5.a. SERS intensities at 1580 cm^{-1} in the above spectra were plotted with respect to time in minutes as shown in fig. 5.5.b. The data obtained in the fig. 5.5.b were best fitted using 1st order exponential growth kinetics. It was observed, SERS intensity achieved saturation after about 10 minutes. All spectra in further experiments were thus

recorded after 10 minutes of addition of HCl to SC and AgNPs solutions. Based on the above information, one can safely consider this method as very fast.

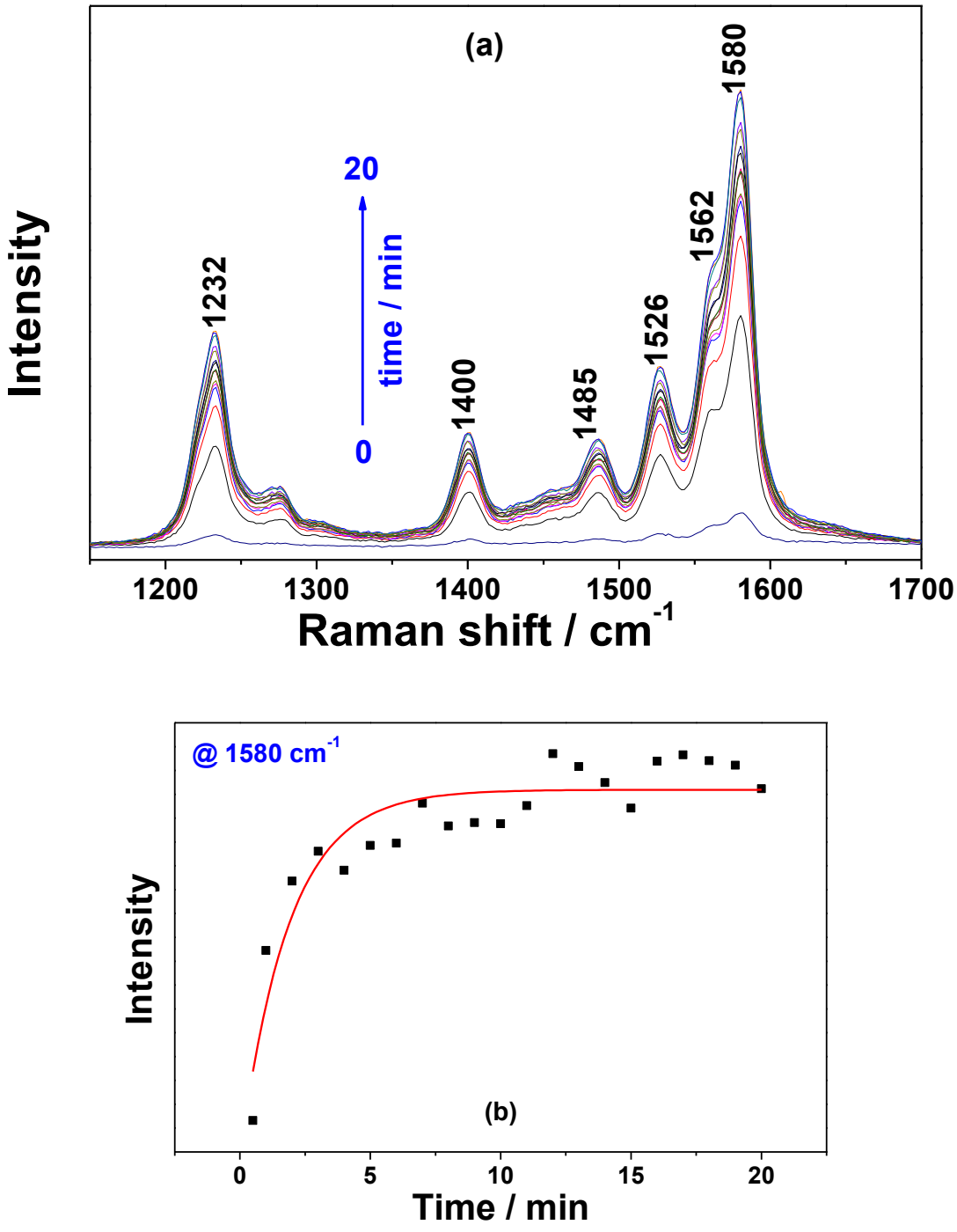

Figure 5.5. *(a) SERS spectra for 10^{-6} M SC in AgNPs solution at different time intervals after addition of HCl. (b) SERS intensity at 1580 cm^{-1} w.r.t. time in minutes, data as*

acquired from fig. 5.5.a. Red line is indicative 1st order exponential growth fitting of the data points.

The effect of concentration on SERS spectra by varying the concentration of SC in AgNPs solution was investigated. The concentration of SC was reduced from 10^{-4} to 10^{-7} M in AgNPs solution at pH 2.0 and SERS spectra were recorded at an exposure of 60 s under excitation of 514 nm, is shown in fig.5.6.a. Maximum SERS intensity was observed in the spectrum of 10^{-6} M SC in AgNPs. This phenomenon can be attributed to monolayer adsorption of SC on AgNPs[308]. Higher concentration of SC shows lower SERS intensity owing to self absorption[308].On further lowering of the concentration of SC, sub monolayer adsorption of SC lead to lowering of SERS intensity. In order to investigate concentrations of SC lower than 10^{-7} M, exposure time for recording of SERS spectra was increased to 120 s. SERS spectrum of 10^{-7} M to 10^{-11} M SC added to AgNPs solution were recorded under 514 nm excitation at 120 s exposure is shown in fig. 5.6.b.Comparison of experimental Raman and SERS spectra of SC as shown in fig. 5.3.b and 5.6.a.iii, respectively, revealed that both the spectra show a very good mutual correspondence, with a constant difference of 3-5 cm^{-1} (table 5.1). This indicates that SERS enhancement observed above is purely electromagnetic [309] in nature.

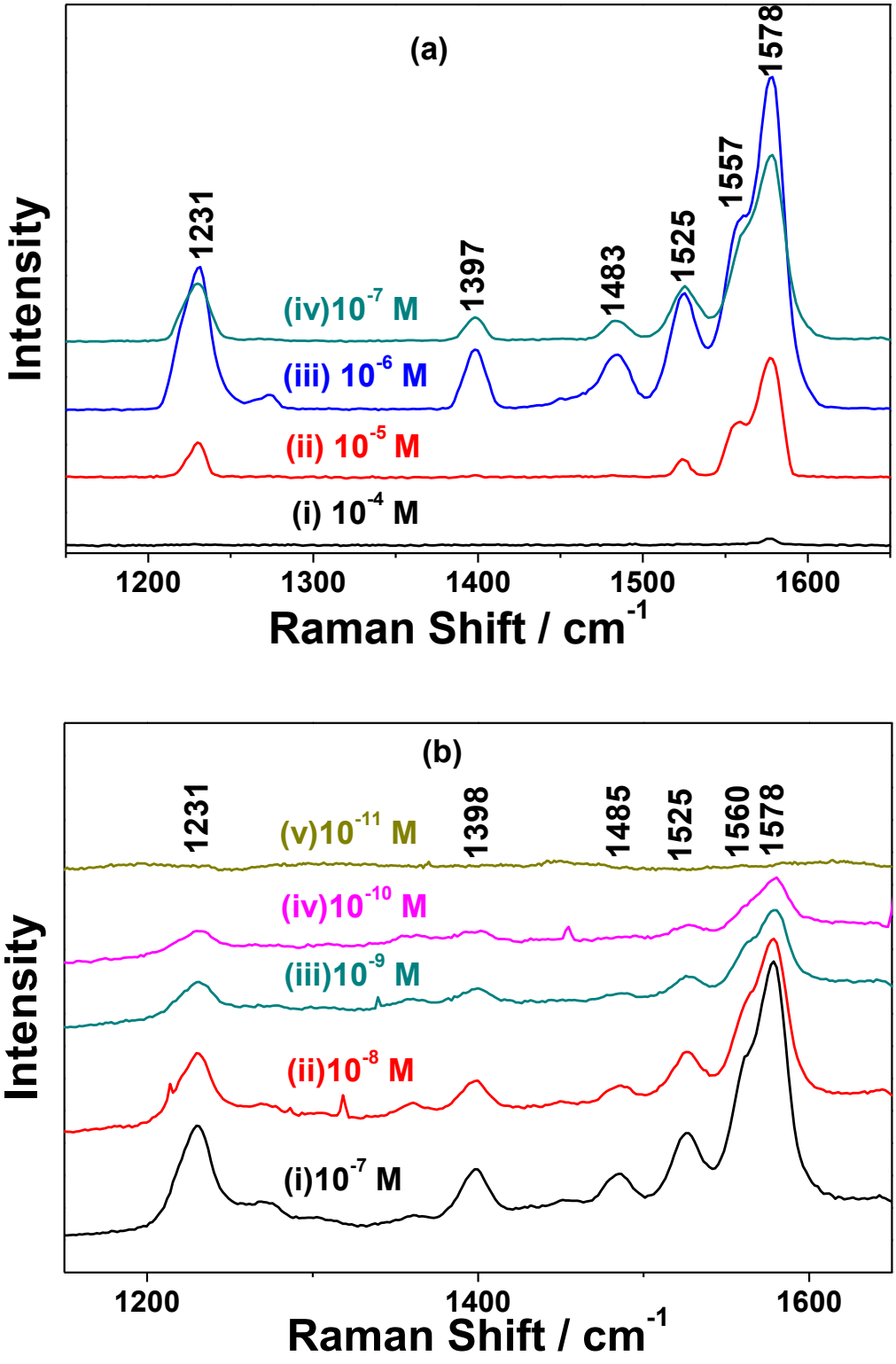

Figure 5.6. *SERS spectra of (a) (i) 10^{-4} M, (ii) 10^{-5} M, (iii) 10^{-6} M and (iv) 10^{-7} M SC in AgNPs solution recorded at 514 nm excitation under 60 s exposure and (b) (i) 10^{-7} M, (ii)*

10^{-8} M, (iii) 10^{-9} M, (iv) 10^{-10} M and (v) 10^{-11} M SC in AgNPs solution recorded at 514 nm excitation under 120 s exposure.

In order to determine the linearity range for detection of SC by the method discussed above, SERS intensity at 1578 cm^{-1}, most intense characteristic peak of SC corresponding to phenyl C=C stretching in SC, was plotted with respect to –log of concentration of SC, which is shown in fig. 5.7.a and b. For the concentration of SC from 10^{-4} M to 10^{-6} M, a monotonic increase in intensity of SERS signal was observed as shown in fig. 6 (a). Again, for the concentrations of SC from 10^{-7} M to 10^{-10} M, a monotonic decrease in SERS signal was observed as shown in fig 5.6.b. An ambiguity in concentration quantification may arise due to the observed monotonic increase in SERS intensity below 10^{-6} M which is the monolayer concentration[310]and for concentrations below 10^{-7} M, where a monotonic decrease in SERS intensity is observed, as shown in fig. 5.7.a and b, respectively. This can be resolved by recording two SERS spectra of SC in AgNPs solution, with a specific concentration of SC and a ten times diluted concentration of the same. By observing the trend whether decreasing or increasing, the concentration of SC can be quantified.

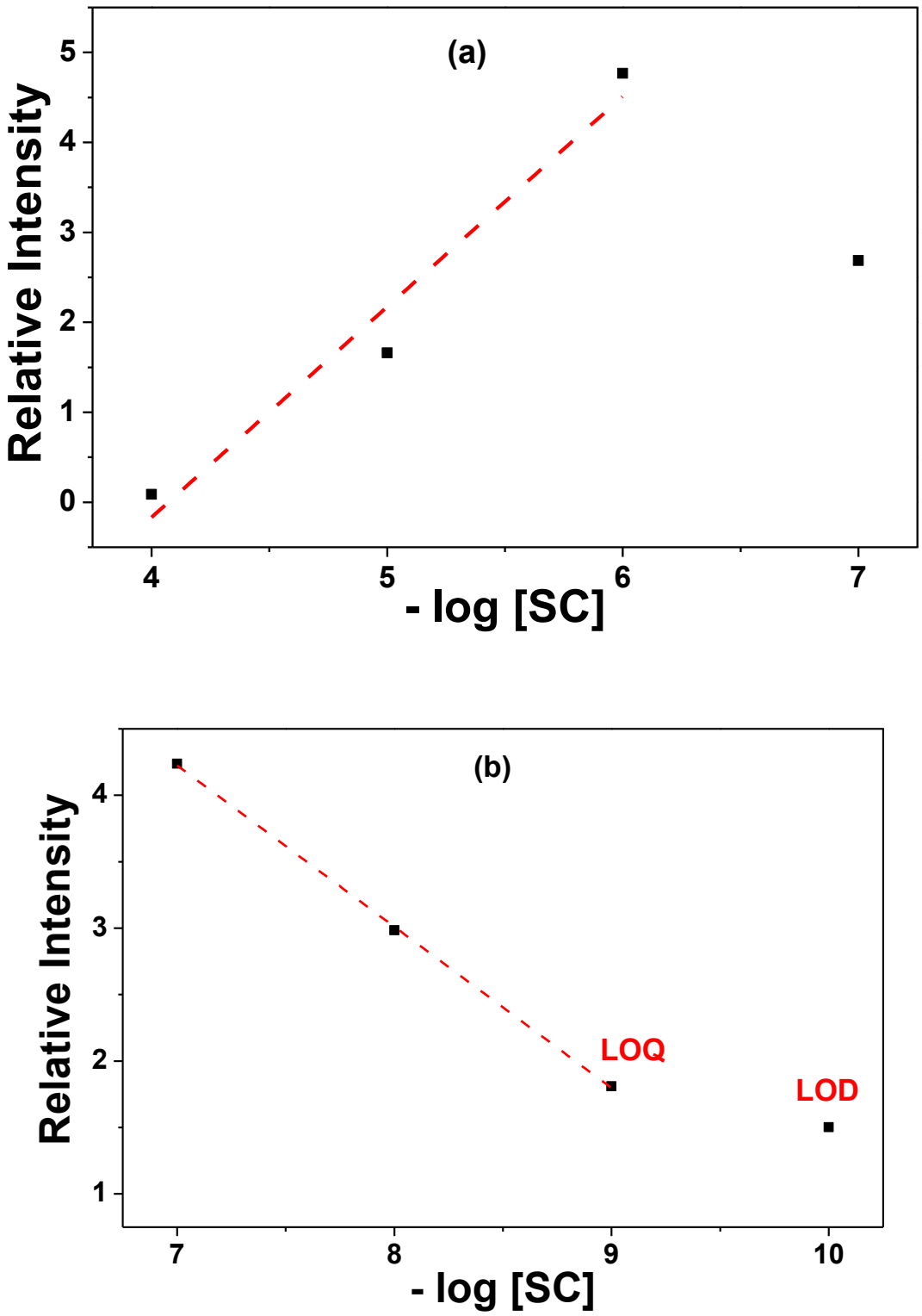

Figure 5.7. *SERS intensity of (a) 10^{-4} M to 10^{-7} M and (b) 10^{-7} M to 10^{-10} M SC for 1578 cm^{-1} peak w.r.t. –log [SC] as acquired from fig. 6 (a) and (b). [SC] stands for concentration of SC added to AgNPs solution. Red dashed line is indicative of the linear curve fitting of*

the data points. LOQ and LOD stands for limit of quantitation and limit of detection respectively.

OTC drugs for ED contain extracts of ginseng, L-arginine, Yohimbine, etc. There are reports of Raman spectroscopic quantification of various ginseng extracts. Chinese ginseng shows characteristic peak at 980 cm^{-1} whereas, American and Korean ginseng show characteristic peak at 1600 cm^{-1} in dispersive Raman spectroscopy[311]. SERS study of ginseng is yet not reported. L-arginine is another natural component of Herbal OTC drugs used to treat ED. Raman and SERS study of L-arginine shows that there is no interference in 1580 cm^{-1} characteristic region of SC[312]. Moreover, SERS study of SC is being done at pH 2.0, whereas, L-arginine shows SERS at pH 9.0. Yohimbine, another drug used to treat ED, shows vibrational peak at 1571 cm^{-1} in Raman spectrum[313] which is closer to 1580 cm^{-1} peak of SC. This interference may be removed by chromatographically separating SC from Yohimbine matrix. The SERS based methodology discussed in this work is very reliable in terms of qualitative analysis due to its fingerprinting property.

5.1.4.4. Qualitative and quantitative analysis:

Analytical techniques used for detection and quantification of SC such as UV-Visible spectrophotometric method[314],mass spectrometry[292], voltametry[293], potentiometry[315] and spectrofluorimetry[294] are reported with linear range of detection from 1.250 to 25.000µg/ml, 0.125 to 40.000 ng/ml, 29to 320 ng/ml, 6.6 to 600.0µg/ml and 0.004 to 25.000µg/ml, respectively. Separation techniques used for separation of SC from drug matrix such as HPLC[291], micellar electrokinetic chromatography[316], adsorptive stripping[293], polymeric membrane[315] and surfactant mediated methods[294] are reported. Qualitative detection limitor limit of detection (LOD)[317] of 50 pg/ml for electrospray positive ionization (ESI)-mass spectrometry (MS)[292]is the lowest. Qualitative SERS analysis of SC by hand held Raman

spectrometer is reported.[318] Recently, quantitatively detect SC by SERS technique werereported[319-321] with LOD as low as 1μg/ml.[322]

In this work, we could achieve a very low LOD, utilizing a very popular citrate reduced AgNPs sol [299] and pH dependent control of adsorption of SC, unlike other reported methods [319-322]. Two linearityranges,10^{-4} to 10^{-6} M (66.7 to 0.667 μg/ml) in order of increasing SERS intensity with decreasing SC concentration and 10^{-7} to 10^{-9} M (66.7 to 0.667ng/ml) in order of decreasing SERS intensity with decreasing SC concentration, which is shown in fig.5.7.a and b, respectively, were observed. LOD is 10^{-10} M or 66.7 pg/ml for SC whereas, limit of quantitation (LOQ) is 10^{-9} M or 0.667ng/ml for SC using SERS based detection method as discussed in this work, as shown in fig. 5.7.b. LOD is defined as the minimum concentration of an analyte that can be detected but not necessarily quantitated whereas LOQ is the concentration of analyte greater than or equal to the minimum concentration on the calibration curve[317].

5.1.4.5. Potential application in quality control:

SC is effective in doses of 25, 50 and 100 mg, depending upon the extent of ED in a subject. Upon dissolving a tablet or a capsule containing at least 25 mg of SC in 1000 ml, the final concentration stands out to be 25 μg/ml, which is within the higher linearity range shown in fig.5.7.a. SC metabolizes through P450 3A4 pathway[323]. Potent inhibitors of P450 3A4 pathway such as cemitidine, erythromycin or drugs such as amiodarone, digoxin, diltiazem, losartan, nifedipine, atorvastatin, cisapride, etc. which metabolizes through P450 3A4 pathway, reduces the clearance of SC and increases the plasma concentration of SC[323, 324]. Moreover, subjects with severe renal impairment, also reduces clearance of SC from human body[323, 324]. OTC drugs with concentration of SC lower than 1 mg per capsule or tablet, may increase plasma concentration of SC through accumulation due to reduced clearance as

discussed above. In such a case, detection and quantification of SC in concentration range lower than 1 μg/ml can be carried out in the lower linearity range as shown in fig.5.7.b. OTC drugs with SC adulteration are a potential threat to subjects under nitrate medication owing to sildenafil nitrate hypotension interaction[325-327] which leads to synergistic decrease in blood pressure [328]. The above discussion emphasizes on the necessity of development of a quality control method to check SC adulteration in OTC drugs.

5.2. Detection of Sildenafil citrate by AgCl/AgNPs

5.2.1. Background

Researchers indulge in hybrid plasmonic devices investigation of their interesting energy conversion[329-331] and sensing applications[330, 332], worldwide. As discused earlier, plasmonic noble metal nanoparticles (NMNPs) exhibit a unique optical property known as localized surface plasmon resonance (LSPR)[333] which is very specific to the size[334], intra-band transition[79] and dielectric function of the metal nanoparticle[335] as well as that of the medium[335]. Moreover, two or more NMNPs, especially gold and silver, upon approaching each other, their near-fields[336] tends interact, which results in generation of an enhanced electric field at the junction, known as hotspot.[79, 337] The above mentioned near-field interaction is known as plasmon coupling. For example, UV-vis absorption spectra is a manifestation of near-field interaction in the far-field [79] This forms the basis of use of gold[338] and silver[339] nanoparticles in colorimetric sensing. Often assembly[340] or disassembly[341] of NMNPs is associated with a visual colour change. Colorimetric sensing is often used to detect drugs[342], dyes[343], pollutants[344] and ions[341] using NMNPs. Lately, copper nanoparticles (CuNPs) were found to show colorimetric response to sulphide ions[345], due to conversion to non-plasmonic CuS. This is an example of chemical transformation of the nanoparticles leading to colour change. Another facet of application of plasmonic coupling

is surface enhanced Raman scattering (SERS). Raman scattering of molecular vibrations directly depends upon the square of electric field intensity[337]. The informations that can be extracted from SERS has been discussed earlier.[108, 337, 346-350]

Inter-particle coupling observed in hybrid nanoparticle dimers is similar to plasmonic coupling, and has potential application in single molecule SERS sensing.[351] The role of non-plasmonic materials such as graphene[352, 353], titanium dioxide[354, 355], zinc oxide[356, 357], aluminium oxide[358], cadmium selenide[359],etc. towards electric field enhancement in hybrid nanoparticle dimers have also been explored. Recently, it was demonstrated that the inter-particle electron transfer occurs in hybrid nanostructures in which silver clusters has been in reduced graphene oxide (rGO) electrodes which increases the sensitivity of detection of 4-nitrobenzene thiol. The above phenomenon is not only for SERS based sensing but also for electrochemical applications[360]. Photo induced enhanced Raman spectroscopy (PIERS) is also observed in hybrid nanostructures,[361] where UV pre-treated TiO_2 nanoparticles sensitized in vicinity of gold nanoparticles show enhanced SERS signal.[361] Plasmonic nanoparticles is reported to induce charge separation where NMNPs act as photsensitizers in semiconductor nanoparticles. There are few reports related to the interaction of silver nanoparticles (AgNPs) with silver chloride nanoparticles (AgCl NPs) which has revealed that AgCl NPs act as a photocatalyst whereas AgNPs act as photosensitizer. It is known that AgCl has an indirect band gap of 3.25 eV[362] or 381 nm where the conduction band is present 0.09 eV above the Fermi level.[363] Here, AgNPs were found to serve as a photo-sensitizer which provides electron to conduction band even at energies much lower than 3.25 eV. This prospect has been well utilized and studied for potential photocatalytic applications[363, 364]. The implication of AgCl on SERS of molecules adsorbed on AgNPs is yet to be investigated.

In this work, AgCl/Ag nanoparticle dimers (NPDs) were synthesized and its potential application in SERS sensing was explored. Ag/AgCl NPD was isolated in a non-aqueous medium as an intermediate by Chen et al. where AgNPs were synthesized from AgCl in ethylene glycol medium.[365] In this work, the premise of synthesis of AgCl decorated AgNPs in aqueous medium has been explored. Synthesis of non aqueous solvents has been avoided as they tend to have their own vibrational bands in the region 200-2000 cm^{-1} which is the finger-printing region. Sildenafil citrate (SC) was chosen as a suitable adsorbate whose detection is important for quality control of herbal medicines.[366] It is known that SC has two possible donor N-atom available to bind with AgNPs. SERS of SC on silver dendritic nanostructures was demonstrated by Meng Lv et al[319].The molecules with N-donor centres bind selectively to the surface of AgNPs is recently reported.[111] The aim of the work involves the synthesis of AgCl/Ag NPD, in aqueous medium, which is crucial for photocatalytic applications[367] as there are speculation revolving around the role of e_{aq}^- during photocatalysis in aqueous medium. A systematic study of addition of varying concentration of SC in presence of a fixed concentration HCl to AgNPs leading to the synthesis of AgCl/Ag NPD, is shown in this work. Detailed SERS study at varying excitation wavelength gave crucial information regarding the chemical processes occurring on the surfaces of AgCl-NPs and AgNPs, upon illumination. Moreover, a pulse radiolysis study of SC under reducing condition aided in establishing the mechanism of light induced surface reactions observed in the case of SC on the AgCl/Ag NPD.

5.2.2. Instrumentation details

UV-vis absorption spectroscopy, Raman spectroscopy and transmission electron microscopy (TEM) has be done by using the instruments mentioned in section 5.1.2. The pulse radiolysis kinetic spectrophotometric detection setup of energy 7 MeV was used in this study and the data analysis protocols have been discussed by Kapoor et. al.[368] Briefly, the

samples were irradiated in a suprasil quartz cuvette of dimension 1 cm x 1 cm, kept at a distance of 12 cm approximately from the electron beam window. The beam diameter is approximately 1 cm. Electron pulses of 50 ns were used. 10^{-2} M KSCN solution (aerated) was used for dosimetry, and the $(SCN)_2^{\bullet-}$ radical was monitored at 475 nm. The absorbed dose per pulse was calculated[1] assuming $G\varepsilon[(SCN)_2^{\bullet-}] = 2.6x10^{-4}$ m^2 J^{-1} at 475 nm. Absorbed dose was of the order of 14 Gy per pulse.

The radiolysis of water produces reactive free radicals, hydrated electrons (e_{aq}^-), OH radicals and H atoms, and molecular products H_2O_2 and H_2, as per the stoichiometry[1, 369] shown in reaction (5.1)

$$H2O \rightsquigarrow e_{aq}^-(0.28), {}^{\bullet}OH(0.28), {}^{\bullet}H(0.06), H_2(0.05), H_2O_2(0.07), H_3O^+(0.27) \qquad (5.1)$$

where the numbers in parentheses represent the radiolytic yields expressed in terms of G-values which is defined as the quantity of species formed per Joule of energy deposited at pH 7 in μmol J^{-1}. For studying the e_{aq}^- reaction, $^{\bullet}OH$ radicals were scavenged by addition of tert-butanol (reaction 5.2)

$$^{\bullet}OH + (CH_3)_3COH \rightarrow H2O + {}^{\bullet}CH_2(CH_3)_2COH \qquad (5.2)$$

5.2.3. Experimental Section

5.2.3.1. Chemicals

Silver nitrate ($AgNO_3$, 99.9999%), sildenafil citrate (≥98%) and sodium borohydride ($NaBH_4$, 99.99%) were obtained from Sigma-Aldrich and were used as received. Hydrochloric acid (30%) was obtained from Merck. All the experiments were performed in Millipore purified water.

5.2.3.2. Synthesis of silver nanoparticles:

Silver nanoparticles (Ag NPs) were synthesized by reduction of silver nitrate by sodium borohydride as described by Creighton et. al[370]. Drop wise addition of 10 mL $AgNO_3$ (1 mM) solution was done to 30 mL of 2 mM $NaBH_4$ (0-5°C) with slow stirring. The AgNPs solution, thus formed was yellow in colour and was found to be stable at room temperature for several weeks. The AgNPs synthesized were at pH~9. The above synthesized AgNPs solution was stored at 8 °C for 24 hours before conducting any further experiment and was marked as AgNP stock.

5.2.3.3. Synthesis of silver chloride decorated silver nanoparticles:

The above Ag NP stock solution was diluted three times with Millipore water and then to the above diluted AgNPs solution, different concentrations of sildenafil citrate (SC) were added followed by addition of conc. HCl while stirring vigourously, so that the concentration of chloride ion is 0.03 M in the final solution.

5.2.4. Results and Discussion:

5.2.4.1. UV-vis absorption study

UV-vis absorption spectra of synthesized AgNPs were recorded in a cuvette of pathlength 3 mm after 1 hour and 24 hours from the onset of the reduction of $AgNO_3$ by $NaBH_4$[141] which is shown in fig. 5.9.a and b. The reduction of Ag^+ ion by $NaBH_4$ is summarized in chemical equation 5.3.

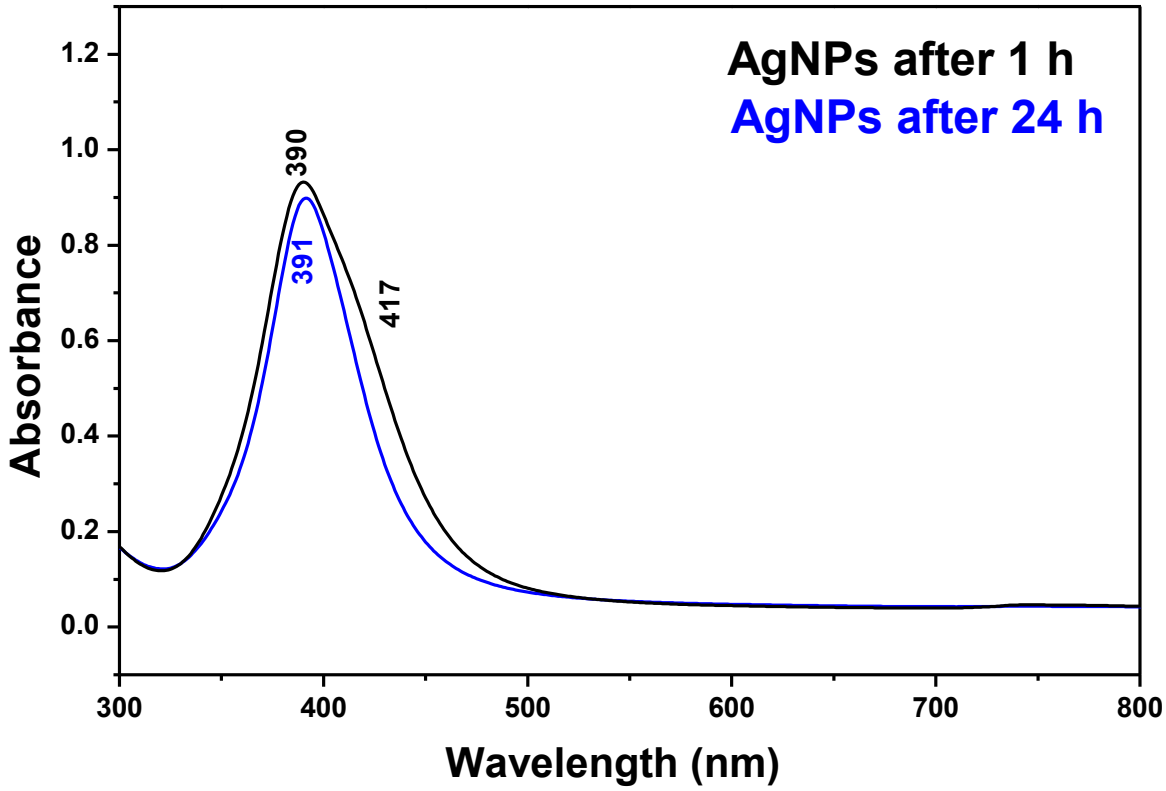

Figure 5.8. *UV-vis absorption spectra of Ag NPs recorded after (a) 1 h and (b) 24 h of reduction, at ambient conditions (pH~9) measured in 3 mm path length quartz cell.*

$$nAg^{+} + nBH_4^{-} + nH_2O \rightarrow Ag_n^{0} + B(OH)_3 + 7/2\ n\ H_2 \qquad (5.3)$$

After 24 hours of the onset of the reduction reaction, UV-Vis spectrum of AgNPs was found to show no further change. The LSPR band of AgNPs appears at 390 nm after 1 hour of the onset of the reduction reaction, along with an appearance of a slight shoulder at 417 nm (fig. 5.9.a). After 24 h, the LSPR band of Ag NPs evolved into a sharp and symmetrical peak at 391 nm (fig. 5.9.b) indicating that the Ag NPs obtained are spherical and monodispersed.[207]

The fate of AgNPs after chlorination by conc. HCl was studied in the absence of SC. The absorption spectrum of AgNPs in presence of 0.03 M HCl was recorded (fig. 5.9.a). The above figure showed that the absorbance of AgNPs at 394 nm reduced with time. Total time taken for the reduction of the absorbance was 35 minute. The reduction in absorbance may

be due to oxidation of AgNPs to AgCl. The above reaction mixture also contained Na^+ and NO_3^- ion. HCl[371] is reported to be a stronger acid than HNO_3[141]. As a result. the reaction of $NaNO_3$ with HCl, yielded HNO_3 as per equation 5.4:

$$\mathbf{NaNO_3 + HCl \rightarrow NaCl + HNO_3} \qquad (5.4)$$

Moreover, dil. HNO_3 is an oxidising agent[372] which would Ag^0 on AgNPs to Ag^+ as per equation 5.5:

$$\mathbf{Ag_n^0 + 4/3\ n\ HNO_3 \rightarrow nAgNO_3 + 1/3\ n\ NO + 2/3\ n\ H_2O} \qquad (5.5)$$

Since, the solubility product of AgCl[373] is very low, i.e., in the order of 10^{-10}, $AgNO_3$ and NaCl would react to give insoluble AgCl and soluble $NaNO_3$. This accounts for the disappearance of LSPR upon addition of HCl to AgNPs solution.

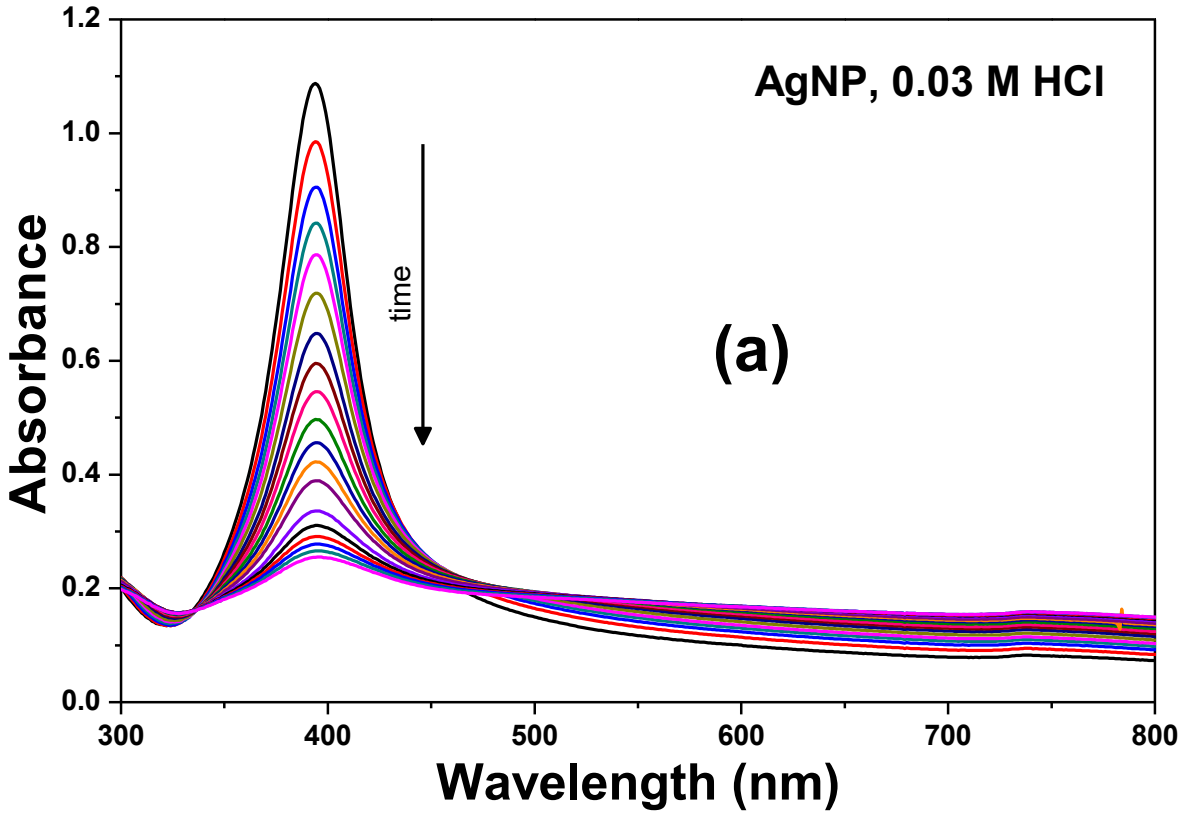

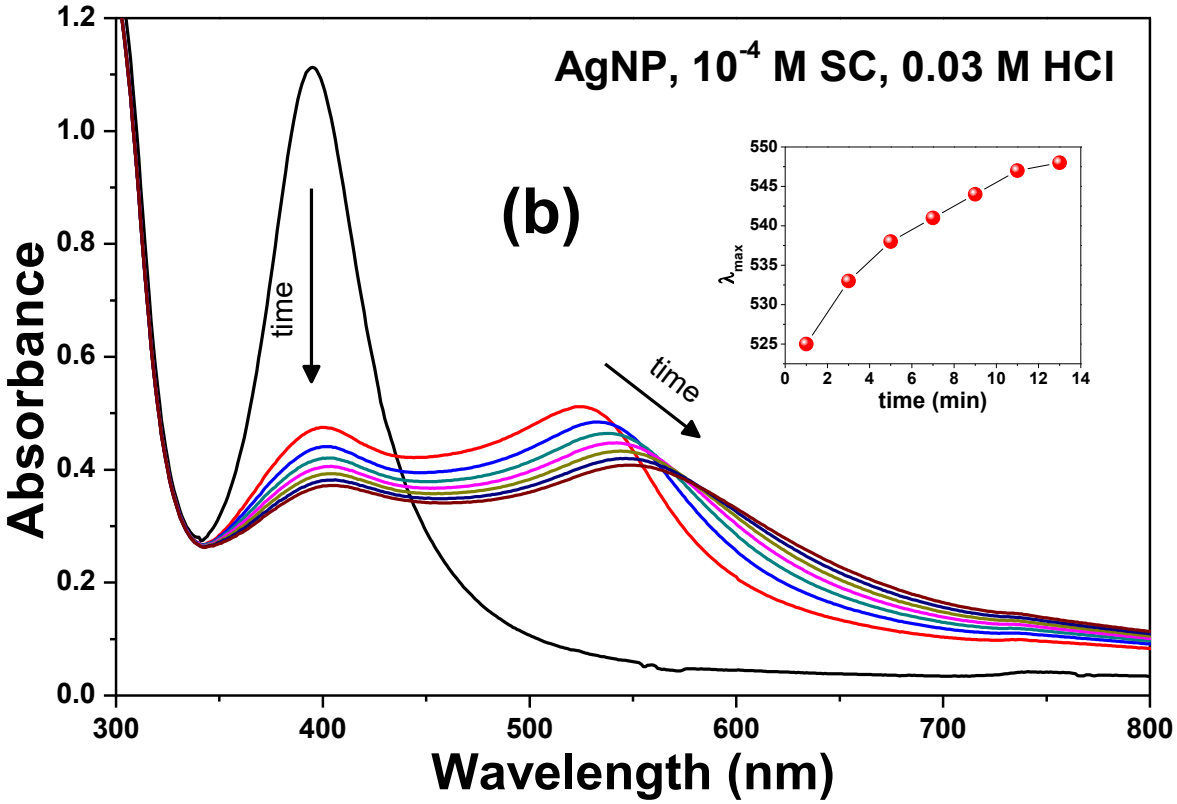
AgNP, 10-4 M SC, 0.03 M HCl
(b)
time
time
Absorbance
Wavelength (nm)
λmax
time (min)

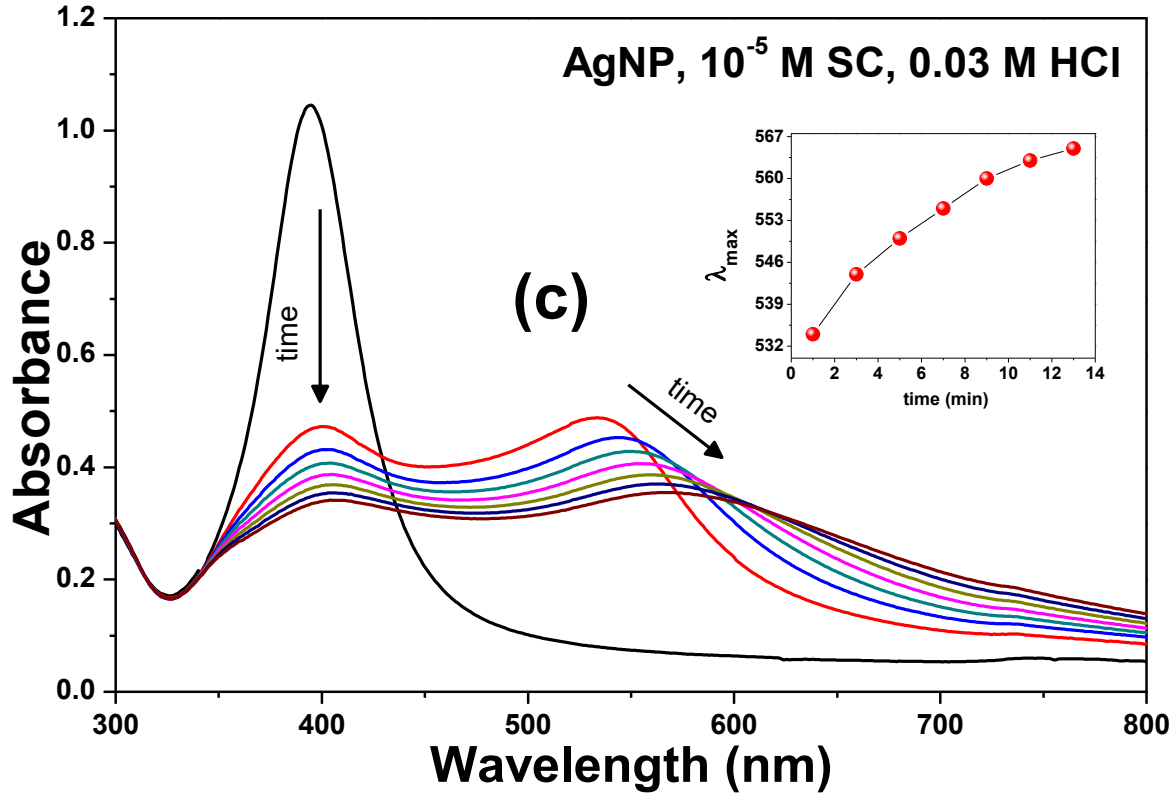
AgNP, 10-5 M SC, 0.03 M HCl
(c)
time
time
Absorbance
Wavelength (nm)
λmax
time (min)

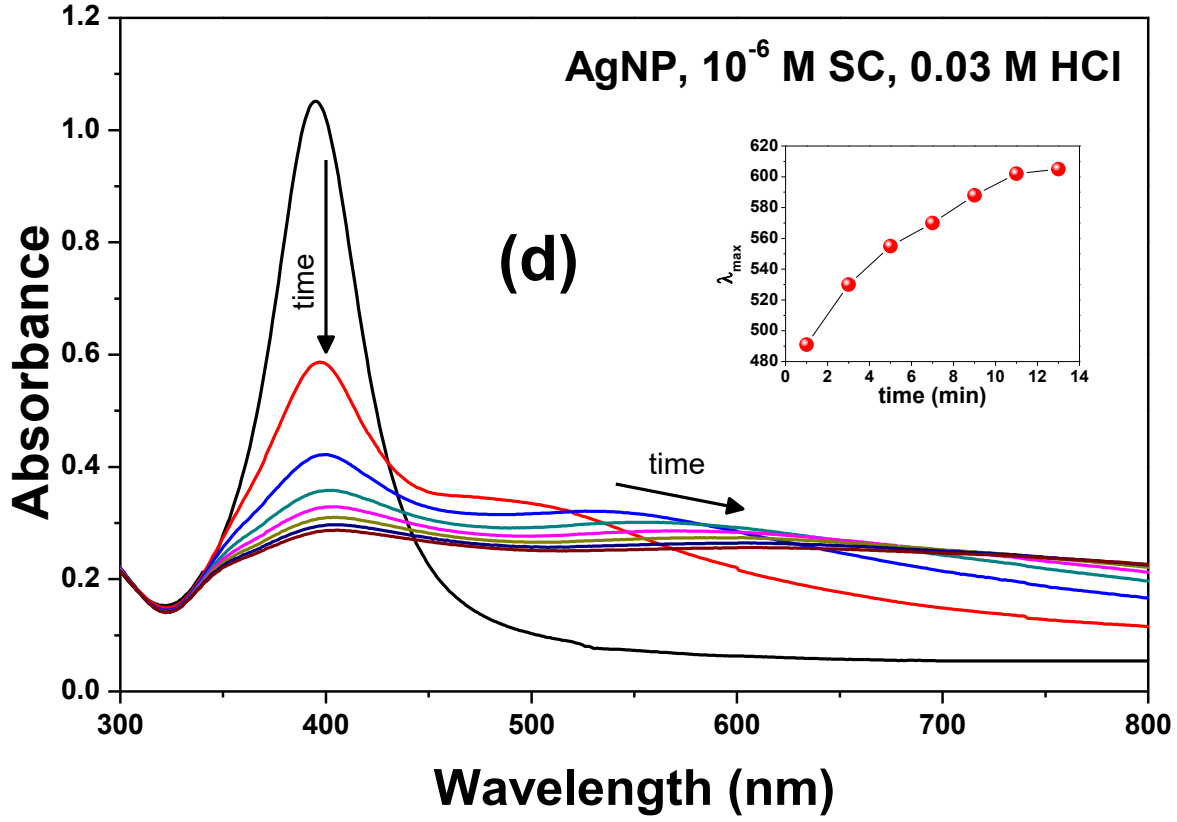

Figure 5.9. *Absorption spectra of Ag NPs recorded in (a) absence of SC and in presence of (b) 10^{-4} M, (c) 10^{-5} M and (d) 10^{-6} M SC in presence of conc HCl (0.03 M) in a 10 mm quartz cell at specific time intervals. Inset: for fig. (b)-(d), shift of absorption maxima of coupled plasmon peak with time (min).*

In presence of SC, the addition of conc. HCl has other effects apart from chlorination of AgNPs. It was observed in fig. 5.9.(b-d), that after addition of conc. HCl to a solution of SC and AgNPs, a red shifted peak appeared. This peak was found to shift towards higher wavelength along with further reduction in LSPR peak intensity of AgNPs, which was observed at 394 nm, with time. In order to understand the above observation, the different processes taking place simultaneously in the above-mentioned systems, must be taken into consideration. Firstly, after addition of HCl, the ionic strength of the medium increased, which in turn reduced the double layer thickness around AgNPs[374]. This process led to the

coalescence of AgNPs to form larger particles. This observation was further confirmed later from TEM study (vide infra). Secondly, after addition of HCl, the pH of the medium gets lowered to 1.52. This results in attaining of positive charge by SC molecules upon protonation which gets adsorbed on the AgNPs surface via ionic interaction with negatively charged AgNP surface[375] which has a capping of borate ions. The reported pKa values of SC are 7.10 and 9.84[303, 304] due to tertiary amide of piperazine moiety and secondary amide of pyrimidinone moiety respectively. Thirdly, AgNP agglomerates are formed which shows red-shifted LSPR, formed as a result of thinning the double layer. The red-shifted LSPR appeared due to plasmon coupling. In case of fig. 5.9.b and c, it is observed that agglomeration of particles take place, after to the addition of conc. HCl to the solution of AgNPs and SC (10^{-4} and 10^{-5} M),. In case of 10^{-4} M SC on AgNPs, the red-shifted LSPR (plasmon coupled) appeared at 525 nm just after 1 minute of the addition of conc. HCl, which is stabilized after about 13 minutes at 549 nm (fig. 5.9.b). Similarly, for 10^{-5} M SC on AgNPs, the red-shifted LSPR (plasmon coupled) first appeared at 533 nm, which was further stabilized after 13 minutes at 565 nm (fig. 5.9.c). The observed red-shift in coupled plasmon peak upon changing the concentration of SC from 10^{-4} to 10^{-5} M, on AgNPs, may be due to the higher degree of interaction between AgNPs as the capping of SC becomes less dense upon decreasing the concentration of SC in the solution. This observation is further confirmed by TEM studies (vide infra). Fourthly, HCl reacts with AgNPs to form layer of AgCl around them. The shift in absorption maxima of the red-shifted LSPR peak with time as shown in inset of fig. 5.9.b and c, pointed towards the slow agglomeration process. The sudden decrease in absorbance of LSPR peak at 394 nm, within 1 minute, was also observed which indicated that the rate of agglomeration of AgNPs is faster than formation of AgCl as shown in fig. 5.9.b and c. Further agglomeration continued upto 13 minutes.

In fig. 5.9.d, in presence of 10^{-6} M SC, the reduction in LSPR peak absorbance at 394 nm was not drastic in comparison to that in presence of 10^{-4} and 10^{-5} M of SC (fig. 5.9.b and c). This indicated that as the concentration of SC was reduced to 10^{-6} M, the extent of adsorption of SC was lowered in comparison to the above two cases, which led to lesser extent of agglomeration of AgNPs. This was also evident from the appearance of red-shifted coupled plasmon peak closer to the LSPR (394 nm) of AgNPs after 1 minute of addition of 10^{-6} M SC in presence of 0.03 M HCl. In the above case, the coupled plasmon peak appeared at 491 nm which stabilized finally at 605 nm (fig. 5.9.d). The total shift in coupled plasmon is drastic (114 nm) in this case as compared to the above two cases (10^{-4} and 10^{-5} M SC). Another important observation was that in fig. 5.9.b and c, a slight shoulder appeared at ~350 nm which may be the direct band gap transition of AgCl. Direct band gap transition of AgCl is reported to appear at 241 nm or 5.13 eV[376]. The band structure is calculated based on bulk parameters, as a result, the direct band gap transition may be shifted in nanometric dimensions. There was also a possibility of assisted indirect band gap transition by AgNPs[377].The observed absorbance of partly AgCl on AgNPs in presence of 10^{-5} M SC is lower compared to 10^{-6} M SC (fig. 5.9.b and c). But in fig. 5.9.b, no trace of partially formed AgCl on AgNPs was observed in the absorption spectrum, in presence of 10^{-4} M SC. The above observation indicated that lower concentration of SC favoured the formation of AgCl on AgNPs. Moreover, non-appearance of partially formed AgCl on AgNPs in the UV-visible absorption spectra of AgNPs in absence of SCwas observed, which is shown in fig. 5.9.a. The above discussion suggested that SC played an important role in stabilization AgCl in nanometric dimension.

5.2.4.2.TEM and SAED study of SC-AgNPs-HCl systems

TEM study of the above systems shed more light on the morphological details of AgNPs. AgNPs formed by the reduction of Ag^+ using sodium borohydride were observed to be 3-8

nm in size, which is shown in fig. 5.10.a. Addition of HCl (0.03M) to a solution 10^{-4} M SC and AgNPs, led to coalescence of AgNPs in the high ionic strength of the medium, which led to formation of larger AgNPs of 15-20 nm in size, which is shown in fig. 5.10.b. It can be clearly seen that particles are fairly spherical and agglomeration only occurs after addition of SC. Spherical shape of any particle is indicative of minimum surface energy, achieved as a result of efficient capping[378]. SC served as the capping agent. Similarly, in a solution of SC (10^{-5} M) and AgNPs, in presence of HCl, larger AgNPs of size 20-50 nm are also observed which is shown in fig. 5.10.c. The above AgNPs were found to be less spherical in shape as compared to those shown in fig. 5.10.b. This may be due to reduced extent capping of AgNPs by lower concentration of SC, i.e., 10^{-5} M, that in the case shown in fig. 5.10.a. Moreover, a slightly extent of agglomeration was also observed in fig. 5.10.b. Upon further lowering of concentration of SC to 10^{-6} M, which was added to AgNPs, followed by the addition of HCl (0.03 M), no further agglomeration of AgNPs (fig. 5.10.d) was observed. Instead, isolated dimers of AgNPs were observed. Neither AgNPs are effectively stabilized in 10^{-6} M SC nor was agglomeration induced in AgNPs, which is unlike the above cases (fig. 5.10.b and c). It was observed from the TEM image shown in fig. 5.10.d, spherical AgCl nanoparticles (vide infra) were formed along with every AgNPs. This was observed even for larger AgNPs (size > 50 nm). A work reported by Chen et al. where AgNPs were synthesized from AgCl, provided the essential clue which led to the inference discussed above. The reaction intermediate Ag/AgCl NPD were obtained in ethylene glycol medium[365]. They have reported two types of particles with different contrast in the TEM study. The particles with darker shades corresponded to AgNPs whereas lighter shade corresponded to AgCl NPs.

Selective area electron diffraction (SAED) pattern were also recorded along with TEM images , in oder to fetch addition information for identification of crystal lattice of Ag and

AgCl (vide infra). In fig. 5.10.d, AgCl/Ag nanoparticles dimers (NPD) were observed to have formed upon chlorination of AgNPs in presence of weaker capping by SC. Again, the AgCl nanoparticles as formed in the above case were stabilized by 10^{-6} M SC. In absence of SC, upon HCl addition to AgNPs, led to the formation of larger non spherical AgNPs, which is shown in fig. 5.10.e.

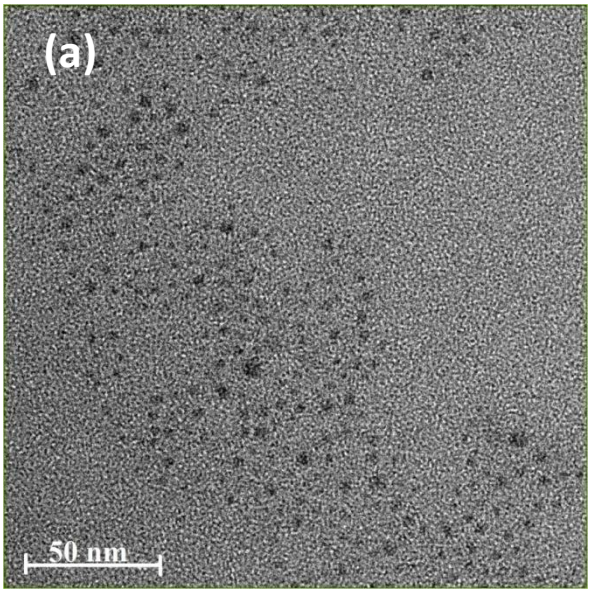

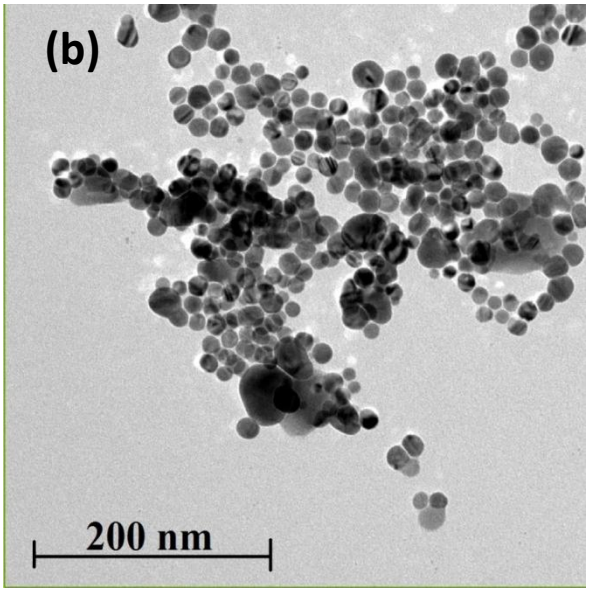

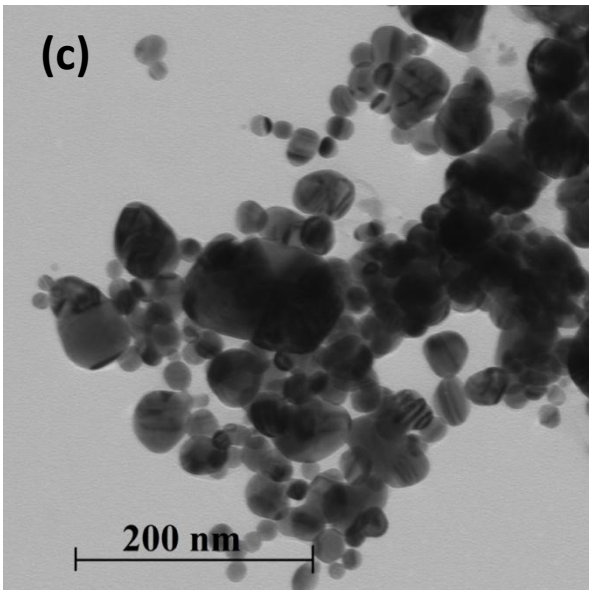
(c)
200 nm

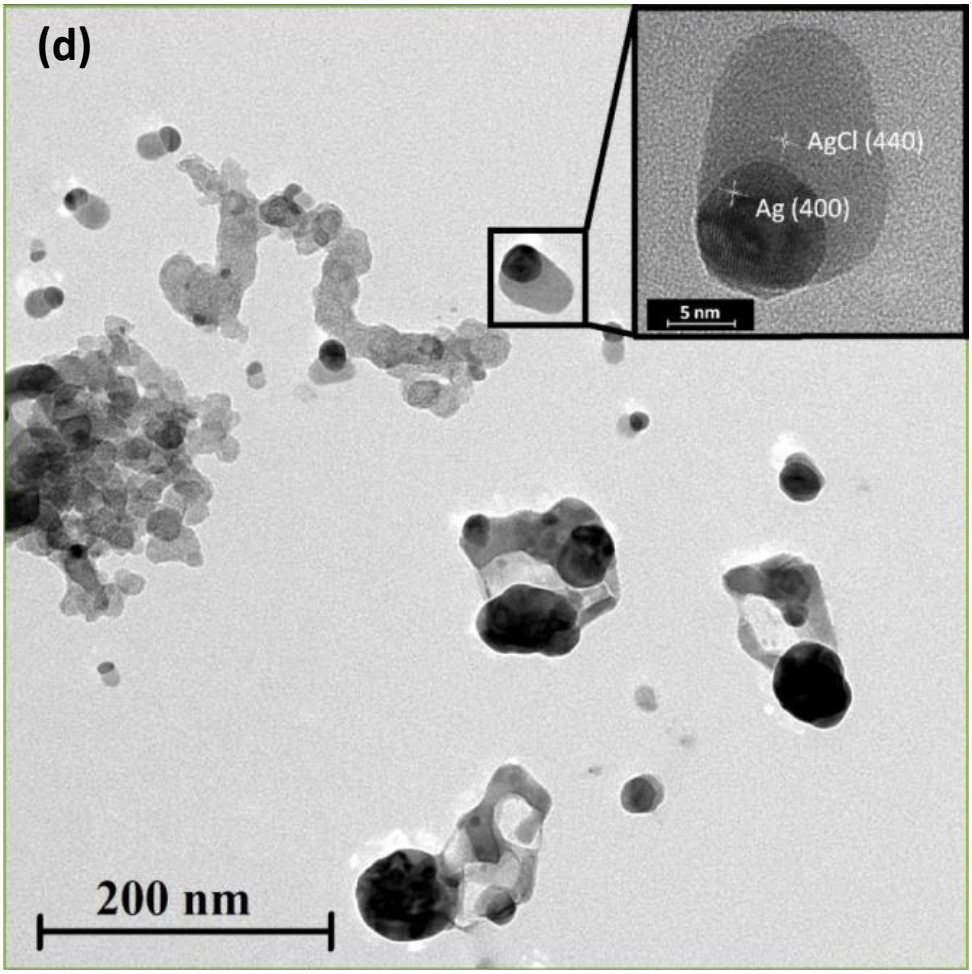
(d)
AgCl (440)
Ag (400)
5 nm
200 nm

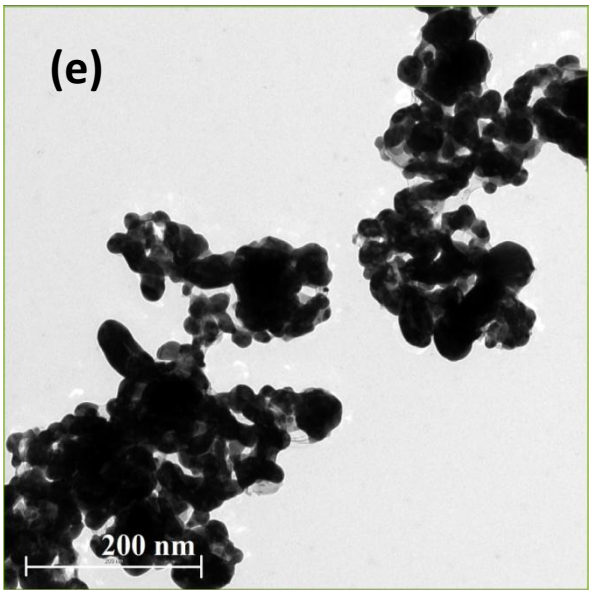

Figure 5.10. *Transmission electron microscopy (TEM) image of (a) Ag NPs (stock solution), AgNPs in presence of (b) 10^{-4} M, (c) 10^{-5} M, (d) 10^{-6} M SC and in (e) absence of SC, after addition of 0.03 M HCl. Inset in fig. d, shows magnified TEM image of AgCl/Ag nanoparticle dimer with lattice fringes corresponding to 400 and 440 planes of Ag and AgCl, respectively.*

The SAED patterns of various combinations of AgNP and SC in presence of HCl further substantiated the UV-vis absorption and TEM data. The SAED pattern of AgNPs solution in absence of SC as well as HCl showed two prominent spots corresponding to 200 and 111 plane of Ag[379] which is shown in fig. 5.11.a. In presence of SC, AgNP solution with 0.03 M HCl showed spots and rings which are characteristic of both Ag and AgCl,[380] which is shown in fig. 5.11. (b-d). In fig. 5.11.b and c, planes corresponding to Ag lattice showed more prominent spots and rings with slight contribution from that of AgCl. In fig. 5.11.d, the contribution of lattice of both Ag as well as AgCl was significant. The above observations were further consolidated the observation made in fig. 5.10.d as well as in fig. 5.9.d. In fig. 5.11.e, the degradation of AgNPs by HCl in the absence of SC was recorded in which the lattice planes corresponding to both Ag as well as AgCl were observed

(a)

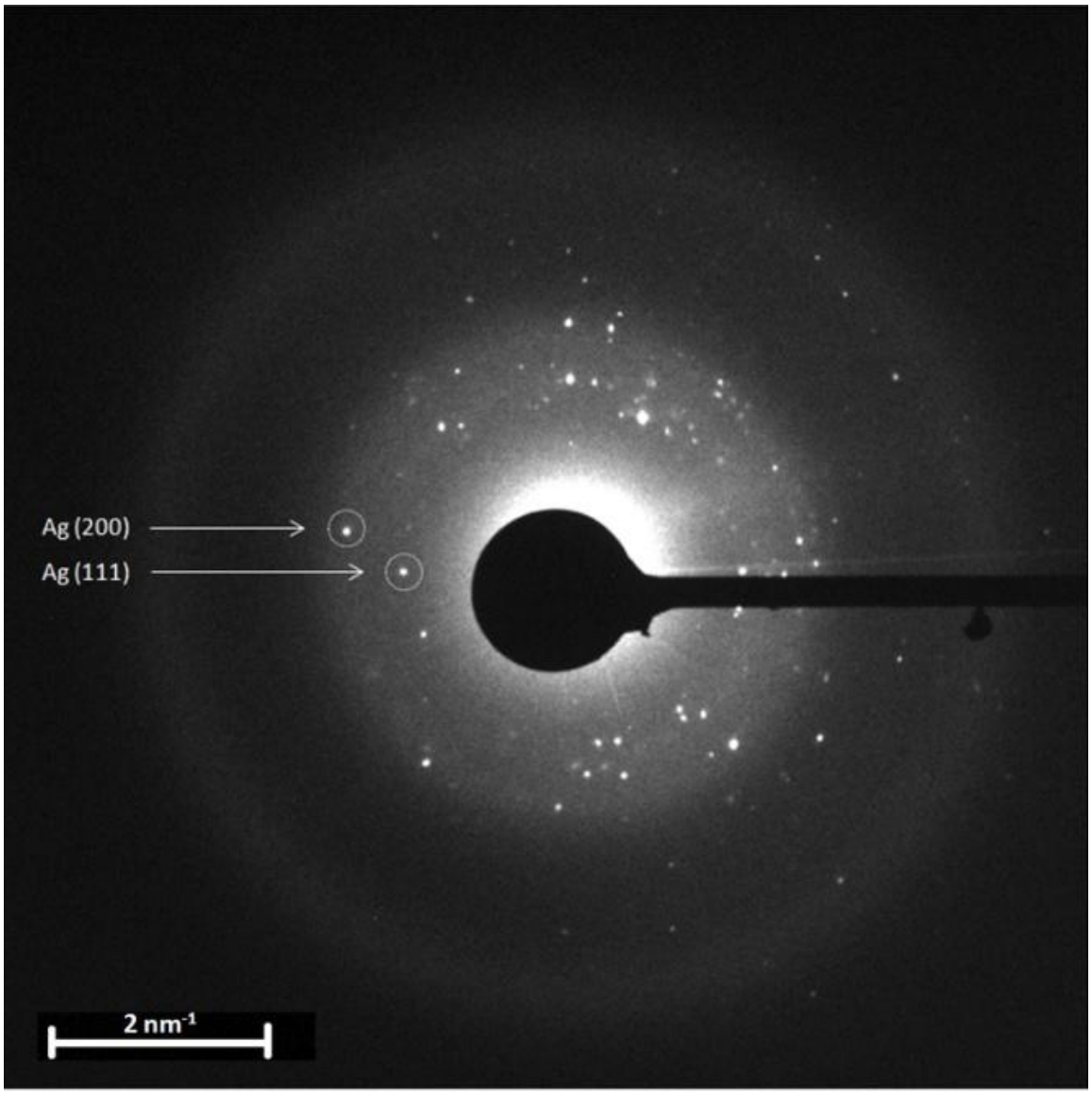

(b)

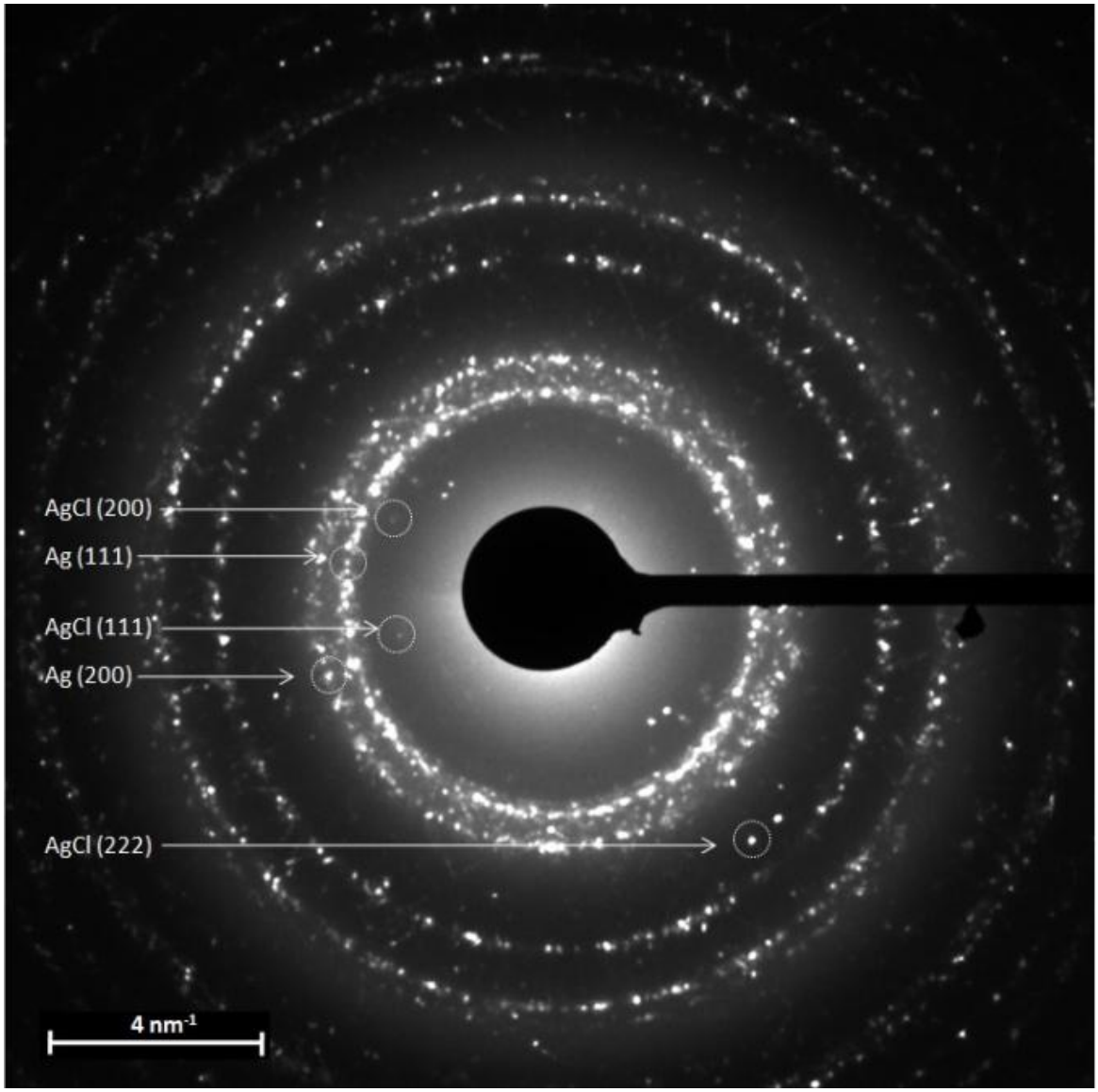

(c)

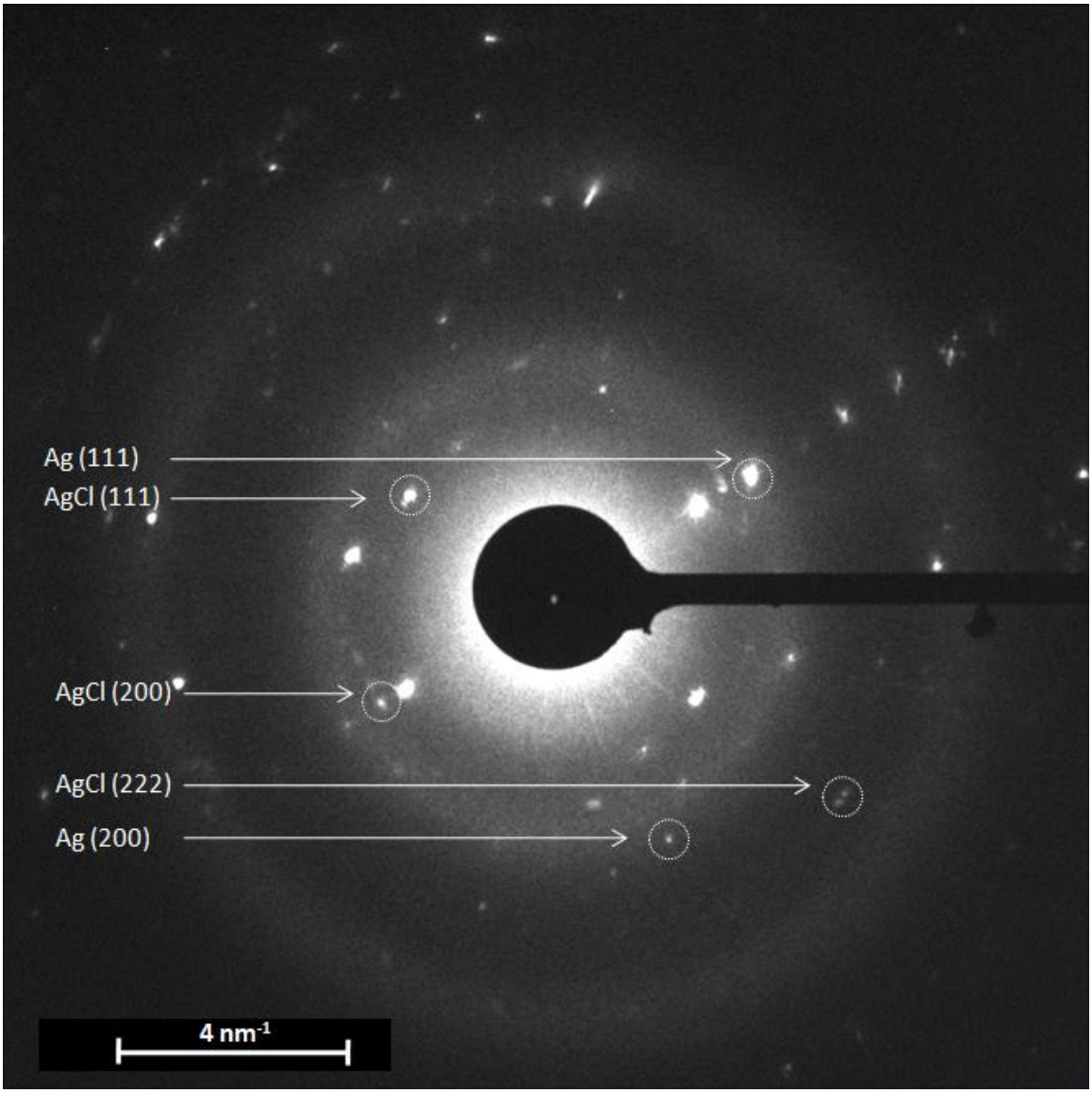

(d)

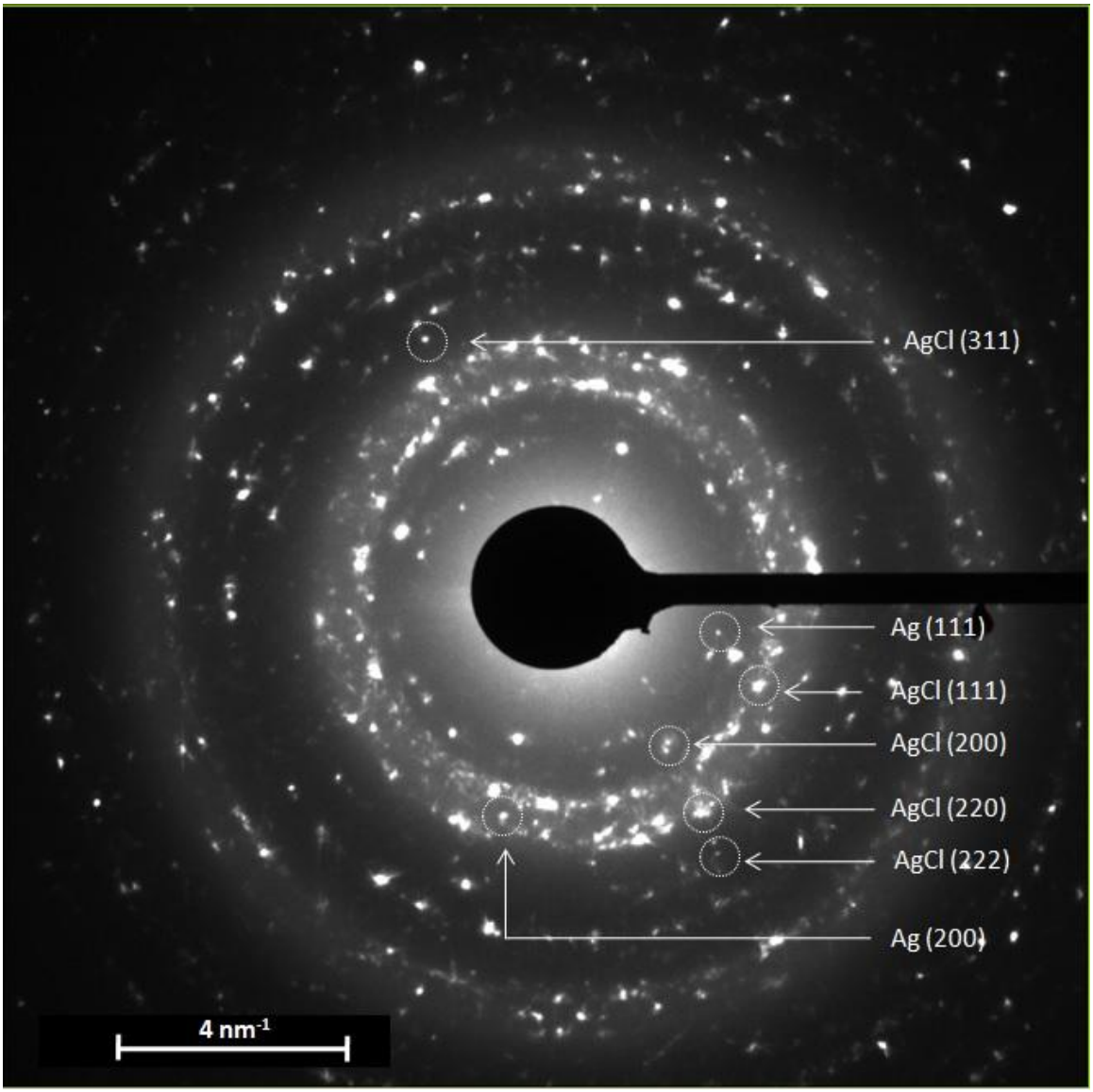

(e)

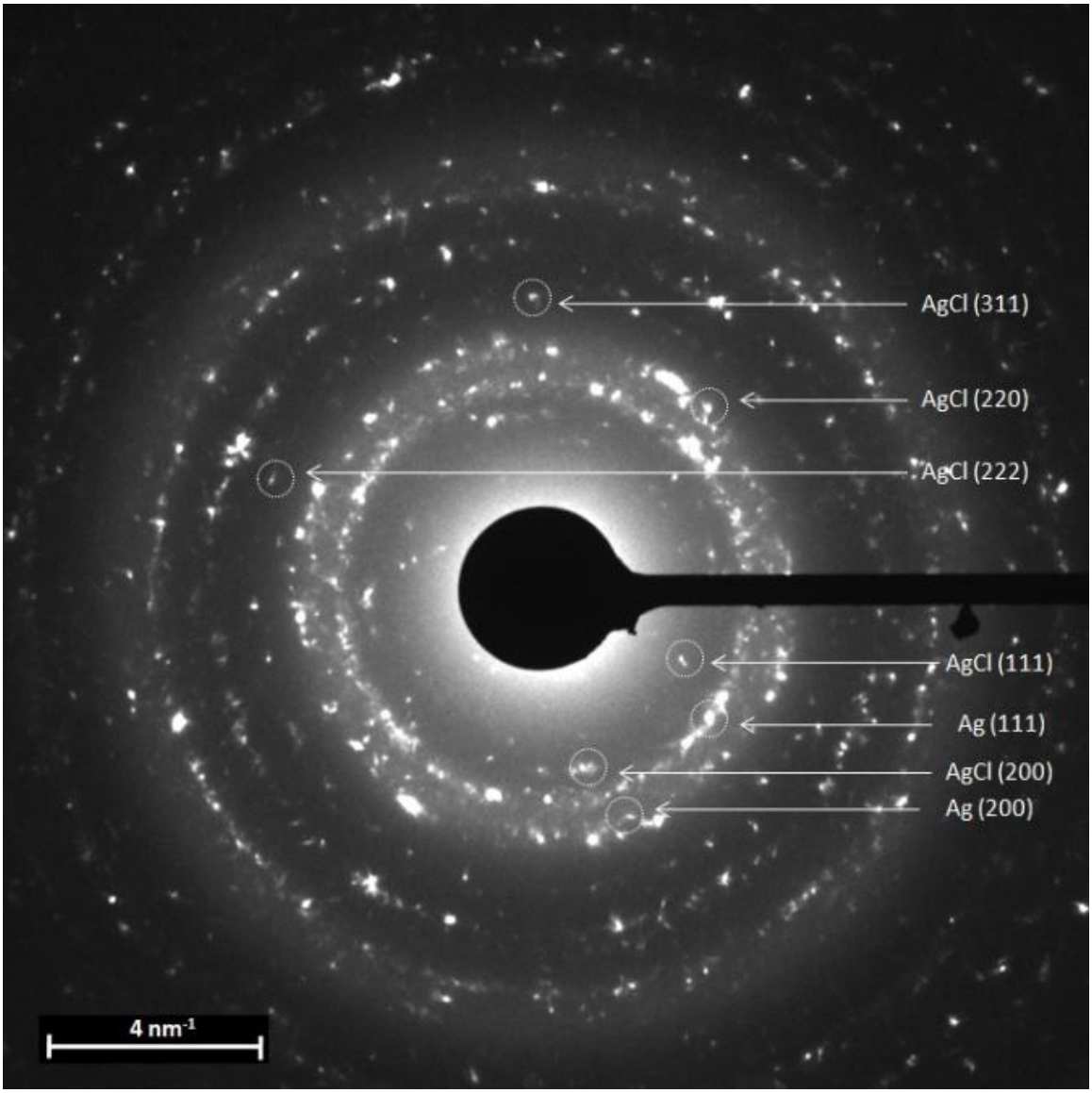

Figure 5.11. *Selected area electron diffraction (SAED) patterns of (a) Ag NPs (stock solution), AgNPs in presence of (b) 10^{-4} M, (c) 10^{-5} M, (d) 10^{-6} M SC and in (e) absence of SC, after addition of 0.03 M HCl.*

The observations made from UV-vis absorption, TEM and SAED study together forms a definite idea about the morphology of the particles. SC acted as a stabilizer for larger AgNPs and sometimes for AgCl NPs (fig. 5.10.b, c and d), formed due to the coalescence or chlorination of the stock AgNPs (fig. 5.10.a) in presence of 0.03 M HCl. It was observed that upon reduction of the concentration of SC from 10^{-4} to 10^{-6} M, the AgNPs became less

spherical. In presence of 10^{-6} M SC, AgNPs were weakly stabilized, which led to its chlorination, forming AgCl-NPs (fig. 5.10.d). AgCl-NPs were also stabilized by SC which was evident from its spherical shape. Both AgNPs and AgCl-NPs were present adjacent to each other, leading to formation of a hybrid Ag/AgCl NPD. At higher concentrations of SC (> 10^{-6} M), SC effectively screened AgNPs from chlorination (fig. 5.10.b and c) by Cl^- ion. Although the SAED patterns of AgNPs in presence of 10^{-4} and 10^{-5} M SC showed the presence of AgCl (fig. 5.11.b and c). The possibility of partial chlorination of surface of AgNPs[375] cannot be negated. In a work reported by Sloufova et. al, the effect of chlorinated sites on AgNPs towards SERS signal [375] was studied and the deviation of surface enhanced resonance Raman scattering (SERRS) from SERS signal may be due to higher contribution of chemical enhancement was attributed to formation of AgCl on the surface of AgNPs.

5.2.4.3. Computational study of conformers of SC by DFT

In order to acquire structural information of SC from the vibrational spectra of different concentration of SC adsorbed on the surface of AgNPs as well as AgCl/Ag NPD, Raman spectra of solid SC as SERS spectra of SC on AgNPs solution were recorded and the data was compared with the Raman spectra obtained from computational methods. Pyrazolo[4,3-d]pyrimidin-7-one (PPO), with methyl, propyl and 2-ethoxy-5-(4-methylpiperazin-1-yl)sulfonylphenyl groups at 1st, 3rd and 5th positions, respectively, constitutes the structure of sildenafil. Again , there are four nitrogen atoms at positions 1, 2, 4 and 6 in SC. SC shows amine-imine tautomerism among two tautomers, 4H-PPO and 6H-PPO, where a H-atom maybe bonded to N-atom at 4^{th} and 6^{th} position, respectively. , There is also a possibility of ketamine-iminol tautomerism which results in an 'enol' tautomer. Thus, SC has three possible conformers which are termed as 4H-PPO, 6H-PPO and Enol as shown in fig. 5.12.a, b and c, respectively. The geometry optimization was performed for the three tautomers of SC, namely 4H-PPO, 6H-PPO and enol, by density functional theory (DFT)

with B3LYP functional and 6-31+G(d,p) basis set. The structural arrangements of conformers of SC are discussed below.

a. 6H-PPO tautomer of SC:

The geometry optimization of 6H-PPO tautomer led to computation of theoretical Raman spectra (fig 5.13.c), which matched well with the experimental Raman spectra of solid SC recorded at 632 and 514 nm (fig. 5.13a and 5.13b). **T**he dihedral angle, Ψ between phenyl ring at 5^{th} carbon and the pyrazole ring i.e. ∠N(4)-C(5)-C(1')-C(6'), was obtrained to be 5°.

b. 4H-PPO tautomer of SC:

Theoretical Raman spectra as computed from the optimized geometry of 4H-PPO tautomer, did not match well with the experimental Raman spectra of solid SC recorded at 514 and 632 nm(fig. 5.13.d).The dihedral angle, Ψ of 55° was obtained.

c. Enol tautomer of SC:

Theoretical Raman spectra as computed from the optimized geometry of enol tautomer, did not match well with the experimental Raman spectra of solid SC recorded at 514 and 632 nm (fig. 5.13.e).

d. Ag-6H-PPO and Ag-4H-PPO complex:

In order to investigate the reason behind the anomalous behaviour behind the surface enhanced Raman scattering (SERS) spectra of 10^{-6} M SC on AgNPs, a complex of Ag-6H-PPO was geometry optimized using DFT (Unrestricted B3LYP functional and GEN basis set) to obtain theoretical Raman spectra. The obtained computed Raman spectrum did not match with that of the experimental SERS spectra of 10^{-6} M SC on AgNPs recorded at 632 nm (fig. 5.16), thus eliminating the possibility of charge-transfer complex formation between SC and AgNPs in aqueous solution.

The geometry optimized structures of SC conformers are also shown in fig. 5.12.(a-c). 6H-PPO was found to be the most stable conformer.

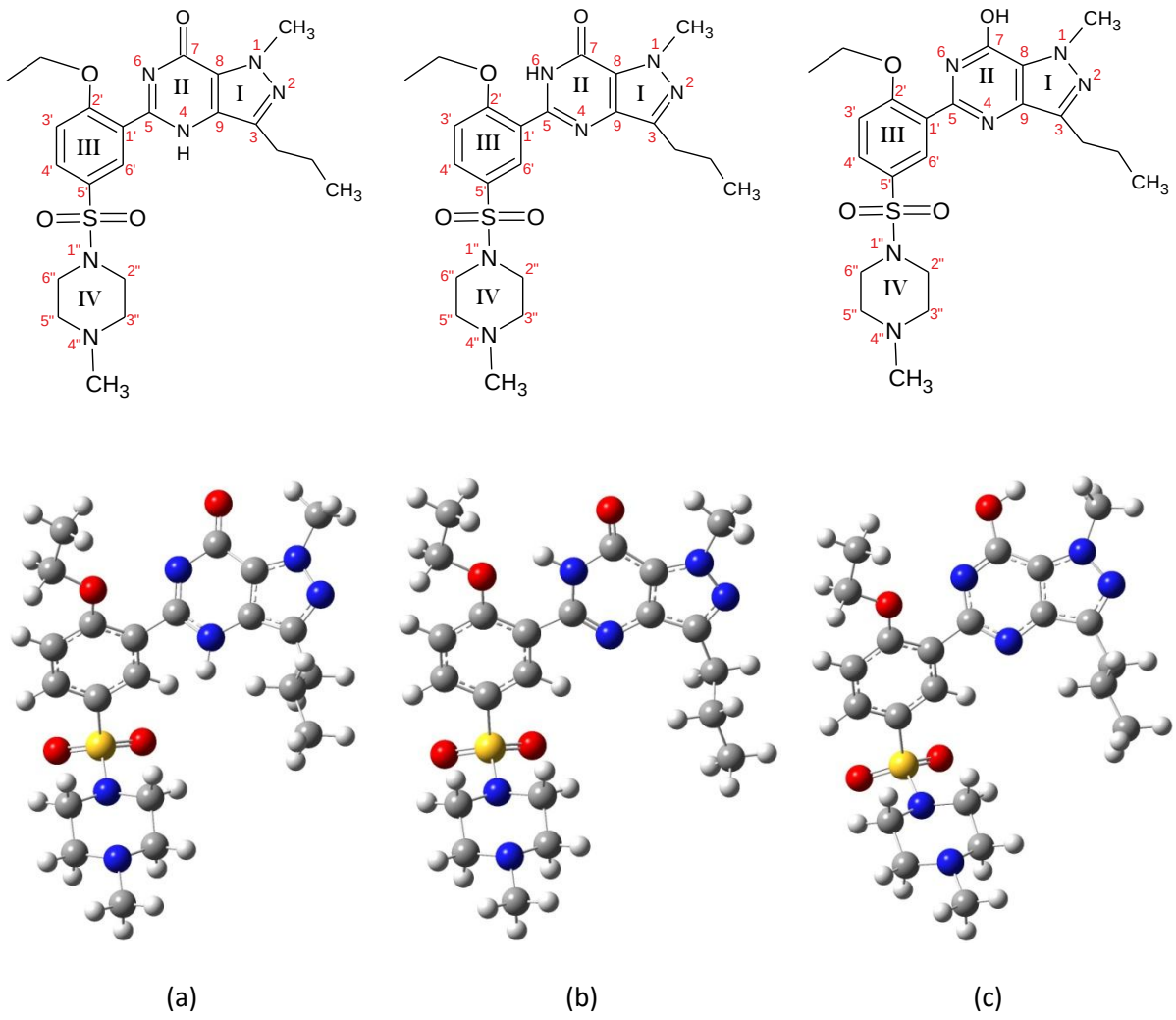

Figure 5.12. *Structural formula and geometry optimized structures different conformers of sildenafil citrate (SC) namely (a) 4H-pyrazolo[4,3-d]pyrimidin-7-one (4H-PPO), (b) 6H-pyrazolo[4,3-d]pyrimidin-7-one (6H-PPO) and (c)pyrazolo[4,3-d]pyrimidin-6-en-7-ol (enol) are shown. Colour code of atoms: hydrogen (white), carbon (grey), nitrogen (blue), oxygen (red), and sulphur (yellow).*

5.2.4.4. Raman spectra of solid SC and assignment of modes of vibration

Raman spectra of solid SC, recorded at excitation wavelengths of 514 and 632 nm, showed high mutual match which is shown in the fig. 5.13.a and b. The strong Raman spectrum bands at 1578, 1562, 1529, 1403 and 1238 cm^{-1} were observed. The bands at 1578, 1562, 1529, 1403 and 1238 cm^{-1} were assigned to phenyl C-C-C stretch (asymstr), C5=N4 str,

C8=C9 str, phenyl C-C-C stretch (symstr) and ring breathing modes. Raman bands of medium intensity at observed at 1484 and 1270 cm^{-1} were assigned to alkyl CH_2 scissoring and N1-N2 str. The Raman bands of weak intensity observed at 1700, 1442, 1169, 1098, 1052, 992, 925, 817, 739, 650 and 565 cm^{-1} were assigned to C7=O str, N-CH_3 bend, phenyl CH wagging (out-of-plane), phenyl CH wagging (in-plane), alkyl C-O bend (ethoxy group), N4-C5-N6 bending, phenyl ring breathing, ring breathing (ring II,III), ring bend (ring I,II), ring breathing (ring I,II, III) and ring distortion (out of plane) modes, respectively. The assignment of bands observed in Raman spectra of solid SC (fig. 5.13.a and b) was done by comparing with the computed Raman spectrum of 6H-PPO which is shown in fig. 5.13.c. The above assignments corroborated to the reported values[307]. According to the above observations, SC exists majorly as 6H-PPO tautomer in the ground states, although slight contributions from 4H-PPO (fig. 5.13.d) and Enol (fig. 5.13.e) conformers may not be negated. A detailed comparison of the Raman bands in the computed spectra of SC and Raman spectrum of solid SC is provided in table 5.2 (vide infra). Recording of the Raman spectrum of aqueous solution of SC was not possible due to low solubility of SC which led to very poor signal to noise ratio in the Raman spectrum of a saturated solution of SC (10^{-3} M), probably due to low Raman scattering cross section.

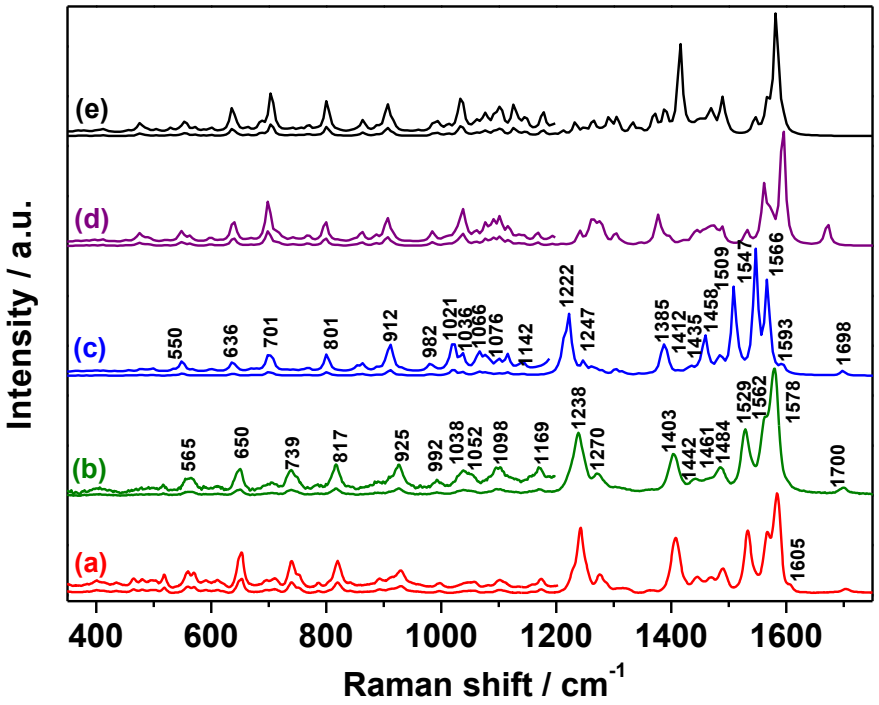

Figure 5.13. *A comparison of Raman spectra of (a) solid SC excited at 632 nm, (b) solid SC excited at 514 nm, (c) 6H-PPO tautomer of SC (theoretical), (d) 4H-PPO tautomer of SC (theoretical) and (e) Enol tautomer of SC (theoretical). Intensity magnified Raman spectra are overlaid on the corresponding Raman spectra for the region 350-1200 cm^{-1}.*

5.2.4.5. SERS spectra of different concentrations of SC adsorbed on AgNPs in presence of 0.03 M HCl

The SERS spectra of SC (10^{-4}, 10^{-5} and 10^{-6} M) adsorbed on Ag NPs in presence of 0.03 M HCl were monitored. In fig. 5.9.(b-d), the UV-vis absorption spectra of the above solutions are shown. It was observed that only in presence of 0.03 M HCl, SERS spectra of maximum intensity was observed for the above solutions, which may be attributed to efficient adsorption of positively charged protonated SC molecule as well as associated AgCl induced agglomeration phenomenon, which is reported by Sloufova et. al. [375]

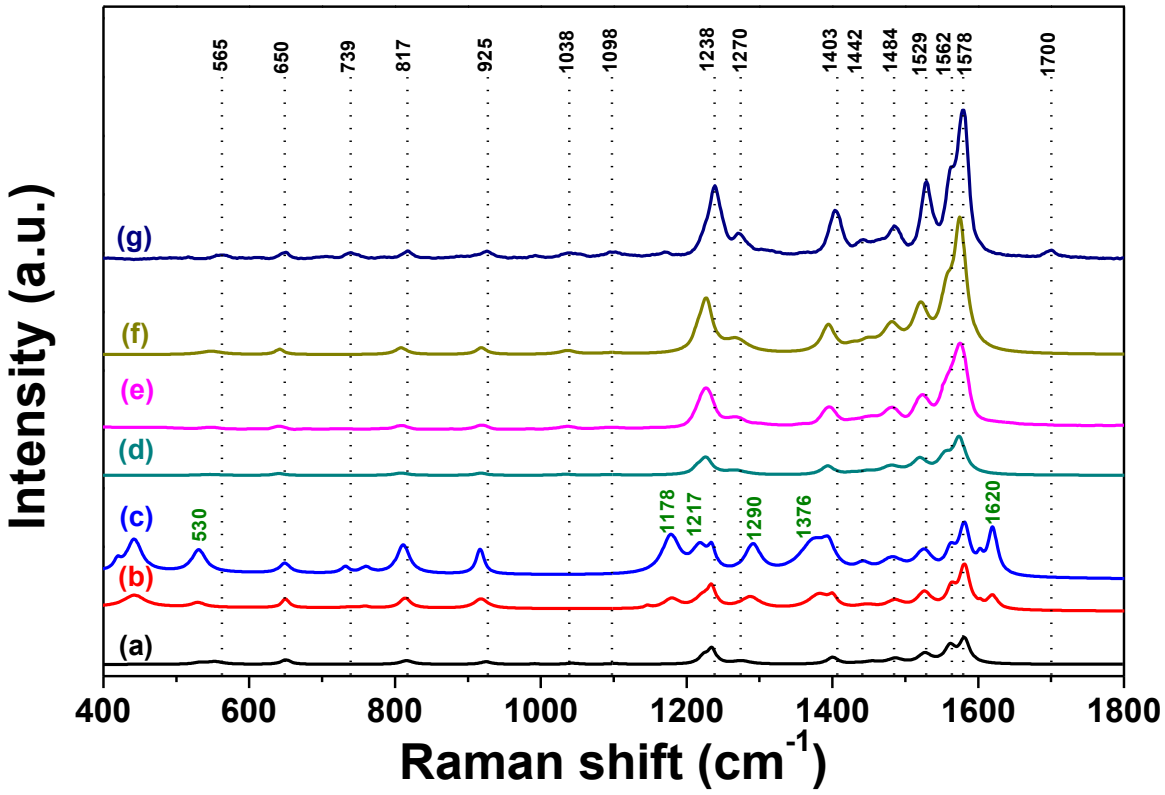

Figure 5.14. *A comparison of Raman/SERS spectra of (a) 10^{-4} M SC adsorbed on AgNPs excited at 632 nm, (b) 10^{-5} M SC adsorbed on AgNPs excited at 632 nm, (c) 10^{-6} M SC adsorbed on AgNPs excited at 632 nm, (d) 10^{-4} M SC adsorbed on AgNPs excited at 514 nm, (e) 10^{-5} M SC adsorbed on AgNPs excited at 514 nm, (f) 10^{-6} M SC adsorbed on AgNPs excited at 514 nm, and (g) solid SC excited at 514 nm.*

The SERS spectrum of 10^{-4} M SC adsorbed on Ag NPs were almost indistinguishable recorded at 632 (fig. 5.14.a) and 514 nm (fig. 5.14.d) excitations. Moreover, the above spectra also matched reasonably with the Raman spectrum of solid SC (fig. 5.14.g). This implies that the presence of AgNPs closer to SC (10^{-4} M) molecule imparted almost no effect on the peak positions in the SERS spectra (fig. 5.14.a and d). Thus, it can be said that the observed signal enhancement in the above case, is mainly due to the electromagnetic effect with negligible contribution from metal-ligand charge transfer. Moreover, a good

match of the above SERS spectra with the solid SC Raman spectrum shows that SC exists in 6H-PPO form on the Ag NPs surface. The assignment of the SERS bands is shown in table 5.2.

Table 5.2. *Assigned Raman bands as observed in experimental Raman and SERS of SC under 514 and 632 nm excitation by comparing with the computed vibrational modes in 6H-PPO and 4H-PPO tautomers of SC. Rings in SC moiety are designated as RI, RII, RIII and RIV as shown in fig 5.12.a and b. Vibrations specific to 6H-PPO and 4H-PPO are designated by # and †, respectively. Strong, medium and weak peaks are denoted by s,m and w respectively. The short notations str, sym, asym, wag, sci, bend, dis and twi stands for stretching, symmetric, asymmetric, wagging, scissoring, bending, distortion and twisting, respectively.*

Sl. No.	Experimental				Computed		Vibrational Modes
	Solid		SERS		6H	4H	
	514 nm	632 nm	514 nm	632 nm	X 0.97	X 0.97	
1.	1700w	1703w			1698	1671	RII: C7=O str
2.		1605w		1620s	1593	1593	RIII: C2'-C3'-C4'asym str, C5'-C6'-C1' asym str, C-H wag.
3.	1578s	1584s	1574s	1580s	1566	1573	RII: N4-C5 str$^{\#}$, C5-N6 str†. RIII:C1'-C2'-C3'asymstr,C4'-C5'-C6' asym str
4.	1562s	1567s	1559s	1563s	1547	1561	RI: N1-C8 str$^{\#}$ RII:N4-C5 str$^{\#}$,N6-H wag$^{\#}$,C5-N4-C9 asym str†,‡,N4-H wag†. RIII:C3'-C4'-C5' asym str$^{\#,\dagger}$,C4'-C5'-C6' asym str,C-H wag.
5.	1529s	1533s	1521m	1525m	1509	1531	RI:C8-C9 str,C3-C str$^{\#}$. RII:N6-H wag$^{\#}$,C5-N6 str†,N4-H wag†.
6.	1484m	1490m	1481m	1482m	1458	1488	RIII:Terminal H-C-H Sci$^{\#}$ (C2'-O-CH_2-CH_3), H-C-H Sci† (C2'-

						1475	O-CH_2-CH_3), C-H wag†. RI: N1-CH_3H-C-H sci.
7.	1461w	1469w	1447w		1427 1435	1444	RI: H-C-H sci$^{\#,\dagger}$ (C3-CH_2-CH_2-CH_3),CH_3 bend$^{\#,\dagger}$(N1-CH_3). RII:N6-H wag$^{\#}$.
8.	1442w	1445w	1425w		1412	1424	RI:CH_3 bend$^{\#,\dagger}$ (N1-CH_3). RII:N6-H wag$^{\#}$,N4-H wag†.
9.	1403s	1407s	1394s	1392s	1385	1377	RIII: C1'-C6'-C5' sym str,C2'-C3'-C4' sym str,C(4',5')-H wag, terminal CH_3 bend (C2'-O-CH_2-CH_3). RI:terminal CH_3 bend†(C3-CH_2-CH_2-CH_3), N2-C3 str†.
10.	1270m	1275m	1265m		1247 1279 1270	1301 1275 1270 1262	RI:N1-N2 str, H-C-H wag (N1-CH_3), N4-H wag†. RII: N6-C7 str. RII: C2'-O str†, C(3',4')-H wag†. O=S=O asym str†. C5-C1' str (RI and RII)† RII:N4-H wag†. RIII:C6'-H wag†.
11.	1238s	1242s	1226s	1233s	1222	1240	RI: CH2 wag (C3-CH_2-CH_2-CH_3), Breathing†. RII: N6-H wag$^{\#}$, N4-H wag†, Breathing†. RIII: Breathing, C(3',6')-H wag†.
13.	1098w	1101w	1097w		1066 1076		RIII: C(3',4')-H wag$^{\#}$ in-phase.
14.	1052w 1038w	1059w 1043w	1036w		1036 1021		RIII: Alkyl C-O str$^{\#}$ (C2'-O-CH_2-CH_3).
15.	992w	997w			982	985	RII: N4-C5-N6 bend.
16.	925w	930w	918w	916s	912	905	RIII: Terminal C-H wag$^{\#}$(C2'-O-CH_2-CH_3), Breathing, C6'-H wag† (out-of-plane).
17.	817w	819w	808w	811s	801	798	RII:Breathing. RIII: Terminal C-H wag(C2'-O-CH_2-CH_3), Breathing.
18.	739w	739w		732w	701	714	RI: Ring bend (out-of-plane). RII:N6-H wag$^{\#}$ (out-of-plane), Ring bend (out-of-plane).
19.	650w	652w	641w	649m	636	638	Ring breathing (RI, RII and RIII)
20.	565w	564w	546w		550	563	Ring dis (RI, RII and RIII)

The overall intensity of the SERS spectra, at 514 nm excitation, increased upon lowering the concentration of SC from 10^{-4} (fig. 5.14.d) to 10^{-6} M (fig. 5.14.f) which may be due to the monolayer coverage of SC on Ag NPs[310]. The above observation was quantified by comparing the observed intensities at 1226 and 1574 cm^{-1} in all the above SERS spectra (fig. 5.14.d, e and f) which is shown in fig. 5.15. Upon lowering the concentration of SC below 10^{-6} M led to observation of SERS spectra with lower intensity due to sub monolayer formation (10^{-7} M SC). The SERS spectrum of 10^{-6} M SC adsorbed on Ag NPs in presence of 0.03 M HCl, recorded at 514 nm excitation (fig. 5.14.f.) was found to match reasonably with the Raman spectrum of solid SC (fig. 5.14.g). Similarly, the SERS spectrum of SC (10^{-6} M) on Ag NPs recorded at 632 nm excitation (fig. 5.14.c) was expected to match well with the solid SC Raman spectrum, similar to that under 514 nm excitation. The intensities of the band at 1234 and 1580 cm^{-1} in the SERS spectra of the above system under 514 and 632 nm, were also compared (fig. 5.15.a).

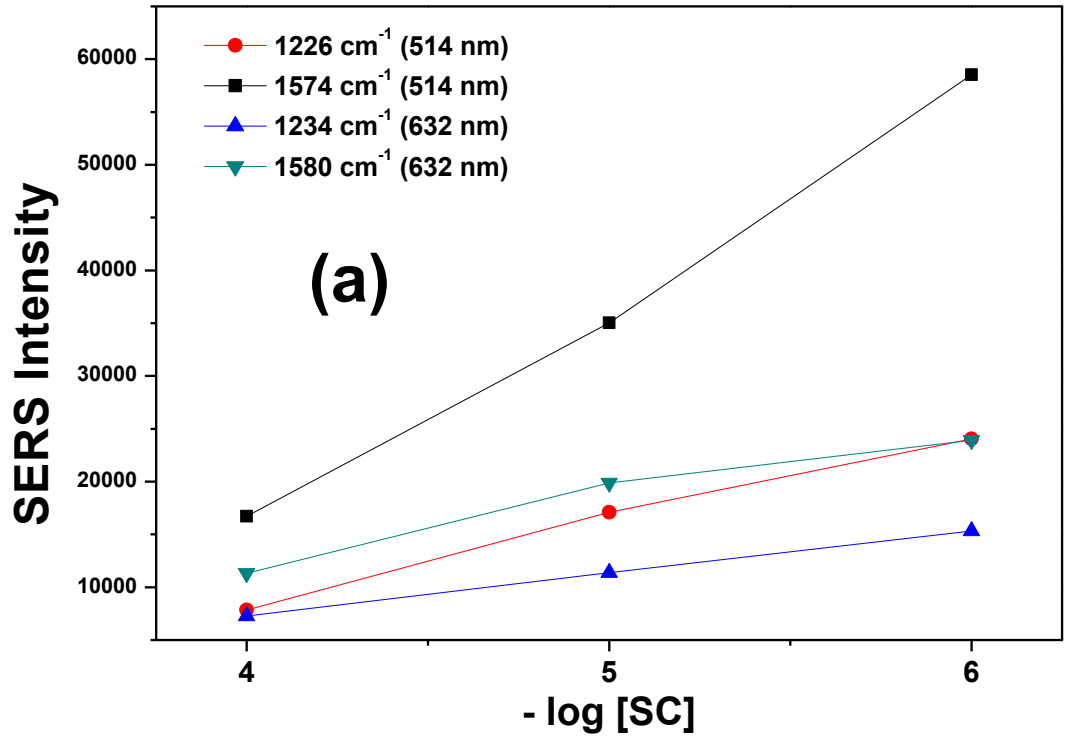
1226 cm-1 (514 nm)
1574 cm-1 (514 nm)
1234 cm-1 (632 nm)
1580 cm-1 (632 nm)
(a)
SERS Intensity
60000
50000
40000
30000
20000
10000
4
5
6
- log [SC]

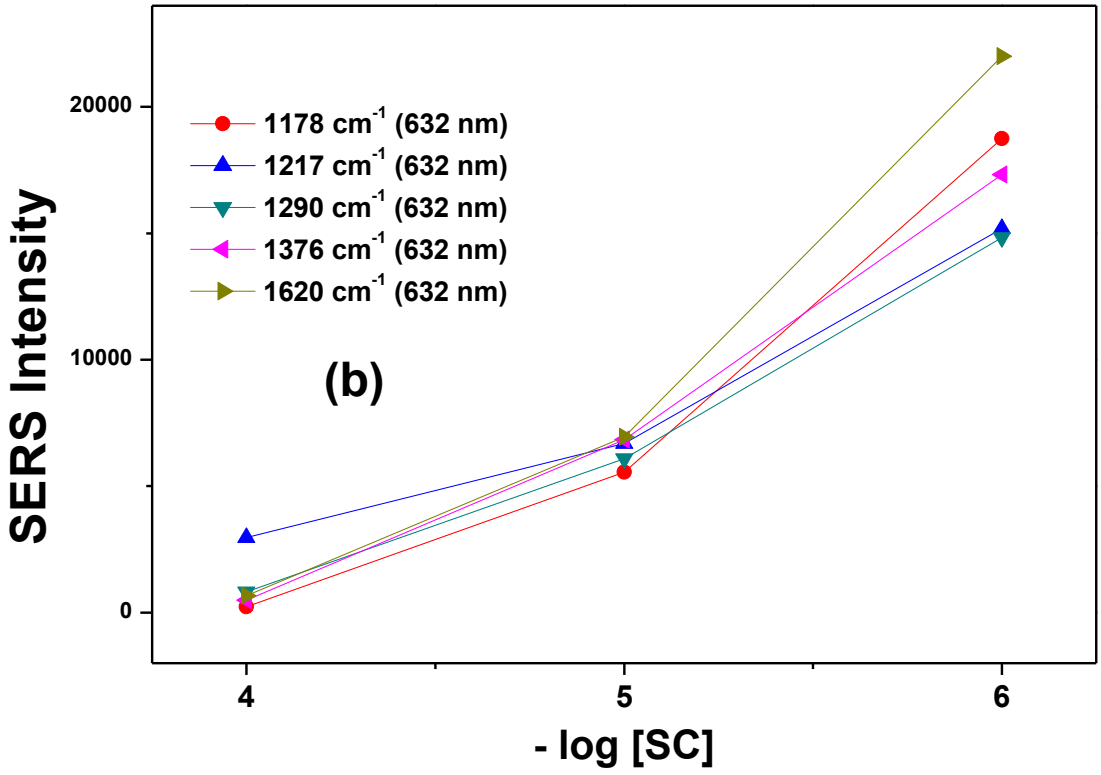
1178 cm-1 (632 nm)
1217 cm-1 (632 nm)
1290 cm-1 (632 nm)
1376 cm-1 (632 nm)
1620 cm-1 (632 nm)
(b)
SERS Intensity
20000
10000
0
4
5
6
- log [SC]

Figure 5.15. *(a) The intensity of SERS peaks at 1226 and 1574 cm^{-1} as shown in fig. 5(d-f) and that of peaks at 1234 and 1580 cm^{-1} as shown in fig. 5.14.(a-c).*

(b) SERS intensity of anomalous peaks at 1178, 1217, 1290, 1376 and 1620 cm^{-1} as shown in fig. 5.14.(a-c).

It was interesting to note that the Raman peaks of SC below 1000 cm^{-1}in fig. 5.14.c, which were very weak in case of solid SC (fig. 5.14.g) as well as in the SERS spectrum of 10^{-4} M SC (fig. 5.14.a), gained in intensity in comparison to the characteristic peak at 1578 cm^{-1}(table 5.2). The SERS peaks of high intensity at 1620, 1580, 1392, 1376, 1290, 1233, 1217, 1178, 916, 811, 530 and 442 cm^{-1} were observed in fig. 5.14.c. Bands at 1563, 1525, 649 and 420 cm^{-1} were found to be of medium intensity (fig. 5.14.c). The SERS bands of weak intensity were observed at 1442 and 732 cm^{-1} (fig. 5.14.c). The assignments of the SERS bands are listed in table 5.2. Some of the SERS bands, such as 1580, 1563, 1525, 1482, 1392, 1233, 1217,916, 811, 649, 530 cm^{-1} were observed in the case of solid (fig. 5.14.g) as well as for the SERS spectra of 10^{-5} and 10^{-6} M of SC on AgNPs at an excitation wavelength of 514 nm (fig. 5.14.e and f). Some additional Raman bands were observed in the case of SERS of 10^{-5} and 10^{-6} M SC on AgNPs with 632 nm excitation at 1620, 1376, 1290, 1217 and 1178 cm^{-1}. The intensity of the above bands was found to increase upon decreasing concentration of SC, which is shown in fig. 5.15.b. Coincidentally, the formation of AgCl/Ag NPD was observed at lower concentration of SC (vide supra) by TEM and SAED study. Moreover, few low energy bands were also observed in the range of 400 to 600 cm^{-1}, which were absent in the computed Raman spectrum of 6H-PPO form of SC (fig. 5.13.c). The assignment of the above additional bands was carried out after further investigations by other parallel experiments (vide infra). In order to rule out contributions from the laser intensity to the above observations, SERS spectra of 10^{-6} M SC on AgNPs in presence of 0.03 M HCl was carried out at varying laser intensity. There are reports of surface reactions

on silver electrodes at high laser power.[381] The above observations were found to be independent of any contributions from laser intensity. Again the contribution of laser energy was also validated by energy dependent SERS spectra. Thus, the SERS spectrum of 10^{-6} M SC on AgNPs, recorded at 785 nm excitation, was found to be similar to that at 514 nm excitation and dissimilar to that at 632 nm excitation. The observation was attributed to the energetical closeness of wavelength of excitation laser (632 nm) to the coupled plasmon in AgCl/Ag NPD as shown in fig. 5.9.d. Additionally, the incorporation of polarizer at parallel and perpendicular orientation with respect to the polarization of laser excitation source while recording the SERS spectra of 10^{-6} M SC on AgNPs both at 514 and 632 nm excitations, resulted in reduction of overall SERS intensity upon changing the polarization of the polarizer from parallel to perpendicular orientation. The above observation ruled out the effect of depolarization of surface enhanced Raman scattered photons[382] in the above system. Computed Raman spectra of Ag-SC complex which was discussed in section 5.2.4.3.d. is shown in fig. 5.16. The Raman spectrum of Ag-SC complex and SERS spectrum of 10^{-6} M SC on AgNPs excited at 632 nm did not match. Thus the possibility of charge transfer complex formation between AgNPs and SC is significantly reduced.

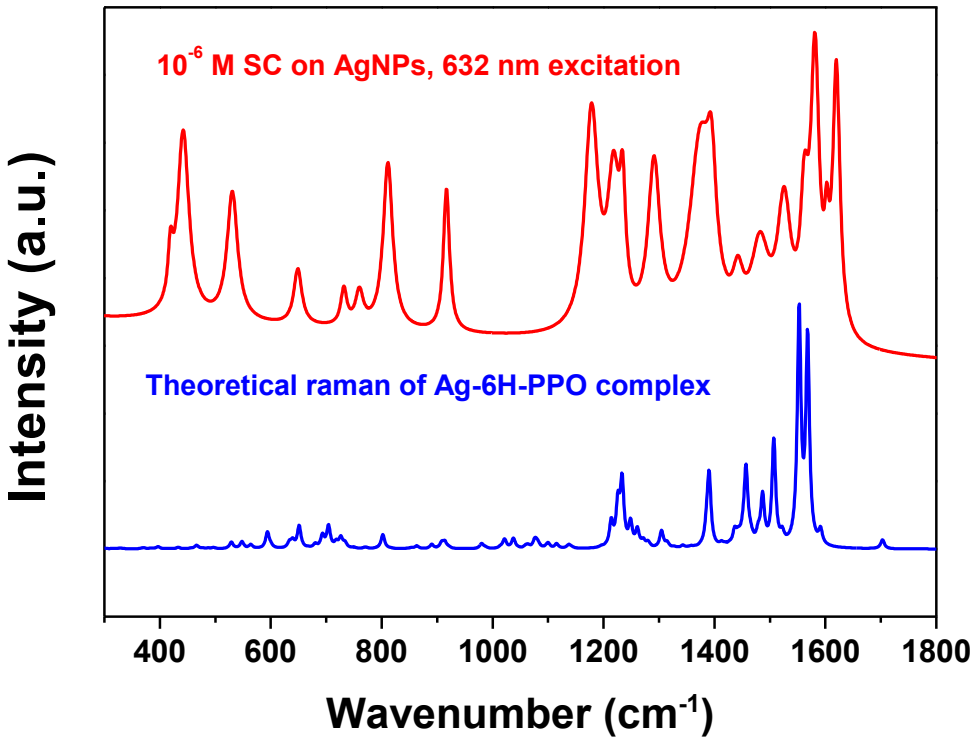

Figure 5.16. *A comparison of (a) SERS spectrum of 10^{-6} M SC on AgNPs, 0.03 M HCl excited at 632 nm and (b) theoretical Raman spectrum of Ag-6H-PPO complex.*

The observed new peak at 1620 cm^{-1}, as shown in fig.5.14.c, resembled the peak at 1595 cm^{-1} in case of theoretical Raman spectra of 4H-PPO, as shown in fig. 5.13.d. The above resemblance hinted towards the protonation of N-atom in ring II at 4^{th} position (fig. 5.12.b). This consolidated the consideration of prospect of possible reaction of SC on the surface of AgCl/Ag NPD. AgCl/AgNP nanocomposites are often reported to be used as photocatalyst where AgNPs would supply electrons to the conduction band of AgCl upon excitation at energies below band gap energy of AgCl[363], as per our earlier discussion in section 5.2.1. It is known that the LSPR of any material is decided by the bulk plasma frequency of the material[79], ω_{sp}, which is again dependent on the density of free electron, N. The bulk plasma frequency of any material is given by the following equation (5.6):

$$\omega_{sp} = \sqrt{\frac{Ne^2}{m_e \varepsilon_0 (\varepsilon_\infty + \kappa \varepsilon_m)}} \quad (5.6)$$

where, m_e is the rest mass of an electron, ε_0 is the permittivity in vacuum, ε_∞ is the dielectric constant of the metal, ε_m is the dielectric constant of the dispersing medium and κ is the shape factor of the particles. It is known fot spherical particles, the value of κ is 2. AgCl do not exhibit any LSPR band[383] due to defieciency of electrons in the conduction band. It has been reported that the UV-vis absorption spectra of Ag/AgCl nanocomposite is due LSPR of AgNPs[377]. Under visible light excitation, strong LSPR of AgNPs may create electron hole – pairs in adjacent AgCl-NP[363, 377]. This may result in observation of LSPR of AgCl- at a frequency lower than that of AgNPs, due to the fact that the electron density of free electron in conduction band of AgCl-NP is comparatively lower than that of Ag-NP. There is also a possibility of coupling of plasmons of AgNP and AgCl-NP in AgCl/Ag NPD (fig. 5.10.d) which may be polarized in a direction parallel to the principal axis of the NPD[351]. From the UV-vis absorption spectra of AgCl/Ag NPD (fig. 5.9.d), it was observed that the red-shifted coupled LSPR band appears at 605 nm (2.04 eV). Excitation of AgCl/Ag NPD at 632 nm (1.96 eV), led to creation of electron-hole pairs which would polarize the coupled surface plasmon. This polarized plasmon may possibly promote interfacial electron transfer from the surface of AgCl/Ag NPD to SC molecule for protonation of 6H-PPO at 4^{th} N-atom in ring II. Moreover, the enhancement of the vibrational modes below 1000 cm^{-1} in the SERS spectra (5.14.c) may be due to the electric field associated with electron-hole pair which is analogous to reported enhanced SERS spectrum in presence of external electric field[384]. A parallel experiment was carried out to study the electron transfer reaction of SC essentially to assign the unexplained peaks as observed in fig. 5.14.c. In a reported work, Stafford et al. has shown that TiO_2-assisted degradation of 4-chlorophenol involved direct electron transfer reactions whereas radiolytic degradation of the same involved hydroxyl radicals.[367] For the

above discussed aim, a pulse radiolysis study of aqueous solution of SC was carried out under reducing condition to understand the e_{aq}^-reactions associated with SC as per earlier discussion in section 5.2.2.

It is proposed based on earlier reports[385] that the SC molecule may react with e^-_{aq} in aqueous medium under reducing conditions to generate radicals at 5th and 7th position in ring II (fig. 5.12.b) along with fast protonation of nitrogen at 4th position and oxygen attached to 7th carbon of ring II, respectively. Similar, observations were made for guanine molecule which is structurally similar to SC.[385] Moreover, geometry optimizations by DFT for SC molecule also pointed towards the above discussed possibility by taking the Mulliken population of electrons[386] into consideration, which is shown in fig. 5.17.

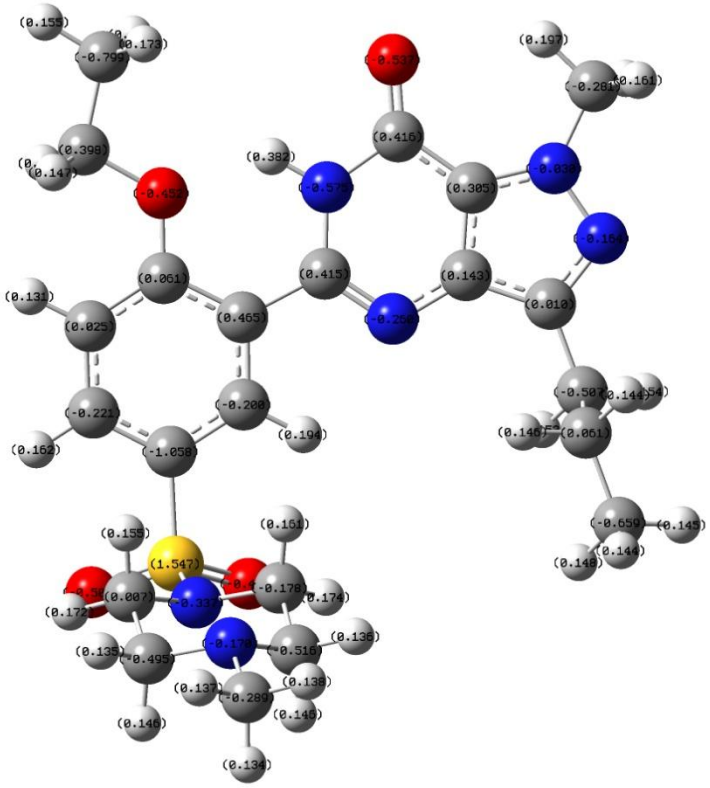

Figure 5.17. *Mulliken population analysis of electron on geometry optimized structure of6H-pyrazolo[4,3-d]pyrimidin-7-one(6H-PPO). Colour code of atoms: hydrogen (white),*

carbon (grey), nitrogen (blue), oxygen (red), and sulphur (yellow). Numbering of atoms is shown in fig. 5.12.

5.2.4.6. Pulse radiolysis of SC

An aqueous solution of SC of concentration 10^{-4} M was irradiated with 50 ns e^- pulse of average dose of 12 Gy per pulse at pH 7.2 under nitrogen atmosphere and in presence of 1 M t-BuOH. Primary free radical, $^{\bullet}OH$, formed due to radiolysis of water, is scavenged by t-BuOH (reaction 5.2). The transient absorption spectra of the free radical generated, under reducing conditions, as a result of the reaction of e^-_{aq} with SC is shown in fig. 5.18.a. The transient absorption spectra of 1 M t-BuOH solution at pH 7.2 (1 mM) under nitrogen atmosphere which serves as the background is shown in fig. 5.18.b. It was observed that two distinct peaks at 375 and 490 nm were formed at 15.2 μs after the 50 ns electron pulse. In fig. 5.18.b, the tail of the absorption peak of e_{aq}^- is observed as background at 1.12 μs and 1.44 μs. At 15.2 μs, the tail of absorption peak of e_{aq}^- disappeared suggesting complete consumption of e_{aq}^- either due to recombination with $H20^+$ or reaction with SC. The above observation conclusively indicated that the e_{aq}^- reacted with SC which led to the formation of a free radical with transient absorption band at 375 and 490 nm after 15.2 μs of the 50 ns electron pulse. The irradiation of aqueous solution of SC (10^{-4} M) with 50 ns e^- pulse of dose 12 Gy per pulse under reducing conditions and in presence 0.03 M HCl did not yield significant amount of free radical which is shown in fig. 5.18.c. It is known that e_{aq}^- is quenched by H^+ ion below pH 4.8 to form hydrogen radical. A comparison of the transient absorption spectra of SC (10^{-4} M) in 1 M t-BuOH under nitrogen atmosphere at pH 7.2 and 0.03 M HCl, indicated that the rate constant for bimolecular reaction between SC and hydrated electron is comparatively higher than that between SC and hydrogen radical, which means there is a high probability of reduction of SC by e_{aq}^- than by hydrogen radical. For the

sake of completion, the transient absorption spectrum of a solution of 1 M t-BuOH solution and 0.03 M HCl under nitrogen atmosphere was recorded as background (fig. 5.18.d).

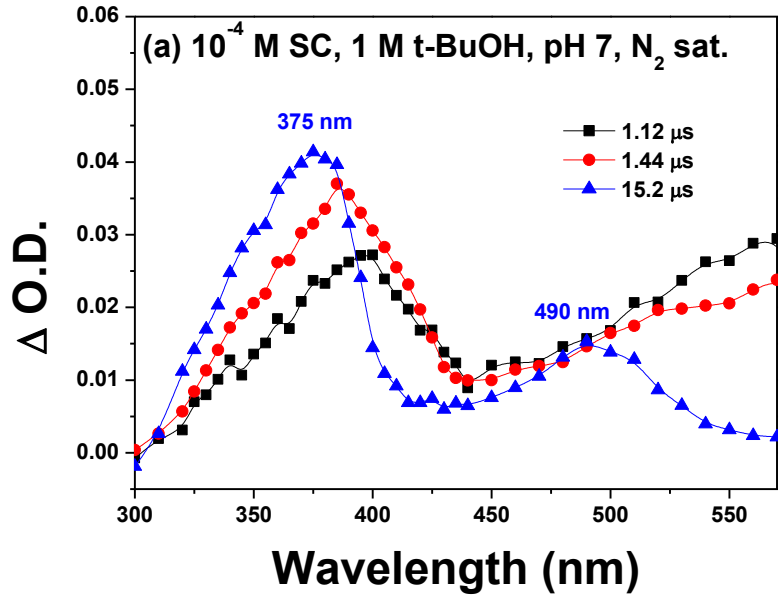

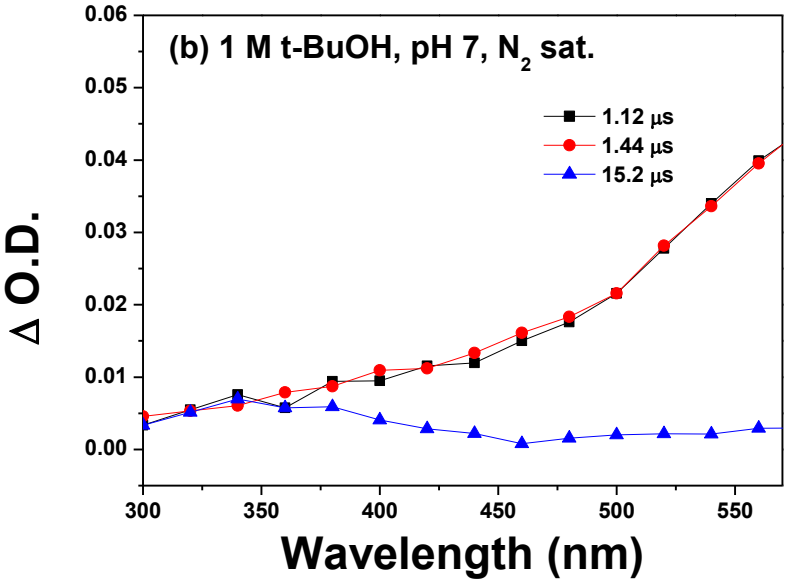

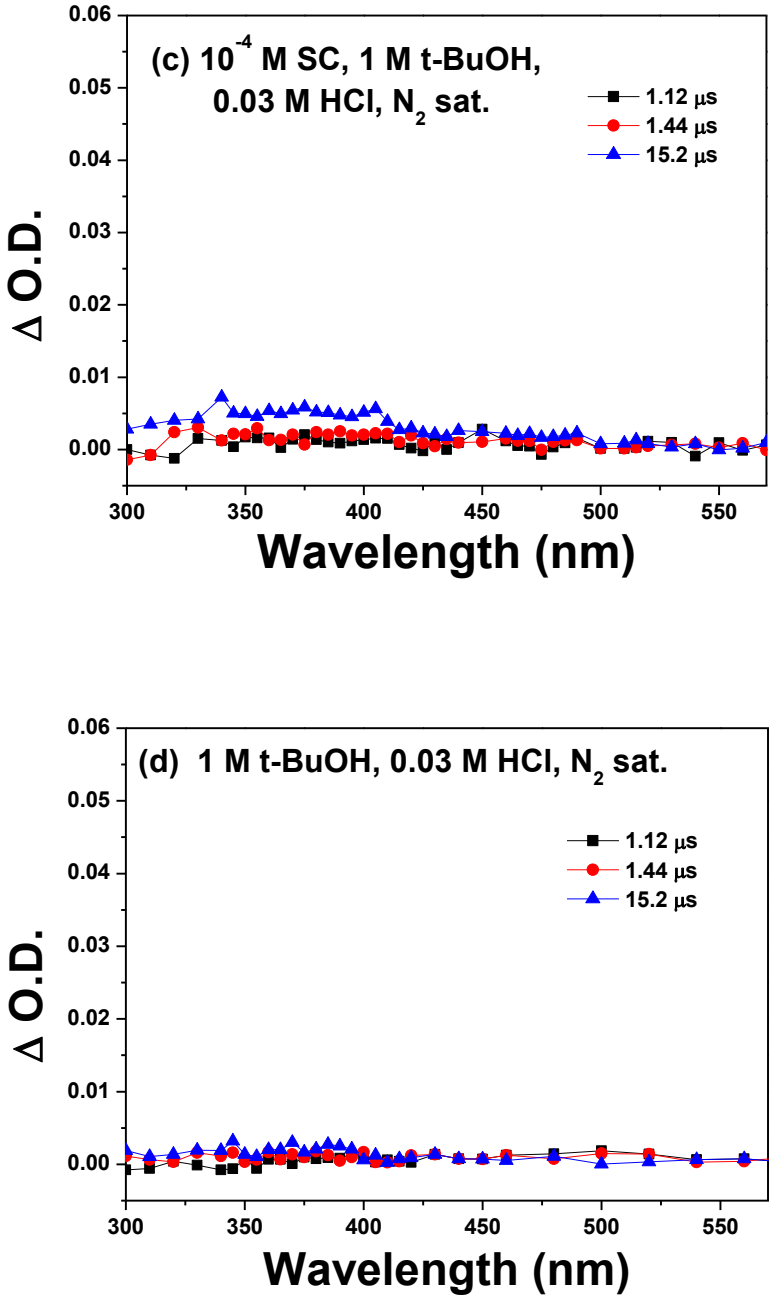

Figure 5.18. *Transient absorption spectra obtained in the pulse radiolysis of an N_2-purged solution of (a) SC ($1x10^{-4}$ M) in 1 M t-BuOH solution at pH 7.2 (1mM), (b) 1 M t-BuOH solution at pH 7.2 (1mM), (c) SC ($1x10^{-4}$ M) in 1 M t-BuOH solution in presence of 0.03 M HCl, and (d) 1 M t-BuOH solution in presence of 0.03 M HCl, 1.12 µs (■), 1.44 µs (•) and 15.2 µs (▲) after 50 ns electron pulse of dose 12 Gy per pulse.*

A schematic representation of the predicted free radicals formed as a result of the reaction of SC with e_{aq}^- is shown in scheme 5.2. Time dependent DFT (TD-DFT)[385] calculations were performed for the determination of the electronic transition as well as associated oscillator strengths in the generated free radicals shown in scheme 5.2. Moreover, the calculated transient absorption spectra of the free radicals formed due to the reaction of SC with e_{aq}^- under reducing conditions are shown in fig. 5.19. The radical A (fig. 5.19.a) was found to show reasonably good matching with the experimentally observed transient absorption spectra of the above reaction which is shown in fig. 5.18.a.

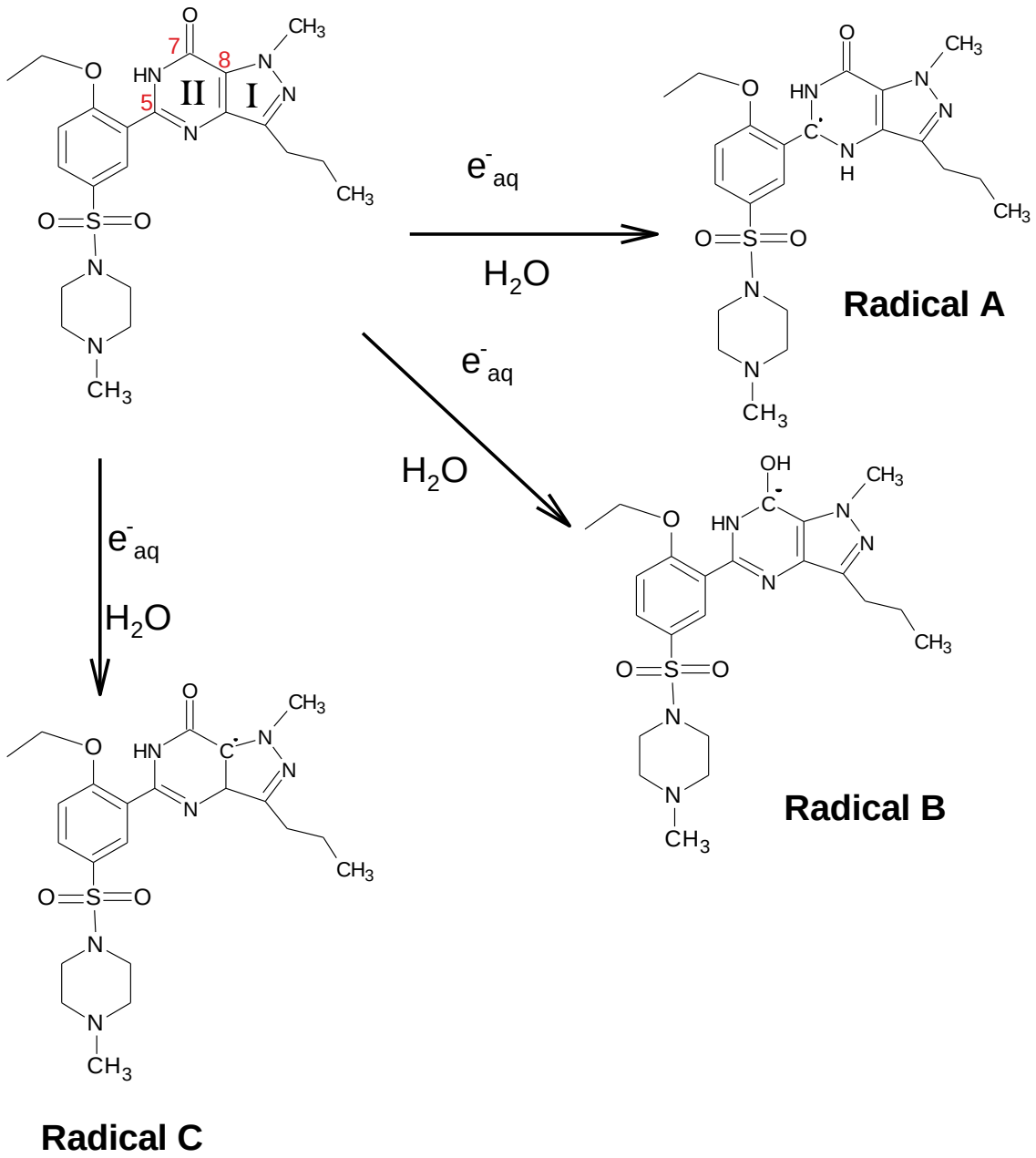

Scheme 5.2. *Probable reactions of e_{aq}^- with SC in presence of 1 M t-BuOH under nitrogen atmosphere.*

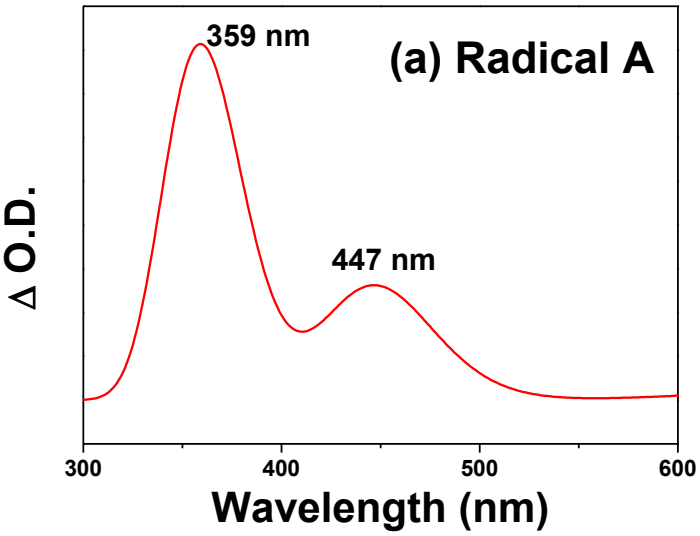
359 nm
(a) Radical A
447 nm
Δ O.D.
300
400
500
600
Wavelength (nm)

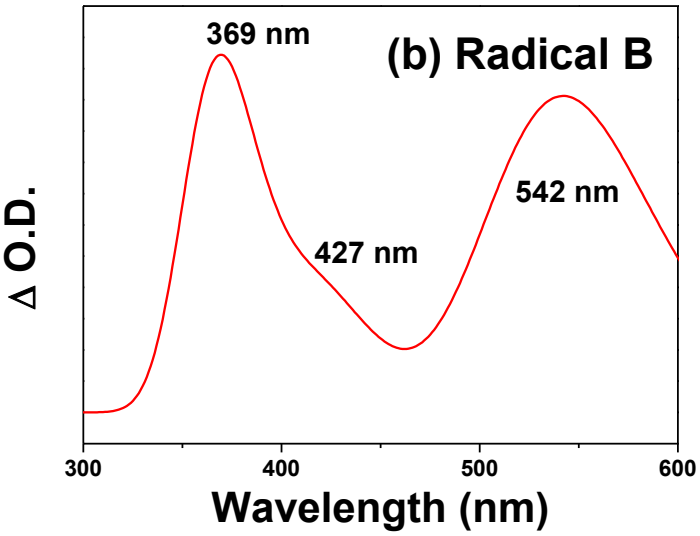
369 nm
(b) Radical B
542 nm
427 nm
Δ O.D.
300
400
500
600
Wavelength (nm)

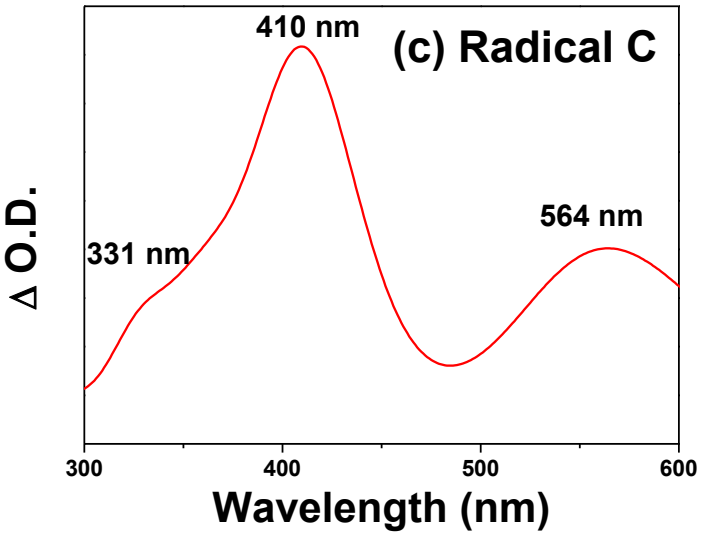

Figure 5.19. *A comparison of theoretical absorption spectra of (a) radical A, (b) radical B, and (c) radical C mentioned in scheme 5.2.*

A strong transition at ~359 nm and a weak transition at ~447 nm was observed in Radical A. The deviation in absorption maxima in calculated spectrum of Radical A from the experimental transient absorption of SC may be due to non consideration of H_20 molecules around the Radical A during computation, as it is know that the environment affects the calculated values. All the theoretical calculations were done in gas phase considering non-interaction of the subject molecule with any other molecule to reduce complexity of the calculations. It can be thus said that the reaction of SC with e_{aq}^- in aqueous medium forms a radical species (Radical A) with an unpaired electron at 5^{th} position of ring II of SC (scheme 5.2). Furthermore, the Radical A (fig. 5.18.a) showed 80% retention of absorptance over a period of 45 μs after the pulse (fig. 5.20). This reflects on the stability of radical formed by reaction of e_{aq}^- with SC, which is sufficient to show SERS signal when direct electron transfer reaction to SC occurs on the surface of AgCl/Ag NPDs.

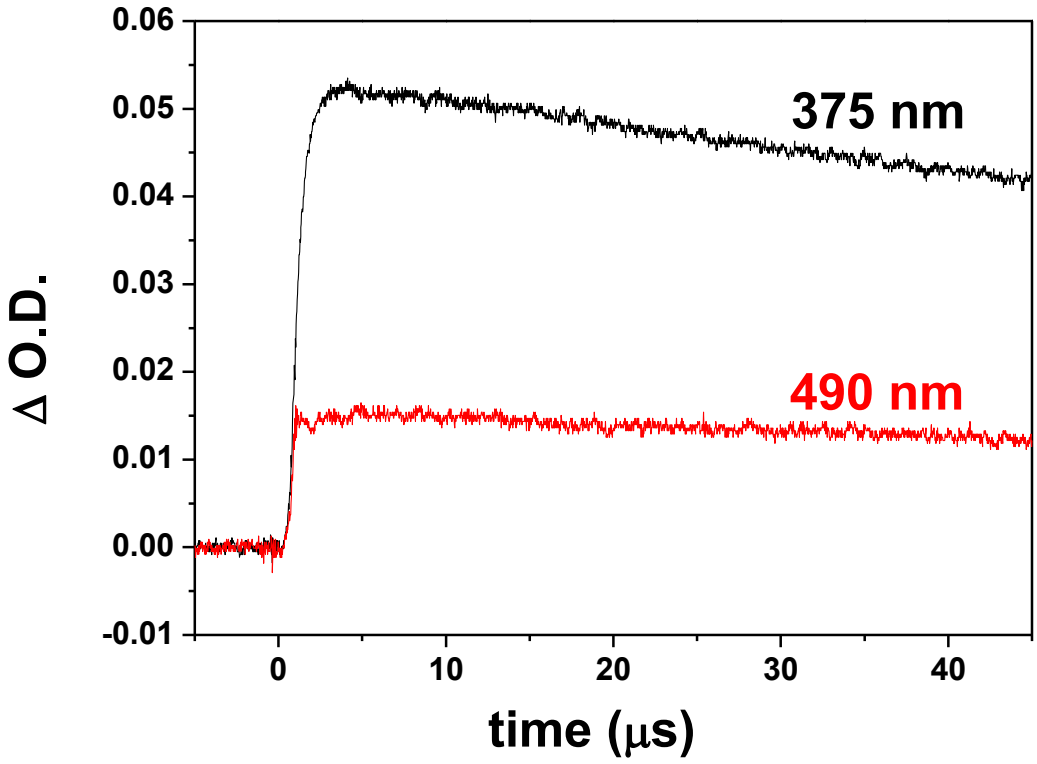

Figure 5.20. *Decay trace of N_2-purged solution of SC ($1x10^{-4}$ M) in 1 M t-BuOH solution at pH 7.2 (1mM) at 375 and 490 nm (see fig. 5.18.a) after 50 ns e^- pulse.*

In another parallel experiment, the $^{\bullet}OH$ and SC reaction was recorded at 350 nm (λ_{max}). It was observed that the transient free radical generated in the above case, showed 60% decay in 45 μs after the pulse (fig. 5.21). This negated the possibility of $^{\bullet}OH$ radical reaction of SC on the surface of AgCl/Ag NPD over e_{aq}^- reaction.

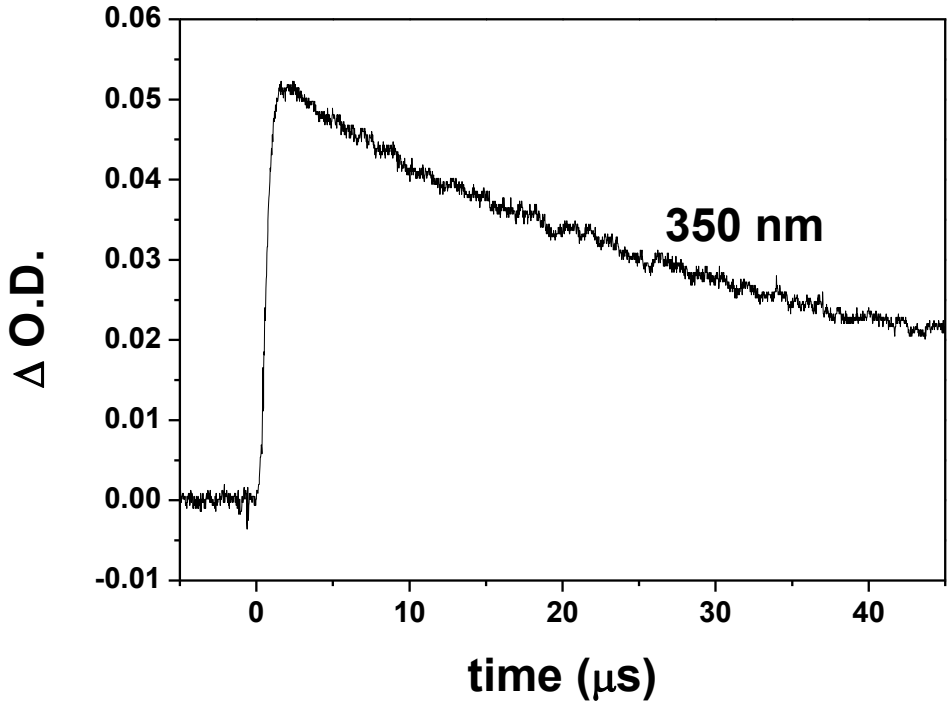

Figure 5.21. *Decay trace of N_2O-purged aqueous solution of SC ($1x10^{-4}$ M) at pH 7.2 (1mM) at 350 nm after 50 ns e^- pulse.*

Theoretically calculated Raman spectrum of radical A (fig. 5.22.a) and the SERS spectrum of 10^{-6} M SC on AgCl/Ag NPD in presence of 0.03 M HCl excited at 632 nm (fig. 5.22.b), showed reasonably good mutual correspondence. The unexplained peaks observed in fig. 5.14.c could be explained from the calculated Raman spectrum of radical A (fig. 5.22.a). The optimized geometry of Radical A suggest that the unexplained peaks observed in fig. 5.14.c such as 1620, 1376, 1290, 1217 and 1178 cm^{-1} corresponded to C5-C1' str, N4-H wag, N6-H wag, C2'-O str and N4-H wag with ring breathing modes, respectively. Thus, the appearance of the above bands is due to the unpaired electron generated at C5 position. Moreover, the band observed at 1620 and 1217 cm^{-1} appeared due to delocalization of electron in ring III. All the N-H wag modes were found to be associated with the adjacent unpaired electron on C5 atom. The exact match of SERS and theoretical Raman spectra was

not achieved due to insufficient information pertaining to the micro-environment of SC adsorbed on AgCl/Ag NPD.

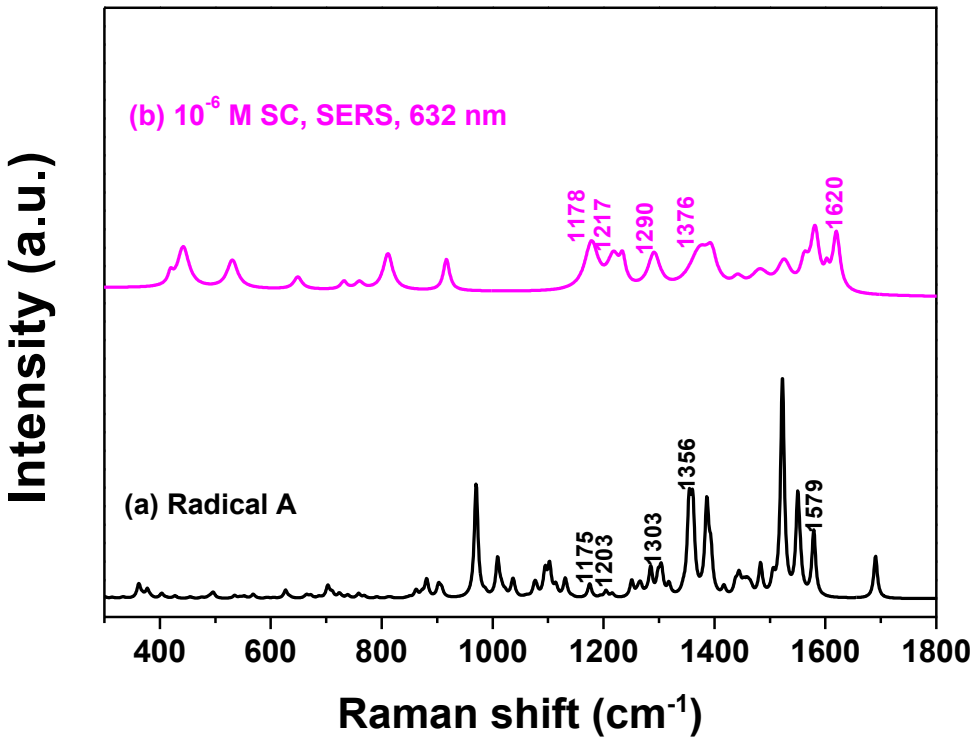

Figure 5.22. *A comparison of Raman/SERS spectra of (a) radical A (theoretical) and (b) 10^{-6} M SC adsorbed on AgCl/Ag NPD excited at 632 nm.*

The above discussion based on the reaction of SC with e_{aq}^- as shown in scheme 5.2, hinted towards a possibility of occurrence of direct electron transfer reaction on the surface of AgCl/Ag NPD to SC under excitation which is energetically closer to the coupled plasmon peak (fig. 5.9.d).

5.3. Conclusion

In this chapter, two types of AgNPs were synthesized, one by citrate method and the other by borohydride method. Citrate capped AgNPs were found to be receptive to addition of SC,

i.e., upon addition of SC to AgNPs at low pH (~ 2), SERS spectra of SC of high intensity were observed. In case of borohydride (actually borate) capped AgNPs, SC adsorbed on the surface of the nanoparticles only in presence of 0.03 M HCl. It was found that the adsorption of SC was facilitated by AgCl formed on AgNPs. Moreover, at low concentration of SC, AgCl/Ag NPD was formed leading to anomalous SERS spectra of SC, attributed to the formation of transient free radical of SC due to direct electron transfer from AgCl/Ag NPD surface to adsorbed SC molecules. The citrate capped AgNPs showed potential for future application in the quality control of SC in herbal drugs. A tentative methodoly for the same has been discussed in detail.

6

Study of interaction of plasmonic nanoparticles with biologically important molecules by surface enhanced Raman scattering

Two different application of noble metal nanoparticles associated with sensing of organic molecules is discussed in this chapter. Two molecules that have been used for SERS sensing are 2,5-Dimercapto-1,3,4-thiadiazole (DMTD) and Thioflavin T (ThT).

6.1. SERS study of 2,5-Dimercapto-1,3,4-thiadiazole (DMTD)

6.1.1. Background

Surface-enhanced Raman scattering (SERS) is a highly sensitive spectroscopic tool used to obtain enhanced Raman signal from Raman-active analytes which are adsorbed on the surface of specially prepared nanometer-sized metal particles.[387, 388]In SERS, the enhanced Raman signals are basically explained on the basis of two separate effects namely, the electromagnetic (EM)[389] effect and the chemical (CM)[390-392] or charge-transfer effect. Both EM and CM effect can occur simultaneously to give enhanced Raman signals. Recently, it has been reported that by using spacers or by increasing the chemical interaction between the adsorbed molecule and the surface of metal nanoparticle (NP), the chemically enhanced modes can be segregated from the electromagnetically enhanced modes in the SERS spectrum.[393] The SERS technique has been widely used for the purpose of identification of biomolecules, drugs and proteins as essential information about the interaction between analytes and the metal surface, can be extracted from SERS signal which is dependent on the nature of the binding sites and the orientation of the adsorbates on the metal surfaces.[238,

[309, 394-406] SERS has also been employed for studying surface-catalyzed oxidation processes[407, 408] and charge rearrangement reactions[409]taking place on the surface of the plasmonic NPs as they serve as an ideal substrate for the study of such interactions. As discussed in earlier chapters, silver (Ag) and gold (Au) nanoparticles have gained special attention due to their unique physicochemical properties, namely; (i) their surface plasmon resonance (SPR) band which lies in the visible region[410] of the electromagnetic spectrum and (ii) their large effective scattering cross section, enabling them to serve as ideal candidates for molecular labeling.[411]

In this chapter, we have discussed the work encompassing the detailed structural and conformational analysis for study of the different tautomeric forms of 2,5-Dimercapto-1,3,4-thiadiazole (DMTD) in solid state, aqueous solution and its binding affinity towards Ag and Au NPs by Raman spectroscopy and SERS in combination with density functional theoretical (DFT) calculations. DMTD which is popularly also known as Bismuth I and its derivatives have been extensively studied as chelating agents[412-416] due to their unique structure that contains both nitrogen and sulfur atoms. Apart from the chelating property, DMTD has been widely studied for applications in industry as additives in motor oils for antioxidation,[417] anticorrosion,[418, 419]and antifrictionproperties,[420-422] as metal deactivators[423, 424]and also as polymercross-linkers.[425, 426]Though DMDT has been used extensively as surface-active agents, its surface chemistry is not very well explained[427-429] and relatively few studies have successfully characterized DMTD.[415, 430-440] DMTD consists of four potential electron donor sites which are available for its adsorption on the surface of metal NPs. DMDT can function as a bidentate ligand with (a) both the thiadiazole ring nitrogen atoms, (b) the ring sulphur atom, (c) both the thiocarbonyl sulphur atoms, or (d) one nitrogen atom and one sulphur atom on either the same side or different sides of the molecule. In addition, there is also a possibility that the delocalized π-electrons in the

heterocyclic ring can also bind to the Ag and Au NP surfaces. Various studies have been carried out in the past by different groups to ascertain the most stable ground state tautomer of DMDT. The study of IR, UV and pKa measurements of DMDT suggests that the thione-thiol tautomer to be the most prevalent[436] whereas, the ^{15}NNMR study[434]indicates that the dithiol tautomers as the most stable. Again, the FT-IR and FT-Raman studies on DMTD indicated the dominance of the dithiol form in the solid state.[436]

In this work, a detailed study has been done for the following two objectives:

(i) Identifcation of most stable ground state tautomer of DMTD in solid and in aqueous solution; and

(ii) Determination of conformation and orientation of DMDT on the surface of plasmonic NPs using SERS in combination with DFT calculations (B3LYP functional with 6-31+G*, aug-cc-pvdz and LANL2DZ basis sets).

In this work it was observed that the different tautomeric forms of DMTD as well as their neutral Ag, Au, Ag4 and Au4 complexes, a selective binding between DMDT and surface of metal nanoparticles takes place. DMDT tends to bind to Ag via the ring N atom whereas it binds to Au exclusively through the thiocarbonyl S atoms. The tautomeric forms were found to be strongly dependent on the pH of the medium.

6.1.2. Experimental Section

6.1.2.1. Chemicals used

2,5-Dimercapto-1,3,4-thiadiazole (DMTD), hydrogen tetrachloroaurate, AgNO3, trisodium citrate and sodium borohydride, used for the preparation of colloidal Au and Ag NPs were from Aldrich chemicals, and S. D. fine chemicals, India. All the experiments were performed with Millipore water having resistivity of 18.2 MΩ·cm at 25 °C.

6.1.2.2. Synthetic procedure of silver and gold NPs

AgNPs solution was prepared by the chemical reduction of silver nitrate with sodium borohydride using method reported by Creighton et. al..[441] 10 ml of 1 mM $AgNO_3$ solution was added to 30 ml of 2 mM ice-cold $NaBH_4$drop wise with slow stirring. The reaction mixture was allowed to reach room temperature while stirring. The colour of solution changed from colourless to yellow. The pH of the solution was found to be ~ 9. The solution was kept overnight foruse in further experiments.

Gold nanoparticles (GNPs) solution was synthesized by modified Turkevich method.[300] 100 ml of 10^{-4} M $HAuCl_4.3H_2O$ solution was heated till boiling, followed by addition of 3 ml of 1% sodium citrate solution to the boiling solution. Boiling was continued for another 15 min till the colour of the solution turned bright red. The solution was then cooled down to room temperature before use in further experiments. The pH of the GNPs solution was found to be ~ 6.5. The above AgNP and GNP solution were used as substrate to study DMDT by SERS.

6.1.2.3. Instrumentation details

UV-Vis absorption, transmission electron microscopic (TEM) and Raman techniques were used to characterize Ag as well as Au NPs in presence and absence of DMDT. The UV-Vis absorption spectra were recorded using a Jasco V-650 spectrophotometer. For TEM measurements, the sample was prepared by adding one drop of sample solution onto a carbon-coated copper grid. The evaporation of the solvent leaves the NP on the surface and TEM measurements were carried out with JEM Model CM (200kV), Philips. The Raman spectra of DMTD in solid state, aqueous solution and adsorbed over Ag NPs were recorded at room temperature using the 532 nm line, from a diode-pumped solid state (DPSS) Nd^{3+}:YAG laser (Cobolt Samba 0532-01-0500 -500) M/s Cobolt AB, Sweden. The SERS

measurements of DMTD functionalized Au NPs were recorded using the 660 nm line from a DPSS laser (Ignis 660-500) M/s Laser Quantum Ltd. England. The laser power used to record the Raman spectrum was 25 mW and the spot size on the sample was ~ 50 μm. For all the Raman and SERS measurements, the sample solution was taken in a standard 1 x 1 cm^2 cuvette and the Raman scattered light was collected at 90° scattering geometry and detected using a charge-coupled device (CCD, Synapse, Horiba Jobin Yvon) based monochromator (Triax550, Horiba Jobin Yvon, France) together with edge filters for 532 and 664 nm, covering a spectral range of 200-1600 cm^{-1}. The Raman spectrum of indene was used to calibrate the spectrometer, and the accuracy of the spectral measurement was estimated to be better than 1 cm^{-1}.

6.1.3. Computational methods

Computational methods provide an insight into the structural details of any molecule. When a simulated molecule is subjected to *ab initio* quantum mechanical calculation under simulated experimental conditions, the optimized geometries of the most stable ground state structure as well as its other stable conformers is obtained. A study of vibrations associated with the conformers of the molecules can aid in construction of a simulated Raman spectra which is subsequently matched with the experimental Raman or SERS spectra to draw inference.

The geometry optimization was performed for various tautomeric forms of DMTD, its mono-anionic forms, its di-anionic form and their neutral Ag, Au, Ag4 and Au4 complexes using DFT [Gaussian 03 program[442]] with B3LYP functional[443] and 6-311+G* or aug-cc-pVDZ basis set for DMTD. For Ag and Au, LANL2DZ basis set was used. DMTD exists in three possible tautomeric forms, dithiol, thione-thiol and dithione as shown in scheme 6.1. Geometry optimization was carried out for all the three tautomeric forms of DMTD.

Theoretical Raman spectra as obtained from computed vibrational frequencies at the optimized geometry of the tautomers were compared with the experimental Raman spectra of DMDT at solid state as well as in solution under neutral and acidic conditions. Geometry optimization was also performed for the thiol-thiolate, thione-thiolate and the dithiolate forms of DMTD (Scheme 1).

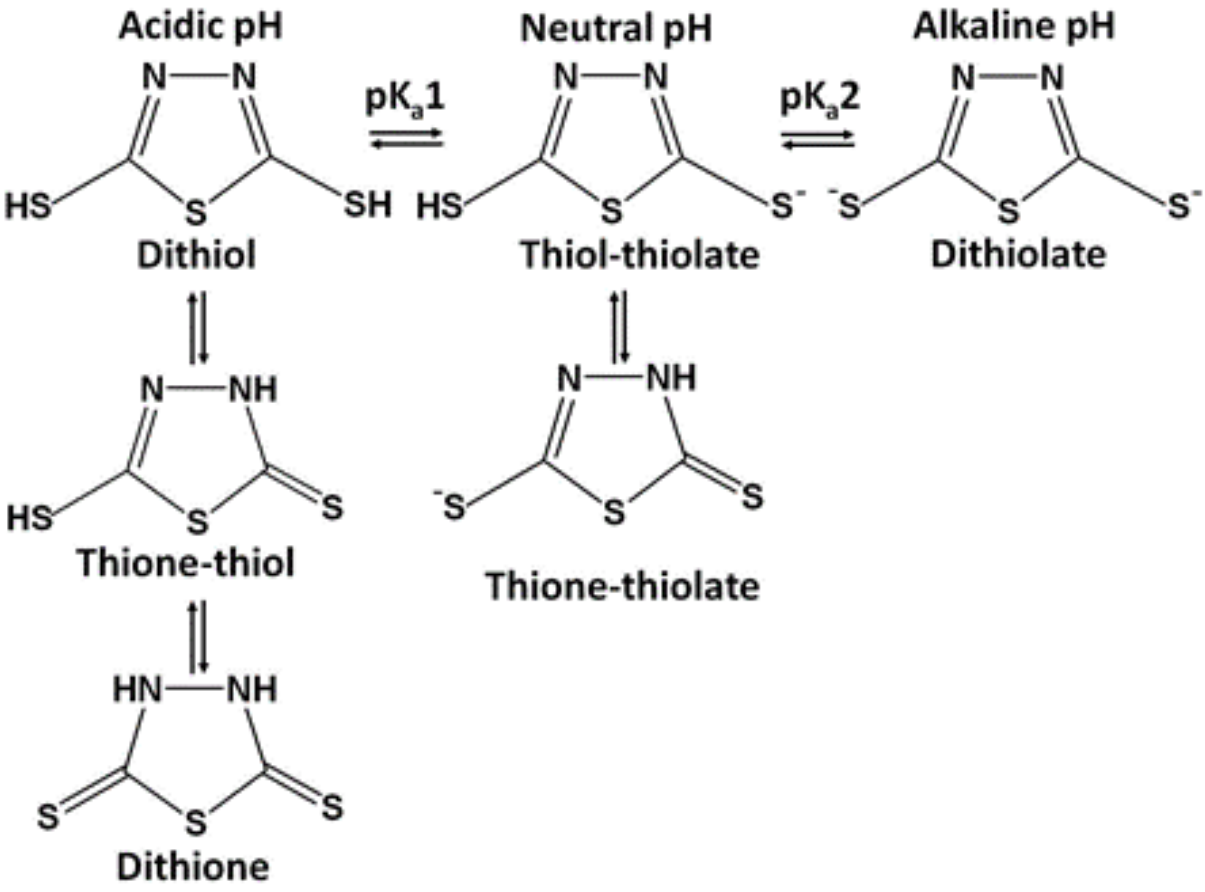

Scheme 6.1. *Scheme showing the proton dissociation equilibria of DMTD.*

No symmetry restriction was applied during geometry optimization. The theoretical Raman spectra computed using the predicted vibrational frequencies for the thiol-thiolate, thione-thiolate and dithiolate forms of DMTD were computed such that their energies correspond to a local minimum on the potential energy surface and not to saddle points. Geometry optimization was also carried out for the various possible neutral Ag, Au, Ag_4 and Au_4

complexes of DMTD. Ag_4 and Au_4 clusters were selected in order to justify the binding of DMDT to the surface of Ag or Au nanoparticle and not just to a single Ag or Au atom. The computed spectra of DMDT complexes at the optimized geometry were compared with the experimentally observed SERS spectrum.

6.1.4. Result and Discussions

6.1.4.1. UV-visible absorption study

As discussed in earlier chapters, UV-visible absorption spectra of metal NPs are related to their LSRP band,[444] whose peak maxima depends strongly on the extent of aggregation of the NPs. The size and shape of the NPs as well as the dielectric constant of the medium and the surface-adsorbed species determines the position and shape of the LSPR band. The UV-vis absorption spectra of bare Ag NPs and with varying concentrations of DMTD were recorded. Bare Ag NPs showed a single absorption peak centred at 389 nm due to the LSPR band, as shown in fig. 6.1.a. The absorption spectra of DMTD adsorbed on Ag NPs at concentrations 1, 5, 10, 50 and 100 µM, are shown in fig.6.1.a. It was observed that upon addition of 1 µM DMTD to AgNPs solution, the absorbance at 389 nm is reduced. This can be attributed to increased plasmon coupling of AgNPs aggregates.[445, 446]Upon increasing the concentration of DMTD progressively, as shown in fig. 6.1.a., the colour of the Ag NPs changed from yellow to dark brown due to adsorption of DMTD on the Ag NP surface and the red-shifted bands appeared at 432, 465, 481 and 501 nm for DMDT concentration corresponding to 5, 10, 50 and 100 µM, respectively. UV-vis absorption spectra for the bare Au NPs and DMTD (100 µM) adsorbed on Au NPs is shown in fig. 6.1.b.Bare Au NPs (bright red) show a sharp LSPR band at 519 nm. Upon addition of 100 µM DMTD to the stable bare Au NPs, a change in colour from bright red to purple along with a reduction in the absorbance at 519 nm and appearance of a broad peak with maximum at 710 nm is

observed. The red-shifted peak at 710 nm can be attributed to plasmon coupling. UV-vis absorption spectrum of 100 µM aqueous solution of DMTD as shown in fig. 6.1.b., show a strong band with at λ_{max} ~ 328 nm (π-π* transition) along with a weak broad peak at λ_{max} ~ 473 nm (n-π* transition).

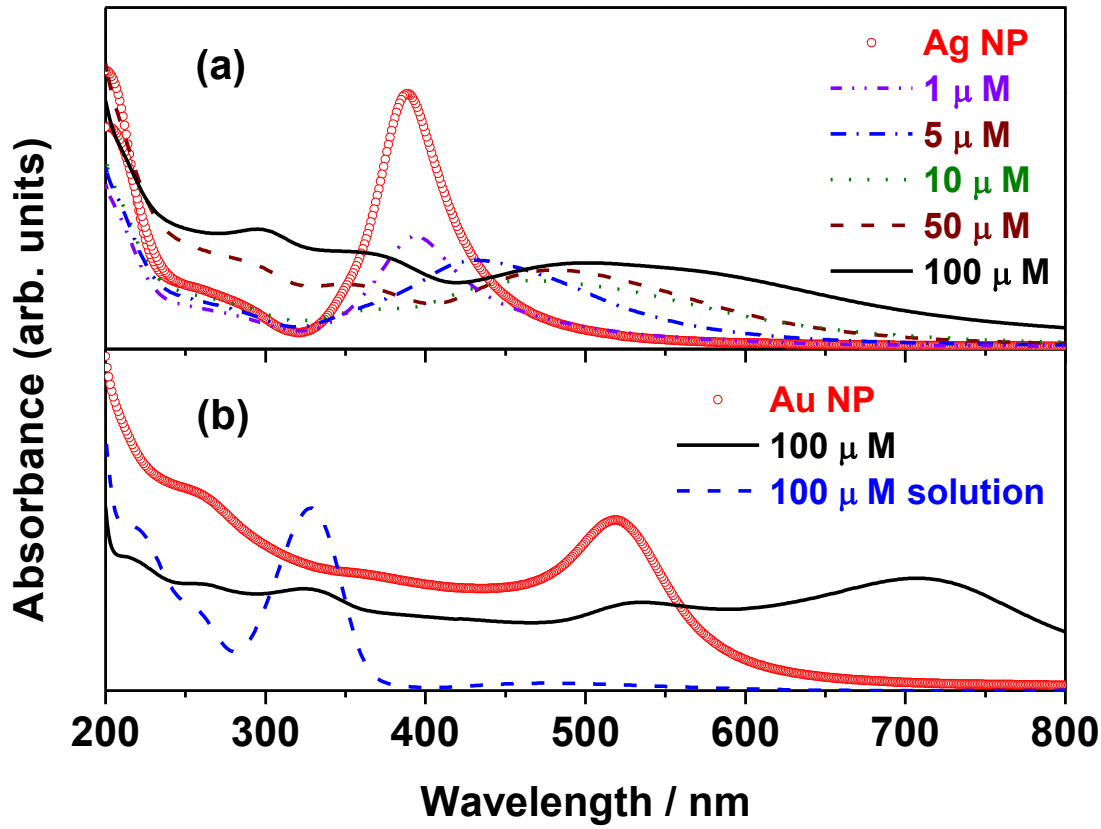

Figure 6.1. *Surface plasmon resonance (SPR) bands of (a) Ag NPs and DMTD (1-100 µM) functionalized Ag NPs. (b) Au NPs, surface modified Au NPs with DMTD (100 µM) and 100 µM DMTD solution.*

6.1.4.2. TEM measurements

TEM analysis was performed to characterize the shape and size of bare nanoparticles as well as GNPs and AgNPs in presence of DMDT. Borohydride reduced Ag NPs were found to be of size 15-20 nm particles with high monodispersity which is shown in fig. 6.2.a. In presence of 100 µM DMTD, Ag NPs were found to be aggregated, as shown in fig. 6.2.b., which confirms the observation in fig. 6.1.a. It is clearfrom the above that adsorption of DMTD and subsequent interparticle interaction facilitates the aggregation of Ag NPs. There was a slight increase in the average size of the particles with retention of spherical shape. Associated photographs representative of the observed color changes are also shown in fig. 6.2.a and b. The colour of the Ag NPs solution was found to change from yellow to dark brown upon the addition of DMTD. Similar observations were noted in case of GNPs. Citrate reduced GNPs were found as monodispersed spherical nanoparticles with average size 20-25 nm, as shown in fig. 6.2.c. In this case also addition of DMDT was found to induce aggregation of GNPs, which is evident from fig. 6.2.d. The average size of the aggregated GNPs was found to be 35 nm with retention of spherical shape. The photographic images of associated colour change from dark red to purple upon aggregation, in GNPs, is also shown in the above figure.

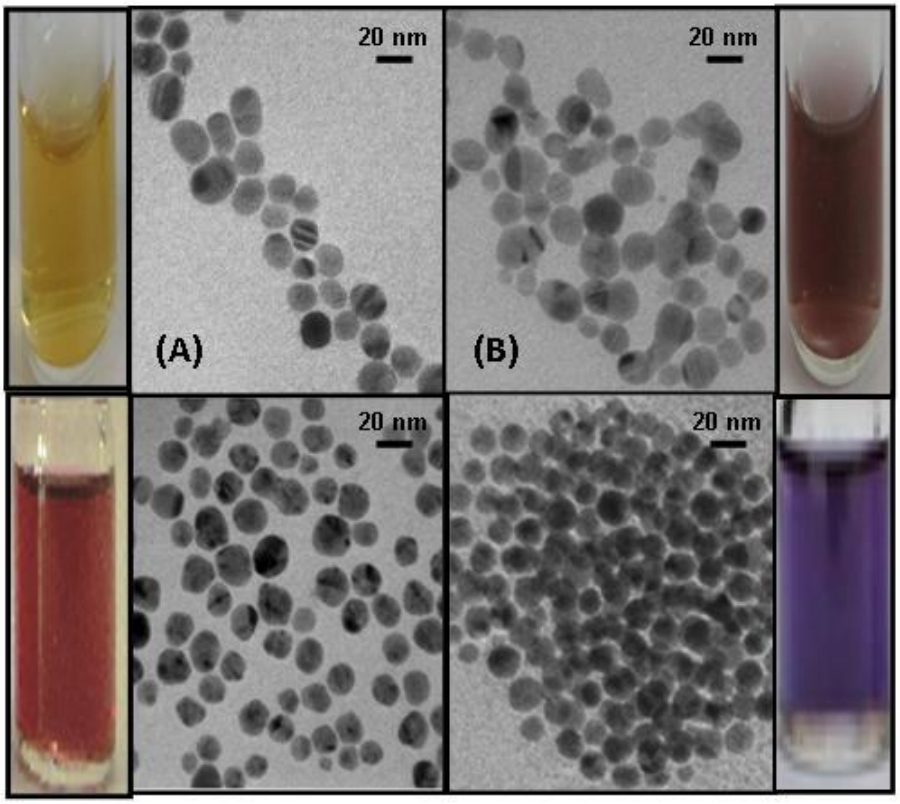

Figure 6.2. *TEM image of (A) Ag NPs, (B) DMTD functionalized Ag NPs, (C) Au NPs and (D) DMTD functionalized Au NPs. On the sides of the figures are shown the colours of the bare and aggregated NPs.*

6.1.4.3. Computational Results

Thetautomersof DMDT, namely, dithiol, thione-thiol and dithione as well as mono-anionic and di-anionic forms of DMDT were geometry optimized using B3LYP functional with 6-311+G* and aug-cc-pvdz basis sets. The optimized structures of dithiol, thione-thiol and dithione forms of DMTD are shown in fig. 6.3.(a), (b) and (c). The relative stability of the different tautomers of the molecule in the gas phase was obtained upon comparison of the minimum energies at their respective optimized geometries. The thione-thiol form was found to be the lowest upon comparison of the relative computed energies of the neutral tautomersof DMDT, which directly indicates that this is the most stable tautomer. The

dithione and dithiol forms were found to be less stable in energy in comparison with the thione-thiol tautomer by 5.49 and 8.48 kcal mol^{-1}, respectively. Thus, the dithiol form DMDT was found to be the least stable among the above neutral conformers. The monovalent ionic forms of DMTD such as thiol-thiolate and thione-thiolate were optimized as above. The optimized structure of mono-anionic forms of DMDT is shown in fig. 6.3. (d) and (e).Again, the optimized structure of di-anionic tautomer of DMTD, dithiolate is shown in fig. 6.3 (f). The computed energies thus obtained after geometry optimization indicates that the thione-thiolate form is more stable than the thiol-thiolate tautomer by 14.94 kcal mol^{-1} and the dithiolate form has the highest energy and is the least stable tautomer. The tautomeric forms of DMTD are in the following order of stability in the gas phase: thione-thiol (0 kcal mol^{-1}) >dithione (5.49 kcal mol^{-1}) > dithiol (8.48 kcal mol^{-1}) >thione-thiolate (310.11 kcal mol^{-1}) > thiol-thiolate (325.05 kcal mol^{-1}) >dithiolate (724.22 kcal mol^{-1}). The experimental Raman spectra of DMDT in solid state and aqueous solution under different pH as well as the SERS spectra of complexes of DMDT with GNPs and AgNPs were compared with the computed Raman spectra for interpretation and analysis in this work.

(A)

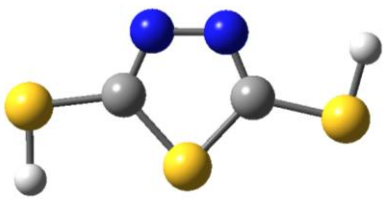

(D)

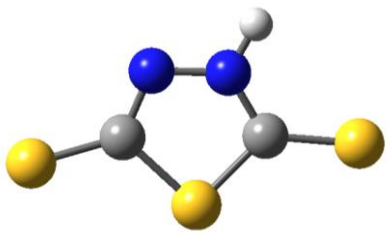

(B)

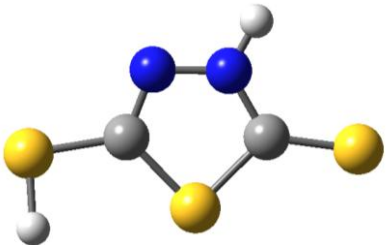

(E)

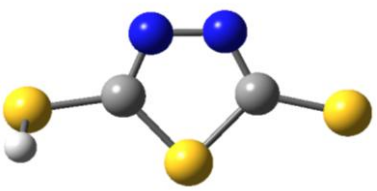

(C) **(F)**

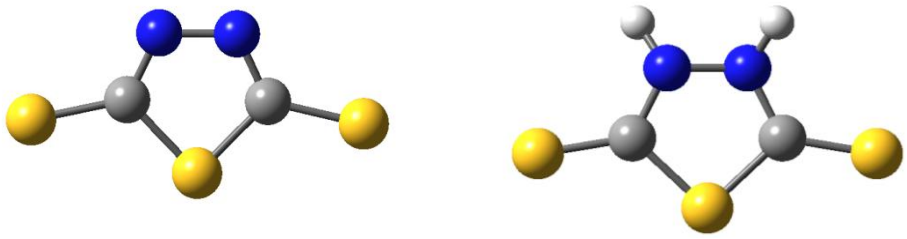

Figure 6.3. *Optimized structures of (A) dithiol, (B) thione-thiol, (C) dithione, (D) thione-thiolate, (E) thiol-thiolate and (F) dithiolate forms. The colour codes used to identify the atoms are N (blue), S (yellow), C (grey) and H (white).*

The acid dissociation constants or pK_a values of DMTD are reported to be 1.4 and 7.4[447] (2.1 and 7.5)[448], indicating that its neutral form (dithiol, thione-thiol and dithione) is a strong acid whereas its monoanionic form (thione-thiolate and thiol-thiolate) is a weak acid. Thus, under acidic conditions, i.e., below pH 1.5, DMTD exists mainly in the neutral form as dithiol, thione-thiol or dithone whereas, at pH ~ 8, it remains as dithiolate. In the intermediate pH range i.e. between pH 2 to 8, DMTD exists mainly in the mono-anionic form, viz. thione-thiolate or thiol-thiolate. In this work, the pH of the aqueous solution was varied to identity the features arising in the experimental Raman spectra due to the neutral, monoanionic or dianionic forms of DMTD. Similarly, the extent of adsorption, orientation as well as conformation of the adsorbed DMDT molecule in its neutral (dithiol, thione-thiol, dithione), monoanionic (thione-thiolate and thiol-thiolate) or dianionic (dithiolate) forms was monitored at pH 1.5 and pH 7 on the Ag and Au NP surfaces.

Again for the DMTD-Ag and DMTD-Au complexes as discussed earlier, various conformations are possible. The dithiol and thione-thiol tautomers of DMTDcan potentially bind to AgNPs or GNPs surfaces through the ring N atoms, ring S atom, the thiocarbonyl S atom or the π electrons of the thiadiazole ring. Likewise, the dithione form can also bind to AgNPs or GNPs through the ring S atom, the thiocarbonyl S atom and the π electrons of the

thiadiazole ring. B3LYP functional with aug-cc-pvdz (for DMTD) and LANL2DZ (for Ag and Au) basis sets were used for simulation of the optimized structure of various Ag, Au, Ag_4 and Au_4 complexes of dithiol, thione-thiol as well as dithione. The optimized structures of the neutral dithiol-Ag, thione-thiol-Ag and dithione-Ag complexes are shown in fig. 6.4.(a-i).

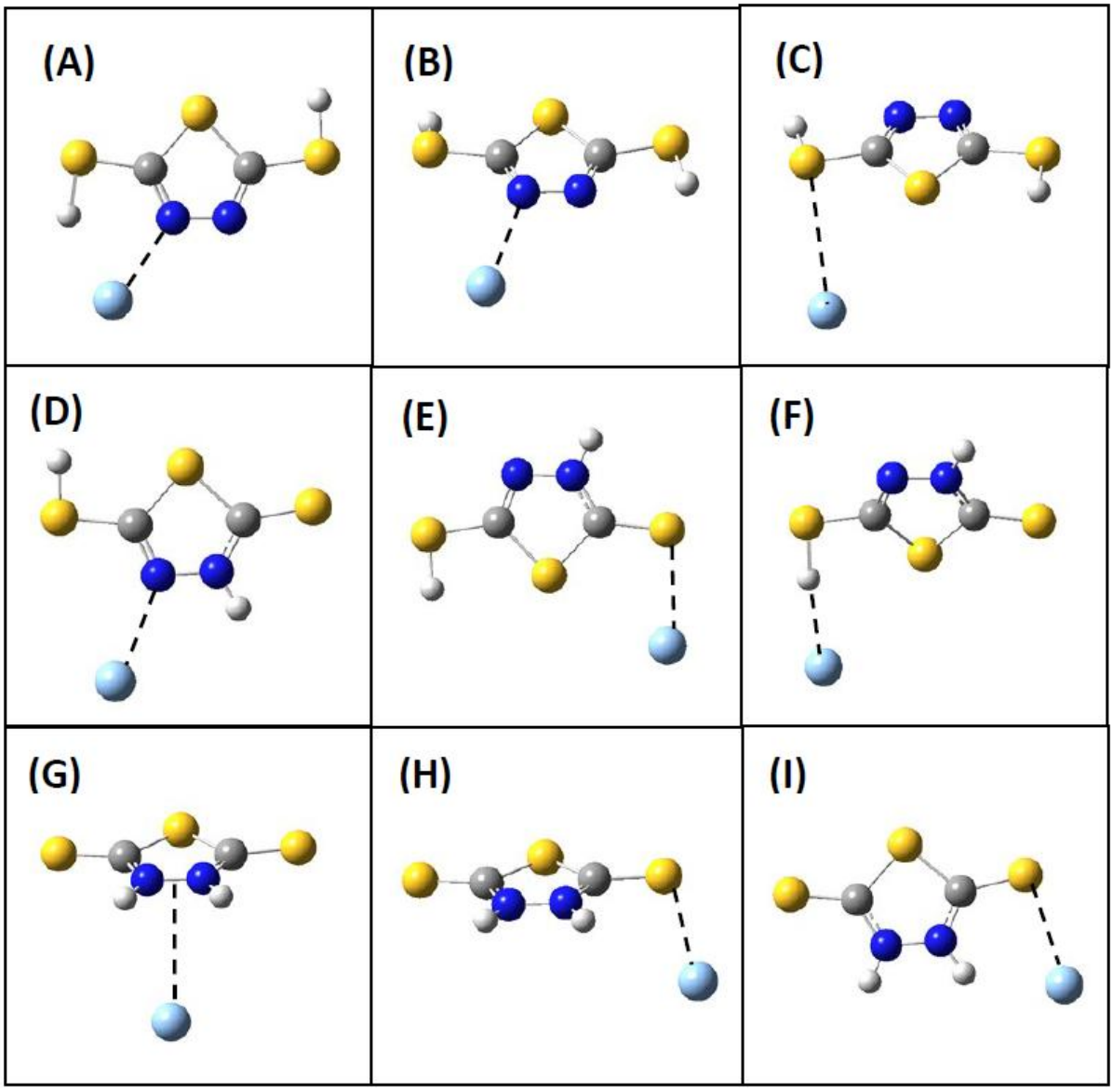

Figure 6.4. *Optimized structures of three possible dithiol-Ag complexes (a) bound through ring N (S-H pointing towards Ag), (b) bound through ring N (S-H pointing away from Ag), (c) bound through thiol S; three possible thione-thiol-Ag complexes (d) bound*

through ring N, (e) bound through thione S, (f) bound through thiol S-H and three possible dithione-Ag complexes g) bound through ring N-N bond, (h) bound through thione S-S (Ag out of plane with dithione) and (i) bound through thione S (Ag in plane with dithione).

The theoretical Raman spectra of the various possible Ag and Ag_4 complexes of DMDT were compared with the experimental SERS spectrum of DMDT on AgNPs at acidic pH. The molecular structures were also geometry optimized for the mono and divalent ionic forms of DMTD-Ag and DMTD-Ag_4 complexes i.e. thione-thiolate-Ag, thiol-thiolate-Ag, dithiolate-Ag, thione-thiolate-Ag_4, thiol-thiolate-Ag_4 and dithiolate-Ag_4 complexes. The optimized structures of the thione-thiolate-Ag, thiol-thiolate-Ag and dithiolate-Ag complexes are shown in fig. 6.5. (a-i).

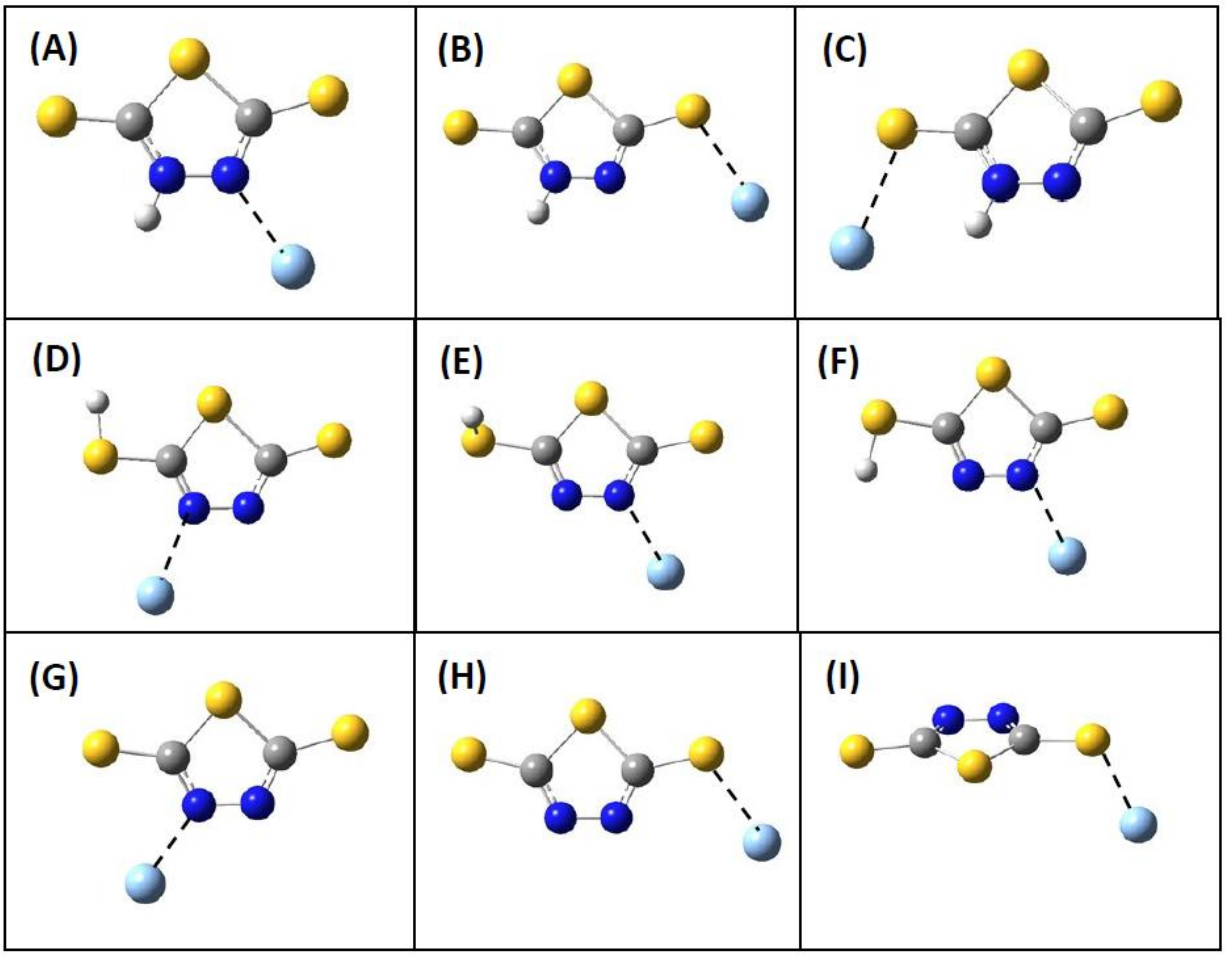

Figure 6.5. *Optimized structures of three possible thione-thiolate-Ag complexes (A) bound through ring N, (B) bound through thione S, (C) bound through thione S with N-H in proximity, (C); three possible thiol-thiolate-Ag complexes (D) bound through ring N with S-H facing towards ring S, (E) bound through ring N with S-H out of plane with the ring, (F) bound through ring N with S-H facing towards ring N; and three possible dithiolate-Ag complexes (G) bound through ring N, (H) bound through thione S (Ag in plane with dithiolate) and (I) bound through thione S (Ag out of plane with dithiolate).*

The theoretical Raman spectrum of the mono and divalent ionic forms of DMTD-Ag as well as DMTD-Ag4 complexes were compared with the SERS spectrum of DMTD on Ag NPs at pH 7. Similarly, various possible conformers for the DMTD-Au and DMTD-Au_4 complexes were geometry optimized using B3LYP with aug-cc-pvdz basis set for DMTD and LANL2DZ basis set for GNPs. The geometry optimized structures of the Au complexes of the neutral tautomers (dithiol, thione-thiol and dithione) of DMTD are shown in fig. 6.6 (a-i).The vibrational frequencies were also calculated at the respective optimized geometries in order to obtain theoretical Raman spectra for the Au and Au_4 complexes of DMTD and compared with the experimental SERS spectrum at acidic pH.

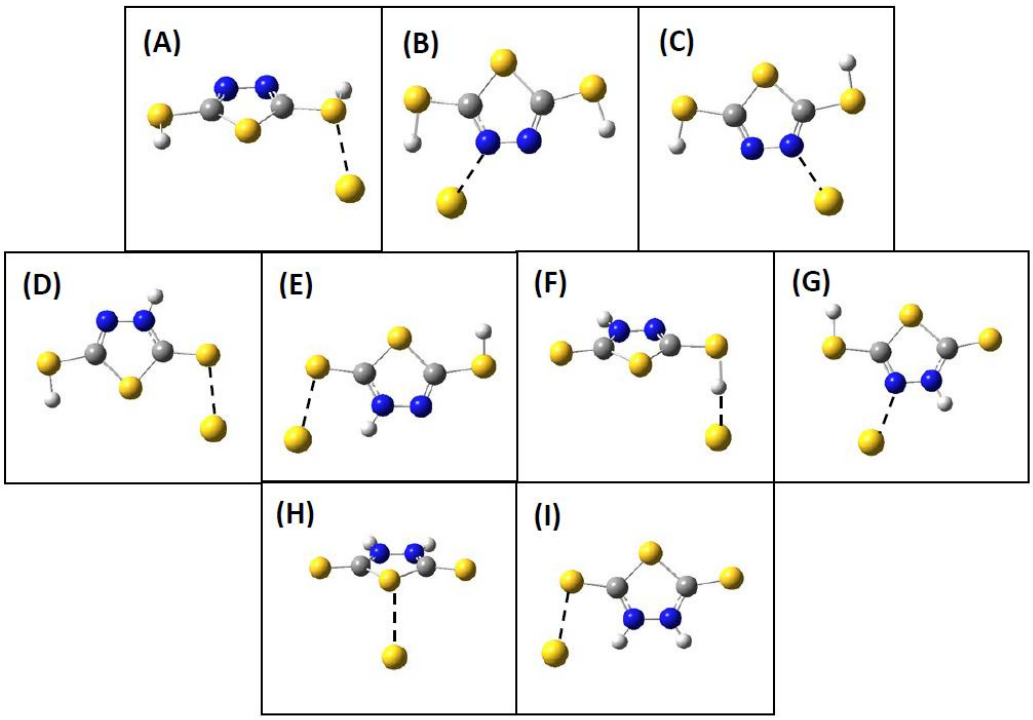

Figure 6.6. *Optimized structures of three possible dithiol-Au complexes (A) bound through thiol S (B) bound through ring N with S-H facing the ring N atoms, (C) bound through ring N with S-H facing away from the ring N atoms; four possible thione-thiol-Ag complexes (D) bound through thione S, (E) bound through thione S with N-H in proximity, (F) bound through thiol S-H, (H) bound through ring N and two possible dithione-Ag complexes (H) bound through ring S (Ag out of plane with dithione) and (I) bound through thione S (Ag in plane with dithione).*

6.1.4.4. Vibrational Assignments of DMTD from the Raman Spectra (theoretical and experimental)

The neutral conformers of DMTD, namely, dithiol, thione-thiol and dithione has 9 atoms with 21 fundamental modes of vibrations. Among the above forms, the dithiol and dithione tautomers belong to the C_s point group and have 15 in-plane (A′) and 6 out-of-plane (A″) fundamental vibrations, whereas, the structure of thione-thiol form belongs to the C_1 point

group. All the fundamental vibrations of the above the neutral conformers of DMTD are expected to be Raman-active as well as infrared spectra. The experimental Raman spectra of solid DMTD for the region 200-1600 cm^{-1} is shown in fig. 6.7. All the observed Raman vibrations are tabulated in table 1. The assignments of the Raman bands to the different modes of vibrations of the thiadiazole ring as well as the mercapto groups are based on the comparison of the Raman spectrum of the solid with the calculated Raman spectrum. The calculated Raman spectrum of different neutral forms of DMDT were used for assignment of the different modes of vibrations of the dithiol, thione-thiol and dithione forms which is shown in 6.7. The Raman spectrum of solid DMTD exhibits two strong bands at 1458 and 663 cm^{-1}which were assigned to C=N stretching (str) in combination with CSH bending and CSC endocyclic symmetric (sym) str or ring breathing mode. Raman bands with medium intensity are observed at 1518, 1483, 1398, 1288, 1107, 1039, 1021, 544, 500, 382, 329 and 215 cm^{-1}. The 1518, 1483 and 1288 cm^{-1} vibrations were assigned to C=N str, C-N asymmetric (asym) str and C-N sym str, respectively. The bands at 1398 and 1107 cm^{-1}were attributed to ring C=N str and N-N str in combination with N-H bend. The 1039 and 1021 cm^{-1} bands are assigned to N-N str and C-S str. The Raman bands at 544 (500), 382, 329 and 215 cm^{-1} are attributed to ring distortion in combination with NH out of plane (oop) bend, NH wagging, CSC sym bend and HNNH torsion, respectively. Weak bands are observed at 1080, 725, 405 and 259 cm^{-1}. Of these vibrations, the modes observed at 1080 and 725 cm^{-1} corresponded to N-N str and CNN bend while the bands at 405 and 259 cm^{-1} are attributed to NH twisting and ring rotation, respectively. A close examination of the solid Raman spectrum [fig. 6.7.] and comparing the same with the theoretical Raman spectrum of all the tautomeric forms of DMTD, namely, dithiol [fig.6.9.(A)(b)], thione-thiol [fig.6.9.(A)(c)] and dithione [fig.6.9.(A)(d)], which were computed using B3LYP functional and aug-cc-pVDZ basis set, indicates that the solid spectrum consists of features

corresponding to all three tautomeric forms of DMTD. Moreover, the presence of the peak around 2499 cm^{-1} (shown in fig. 6.8.a.) of medium intensity is attributed to S-H str in the Raman spectra of solid indicating, the preferential existence of the dithiol or the thione-thiol form of DMTD in the solid state. Weak Raman band is observed around 3062 cm^{-1} indicating H-bonded N-H stretch [fig. 6.8.a.]. The simulated Raman spectrum [fig.6.9.(A)(e)] obtained as a result oflinear addition of theoretical spectra with contributions of 44%, 36% and 20% from dithiol, dithione and thione-thiol, respectively, matches well with the solid Raman spectrum which validates the existence of all the three tautomers DMDT in its solid form.

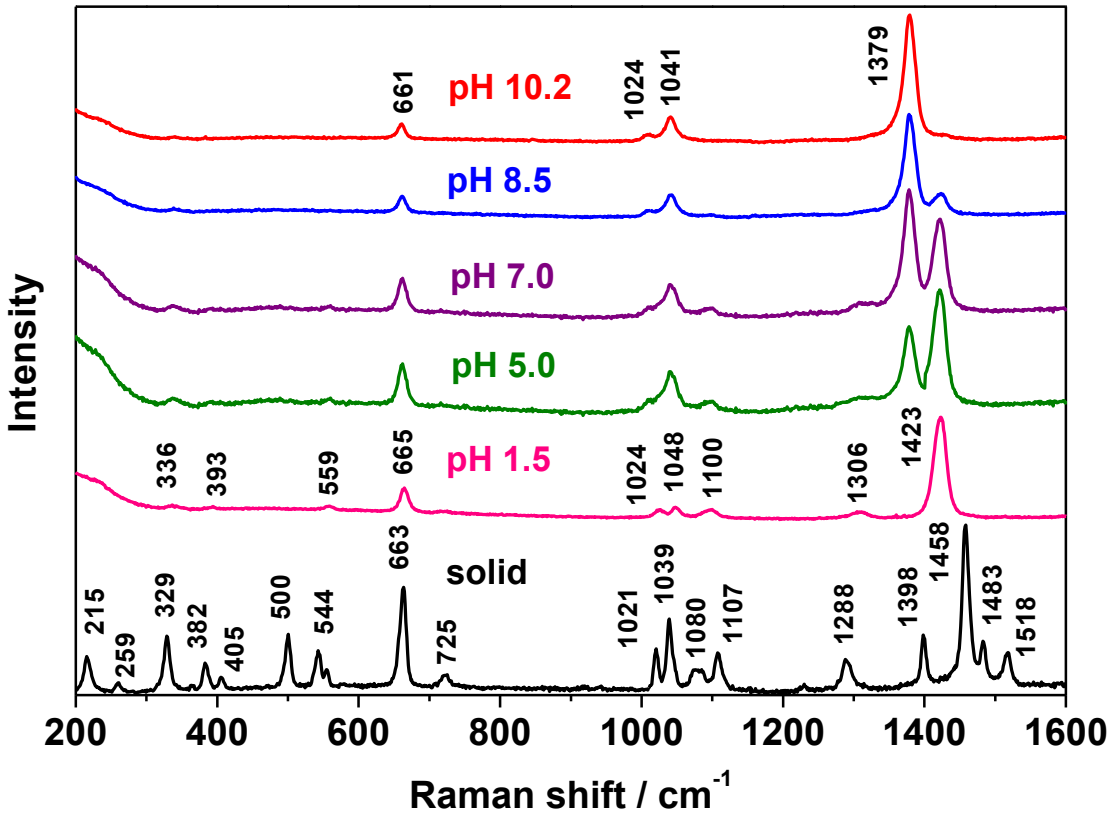

Figure 6.7. *Raman spectra of solid DMTD and its 10^{-2} M solution under different pH conditions.*

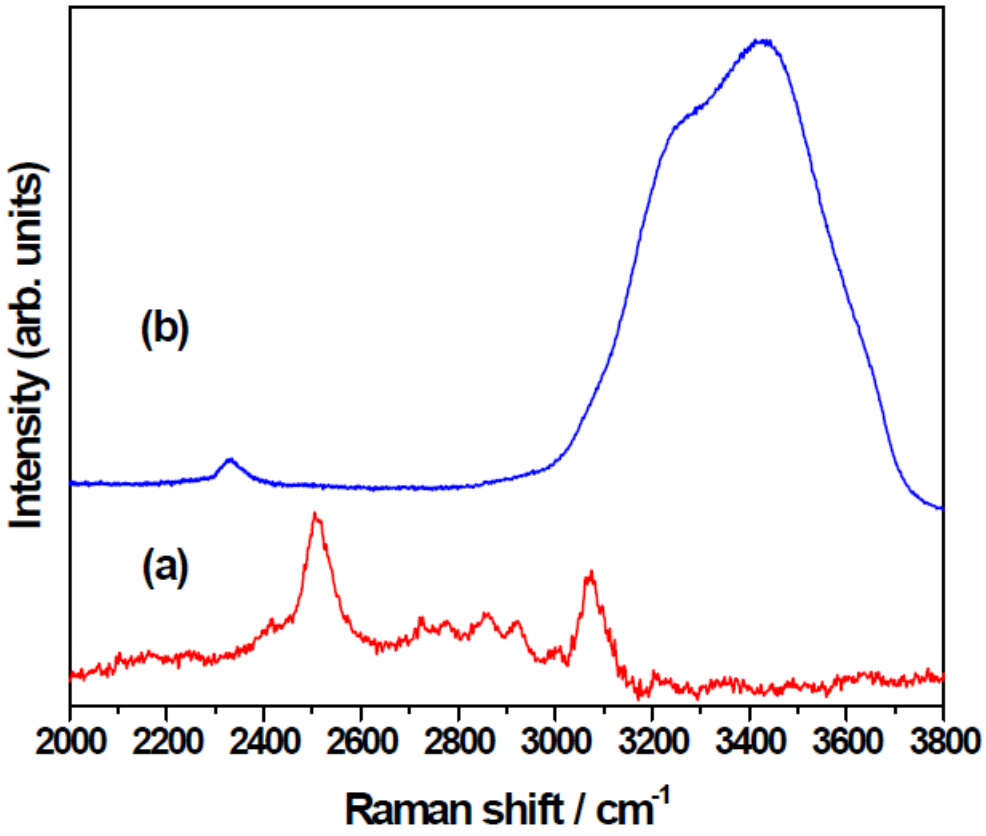

Figure 6.8. *Raman spectra of (a) solid DMTD and (b) 10^{-2} M DMTD solution at pH 1.5 in the higher frequency region from 2000-3800 cm^{-1}.*

6.1.4.5. pH-dependent normal Raman spectra of DMTD in aqueous solution

The Raman spectra of 10^{-2} M aqueous solution of DMTD at different pH are shown in fig. 6.7. for the 200-1600 cm^{-1} region was analyzed and the corresponding Raman vibrations are tabulated in Table 2. As shown in fig. 6.7., at pH 1.5, an intense peak is observed at 1423 cm^{-1} followed by a medium intense band at 665 cm^{-1}. Few weak Raman bands are also observed at 1306, 1100, 1048, 1024, 559, 393 and 336 cm^{-1}. Of these modes, the 1423 cm^{-1} band is assigned to C=N stretch in combination with CSH bend which was also observed in case of solid DMDT at 1458 cm^{-1}. The vibration observed at 665 cm^{-1} is attributed to CSC endocyclic sym str which was observed in case of solid DMDT at 663

cm^{-1}. The weak Raman bands at 1306, 1100 (1048), 1024, 559, 393 and 336 cm^{-1} are assigned to C-N sym str, N-N str, C-S str, ring distortion, NH wagging and CSC sym bend, respectively. A close examination of the Raman spectrum at pH 1.5 [fig. 6.9.(B)] and upon comparison with the theoretical Raman spectrum of the three tautomeric forms of DMTD namely, dithiol, thione-thiol and dithione [fig. 6.9.(B)], it can be evidently stated that the solution spectrum has 48%, 32% and 20%contributions from dithiol, dithione and thione-thiol, respectively.

Table 6.1. *Assignments of Raman (solid) and B3LYP/aug-cc-pvdz calculated vibrations (in cm^{-1}) for the dithiol, thione-thiol and dithione tautomeric forms of DMTD.*

Raman	**Calculated Vibrations**			**Assignments**
Solid	*dithiol*	*thione-thiol*	*dithione*	
3062w				N-H str
2499m				S-H str
1518m		1533		C=N str, NH bend
1483m		1430	1458	C-N asym str, NH bend
1458s	1438	1483s		C=N str, CSH bend
1398m	1416		1408	C=N str, N-N str, NH bend
1288m			1304	C-N sym str, NH bend
1107m		1123		N-N str, NH bend
1080w	1053	1056		N-N str, CSH bend
1039m	1090		1089	N-N str
1021m			1019	C-S str, NH bend
725w	699	685		CNN bend, CSH bend
663s	610	623	641	CSC endocyclic sym str / ring breathing
544m 500m	487	521	532	ring distortion, NH oop bend
405w			462	NH twisting

382m			439	NH wagging
329m			362	CSC sym bend
259w			314	ring rotation
215m			251	HNNH torsion

Abbreviations used: s: strong, m: medium, w: weak; asym: asymmetric, sym: symmetric, str: stretch, oop: out-of-plane.

At pH 1.5, a weak band is also observed at 2330 cm^{-1} assigned to the S-H str which is shown in fig. 6.8.b. The N-H str vibration around 3000 cm^{-1} is not observed in the Raman spectrum of the solution at pH 1.5 due to completely masking by the broad O-H str vibration (3600 cm^{-1}) of water. In the normal Raman spectrum of 10^{-2} M DMTD solution at pH 5.0, a new band at 1379 $cm^{-1}$was observed to appear in addition to the increase in intensity of the 1048 cm^{-1} band corresponding to N-N str. All the other vibrational features were found to be similar to the Raman spectrum of DMTD solution at pH 1.5. The 1379 cm^{-1} band was found to correspond to the C=N str in combination with N-N str and NH bend. The Raman spectrum of DMTD at pH 7.0 was almost similar to that at pH 5.0 with the only exception that the 1379 cm^{-1} band shows an additional increase in intensity which is relatively greater than that at 1423 cm^{-1}. From the above data one can clearly see that such a scenario of growth of N-N bond is possible when there is a steady flow of electron density from one thiol group to another thiolate group and vice versa possible due to thione-thiolate and thiol-thiolate equilibrium. The Raman spectra at pH 5.0 and pH 7.0 were found to be comparable to the calculated Raman spectra of thione-thiolate and thiol-thiolate as shown in fig. 6.9. (C). The Raman spectrum of DMTD recorded at pH 8.5 shows sharp reduction in the intensities of the 1423 and 1100 cm^{-1} bands along with further growth of the 1379 cm^{-1} band with the latter having enhanced intensity as compared to the 1423 cm^{-1} band. This indicates towards preference of thiol-thiolate tautomer as shown in

fig. 6.9. (C). Other features were almost similar to that at pH 5.0 and pH 7.0. The above figure, clearly show that around pH 5-8 DMTD solution exists as a combination of the mono valent tautomers, such as. thione-thiolate and thiol-thiolate. At pH 10.2, the Raman band at 1379 cm^{-1} is found to be very intense indicating loss of proton from thiol-thiolate form. Moreover, two medium intense peaks are observed at 1041 and 661 cm^{-1} along with a weak band at 1024 cm^{-1}. In fig. 6.9. (D), the Raman spectra recorded at pH 8.5 and 10.2 are shown along with the calculated Raman spectra [B3LYP/aug-cc-pVdz and B3LYP/6-311+G(d,p)] of the divalent anionic dithiolate tautomer of DMTD.

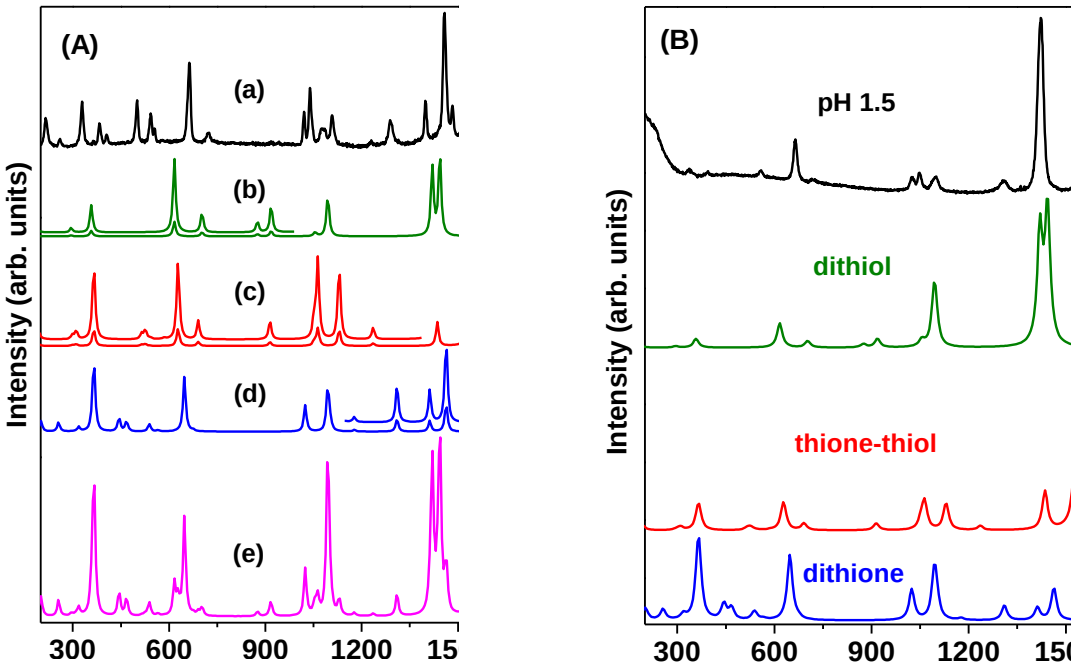

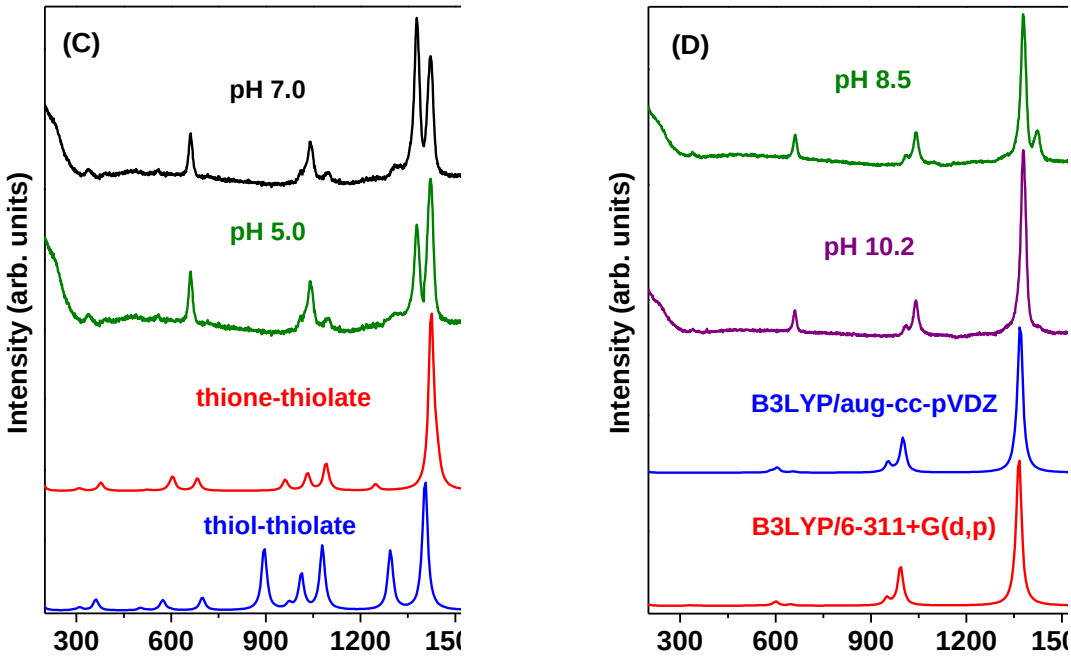

Figure 6.9. *(A)(a) Raman spectrum of solid DMTD and calculated (B3LYP/aug-cc-pVDZ) Raman spectra of (b) dithiol, (c) thione-thiol, (d) dithione and (e) sum of dithiol, thione-thiol and dithione. Raman spectrum of 10^{-2} M DMTD solution (B) at pH 1.5 and the calculated Raman spectra of dithiol, thione-thiol, dithione, (C) at pH 7.0 and pH 5.0 and the calculated Raman spectra of thione-thiolate and thiol-thiolate and (D) at pH 8.5 and pH 10.2 and the calculated Raman spectra [B3LYP/aug-cc-pVdz and B3LYP/6-311+G(d,p)] of dithiolate.*

The above figure suggests that at pH 10.2, DMTD exists as dithiolate in aqueous solution. Upon comparison of the Raman spectra over the entire pH range shows that the Raman spectrum is similar around pH 5-9 with slight variations in the relative intensities of the 1379 and the 1423 cm^{-1} peak. At acidic pH 1.5, the 1423 cm^{-1} band is strong with complete disappearance of the 1379 cm^{-1} peak whereas, the trend was reversed at alkaline pH 10.2.

Table 6.2. *Assignments of Raman (10^{-2} M solution) and SERS spectra of DMTD at varying pH.*

Raman Spectra (Solution)			SERS spectrum			Assignments
			Ag NPs		*Au NPs*	
pH 1.5	**pH 5.0**	**pH 10.2**	**pH 1.5**	**pH 7.0**	**pH 1.5**	
2330w						S-H str
1423s	1423s		1413vs		1412s	C=N str, CSH bend
	1379s	1379vs	1358vs	1362vs		C=N str, NN str, NH bend
1306w					1299w	C-N sym str, NH bend
1100w						N-N str, NH bend
1048w	1042m	1041m	1062s	1064s	1058m	N-N str
1024w		1024w			1027m	C-S str, NH bend
					720w	CNN bend, CSH bend
665m	662m	661m	664m	668s	657s	CSC endocyclic sym str / ring breathing
559w			546m	542m	542m	ring distortion, NH oop bend
					485m	NH twisting
393w			382m	384m	385s	NH wagging
336w			346w	352w		CSC sym bend

Abbreviations used: s: strong, m: medium, w: weak; sym: symmetric, str: stretch, oop: out-of-plane.

6.1.4.6. Surfaced-Enhanced Raman Scattering (SERS) Spectra of DMTD

The SERS spectra of different concentrations of DMTD (0.1 to 100 µM) adsorbed on the Ag NPs surface were recorded at pH 7.0 which is shown in fig. 6.10. The SERS spectra of DMDT was found to enhance upon increasing the concentration DMDT from 0.1 to 0.5µM. Maximum enhancement SERS spectra is observed at the concentrations of 1 and 0.5 µM DMTD, which may be attributed to monolayer formation on the surface of AgNPs. Further increase in concentration of DMDT leads to reduction in SERS intensity due to multilayer

coverage. SERS spectra showed intense peaks at 1362 (C=N str), 1064 (N-N str), 668 (CSC endocyclic sym str) and 384 (NH wagging) cm^{-1} with medium and weak intensities at 542 (ring distortion) and the 352 (CSC sym bend) cm^{-1}, respectively. From fig. 6.10.a., it was observed that upon changing the concentration of DMTD resulted the change of intensities only. Peak positions were unaffected by the change in concentrations of DMDT. This means that upon variation of concentrations of DMDT, neither the mechanism of binding of DMDT nor the orientation of DMDT on the surface of AgNPs is altered.As discussed earlier, in the pH range 5-8, DMTD exists as monovalent ion i.e. as thione-thiolate or the thiol-thiolate tautome in aqueous solution. Similar structure was found to be retained even on the surface of AgNPs.

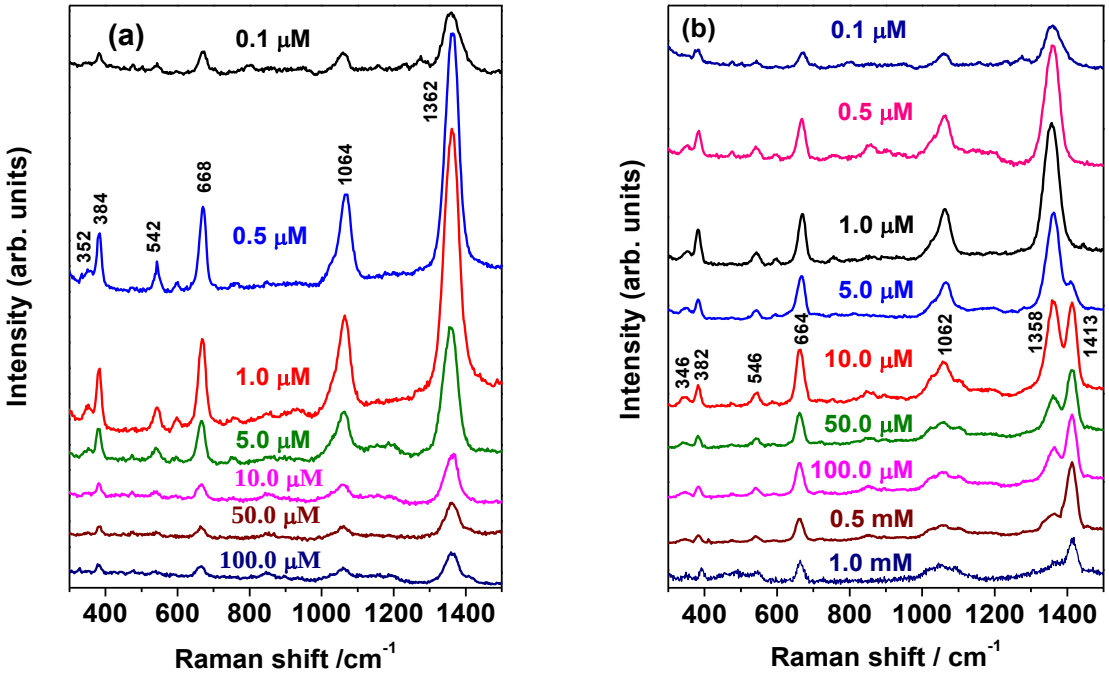

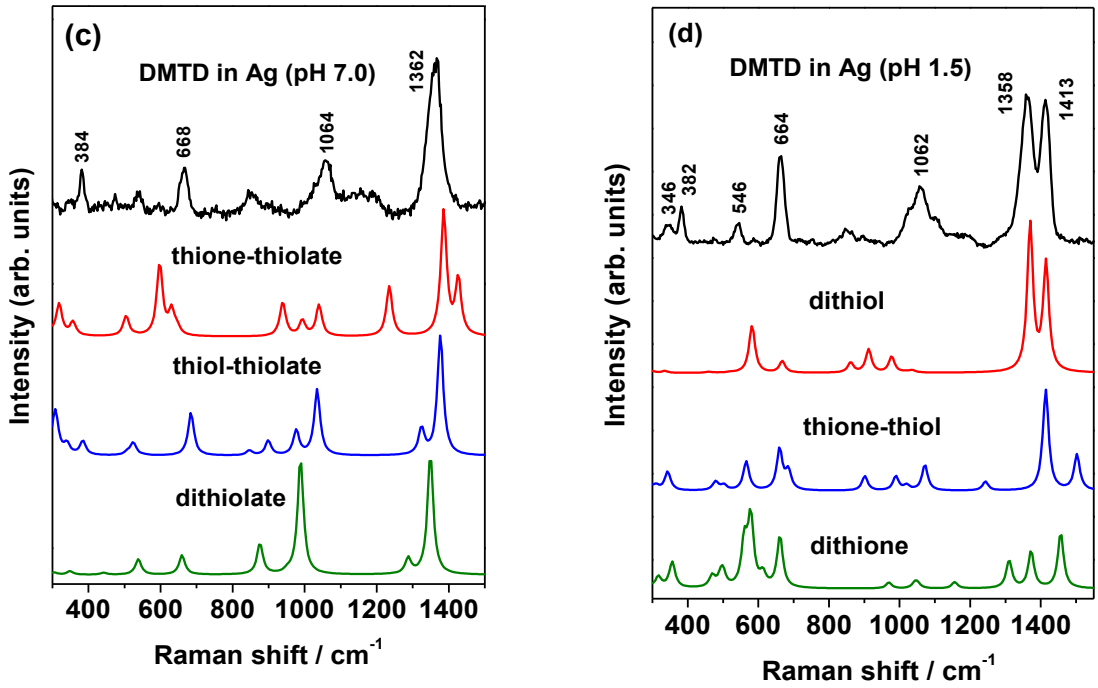

Figure 6.10. *Concentration-dependent SERS spectra of DMTD functionalized Ag NPs at (a) pH 7.0 and (b) pH 1.5. Comparison of the SERS spectrum (c) at pH 7.0 with the calculated Raman spectra of thione-thiolate-Ag4, thiol-thiolate-Ag_4 and dithiolate-Ag_4 complexes and (d) at pH 1.5 with calculated Raman spectra of dithiol-Ag_4, thione-thiol-Ag_4 and dithione-Ag_4 complexes.*

Under acidic conditions (pH 1.5), DMDT adsorbed on AgNPs, showed a slight variation in structure as inferred from the SERS spectra as shown in fig. 6.10.b.. Under acidic condition, similar trend of SERS intensity was observed upon increasing the concentration of DMDT from 0.1 to 100 µM on the surface of AgNPs. Maximum enhancement was observed for 1µM concentration of DMDT on AgNPs surface, due to monolayer coverage. At concentrations lower than 1 µM of DMDT on AgNPs surface, there is a decrease in SERS intensity due to sub-monolayer coverage. At further concentrations higher than 1µM, Multilayers of DMDT is formed over AgNPs which behave like bulk solution. It is to be

noted that at minimum concentration of 0.1 µM of DMTD on AgNPs, the Raman bands at 1358, 1062, 664 as well as 382 cm^{-1} were observed and were assigned to C=N stretch in combination with N-N str, N-N str., CSC endocyclic sym str and NH wagging, respectively. At higher concentrations of DMTD such as 0.5, 1 and 5 µM, the Raman bands at 1358, 1062, 664 and 382 cm^{-1}showed an increased intensity along with appearance of new features at 1413, 546 and 346 cm^{-1}which were assigned to C=N str, ring distortion and CSC sym bend, respectively. Upon further increase in concentration, i.e., at 10 µM, 50 µM, 100 µM, 0.5 mM and 1 mM of DMDT on AgNPs, 1413 and 1358cm^{-1} bands showed simultaneous increase and decrease in intensity. The decrease in intensity of 1358 cm^{-1} band progresses with increasing concentration of DMDT on AgNPs in such a way that upon reaching 1 mM concentration of DMDT, the above band is reduced to a mere shoulder on 1413 cm^{-1} band. The above observation indicates towards a tautomeric transformation. Therefore, the concentration-dependent SERS study of structural behavior of DMTD show a possible tautomeric change on the surface of AgNPs at pH 1.5. Such a change was not encountered upon varying the concentration of DMDT in solution phase. Moreover, it seems that surface of AgNPs as well as nature of binding of DMDT with AgNPs influence such a transformation. This may be due to a preferential existence of dithiol, thione-thiol and dithione forms of DMTD on the Ag NP surface at acidic pH. The above inference was drawn after comparison of the comparison of the SERS spectra with the theoretical Raman spectra as shown in fig. 6.10.b.Upon lowering the concentrations of DMTD, the 1358 cm^{-1}band (C=N stretch coupled to N-N str), undergoes enhacement, indicating the favored existence of dithione form on the Ag NP surface at pH 1.5.

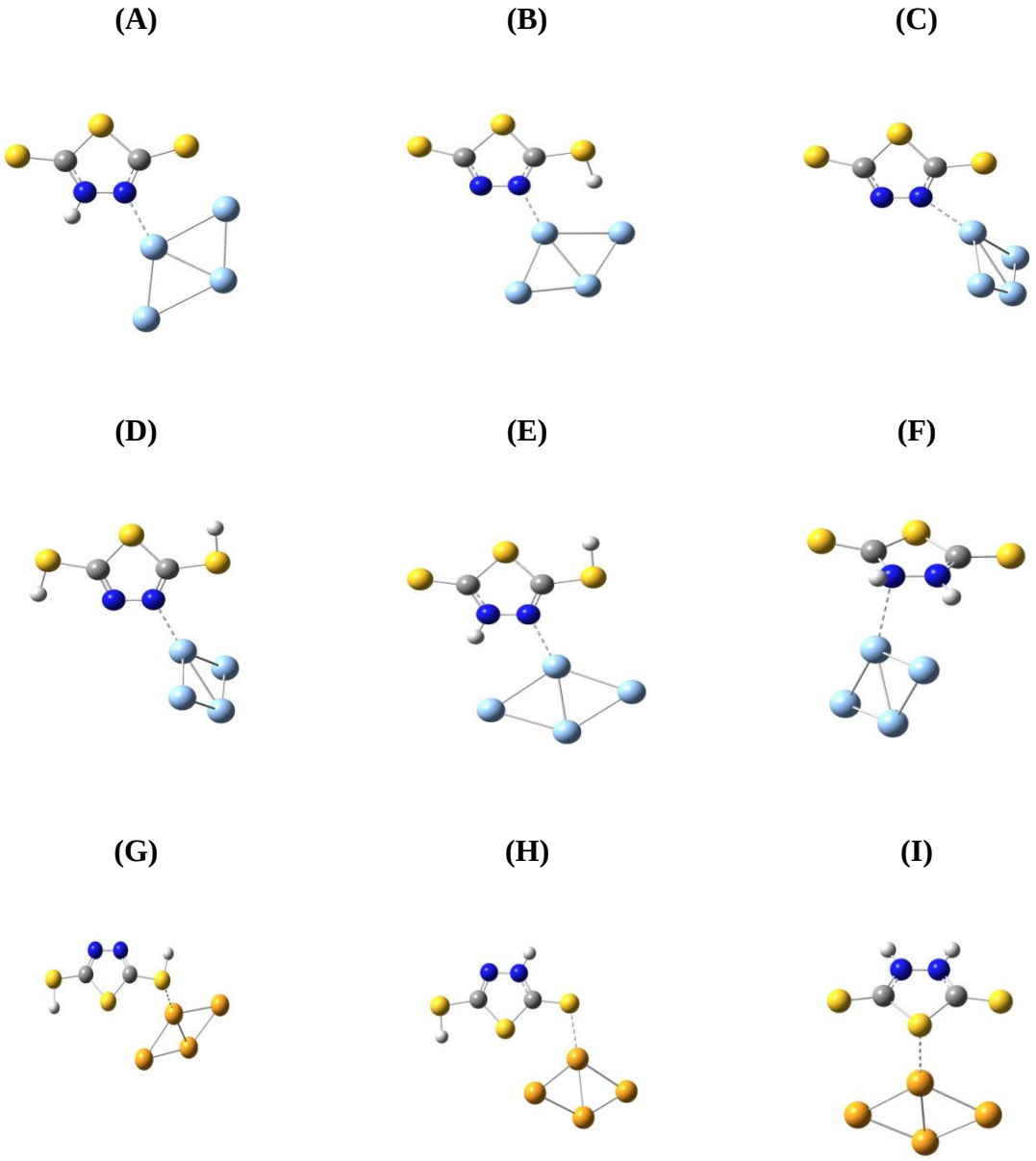

Figure 6.11. *Optimized structures of (A) thione-thiolate-Ag_4, (B) thiol-thiolate-Ag_4, (C) dithiolate-Ag_4 (D) dithiol-Ag_4, (E) thione-thiol-Ag_4, (F) dithione-Ag_4, (G) dithiol-Au_4, (H) thione-thiol-Au_4, (I) dithione-Au_4 complexes. The colour codes used to identify the atoms are N (blue), S (yellow), C (grey), H (white), Ag (light blue) and Au (orange).*

A gradual increase in the intensity of the 1413 cm^{-1} band (C=N str) with simultaneous decrease in the 1358 cm^{-1} peak upon gradually increasing the concentration of DMDT from 5 to 500 µM). This indicates favourable existence of the dithiol form on the Ag NP surface at multilayer coverage which is similar to bulk solution conditions. Similar results in the

bulk solution was discussed in fig. 6.9.b. A slight contribution from the thione-thiol form cannot be completely neglected. Thus, in 1 mM of DMTD adsorbed on AgNPs, the presence of the SERS bands at 1413 and 664 cm^{-1} confirms the prevalence of the dithiol form on the Ag NP surface.

The SERS spectra of 10µM of DMTD adsorbed on AgNPs at neutral and acidic show high matching in the range 300-1300 cm^{-1} whereas in the region 1300-1500 cm^{-1}strikingdifferences were noted. At neutral pH, a strong broad single band was observed at 1362 cm^{-1} whereas at acidic pH, two Raman bands with almost equal intensities at 1358 and 1413 cm^{-1} were observed. This maybe due to existence of different tautomeric forms of DMTD at pH 7.0 and pH 1.5. At neutral pH, DMTD was found to exists as thione-thiolate and thiol-thiolate form with slight contribution from the dithiolate form. The presence of the dithiolate form, may be as upon adsorption to AgNPs surface the pKa value of the mercapto group may have lowered. Moreover upon increasing the pH to 10.2 does not lead tofurther adsorption of the dithiolate form on the Ag NP surface.

The nature of adsorption of DMTD on the Ag NP surface at neutral pH 7.0 was studied by comparison of its SERS spectrum with that of the calculated Raman spectrum of the mono-anionic forms of DMTD-Ag_4 complex i.e. thione-thiolate-Ag_4 and thiol-thiolate-Ag_4which is shown in fig. 6.10.c. Moreover, the Raman spectrum for the dithiolate-Ag_4 complex was taken into consideration in the above figure for comparison. The geometry optimized structures of the thione-thiolate-Ag_4, thiol-thiolate-Ag_4 and dithiolate-Ag_4 complexes are shown in fig. 6.11. (a-c). It was observed from the fig. 6.10.c., that the SERS spectrum was found to match reasonably well with the theoretical Raman spectra of thiol-thiolate-Ag_4 complex of DMTD indicating the abundance of thiol-thiolate form on the Ag NP surface bound exclusively through the ring N atom. Again, the dithiolate-Ag_4or the thione-thiolate-Ag_4complexes may have also contributed slightly.

The binding affinity of DMTD adsorbed on the Ag NP surface at acidic pH can also be studied by comparing its SERS spectrum with the calculated Raman spectrum of the neutral tautomeric forms of DMTD-Ag_4 complex such as dithiol-Ag_4, thione-thiol-Ag_4 and dithione-Ag_4which is shown in fig.6.10.d. The geometry optimized structures of dithiol-Ag_4, thione-thiol-Ag_4 and dithione-Ag_4 complexes are shown in fig. 6.11.d-f. In fig. 6.10.d. it is clearly shown that there is a high matching of the SERS spectrum with the theoretical Raman spectrum of dithiol-Ag_4. This clearly indicates the dithiol form of DMTD on the Ag NP surface is abundant at pH 1.5 where the dithiol tautomer is bound to the surface of AgNPs via the thiadiazole ring N atom. Moreover, the SERS spectrum in the region 300-800 cm^{-1}matches well with the theoretical Raman spectrum of the thione-thiol-Ag_4 complex indicating the presence of thione-thiol conformer also on the surface of Ag via N atom. Contributions from dithione may not be completely ruled out.

Apart from silver nanoparticles, the adsorption behavior of DMDT on GNPs reveal a new dimension to the surface binding properties of DMDT. The SERS spectra recorded for varying concentration of DMDT (100 to 0.1 µM) adsorbed on the surface of colloidal GNPs under acidic pH 1.5, is shown in fig. 6.12.a.It is important to note that the above adsorption behavior was only observed for acidic pH only and was not observed at neutral or alkaline pH. The above adsorption behavior of GNPs was found to be different from that of AgNPs as shown in fig. 6.10., which indicates that AgNPs have more binding affinity towards DMDT in comparison to GNPs. At concentrations 0.1 and 0.5 µM of DMDT, the SERS spectra showed a poor signal to noise ratio upon adsorption of GNPs under acidic pH.Upon increasing the concentration of DMDT from 1 to 100 µM, a good enhancement was observed. The SERS spectrum of DMTD of concentration 1 µM adsorbed on GNPs showed strong Raman bands at 1412, 657 and 385 cm^{-1}corresponding to C=N str, CSC endocyclic sym str and NH wagging, respectively. Again, moderately intense peaks

observed at 1058, 1027, 542 and 485 cm^{-1}were assigned to N-N str, C-S str, ring distortion and NH twisting, respectively. Similarly, SERS peaks of weak intensity were observed at 1299 and 720 cm^{-1} which were assigned to C-N sym str and CNN bend, respectively. Upon lowering the concentration of DMDT to 1 µM on GNPs, 1412 cm^{-1}peak corresponding to C=N str was found to reduce in intensity and a broad band at 1355 cm^{-1} corresponding to C=N stretch in combination with N-N str appeared. In order to compare the peaks observed in SERS spectrum of DMDT on GNPs at acidic pH with that of the theoretical Raman peaks of dithiol-Au_4, thione-thiol-Au_4 and dithione-Au_4 complexes for assignment of peak as well as calculation of relative contribution of each tautomer, a comparative picture is presented in fig. 6.12.b. The above figure shows a reasonable match between SERS spectra with that of dithiol-Au_4 complex in the region of 1000-1550 cm^{-1}indicating compositional dominance of dithiol tautomer on GNPs surface. The peaks at 657 and 720 cm^{-1}region of the above SERS spectrum is also corresponded to that of the theoretical spectra of thione-thiol-Au4 and dithione-Au4 complexes, indicating the simultaneous presence of the above tautomers on GNPs surface.

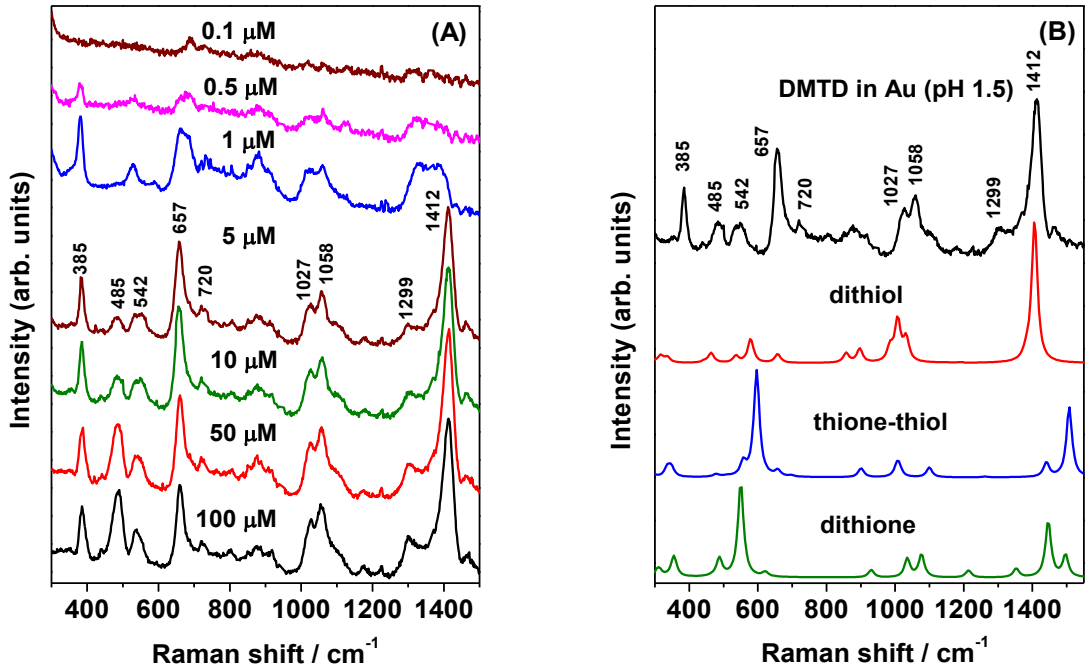

Figure 6.12. *Concentration-dependent SERS spectra of DMTD functionalized Au NPs (a) at pH 1.5 and (b) Comparison of the SERS spectrum at pH 1.5 with the calculated Raman spectra of dithiol-Au4, thione-thiol-Au4 and dithione-Au4 complexes.*

Again in the region 300-600 cm-1, the theoretical Raman spectrum of dithione-Ag_4 tautomer showed some resemblance with the SERS spectra of DMDT over GNPs surface indicating the presence of dithione tautomer. Thus, there is a possibility of all the three neutal tautomers, such as dithiol, dithione and thione-thiol to be present on the surface of GNPs under acidic condition.

Another interesting fact, that in case of AgNPs, DMDT was found to bind to Ag surface via N atom whereas in case of GNPs, DMDT was found to bind with the surface of GNPs via S atom of thiocarbonyl or ring S atom of thidiazole moiety of DMDT. More over upon comparing the SERS spectra under acidic conditions, in case of DMDT-AgNPs, a doublet

peak at 1358 and 1412 cm^{-1} was observed whereas, in case of DMDT-GNPs, a single sharp peak at 1412 cm^{-1}.

Thus, a combined study of SERS with DFT reveal a lot of information about the nature of binding observed in case of DMDT with silver and gold nanoparticles. In short, it can be said that in case of AgNPs, DMDT exist as thiol-thiolate tautomer binds to the surface of AgNPs at neutral pH via thiadiazole ring N- atom whereas under acidic condition also ring N atom of all the neutral tautomers of DMDT binds to AgNPs. In case of GNPs, metal surface interacts with DMDT via thiocarbonyl or thiadiazole ring S atom under acidic condition.

In this study, SERS in combination with DFT studies clearly indicated the presence of the respective tautomeric forms available on the metal surface at particular pH (neutral or acidic) and their binding affinity.

6.2. SERS study of Thioflavin T (ThT)

6.2.1. Background

SERS is often used by researchers to determine analyte concentration through enhance Raman signals,[388, 444] due to adsorbate- metal surface interactions[309, 395-400, 408, 449] which occurs abiding the "surface selection rules."[450, 451]Moreove, SERS has also been reported to aid in investigation of reaction mechanisms by isolation of intermediates on the surface of metal nanoparticles.[452]Moreover, trace level detection of analytes by SERS is also possible.[453]

In order to exploit the surface properties of noble metal nanoparticles for drug delivery applications, informations regarding the molecular structure, orientation as well as the binding mode is essential to predict the efficiency of the processes.[454, 455]Thus, a large

number of researchers are focusing on investigations encompassing the field of development of biosensors, biomaterials as well as biocatalysis.

In recent past a lot of research has taken place to investigate a rotor molecule known as thioflavin T (ThT).[456, 457]ThTis a benzothiazole dye comprising of benzothiazole (BT) and dimethylaminobenzene (DMAB) groups joined by a single bond capable of rotation which makes it a part of the group of molecular rotors.[458]ThT is often used to detect amyloid fibrils.[456, 457] In certain diseases, such as Alzheimer's, Parkinson and type II diabetes,[456] the conversion of normally soluble proteins into amyloid fibrils is a marker for the detection of above diseases.[459]ThTwas found to adsorb on silver nanoparticle (NP) surface which was studied by SERS technique.[460] The authors suggested that ThT existed in two probable structures depending upon the torsional angle (φ) between BT and DMAB rings, on the surface of AgNPs. In this chapter, we have discussed the results obtained from Raman and SERS studies of ThT in solid state, solution phase, colloidal gold nanoparticles (GNPs) and silver-coated films (SCFs). SERS technique has also led to sub-nanomolar sensing of ThT due to its high sensitivity and selectivity. Moreover, the nature of binding of ThT over plasmonic nanoparticles as well as the surface orientation of ThT was also revealed in this study.

6.2.2. Experimental Section

6.2.2.1. Synthesis of SERS substrates

Thioflavin T (ThT), hydrogen tetrachloroaurate, trisodium citrate, $AgNO_3$ and formamide used for the preparation of GNPs and SCFs were from Aldrich chemicals, and S. D. fine chemicals, India. Gold nanoparticles (GNPs) were prepared by the method mentioned in section 6.1.2.2.In this study, instead of silver colloidal solution which is already reported[460], thin silver coated films (SCF) were prepared. In brief, thin SCF were by deposition of freshly prepared AgNPs onto a thoroughly cleaned glass surface in formamide. Glass slides

cleaned by chromic acid and thoroughly washed by Millipore water were dipped in a reaction mixture containing $5x10^{-2}$ M $AgNO_3$ in formamide. In the reaction mixture, Ag^+ is converted to Ag_0 by the solvent, which deposited over glass slides. The detailed characterization is reported elsewhere.[99]For SERS studies, ThT solution was added to GNPs solution whereas SCF were dipped in ThT solution.

6.2.2.2. Instrumentation details

UV-vis absorption, Raman and transmission electron microscopy (TEM) techniques, whose technical details have already been discussed in section 6.1.2.3., were used to characterize the GNPs as well as the ThT adsorbed on GNPs. In addition to the above techniques, the surface morphological studies of the SCFs in non-contact mode was recorded using atomic force microscopy (AFM, model-SPM Solver P47).

6.2.3. Computational Details

The geometry optimization was performed for ThT using the Density Functional Theory (DFT) with B3LYP functional[443]and 6-31+G* basis set using Gaussian 03 program.[442] The computational details are same as mentioned in section 6.1.3.

6.2.4. Results and Discussion

6.2.4.1. Molecular Structure of Thioflavin T (ThT)

The geometry optimized structure of ThT is shown in fig. 6.13. The torsional angle (φ) between the benzothiazole (II) and dimethylaminobenzene (III) ringsin the optimized structure was found to be ~37° which corroborates with the results that were reported by Lopez-Tobar et. al.[460]

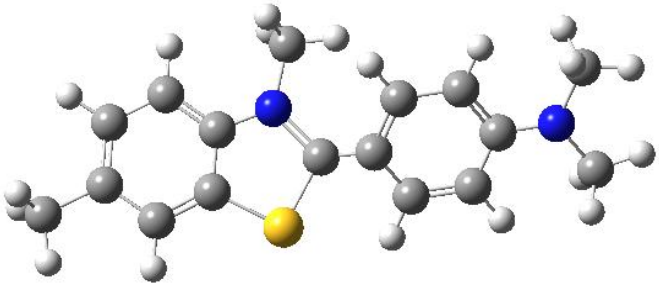

Figure 6.13. *Optimized structure of Thioflavin T (ThT) with the torsional angle (φ=37°) between benzothiazole (BT) and dimethylaminobenzene (DMAB) rings.*

Structure of ThTcould not be optimized to converge atφ ~ 90° and rather converged to φ=37°. The vibrational frequencies obtained from the optimized geometryofThT are tabulated in Table 6.3.

Table 6.3. *Assignment of Raman spectrum of solid ThT, its aqueous solution and SERS vibrations of ThT (GNP and SCF) in cm^{-1}. The apparent enhancement factors (AEF) calculated for the monolayer concentration (10^{-7} M) of ThT is also included.*

Raman Solid	**Raman Soln.**	**SERS**	**SERS**	**Assignments**	**AEF**	
		GNP	SCF	φ=37°	GNP	SCF
1606w	1612m	1601m	1604m	ν_{III} (CC)	3.5×10^5	4.9×10^5
1552s	1553s	1537w	1549m	ν_{III} (CC), $\nu(C_{15}N_{18})$	8.5×10^4	2.6×10^5
1508s	1510s	1506w	1505w	δ(CH3)c11,19,20, ν(C6N5)	1.3×10^5	3.3×10^5
1483s	1485s		1483m	δI(CH), δ(CH3)c11,10		5.7×10^5
1443m	1448m	1439w	1446w	δ(CH3)c11,1	2.6×10^5	6.9×10^5

				9,20, δIII(CH)		
1418w	1420w	1409w		δ(CH3)c11,10,19,20, δI(CH)		
1397s	1404s	1392m	1401s	δ(CH3)c10,11, δI(CH)	1.5×10^5	5.6×10^5
1355w	1356w	1345w		ν(CC), δ(CH), δ(NCCC)		
1329w	1331w	1327w		ν(CC), δ(CH), δ(NCCC)		
1311w	1309w	1301w	1307w 1268w	δ(CH), ν(CC), δ(CH3)c11	2.9×10^5	1.3×10^6
1207s	1210s	1213m		δ(CH), δI(CC)	1.7×10^5	
1159w	1161w	1155w		δI(CH), ρ(CH3)c11	2.4×10^5	
1134s	1135s	1130m	1134s	ρ(CH3)c11,δI(CH),ν(CC)	1.8×10^5	7.2×10^5
		1066w	1074w	ρ(CH3)c11,δ(CH),ν(CC)		
1037w	1039w	1032m	1038w	δI(CCC), νIII(CC)	8.5×10^5	4.3×10^5
977w	979w			δI(CCC), δIII(CH)		
		938m		νbreathIII(CC), ρ(CH3)c10,11		
		881m		δI(CCC), ρ(CH3)c19,20		
796s	798s	794s	801s	ρ(CH3)c11, δ(CCC)	2.7×10^5	5.2×10^5
744m	745m	743s		δ(CCC), νs(C6SC)	4.2×10^5	

699w	700w	697s	707w	δI(CCC), ν(C6SC)	2.0×10^6	7.3×10^5
639w	644w			δIII(CCC), γ(C6CNS)		
617w	619w	608w	625w	γ(C6CNS), γ(CH)	2.5×10^5	6.7×10^5
557w	556w	557w		γ(CCCC), ρ(CH3)	2.6×10^5	
533m	533m	530s	538s	δ(CSC), δI(CCC)	1.3×10^6	1.1×10^6
501w	499w	500w		δI(CCC), δII(CCC)	2.7×10^5	
484w	485w			skeletal vibrations		
425m	423m		428w	skeletal vibrations		3.3×10^5
		246s	232s	ν(AuS) / ν(AgS)		

6.2.4.2. Electronic Absorption spectrum of ThT in colloidal gold nanoparticles (GNPs)

The UV-visible electronic absorption spectra of metal colloids are far field effects of LSPR as discussed in chapter 1. Moreover, the agglomeration behaviour also tends to influence the LSPR due to reasons discussed earlier. Apart from aggregation, size and shape of the particle as well as the dielectric constant of the dispersing medium decides the features of LSPR. Upon monitoring of UV-vis absorption spectra of bare GNPs as well as that with ThT adsorbed on it at varying concentration, revealed interesting hints towards the nature of interaction of ThT with GNPs, which is shown in fig. 6.14. Addition of different concentrations of ThT to GNPs solution, was found to affect the absorption spectra which is

shown in fig. 6.14. In the above figure, base GNPs showed LSPR at 520 nm, which is same as the result obtained in section 6.1.4.1.

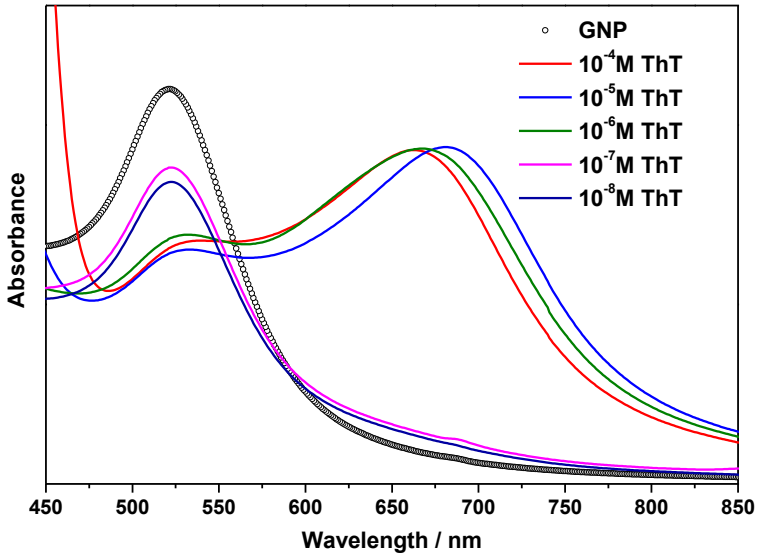

Figure 6.14. *UV-Vis absorption spectrum of colloidal GNPs (open circles) and with different concentrations of ThT (10^{-4} M - 10^{-8} M).*

Addition of very low concentration of ThT, i.e., 10^{-7} and 10^{-8} M, to GNPs, resulted in slight decrease of LSPR with a formation of shoulder above 600 nm. Upon increasing the concentration of ThT, LSPR was found to decrease at 520 nm with formation of broad coupled plasmon at 666, 670 and 685 nm for 10^{-4}, 10^{-5} and 10^{-6} M ThT. Red-shifted peaks are the coupled plasmon peaks arising due to adsorbed ThT induced concentration 10^{-5} to 10^{-7} M of ThT. aggregation of GNPs.

6.2.4.3. TEM and AFM analysis

TEM analysis of morphology of GNPs gives insight about the size, shape and aggregation pattern of GNPs. GNPs were found to have an average size of 25 nm with broad size distribution, as shown in fig. 6.15.a. Upon addition of very low concentration of ThT, 10-7

M, to GNPs, where a broad red-shifted couple plasmon band does not appear in UV-vis absorption spectrum, the GNPs were found to show aggregation as shown in fig. 6.15.b.

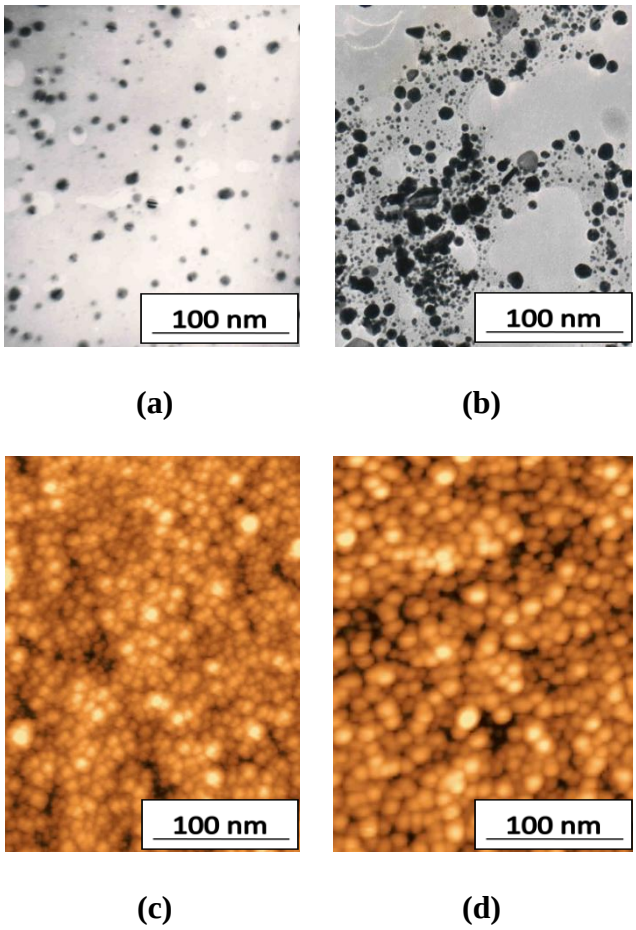

Figure 6.15. *TEM image of (a) colloidal GNP and (b) aggregated GNP obtained on addition of 10^{-7} M ThT to GNP. AFM image showing (c) SCF and (d) 10^{-7} M ThT adsorbed SCF.*

The average particle size upon aggregation was found to be ~ 35-40 nm, with retention spherical shape. In SCF, TEM could not be done due to technical disability associated with drop casting of colloidal solution on copper grids. Thus, in order to characterize the SCF, AFM technique was used instead. The AFM images of bare SCF and ThT adsorbed SCF are shown in 6.15.c. and d., respectively. AFM study showed that the average particle size is ~ 30 nm on glass substrate Upon addition of ThT, no evidence of induced aggregation was found. This may be due to prior immobilization of AgNPs on glass.

6.2.4.4. Normal Raman Spectrum of Thioflavin T (ThT)

ThT molecule consisting of 39 atoms and C_1 symmetry has 111 fundamental vibrational modes. Due to absence of centre of inversion, all the vibrational modes can be Raman active, only their contribution depends on the individual polarizability of the modes of vibration. The Raman spectrum of ThT (solid) in the 300-1700 cm^{-1}range, is shown in fig. 6.16. The modes of vibrations were assigned based on the matching of theoretical and experimental Raman spectra, which is shown in table 6.3.

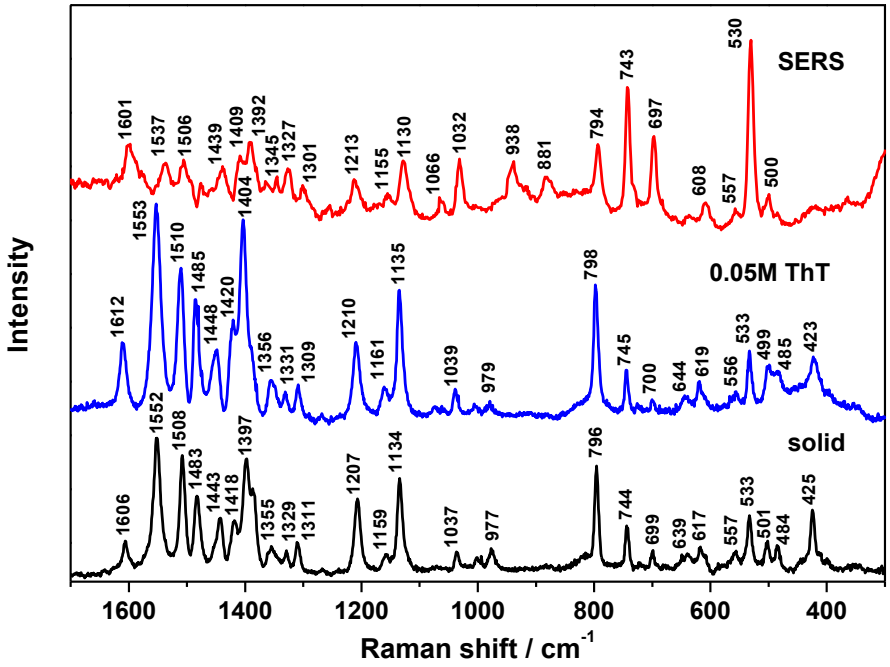

Figure 6.16. *The normal Raman spectrum of solid ThT, 0.05 M aqueous solution of ThT and SERS spectrum of 10^{-7} M ThT in GNP.*

There are 7 strong bands in the region 300-1700 cm^{-1}as observed in the Raman spectrum of solid ThT (fig. 6.16). The Raman bands of high intensity were observed at 1552, 1508, 1483, 1397, 1207, 1134 and 796 cm^{-1}. The 1552 and 1508 (1397) cm^{-1} vibrations were assigned to phenyl CC (ring III) stretch and CH_3 bending for the methyl functional groups (rings I and II). The bands at 1483, 1207 and 1134 (796) cm^{-1}were assigned to CH bending

(ring I), CH, CC bending and CH_3 bending for the N methyl group (ring II). Bands of medium intensity at 1443, 744, 533 and 425 cm^{-1}were assigned to CH_3 bending for the N methyl groups, ring CCC bending, ring CSC bending and skeletal vibrations, respectively. Bands of weak intensitywere observed at 1606, 1418, 1355, 1329, 1311, 1159, 1037, 977, 699, 639, 617, 557, 501 and 484 cm^{-1}. Weak bands at 1606 and 1418 cm^{-1}were assigned to CC stretch (ring III) and CH_3bending. Moreover, the bands at 1355 (1329) and 1311 cm^{-1}were attributed to ring CC stretch and CH bend in combination with CC stretch. The bands at 1159 and 1037 (977, 699) cm^{-1}were assigned to CH and CCC (ring I) bending, respectively. Again, the bands at 639, 617, 557, 501 and 484 cm^{-1}were attributed to CCC ring (III) bending, out of plane (oop) C_6CNS bending, oop CCCC bending, CCC (ring I) bending and skeletal vibrations, respectively.

The Raman spectrum of ThT in aqueous solution (0.05 M) as well as the Raman spectrum of solid ThT as shown in fig. 6.16, were found to be similar to each other.The Raman bands associated with the above figure are shown in table 6.3, and were assigned to their corresponding modes of vibration. In aqueous solution, Raman bands of high intensity at 1553, 1510 (1404), 1485, 1210 and 1135 (798) cm^{-1}were assigned to phenyl CC (ring III) stretch, CH_3 bending for the methyl functional groups, CH bending (ring I), CH, CC bending and CH_3 bending for the N methyl group (ring II). Again, the medium intensity Raman bands at 1612, 1448, 745, 533 and 423 cm^{-1}were assigned to CC stretch (ring III), CH_3 bending for the N methyl groups, ring CCC bending, ring CSC bending and skeletal vibrations, respectively. Weak Raman bands were seen at 1420, 1356, 1331, 1309, 1161, 1039, 979, 700, 644, 619, 556, 499 and 485 cm^{-1}. The Raman bands at 1420 and 1356 cm^{-1}were assigned to CH_3 bending and ring CC stretch. Similarly, the bands at 1331 and 1309 cm^{-1}were assigned to CH bend in combination with CC stretch. The Raman peaks at 1161 and 1039 (979, 700 and 499) cm^{-1}were assigned to CH and CCC bending(ring I),

respectively. The modes at 644, 619, 556 and 485 cm^{-1}wereassigned to CCC bending(ring III), oop C_6CNS bending, oop CCCC bending and skeletal vibrations.

6.2.4.5. Surfaced-Enhanced Raman Scattering (SERS) Spectrum of ThT

SERS spectra of varying concentrations of ThT(10^{-4} M - 10^{-10} M) adsorbed on colloidal GNPs excited at 633 nm are shown in fig. 6.17.

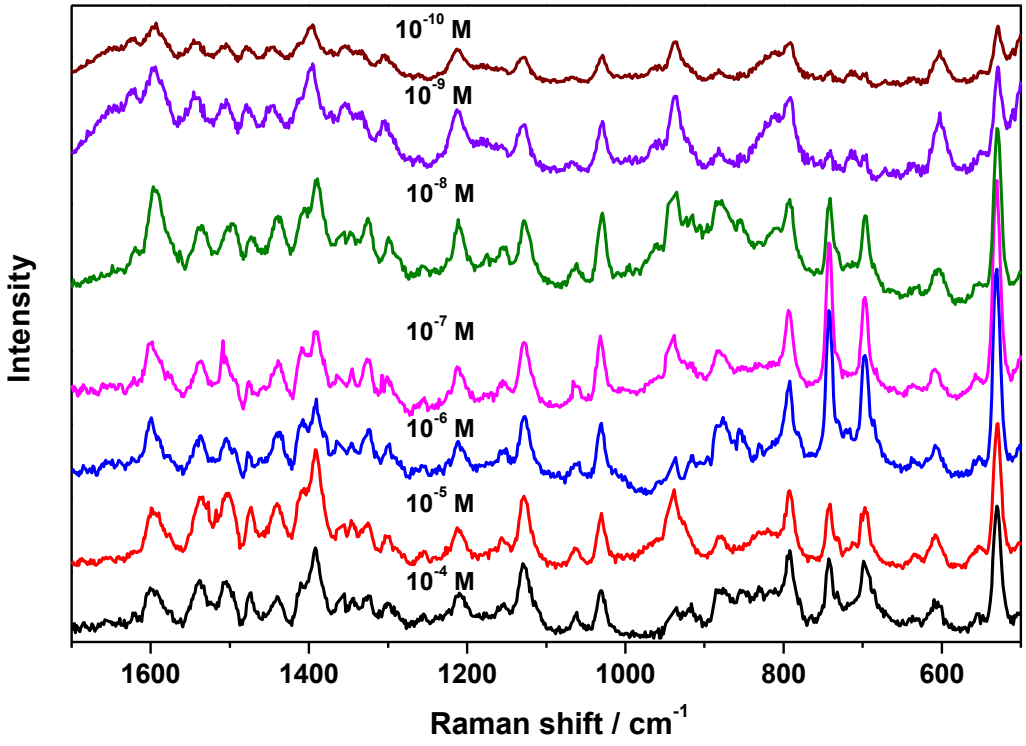

Figure 6.17. *Concentration-dependent SERS spectra of ThT in GNP.*

The SERS spectra in fig. 6.17 show relatively lower enhancements for GNPs with ThT concentrations of 10^{-4}, 10^{-5} and 10^{-8} M. On the other hand, GNPs with ThT concentrations of 10^{-6} and 10^{-7} M show good enhancement. Maximum enhancement was observed for 10-7 M ThT adsorbed on GNPs, which is attributed to monolayer adsorption of ThT over the surface of GNPs. Thus, at concentration of ThT lower than or equal to 10^{-8} M may lead to sub-monolayer coverage. Again, At concentration of ThT higher than or equal to 10^{-6} M

may lead to multi-layer formation where the analyte environment over GNPs is similar to that of bulk. Reasonably good as well as resolvable SERS signal 10^{-10} M (sub-nanomolar) concentration of ThT over GNPs surface, indicating sub-nanomolar detection limit. Moreover at concentration of ThT below monolayer coverage, i.e., 10^{-7} M, slight variation in concentration of ThT leads to no significant change in peak position. This means that at sub-monolayer coverage of ThT, there is possibility that the adsorbed molecules may undergo slight change in its orientation leading to intensity variations.

Upon comparison of SERS spectrum of a molecule and its Raman spectra in aqueous solution recorded under similar conditions, vital information related to the interfacial interactions as well as the geometry of the adsorbed molecules on the surface of NPs can be obtained. For the investigation of intensity changes as well as the peak shape of ThT in asdorbed state over GNPs, the SERS spectrum of 10^{-7} M ThT in fig. 6.17 was compared with the Raman spectra of ThT in solid and aqueous state as shown in fig. 6.16. Significant changes were recorded which give hints about the structural, binding as well as orientation behaviour of ThT over GNPs. The bands in the region 500-1000 cm^{-1} were found to be selectively enhanced. The Bands at 743, 697 and 530 cm^{-1}, which were assigned to in plane CCC bending vibration, CCC (ring I) bending and CSC bending, were enhanced indicating that the phenyl (ring I) as well as the S atom of the thiazole (II) moiety are closer to the surface of GNPs .The band at 530 $cm^{-1}$was found to be consistant with different concentration of TFT whereas the 743 and 697 cm^{-1} bands were greatly enhanced for monolayer and multilayer coverage of ThT over GNPs. SERS bands at 938 and 881 cm^{-1}were observed in SERS spectra but not in the Raman spectrum of aqueous solution, were assigned to ring breathing (ring III) and CCC (ring I) bending. Medium intensity SERS bands at 1601, 1392, 1213, 1032 and 1130 (794) cm^{-1}were assigned to CC stretching (ring III), methyl bending, CH (ring I) bending, CCC (ring I) bending and methyl bending (ring

II). Moreover, the SERS bands with weak intensity at 1537, 1506 (1439, 1409), 1345, 1327 (1301, 1155), 1066, 608, 557 and 500 cm^{-1} were assigned to the CC (ring III) stretch, ip methyl bending, CC stretch, CH bending, oop C6CNS bending, oop CCCC bending and CCC (ring I) bending, respectively.

The SERS spectra of ThT adsorbed on SCFs were recorded using 514 nm excitation and are shown in fig. 6.18.

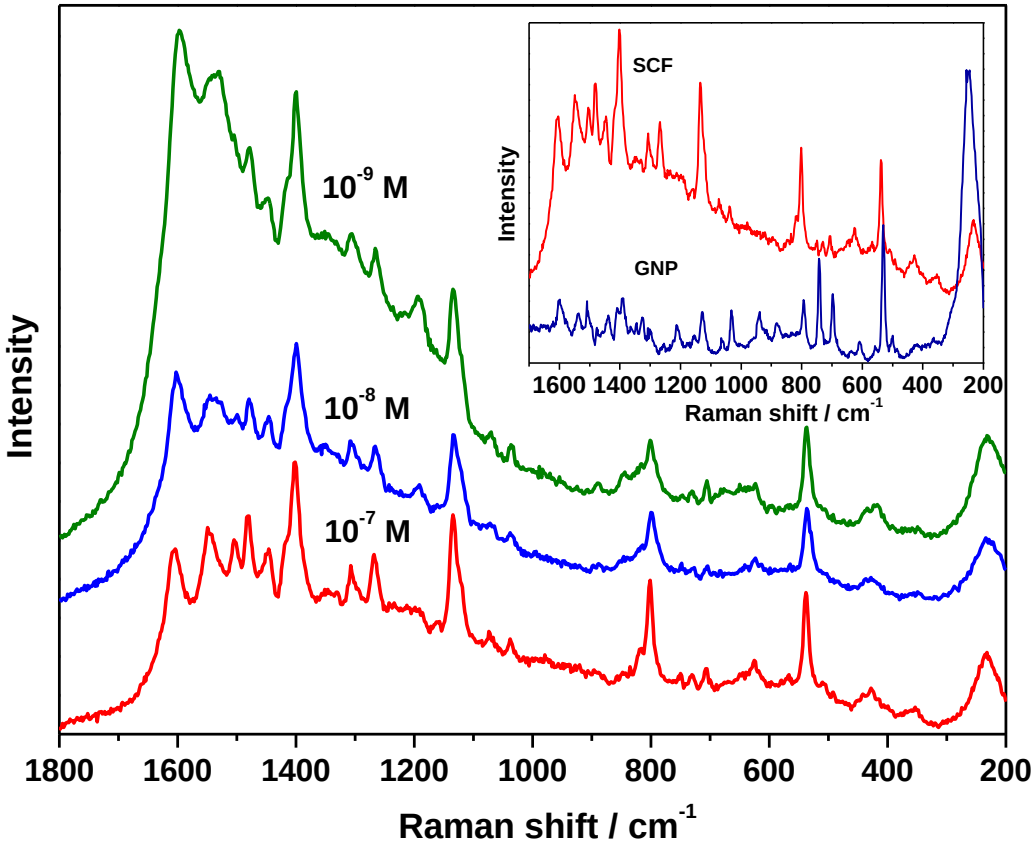

Figure 6.18. *Concentration-dependent SERS spectra of ThT adsorbed over SCFs. Inset shows the SERS spectra of 100 nMThT in GNP and SCF.*

ThT solution of concentration 10^{-7}, 10^{-8} and 10^{-9} M were used for dipping SCFs and SERS spectrum of the ThT loaded SCFs were found to show enhancement in Raman intensity in the range of 200-1700 cm^{-1}. A comparison of the SERS spectrum of ThT over GNPs and

SCFs is shown in inset of fig. 6.18. SERS signal of appreciable intensity was observed for minimum ThT concentration of 1 nM ThT and the signal was found to reduce further upon lowering the concentration of ThT below 1 nM. Differences in SERS of ThT over GNPs and SCFs is clearly visible in inset of the fig. 6.18. The peaks at 697 and 742 cm^{-1}were of medium and high intensity on GNPs, respectively, but the above bands were weak in SCFs. Moreover, the 881, 938 and 1032 cm^{-1} bands observed in SERS of ThT over GNPs whereas they are absent in case of SCFs. In SCFs, strong SERS bands at 801, 1134, 1401 and medium intense bands at 1268 and 1483 cm^{-1}were observed which showed relatively low intensity in GNPs. The band at 232 cm^{-1}appeared in SCFs which was assigned to Ag-S stretching suggested that ThT molecules bind to the surface of silver nanoparticles through S-atom. In the inset of fig. 6.18, the band at 246 cm^{-1} corresponds to Au-S bond in ThT functionalized GNPs. Theoretically the Ag-S bond should be weaker than the Au-S bond as Au surface has higher affinity for S atom. The above is observed in the difference of metal-sulphur bond stretching frequency. Thus the observed differences in the SERS spectra of ThT over GNPs and SCFs, as discussed above, accounts for the differences in interfacial interaction as well as orientation of ThT on the metal surfaces.

6.2.4.6. Binding of ThT with colloidal gold nanoparticles (GNPs) and silver-coated films (SCFs)

The extent of adsorption of any molecule on the surface of a metal nanoparticle is dependent on the nature of the active site of binding of the molecule (adsorbate), which is estimated by the observed enhancement in SERS signal. Moreover, the surface selection rules predicted by Moskovits[450] and Creighton[451] accounts for the orientation dependent SERS enhancement of any molecule. The surface selection rule states that the modes of vibrations in any molecule perpendicular to the surfacewill be enhanced. In case of ThT, the thiazole (ring II) S atom and the N,N-dimethyl group N atom, are the possible sites through which a

binding to the surface of metal nanoparticle can be facilitated. The calculated Raman spectra of ThT, as obtained after optimization of geometry by DFT (B3LYP/6-31+G*), showing a very good match with the Raman spectra of ThT in solid as well as aqueous solution, indicates that the torsional angle (φ) between the BT and DMAB moieties is ~ 37° at ground state. It is reported in a SERS study of ThT on silver nanoparticles surface[460] that ThT may exist in two structural conformers where φ ~ 37° in one andφ ~ 90° in the other. In our study, we obtained that in case of adsorption of ThT on GNPs at concentrations below 10^{-7}M, ThT molecules that are attached to GNPs surface have φ ~ 90°. At concentration higher than 10^{-7} M, the molecules form multilayer where the φ ~ 37°, as the local environment of the molecules in a multilayer is similar to that in an aqueous solution. Moreover, the observation of SERS spectra for ThT concentration as low as 100 picomolar over GNP, indicates that the method has a sub-nanomolar sensitivity.

The apparent enhancement factors (AEF)[461] can be calculated for the enhanced Raman intensity of ThT (10^{-7} M) on GNPs and SCFs,

$$AEF = \frac{\sigma_{SERS}\, C_{NRS}}{\sigma_{NRS}\, C_{SERS}} \qquad (6.1)$$

where C and σ corresponds to the concentration of the molecule and the area of the Raman bands, respectively. The AEF values for the Raman bands are included in Table 6.3. Average AEF as observed for ThT on GNPs and SCFs is in the range of 10^5-10^6.

6.3. Conclusion

In this chapter, upon investigation of structural, conformational information of DMDT on the surface of metal NPs by SERS and DFT techniques, it is revealed that there exists a selectivity in the binding affinity of S and N atom towards Au and Ag surface, respectively, if both the groups are present on the same molecule. SERS study of ThT over GNPs

revealed that at monolayer and sub-monolayer coverage, ThT molecules show as torsional angle, φ ~ 90°, which is different from the φ~ 37°, which is observed in aqueous solution. Thus, the metal surface was found to influence the conformational change in adsorbed of molecules where a molecule can be stabilized at a local minima rather than in a stable global minima.

7

Summary and Future scope

In this chapter, the chapter-wise summary as well as the future scope of the works done in this thesis is discussed

7.1. Chapter-wise discussion of the works discussed in the chapters

7.1.1. Summary and future scope of tryptophan capped GNPs

In chapter 3, Trp was used to reduce Au^{3+} to GNPs mediated through a pH dependent decarboxylation pathway. GNPs which were synthesized at pH 6 were found to be the most stable. GNPs had negative surface charge due to COO^- group of the adsorbed oxidized Trp species. pH played an important role in the synthesis of GNPs as well as in controlling the colloidal stability of GNPs. This synthetic method is novel due to the non-requirement of any stabilizer. Additionally, the pH sensitive property of the surface of GNPs led to accumulation of GNPs at the polar- non polar liquid-liquid interface at low pH. There is a possibility of accumulation of GNPs in the extra-cellular interface, as observed in the case of simulated environment of cell membrane discussed in chapter 3. *In-vitro* MTT assay of GNPs in presence of gamma radiation (2 Gy) in U-87MG showed slight decrease in the survival fractions. Further experiments are in progress to study the effect of low energy X-rays on the survival fraction. At lower X-ray energies, due to high photoelectric absorption cross-section, there is possibility of higher radio-sensitization efficiency.

7.1.2. Summary and future scope of GNPs and AgNPs loaded alginate film

In chapter 4, successful synthesis of Ca-Fe-Alg films as well as AgNPs-Alg films was demonstrated. Both CV and R6G were detected using the noble metal nanoparticle loaded alginate film. Minimum concentration of CV that was detected by this method is 10 nM or ~4

ppb. CV is known to show toxicity and carcinogenicity above 1 ppb dose.[268] It was also found that AgNPs-Alg film showed an enhancement of 29% in the calibrated dose in EBT3 films upon exposure to 57 keV X-ray. Additionally, Raman spectra of the above EBT3 films in absence and presence of AgNPs-Alg films showed a distinct variation in line with the colorimetric study. AgNP-Alg films as well as Au/Ca-Fe-Alg films are being used for further dosimetric study in presence of ^{125}I-source for brachytherapy applications.

7.1.3. Summary and future scope of AgNPs and Ag/AgCl NPDs

In chapter 5, It was observed that AgNPs were used either as intact nanoparticles or as AgCl/Ag NPDs for detection of sildenafil citrate. Citrate capped AgNPs showed best SERS based sensing of SC of concentration as low as 66.7 pg/ml. A concentration of SC of 50 pg/ml was reported to be the lowest achievable detection limit using other contemporary techniques. Both the detection methods were found to be simple, sensitive and rapid. In future, the sensing of derivatives of SC, such as tadalafil, verdenafil, etc. will be taken up. Moreover, sildenafil will also be detected in the matrix of herbal medicines.

7.1.4. Summary and future scope of SERS based sensing of DMDT and ThT

In chapter 6, a detailed structural and conformational investigation based on surface enhanced Raman scattering technique of DMTD and ThT is discussed in this chapter. DMDT was found to show surface selective binding to silver and gold nanoparticles via N-atom and S-atom, respectively. This information is vital for drug delivery applications. Moreover, ThT was also found to show torsional angle, $\varphi \sim 90°$ at a specific condition, indicating the influence of nanoparticle surface on orientation of the rotor molecules. The knowledge garnered through this study will be used for detailed investigation of other molecules with both N as well as S atoms.

List of Abbreviations

AFM	Atomic Force Microscope
AgNPs	Silver Nanoparticles
Alg	Alginate
ATP	Adenosine Triphosphate
CARS	Coherent Anti-Stokes Raman
CCD	Charge Coupled Detector
CM	Chemical
CMC	Critical Micelle Concentration
CNT	Carbon Nanotube
CV	Crystal Violet
DC	Direct Current
DFT	Density Functional Theory
DLVO	Boris Derjaguin And Lev Landau, Evert Verwey And Theodoor Overbeek
DMTD	2,5-Dimercapto-1,3,4-Thiadiazole
DNA	Deoxyribonucleic Acid
ED	Erectile Dysfunction
EM	Electromagnetic
FIR	Far-Infrared
FTIR	Fourier Transform Infrared Spectroscopy
GC	Gas Chromatography
GI50	Growth Inhibition 50%
GMP	Cyclic Guanosine Monophosphate

GNPs	Gold Nanoparticles
HaCaT	Human Transformed Keratinocyte
HOMO	Highest Occupied Molecular Orbital
IR	Infrared
LINAC	Linear Accelerator
LOD	Limit of Detection
LOQ	Limit of Quantitation
LSPR	Localized Surface Plasmon Resonance
LUMO	Lowest Unoccupied Molecular Orbital
LWD	Long Working Distance
MIR	Mid-Infrared
MO	Molecular Orbital
NIR	Near-Infrared
NMNPs	Noble Metal Nanoparticles
NMs	Nanomaterials
NPD	Nanoparticle Dimer
OTC	Over the Counter
PDE-5	Phosphodiesterase-5
PMT	Photomultiplier Tube
PPO	Pyrazolo[4,3-D]Pyrimidin-7-One
PSPR	Propagating Surface Plasmon Resonance
PVP	Polyvinylpyrrolidone
R6G	Rhodamine 6G
ROS	Reactive Oxygen Species
RR	Resonance Raman

SAED	Selective Area Electron Diffraction
SC	Sildenafil Citrate
SCF	Silver Coated Film
SDS	Sodium Dodecyl Sulphate
SEM	Scanning Electron Microscope
SERRS	Surface Enhanced Resonance Raman Scattering
SERS	Surface Enhanced Raman Scattering
SHE	Standard Hydrogen Electrode
SiHa	Human Cervical Cancer
SP	Surface Plasmon
SPR	Surface Plasmon Resonance
SR	Simulated Raman
TD-DFT	Time Dependent Density Functional Theory
TEM	Transmission Electron Microscope
ThT	Thioflavin T
Trp	L-Tryptophan
U-251MG	Human Malignant Glioblastoma
WHO	World Health Organisation

References

1. Buxton G. V. and Stuart C. R., *Journal of the Chemical Society, Faraday Transactions*, 1995, **91**, 279.
2. Zsigmondy R. A., *Properties of colloids*, Elsevier Publishing Company, Amsterdam, 1966.
3. Freestone I., Meeks N., Sax M. and Higgitt C., *Gold Bulletin*, 2007, **40**, 270.
4. Jeevanandam J., Barhoum A., Chan Y. S., Dufresne A. and Danquah M. K., *Beilstein Journal of Nanotechnology*, 2018, **9**, 1050.
5. Siqueira J. R. and Oliveira O. N., 2017, Nanostructures, William Andrew Publishing,p. 233-249.
6. Yadav B. and Kumar R., *International Journal of Nanotechnology and Applications*, 2008, **1**, 15.
7. Thompson B. C. and Fréchet J. M. J., *Angewandte Chemie International Edition*, 2008, **47**, 58.
8. Manish K. and Kaisar R., *Pharmaceutical Nanotechnology*, 2017, **5**, 169.
9. Novoselov K. S., Geim A. K., Morozov S. V., Jiang D., Zhang Y., Dubonos S. V., Grigorieva I. V. and Firsov A. A., *Science*, 2004, **306**, 666.
10. Novoselov K. S., Fal′ko V. I., Colombo L., Gellert P. R., Schwab M. G. and Kim K., *Nature*, 2012, **490**, 192.
11. Li X. and Wei B., *Nano Energy*, 2013, **2**, 159.
12. Katz E. and Willner I., *ChemPhysChem*, 2004, **5**, 1084.
13. Gohardani O., Elola M. C. and Elizetxea C., *Progress in Aerospace Sciences*, 2014, **70**, 42.

14. Lee S. W., Kim J., Chen S., Hammond P. T. and Shao-Horn Y., *ACS Nano*, 2010, **4**, 3889.

15. Yu P. Y. and Cardona M., 2010, Fundamentals of Semiconductors: Physics and Materials Properties, Springer Berlin Heidelberg,p. 17-106.

16. Davydov S. Y., *Technical Physics*, 2002, **47**, 92.

17. Zalevsky Z. and Abdulhalim I., 2014, Integrated Nanophotonic Devices (Second Edition), William Andrew Publishing,p. 179-245.

18. Mead C. A. and Spitzer W. G., *Physical Review*, 1964, **134**, A713.

19. Aldakov D. and Reiss P., *The Journal of Physical Chemistry C*, 2019, **123**, 12527.

20. Mishra Y. K., Murugan N. A., Kotakoski J. and Adam J., *Vacuum*, 2017, **146**, 304.

21. Nair A. K., Mayeen A., Shaji L. K., Kala M. S., Thomas S. and Kalarikkal N., 2018, Characterization of Nanomaterials, Woodhead Publishing,p. 269-299.

22. Singh M., Goyal M. and Devlal K., *Journal of Taibah University for Science*, 2018, **12**, 470.

23. Akbarzadeh A., Rezaei-Sadabady R., Davaran S., Joo S. W., Zarghami N., Hanifehpour Y., Samiei M., Kouhi M. and Nejati-Koshki K., *Nanoscale Res Lett*, 2013, **8**, 102.

24. Fatemeh S., Hamideh P., Ahad M. and Mohammad R., *Current Pharmaceutical Design*, 2015, **21**, 6214.

25. Abbasi E., Aval S. F., Akbarzadeh A., Milani M., Nasrabadi H. T., Joo S. W., Hanifehpour Y., Nejati-Koshki K. and Pashaei-Asl R., *Nanoscale Res Lett*, 2014, **9**, 247.

26. Lee R. W., Shenoy D. B. and Sheel R., 2010, Handbook of Non-Invasive Drug Delivery Systems, William Andrew Publishing,p. 37-58.

27. Yadav H. K. S., Almokdad A. A., shaluf S. I. M. and Debe M. S., 2019, Nanocarriers for Drug Delivery, Elsevier,p. 531-556.

28. Li L.-L., An H.-W., Peng B., Zheng R. and Wang H., *Materials Horizons*, 2019, **6**, 1794.

29. Jijie R., Barras A., Boukherroub R. and Szunerits S., *Journal of Materials Chemistry B*, 2017, **5**, 8653.

30. Yoo S. C., Lee J. and Hong S. H., *Composites Part B: Engineering*, 2019, **176**, 107235.

31. Xu H., Li H., Xia J., Yin S., Luo Z., Liu L. and Xu L., *ACS Applied Materials & Interfaces*, 2011, **3**, 22.

32. Requejo-Isidro J., del Coso R., Solis J., Gonzalo J. and Afonso C. N., *Applied Physics Letters*, 2005, **86**, 193104.

33. Trasatti S., *Journal*, 1986, **58**, 955.

34. Brousseau P. and Anderson C. J., *Propellants, Explosives, Pyrotechnics*, 2002, **27**, 300.

35. Bondi J. F., Oyler K. D., Ke X., Schiffer P. and Schaak R. E., *Journal of the American Chemical Society*, 2009, **131**, 9144.

36. Zola A. S., Ribeiro R. U., Bueno J. M. C., Zanchet D. and Arroyo P. A., *Journal of Experimental Nanoscience*, 2014, **9**, 398.

37. Saif S., Tahir A. and Chen Y., *Nanomaterials (Basel)*, 2016, **6**, 209.

38. Amendola V., Pilot R., Frasconi M., Maragò O. M. and Iatì M. A., *Journal of Physics: Condensed Matter*, 2017, **29**, 203002.

39. Mogensen K. B. and Kneipp K., *The Journal of Physical Chemistry C*, 2014, **118**, 28075.

40. Cueto M., Piedrahita M., Caro C., Martínez-Haya B., Sanz M., Oujja M. and Castillejo M., *The Journal of Physical Chemistry C*, 2014, **118**, 11432.

41. Zheng P., Tang H., Liu B., Kasani S., Huang L. and Wu N., *Nano Research*, 2019, **12**, 63.

42. Thompson D. T., *Nano Today*, 2007, **2**, 40.

43. Hutchings G. J. and Edwards J. K., 2012, Frontiers of Nanoscience, Elsevier,p. 249-293.

44. Suchomel P., Kvitek L., Prucek R., Panacek A., Halder A., Vajda S. and Zboril R., *Scientific Reports*, 2018, **8**, 4589.

45. Cheon J. Y., Kim S. J. and Park W. H., 2019, **2019**, 8.

46. Ojha N. K., Zyryanov G. V., Majee A., Charushin V. N., Chupakhin O. N. and Santra S., *Coordination Chemistry Reviews*, 2017, **353**, 1.

47. Frogneux X., Borondics F., Lefrançois S., D'Accriscio F., Sanchez C. and Carenco S., *Catalysis Science & Technology*, 2018, **8**, 5073.

48. Mei Y., Sharma G., Lu Y., Ballauff M., Drechsler M., Irrgang T. and Kempe R., *Langmuir*, 2005, **21**, 12229.

49. Saha K., Agasti S. S., Kim C., Li X. and Rotello V. M., *Chemical Reviews*, 2012, **112**, 2739.

50. Priyadarshini E. and Pradhan N., *Sensors and Actuators B: Chemical*, 2017, **238**, 888.

51. Makwana B. A., Vyas D. J., Bhatt K. D., Darji S. and Jain V. K., *Applied Nanoscience*, 2016, **6**, 555.

52. Sebastian M., Aravind A. and Mathew B., *Nanotechnology*, 2018, **29**, 355502.

53. Ghoto S. A., Khuhawar M. Y., Jahangir T. M. and Mangi J. u. D., *Journal of Nanostructure in Chemistry*, 2019, **9**, 77.

54. Momeni S., Ahmadi R., Safavi A. and Nabipour I., *Talanta*, 2017, **175**, 514.

55. Liu I. P., Chang C.-H., Chou T. C. and Lin K.-W., *Sensors and Actuators B: Chemical*, 2019, **291**, 148.

56. Wu G.-W., He S.-B., Peng H.-P., Deng H.-H., Liu A.-L., Lin X.-H., Xia X.-H. and Chen W., *Analytical Chemistry*, 2014, **86**, 10955.

57. Dykman L. A. and Khlebtsov N. G., *Acta Naturae*, 2011, **3**, 34.

58. Sharma G., Nam J.-S., Sharma A. R. and Lee S.-S., *Molecules*, 2018, **23**, 2268.

59. Marassi V., Di Cristo L., Smith S. G. J., Ortelli S., Blosi M., Costa A. L., Reschiglian P., Volkov Y. and Prina-Mello A., *R Soc Open Sci*, 2018, **5**, 171113.

60. Hassanien R., Husein D. Z. and Al-Hakkani M. F., *Heliyon*, 2018, **4**, e01077.

61. Tahvilian R., Zangeneh M. M., Falahi H., Sadrjavadi K., Jalalvand A. R. and Zangeneh A., *Applied Organometallic Chemistry*, 2019, **33**, e5234.

62. Pedone D., Moglianetti M., De Luca E., Bardi G. and Pompa P. P., *Chemical Society Reviews*, 2017, **46**, 4951.

63. Vallabani N. V. S. and Singh S., *3 Biotech*, 2018, **8**, 279.

64. Feng Q., Liu Y., Huang J., Chen K., Huang J. and Xiao K., *Scientific Reports*, 2018, **8**, 2082.

65. Bulte J. W. M. and Kraitchman D. L., *NMR in Biomedicine*, 2004, **17**, 484.

66. Böer K. W., *physica status solidi c*, 2017, **14**, 1700206.

67. Blanc F., *ACS Central Science*, 2018, **4**, 1081.

68. Ashoori R. C., *Nature*, 1996, **379**, 413.

69. 1999, II-VI and I-VII Compounds; Semimagnetic Compounds, Springer Berlin Heidelberg,p. 1-5.

70. Raether H., 1988, Surface Plasmons on Smooth and Rough Surfaces and on Gratings, Springer Berlin Heidelberg,p. 1-3.

71. Jackson J. D., *Classical electrodynamics*, Third edition. New York : Wiley, [1999] ©1999, 1999.

72. Kreibig U. and Vollmer M., 1995, Optical Properties of Metal Clusters, Springer Berlin Heidelberg,p. 1-12.

73. Khlebtsov N. G., *Quantum Electronics*, 2008, **38**, 504.

74. Bhattacharya K., *Physica Scripta*, 2016, **91**, 035501.

75. Bertolini D. and Tani A., *Molecular Physics*, 1992, **75**, 1065.

76. Pérez-Juste J., Pastoriza-Santos I., Liz-Marzán L. M. and Mulvaney P., *Coordination Chemistry Reviews*, 2005, **249**, 1870.

77. Burda C., Chen X., Narayanan R. and El-Sayed M. A., *Chemical Reviews*, 2005, **105**, 1025.

78. Encina E. R. and Coronado E. A., *The Journal of Physical Chemistry C*, 2010, **114**, 3918.

79. Jain P. K. and El-Sayed M. A., *Chemical Physics Letters*, 2010, **487**, 153.

80. Braeuer A., 2015, Supercritical Fluid Science and Technology, Elsevier,p. 41-192.

81. , Characterization of Materials.

82. Xu R., *Particuology*, 2015, **18**, 11.

83. Bumbrah G. S. and Sharma R. M., *Egyptian Journal of Forensic Sciences*, 2016, **6**, 209.

84. Berthomieu C. and Hienerwadel R., *Photosynthesis Research*, 2009, **101**, 157.

85. Schlücker S., *Angewandte Chemie International Edition*, 2014, **53**, 4756.

86. Homola J., Yee S. S. and Gauglitz G., *Sensors and Actuators B: Chemical*, 1999, **54**, 3.

87. Banwell C. N. and McCash E. M., *Fundamentals of molecular spectroscopy*, McGraw-Hill, London; New York, 1994.

88. Atkins P. and De Paula J., *Atkins' physical chemistry*, Oxford University Press, Oxford, 2010.

89. Marwa E.-A., 2019, DOI: 10.5772/intechopen.82210.

90. Jiang J., Wang S., Deng H., Wu H., Chen J. and Liao J., *R Soc Open Sci*, **5**, 181099.

91. Gorbachevskii M. V., Kopitsyn D. S., Kotelev M. S., Ivanov E. V., Vinokurov V. A. and Novikov A. A., *RSC Advances*, 2018, **8**, 19051.

92. Liebig F., Henning R., Sarhan R. M., Prietzel C., Bargheer M. and Koetz J., *Nanotechnology*, 2018, **29**, 185603.

93. Cassar R. N., Graham D., Larmour I., Wark A. W. and Faulds K., *Vibrational Spectroscopy*, 2014, **71**, 41.

94. Britto Hurtado R., Cortez-Valadez M., Ramírez-Rodríguez L. P., Larios-Rodriguez E., Alvarez R. A. B., Rocha-Rocha O., Delgado-Beleño Y., Martinez-Nuñez C. E., Arizpe-Chávez H., Hernández-Martínez A. R. and Flores-Acosta M., *Physics Letters A*, 2016, **380**, 2658.

95. Rekha C. R., Nayar V. U. and Gopchandran K. G., *Journal of Science: Advanced Materials and Devices*, 2018, **3**, 196.

96. Wu S.-R., Tian X.-D., Liu S.-Y., Zhang Y. and Li J.-F., *Journal of Raman Spectroscopy*, 2018, **49**, 659.

97. Petti L., Capasso R., Rippa M., Pannico M., La Manna P., Peluso G., Calarco A., Bobeico E. and Musto P., *Vibrational Spectroscopy*, 2016, **82**, 22.

98. Wang R., Zhang L., Zou S. and Zhang H., *Microchemical Journal*, 2019, **150**, 104127.

99. Sarkar A., Kapoor S. and Mukherjee T., *Journal of Colloid and Interface Science*, 2005, **287**, 496.

100. Bassi B., Albini B., D'Agostino A., Dacarro G., Pallavicini P., Galinetto P. and Taglietti A., *Nanotechnology*, 2018, **30**, 025302.

101. Kim A., Barcelo S. J. and Li Z., *Nanotechnology*, 2014, **26**, 015502.

102. Lee J.-C., Kim W. and Choi S., *International Journal of Precision Engineering and Manufacturing-Green Technology*, 2017, **4**, 221.

103. Wei C., Li M. and Zhao X., 2018, **9**.

104. Hussain A., Sun D.-W. and Pu H., *Food Additives & Contaminants: Part A*, 2019, **36**, 851.

105. Maddipatla D., Janabi F., Narakathu B. B., Ali S., Turkani V. S., Bazuin B. J., Fleming P. D. and Atashbar M. Z., *Sensing and Bio-Sensing Research*, 2019, **24**, 100281.

106. Luo Y., Jing Q., Li C., Liang A., Wen G., He X. and Jiang Z., *Sensors and Actuators B: Chemical*, 2018, **255**, 3187.

107. Lee H. K., Lee Y. H., Koh C. S. L., Phan-Quang G. C., Han X., Lay C. L., Sim H. Y. F., Kao Y.-C., An Q. and Ling X. Y., *Chemical Society Reviews*, 2019, **48**, 731.

108. Chulhai D. V. and Jensen L., *The Journal of Physical Chemistry C*, 2013, **117**, 19622.

109. Liang A., Wang H., Yao D. and Jiang Z., *Food Chemistry*, 2019, **271**, 39.

110. Gracie K., Dhamodharan V., Pradeepkumar P. I., Faulds K. and Graham D., *Analyst*, 2014, **139**, 4458.

111. Maiti N., Chadha R., Das A. and Kapoor S., *RSC Advances*, 2016, **6**, 62529.

112. Le Ru E. C., Meyer S. A., Artur C., Etchegoin P. G., Grand J., Lang P. and Maurel F., *Chemical Communications*, 2011, **47**, 3903.

113. Xie W. and Schlücker S., *Chemical Communications*, 2018, **54**, 2326.

114. Harroun S. G., Zhang Y., Chen T.-H., Hsu C.-L. and Chang H.-T., *Journal of Raman Spectroscopy*, 2018, **49**, 376.

115. Farooq M. U., Novosad V., Rozhkova E. A., Wali H., Ali A., Fateh A. A., Neogi P. B., Neogi A. and Wang Z., *Scientific reports*, 2018, **8**, 2907.

116. Kanwal Z., Raza M. A., Riaz S., Manzoor S., Tayyeb A., Sajid I. and Naseem S., 2019, **6**, 182135.

117. Dorsey J. F., Sun L., Joh D. Y., Witztum A., Zaki A. A., Kao G. D., Alonso-Basanta M., Avery S., Tsourkas A. and Hahn S. M. J. T. C. R., *2013*, 2013, **2**, 280.

118. Knoll G. F., 1979.

119. Lechtman E. and Pignol J.-P., *Scientific Reports*, 2017, **7**, 13268.

120. Chow J. C. L., 2016, Handbook of Nanoparticles, Springer International Publishing,p. 41-65.

121. Larson D., Bodell W. J., Ling C., Phillips T. L., Schell M., Shrieve D. and Troxel T., *International Journal of Radiation Oncology*Biology*Physics*, 1989, **16**, 171.

122. Bai C., Zeng G. L. and Gullberg G. T., *Physics in Medicine and Biology*, 2000, **45**, 1275.

123. Weeks K. J., Litvinenko V. N. and Madey J. M. J., *Medical Physics*, 1997, **24**, 417.

124. Hassanpour S. H. and Dehghani M., *Journal of Cancer Research and Practice*, 2017, **4**, 127.

125. Lahue R. S., Au K. G. and Modrich P., *Science*, 1989, **245**, 160.

126. Raviraj J., Bokkasam V., Kumar V., Reddy U. and Suman V., 2014, **25**, 83.

127. Adams G. E. and Dewey D. L., *Biochemical and Biophysical Research Communications*, 1963, **12**, 473.

128. Shukla R., Bansal V., Chaudhary M., Basu A., Bhonde R. R. and Sastry M., *Langmuir*, 2005, **21**, 10644.

129. Rosa S., Connolly C., Schettino G., Butterworth K. T. and Prise K. M., *Cancer nanotechnology*, 2017, **8**, 2.

130. San-Millán I. and Brooks G. A., *Carcinogenesis*, 2016, **38**, 119.

131. Samstein R. M., Ho A. L., Lee N. Y. and Barker C. A., 2014, **2014**, 7.

132. Calipel A., Lux A.-l., Guérin S., Lefaix J.-L., Laurent C., Bernaudin M. and Mouriaux F., *Investigative Ophthalmology & Visual Science*, 2015, **56**, 3085.

133. Iqbal P., Preece J. A. and Mendes P. M., *Supramolecular Chemistry*, 2012.

134. Kulkarni S. K., 2015, Nanotechnology: Principles and Practices, Springer International Publishing,p. 55-76.

135. Schmid G. and Fenske D., *Philosophical Transactions of the Royal Society A: Mathematical, Physical and Engineering Sciences*, 2010, **368**, 1207.

136. Kus M., Alic T. Y., Kirbiyik C., Baslak C., Kara K. and Kara D. A., 2018, Handbook of Nanomaterials for Industrial Applications, Elsevier,p. 392-429.

137. Iravani S., Korbekandi H., Mirmohammadi S. V. and Zolfaghari B., *Res Pharm Sci*, 2014, **9**, 385.

138. Patel K., Bharatiya B., Mukherjee T., Soni T., Shukla A. and Suhagia B. N., *Journal of Dispersion Science and Technology*, 2017, **38**, 626.

139. Sun L., Pu S., Li J., Cai J., Zhou B., Ren G., Ma Q. and Zhong L., *International Journal of Biological Macromolecules*, 2019, **122**, 770.

140. Groenewald T., *Journal of Applied Electrochemistry*, 1975, **5**, 71.

141. Pacioni N. L., Borsarelli C. D., Rey V. and Veglia A. V., 2015, Silver Nanoparticle Applications: In the Fabrication and Design of Medical and Biosensing Devices, Springer International Publishing,p. 13-46.

142. Zarabi M. F., Arshadi N., Farhangi A. and Akbarzadeh A., *Indian J Clin Biochem*, 2014, **29**, 306.

143. de Matos R. A. and Courrol L. C., *Amino Acids*, 2017, **49**, 379.

144. Shankar S. and Rhim J.-W., *Carbohydrate Polymers*, 2015, **130**, 353.

145. Zare D., Akbarzadeh A., Barkhi M., Khoshnevisan K., Bararpour N., Noruzi M. and Tabatabaei M., *Synthesis and Reactivity in Inorganic, Metal-Organic, and Nano-Metal Chemistry*, 2012, **42**, 266.

146. Thiyagarajan K., Bharti V. K., Tyagi S., Tyagi P. K., Ahuja A., Kumar K., Raj T. and Kumar B., *RSC Advances*, 2018, **8**, 23213.

147. Durmazel S., Üzer A., Erbil B., Sayın B. and Apak R., *ACS Omega*, 2019, **4**, 7596.

148. Yakout S. M. and Mostafa A. A., *Int J Clin Exp Med*, 2015, **8**, 3538.

149. Suvarna S., Das U., Kc S., Mishra S., Sudarshan M., Saha K. D., Dey S., Chakraborty A. and Narayana Y., *PLoS One*, 2017, **12**, e0178202.

150. Sambalova O., Thorwarth K., Heeb N. V., Bleiner D., Zhang Y., Borgschulte A. and Kroll A., *ACS Omega*, 2018, **3**, 724.

151. Abrica-González P., Zamora-Justo J. A., Sotelo-López A., Vázquez-Martínez G. R., Balderas-López J. A., Muñoz-Diosdado A. and Ibáñez-Hernández M., *Nanoscale Research Letters*, 2019, **14**, 258.

152. Kalaivani R., Maruthupandy M., Muneeswaran T., Hameedha Beevi A., Anand M., Ramakritinan C. M. and Kumaraguru A. K., *Frontiers in Laboratory Medicine*, 2018, **2**, 30.

153. Zhao X., Li Z., Deng Y., Zhao Z., Li X. and Xia Y., *Materials (Basel)*, 2017, **10**, 557.

154. Kolya H., Pal S., Pandey A. and Tripathy T., *European Polymer Journal*, 2015, **66**, 139.

155. Zhenjiang L., *Synlett*, 2005, **2005**, 182.

156. Ambrosi A., Chua C. K., Bonanni A. and Pumera M., *Chemistry of Materials*, 2012, **24**, 2292.

157. Shiraishi Y., Tanaka H., Sakamoto H., Ichikawa S. and Hirai T., *RSC Advances*, 2017, **7**, 6187.

158. Malassis L., Dreyfus R., Murphy R. J., Hough L. A., Donnio B. and Murray C. B., *RSC Advances*, 2016, **6**, 33092.

159. Khan Z., Singh T., Hussain J. I. and Hashmi A. A., *Colloids and Surfaces B: Biointerfaces*, 2013, **104**, 11.

160. Anu Mary Ealia S. and Saravanakumar M. P., *IOP Conference Series: Materials Science and Engineering*, 2017, **263**, 032019.

161. Turro N. J., Ramamurthy V. and Scaiano J. C., *Principles of molecular photochemistry : an introduction*, Viva Books, New Delhi, 2015.

162. Mayerhöfer T. G., Höfer S. and Popp J., *Physical Chemistry Chemical Physics*, 2019, **21**, 9793.

163. Rabie U. M., *Journal of Molecular Structure*, 2013, **1034**, 393.

164. Abu-Dief A. M. and Mohamed I. M. A., *Beni-Suef University Journal of Basic and Applied Sciences*, 2015, **4**, 119.

165. Goodhew P. J., Humphreys F. J. and Beanland R., 2017.

166. Williams D. B. and Carter B. C., *Transmission electron microscopy. 3, 3*, Springer, New York, 2009.

167. Baxendale J. H. and Busi F., *The study of fast processes and transient species by electron pulse radiolysis*, Reidel, Dordrecht, 1982.

168. Schmidt K. H. and Buck W. L., *Science*, 1966, **151**, 70.

169. Smaller B., Remko J. R. and Avery E. C., *The Journal of Chemical Physics*, 1968, **48**, 5174.

170. Spinks J. W. T. and Woods R. J., *An introduction to radiation chemistry : J.W.T. Spinks and R.J. Woods*, John Wiley & Sons, New York, 1990.

171. Farhataziz R., Rodgers M. A. J. and Farhataziz, *Radiation chemistry : principles and applications*, VCH, Weinheim, 1987.

172. Ahmad S. A., *Atomic, molecular and cluster physics*, Narosa, New Delhi; London, 1997.

173. Jalili N. and Laxminarayana K., *Mechatronics*, 2004, **14**, 907.

174. Anker J. N., Hall W. P., Lyandres O., Shah N. C., Zhao J. and Van Duyne R. P., *Nature Materials*, 2008, **7**, 442.

175. Jain P. K., Huang X., El-Sayed I. H. and El-Sayed M. A., *Accounts of Chemical Research*, 2008, **41**, 1578.

176. De M., Ghosh P. S. and Rotello V. M., *Advanced Materials*, 2008, **20**, 4225.

177. Sperling R. A., Rivera Gil P., Zhang F., Zanella M. and Parak W. J., *Chemical Society Reviews*, 2008, **37**, 1896.

178. Li J. and Lin X., *Sensors and Actuators B: Chemical*, 2007, **126**, 527.

179. Zeng L., Wang H., Bo X. and Guo L., *Journal of Electroanalytical Chemistry*, 2012, **687**, 117.

180. Guo S. and Wang E., *Analytica Chimica Acta*, 2007, **598**, 181.

181. Myroshnychenko V., Rodríguez-Fernández J., Pastoriza-Santos I., Funston A. M., Novo C., Mulvaney P., Liz-Marzán L. M. and García de Abajo F. J., *Chemical Society Reviews*, 2008, **37**, 1792.

182. A.F. L., *Science of Sintering*, 2010, **42**, 15.

183. Li X., Tamada K., Baba A. and Hara M., *Journal of Nanoscience and Nanotechnology*, 2009, **9**, 408.

184. Sardar R., Funston A. M., Mulvaney P. and Murray R. W., *Langmuir*, 2009, **25**, 13840.

185. Jiang J., Oberdörster G. and Biswas P., *Journal of Nanoparticle Research*, 2009, **11**, 77.

186. Bohinc K., Kralj-Iglič V. and Iglič A., *Electrochimica Acta*, 2001, **46**, 3033.

187. Sylvestre J.-P., Poulin S., Kabashin A. V., Sacher E., Meunier M. and Luong J. H. T., *The Journal of Physical Chemistry B*, 2004, **108**, 16864.

188. Delong R. K., Reynolds C. M., Malcolm Y., Schaeffer A., Severs T. and Wanekaya A., *Nanotechnol Sci Appl*, 2010, **3**, 53.

189. Salata O. V., *J Nanobiotechnology*, 2004, **2**, 3.

190. Cai W., Gao T., Hong H. and Sun J., *Nanotechnol Sci Appl*, 2008, **1**, 17.

191. Mesbahi A., *Rep Pract Oncol Radiother*, 2010, **15**, 176.

192. Kim D. and Jon S., *Inorganica Chimica Acta*, 2012, **393**, 154.

193. Hainfeld J. F., Dilmanian F. A., Zhong Z., Slatkin D. N., Kalef-Ezra J. A. and Smilowitz H. M., *Physics in Medicine and Biology*, 2010, **55**, 3045.

194. Brown J. M., *Cancer*, 1985, **55**, 2222.

195. Wilson W. R. and Hay M. P., *Nature Reviews Cancer*, 2011, **11**, 393.

196. Tannock I. F. and Rotin D., *Cancer Research*, 1989, **49**, 4373.

197. Griffiths J. R., *Br J Cancer*, 1991, **64**, 425.

198. Nam J., Won N., Jin H., Chung H. and Kim S., *Journal of the American Chemical Society*, 2009, **131**, 13639.

199. Lee K. Y. and Han S. W., *Bull. Korean Chem. Soc.*, 2005, **26**, 3.

200. Sarkar A., Kapoor S. and Mukherjee T., *Research on Chemical Intermediates*, 2010, **36**, 403.

201. Enustun B. V. and Turkevich J., *Journal of the American Chemical Society*, 1963, **85**, 3317.

202. Samal A. K., Sreeprasad T. S. and Pradeep T., *Journal of Nanoparticle Research*, 2010, **12**, 1777.

203. Brust M., Walker M., Bethell D., Schiffrin D. J. and Whyman R., *Journal of the Chemical Society, Chemical Communications*, 1994, DOI: 10.1039/C39940000801, 801.

204. Jacob J. A., Naumov S., Mukherjee T. and Kapoor S., *Colloids and Surfaces B: Biointerfaces*, 2011, **87**, 498.

205. Iosin M., Baldeck P. and Astilean S., *Journal of Nanoparticle Research*, 2010, **12**, 2843.

206. Thomas S. R. and Stocker R., *Redox Report*, 1999, **4**, 199.

207. Amendola V. and Meneghetti M., *The Journal of Physical Chemistry C*, 2009, **113**, 4277.

208. Verwey E. J. W., *The Journal of Physical and Colloid Chemistry*, 1947, **51**, 631.

209. Đurović M. D., Puchta R., Bugarčić Ž. D. and van Eldik R., *Dalton Transactions*, 2014, **43**, 8620.

210. Streszewski B., Jaworski W., Pacławski K., Csapó E., Dékány I. and Fitzner K., *Colloids and Surfaces A: Physicochemical and Engineering Aspects*, 2012, **397**, 63.

211. Zaheer Z., Malik M. A., Al-Nowaiser F. M. and Khan Z., *Colloids and Surfaces B: Biointerfaces*, 2010, **81**, 587.

212. Leyton P., Brunet J., Silva V., Paipa C., Castillo M. V. and Brandán S. A., *Spectrochimica Acta Part A: Molecular and Biomolecular Spectroscopy*, 2012, **88**, 162.

213. Wangoo N., Bhasin K. K., Mehta S. K. and Suri C. R., *Journal of Colloid and Interface Science*, 2008, **323**, 247.

214. Si S. and Mandal T. K., *Chemistry – A European Journal*, 2007, **13**, 3160.

215. Cooper G. M., *The cell : a molecular approach*, ASM Press ; Sinauer Associates, Washington, D.C.; Sunderland, Mass., 2000.

216. Kotyńska J. and Figaszewski Z. A., *Biochimica et Biophysica Acta (BBA) - Biomembranes*, 2005, **1720**, 22.

217. Huang C.-H., *Biochemistry*, 1969, **8**, 344.

218. Elworthy P. H., *Journal of the Chemical Society (Resumed)*, 1959, DOI: 10.1039/JR9590000813, 813.

219. Tatur S., Maccarini M., Barker R., Nelson A. and Fragneto G., *Langmuir*, 2013, **29**, 6606.

220. Forslund A. H., Hambræus L., van Beurden H., Holmbäck U., El-Khoury A. E., Hjorth G., Olsson R., Stridsberg M., Wide L., Åkerfeldt T., Regan M. and Young V. R., *American Journal of Physiology-Endocrinology and Metabolism*, 2000, **278**, E857.

221. Matthews D. M., *Journal of Clinical Pathology*, 1971, **s3-5**, 29.

222. Michael A. F., Drummond K. N., Doeden D., Anderson J. A. and Good R. A., *The Journal of Clinical Investigation*, 1964, **43**, 1730.

223. Rose D. P., *Journal of clinical pathology*, 1972, **25**, 17.

224. Orellana E. A. and Kasinski A. L., *Bio Protoc*, 2016, **6**, e1984.

225. Mahajan S. D., Law W.-C., Aalinkeel R., Reynolds J., Nair B. B., Yong K.-T., Roy I., Prasad P. N. and Schwartz S. A., 2012, Methods in Enzymology, Academic Press,p. 41-60.

226. Pérez-Mayen L., Oliva J., Torres-Castro A. and De la Rosa E., *Nanoscale*, 2015, **7**, 10249.

227. Tian F., Bonnier F., Casey A., Shanahan A. E. and Byrne H. J., *Analytical Methods*, 2014, **6**, 9116.

228. Ringe E., Langille M. R., Sohn K., Zhang J., Huang J., Mirkin C. A., Van Duyne R. P. and Marks L. D., *The Journal of Physical Chemistry Letters*, 2012, **3**, 1479.

229. Nehl C. L. and Hafner J. H., *Journal of Materials Chemistry*, 2008, **18**, 2415.

230. Derkachova A., Kolwas K. and Demchenko I., *Plasmonics*, 2016, **11**, 941.

231. Du L., Lei D. Y., Yuan G., Fang H., Zhang X., Wang Q., Tang D., Min C., Maier S. A. and Yuan X., *Scientific Reports*, 2013, **3**, 3064.

232. Ghosh S. K. and Pal T., *Chemical Reviews*, 2007, **107**, 4797.

233. Wang X., Li M., Meng L., Lin K., Feng J., Huang T., Yang Z. and Ren B., *ACS Nano*, 2014, **8**, 528.

234. Sanz J. M., Ortiz D., Alcaraz de la Osa R., Saiz J. M., González F., Brown A. S., Losurdo M., Everitt H. O. and Moreno F., *The Journal of Physical Chemistry C*, 2013, **117**, 19606.

235. Laurent G., Félidj N., Truong S. L., Aubard J., Lévi G., Krenn J. R., Hohenau A., Leitner A. and Aussenegg F. R., *Nano Letters*, 2005, **5**, 253.

236. Bruzas I., Lum W., Gorunmez Z. and Sagle L., *Analyst*, 2018, **143**, 3990.

237. Venkata P. G., Aslan M. M., Mengüç M. P. and Videen G., *Journal of Heat Transfer*, 2006, **129**, 60.

238. Maiti N., Chadha R., Das A. and Kapoor S., *Spectrochimica Acta Part A: Molecular and Biomolecular Spectroscopy*, 2015, **149**, 949.

239. Zhu T., Vasilev K., Kreiter M., Mittler S. and Knoll W., *Langmuir*, 2003, **19**, 9518.

240. Deraedt C., Salmon L., Gatard S., Ciganda R., Hernandez R., Ruiz J. and Astruc D., *Chemical Communications*, 2014, **50**, 14194.

241. Nuopponen M. and Tenhu H., *Langmuir*, 2007, **23**, 5352.

242. Tian Y., Liu H., Zhao G. and Tatsuma T., *The Journal of Physical Chemistry B*, 2006, **110**, 23478.

243. Kho K. W., Shen Z. X., Zeng H. C., Soo K. C. and Olivo M., *Analytical Chemistry*, 2005, **77**, 7462.

244. Palgrave R. G. and Parkin I. P., *Chemistry of Materials*, 2007, **19**, 4639.

245. Pilot R., *Journal of Raman Spectroscopy*, 2018, **49**, 954.

246. Wei W., Du Y., Zhang L., Yang Y. and Gao Y., *Journal of Materials Chemistry C*, 2018, **6**, 8793.

247. Lee M., Oh K., Choi H.-K., Lee S. G., Youn H. J., Lee H. L. and Jeong D. H., *ACS Sensors*, 2018, **3**, 151.

248. dos Santos D. S., Goulet P. J. G., Pieczonka N. P. W., Oliveira O. N. and Aroca R. F., *Langmuir*, 2004, **20**, 10273.

249. Lee K. Y. and Mooney D. J., *Progress in Polymer Science*, 2012, **37**, 106.

250. Grant G. T., Morris E. R., Rees D. A., Smith P. J. C. and Thom D., *FEBS Letters*, 1973, **32**, 195.

251. Lee B. B., Ravindra P. and Chan E. S., *Chemical Engineering & Technology*, 2013, **36**, 1627.

252. Benavides S., Villalobos-Carvajal R. and Reyes J. E., *Journal of Food Engineering*, 2012, **110**, 232.

253. Mele E., Anyfantis G. C., Fragouli D., Ruffilli R. and Athanassiou A., *RSC Advances*, 2014, **4**, 20449.

254. Banerjee A., Nayak D. and Lahiri S., *Biochemical Engineering Journal*, 2007, **33**, 260.

255. Min J. H. and Hering J. G., *Water Research*, 1998, **32**, 1544.

256. Suhandy D. and Yulia M., *Int J Food Sci*, 2017, **2017**, 6274178.

257. Brus J., Urbanova M., Czernek J., Pavelkova M., Kubova K., Vyslouzil J., Abbrent S., Konefal R., Horský J., Vetchy D., Vysloužil J. and Kulich P., *Biomacromolecules*, 2017, **18**, 2478.

258. Phukan S., Bharali P., Das A. K. and Rashid M. H., *RSC Advances*, 2016, **6**, 49307.

259. Maher R. C., 2012, Raman Spectroscopy for Nanomaterials Characterization, Springer Berlin Heidelberg,p. 215-260.

260. Das A., Chadha R., Maiti N. and Kapoor S., *Materials Science and Engineering: C*, 2015, **55**, 34.

261. Cañamares M. V., Chenal C., Birke R. L. and Lombardi J. R., *The Journal of Physical Chemistry C*, 2008, **112**, 20295.

262. Balavandy S. K., Shameli K., Abidin Z. Z. and *Int. J. Electrochem. Sci.* , 2015, **10**, 486

263. Das A., Maiti N., Dhayagude A. C., Pathak A. K., Chadha R., Neogy S. and Kapoor S., *Colloids and Surfaces A: Physicochemical and Engineering Aspects*, 2019, **582**, 123864.

264. Zhang K., Zeng T., Tan X., Wu W., Tang Y. and Zhang H., *Applied Surface Science*, 2015, **347**, 569.

265. Liu P., Jin H., Guo Z., Ma J., Zhao J., Li D., Wu H. and Gu N., *Int J Nanomedicine*, 2016, **11**, 5003.

266. Mirza J. A., Park H., Park S.-Y. and Ye S.-J., *Medical Physics*, 2016, **43**, 4520.

267. Talarico O. S., Krylova T. A. and Melnik N. N., *Medical Physics*, 2019, **46**, 1883.

268. Mani S. and Bharagava R. N., 2016, Reviews of Environmental Contamination and Toxicology Volume 237, Springer International Publishing,p. 71-104.

269. Firenzuoli F. and Gori L., *Evidence-based Complementary and Alternative Medicine : eCAM*, 2007, **4**, 37.

270. Hintz T., Matthews K. K. and Di R., *BioMed Research International*, 2015, **2015**, 12.

271. Castro A. C. C. M., Oda F. B., Almeida-Cincotto M. G. J., Davanço M. G., Chiari-Andréo B. G., Cicarelli R. M. B., Peccinini R. G., Zocolo G. J., Ribeiro P. R. V., Corrêa M. A., Isaac V. L. B. and Santos A. G., *Food Chemistry*, 2018, **246**, 48.

272. Huang C.-N., Wang C.-J., Lin C.-L., Lin H.-T. and Peng C.-H., *PLOS ONE*, 2017, **12**, e0189065.

273. Suleman S., Beyene Tufa T., Kebebe D., Belew S., Mekonnen Y., Gashe F., Mussa S., Wynendaele E., Duchateau L. and De Spiegeleer B., *Journal of Ethnopharmacology*, 2018, **213**, 262.

274. Wang H., Shi S. and Wang S., *Journal of Ethnopharmacology*, 2018, **213**, 101.

275. Rates S. M. K., *Toxicon*, 2001, **39**, 603.

276. Liu X., Ahlgren S., Korthout H. A. A. J., Salomé-Abarca L. F., Bayona L. M., Verpoorte R. and Choi Y. H., *Journal of Chromatography A*, 2018, **1532**, 198.

277. Sahoo N., Manchikanti P. and Dey S., *Fitoterapia*, 2010, **81**, 462.

278. Yee S.-K., Chu S.-S., Xu Y.-M. and Choo P.-L., *Health Policy*, 2005, **71**, 133.

279. , 2005, 168.

280. Li H., Jiang H. and Liu J., *Translational Andrology and Urology*, 2017, **6**, 192.

281. Gauthaman K. and Ganesan A. P., *Phytomedicine*, 2008, **15**, 44.

282. Guay A. T., Spark R. F., Jacobson J., Murray F. T. and Geisser M. E., *International Journal Of Impotence Research*, 2002, **14**, 25.

283. Maria J. and Noordin M. I., *Journal of Thermal Analysis and Calorimetry*, 2014, **115**, 1907.

284. Sze-Yin Oh S., Zou P., Low M.-Y. and Koh H.-L., *Journal of Toxicology and Environmental Health, Part A*, 2006, **69**, 1951.

285. Hatzimouratidis K., *Clinical Interventions in Aging*, 2006, **1**, 403.

286. Barnett C. F. and Machado R. F., *Vascular Health and Risk Management*, 2006, **2**, 411.

287. Rosen R. C., Fisher W. A., Eardley I., Niederberger C., Nadel A. and Sand M., *Current Medical Research and Opinion*, 2004, **20**, 607.

288. Rosen R., Janssen E., Wiegel M., Bancroft J., Althof S., Wincze J., Segraves R. T. and Barlow D., *Journal of Sex & Marital Therapy*, 2006, **32**, 215.

289. Sung B.-J., Yeon Hwang K., Ho Jeon Y., Lee J. I., Heo Y.-S., Hwan Kim J., Moon J., Min Yoon J., Hyun Y.-L., Kim E., Jin Eum S., Park S.-Y., Lee J.-O., Gyu Lee T., Ro S. and Myung Cho J., *Nature*, 2003, **425**, 98.

290. Shinlapawittayatorn K., Chattipakorn S. and Chattipakorn N., *Brazilian Journal of Medical and Biological Research*, 2005, **38**, 1303.

291. Sheu M.-T., Wu A.-B., Yeh G.-C., Hsia A. and Ho H.-O., *Journal of Chromatography B*, 2003, **791**, 255.

292. Rodríguez J., Berzas J. J., Castañeda G. and Rodríguez N., *Talanta*, 2004, **62**, 427.

293. Tyszczuk K. and Korolczuk M., *Bioelectrochemistry*, 2010, **78**, 113.

294. Chien Chun Wang L. F., *Journal of Chinese Medicine Research and Development (JCMRD)*, 2012, **1**, 54.

295. Siddiqui M. R., AlOthman Z. A. and Rahman N., *Arabian Journal of Chemistry*, 2017, **10**, S1409.

296. de Veij M., Deneckere A., Vandenabeele P., de Kaste D. and Moens L., *Journal of Pharmaceutical and Biomedical Analysis*, 2008, **46**, 303.

297. Kurouski D., Large N., Chiang N., Greeneltch N., Carron K. T., Seideman T., Schatz G. C. and Van Duyne R. P., *Analyst*, 2016, **141**, 1779.

298. Gicheva G. and Yordanov G., *Colloids and Surfaces A: Physicochemical and Engineering Aspects*, 2013, **431**, 51.

299. Lee P. C. and Meisel D., *The Journal of Physical Chemistry*, 1982, **86**, 3391.

300. Kimling J., Maier M., Okenve B., Kotaidis V., Ballot H. and Plech A., *The Journal of Physical Chemistry B*, 2006, **110**, 15700.

301. Turkevich J., Stevenson P. C. and Hillier J., *Discussions of the Faraday Society*, 1951, **11**, 55.

302. Huynh K. A. and Chen K. L., *Environmental science & technology*, 2011, **45**, 5564.

303. Silva T. D., Toledo C. R. and Vianna-Soares C. D., *Brazilian Journal of Pharmaceutical Sciences*, 2017, **53**.

304. Al Omari M. M., Zughul M. B., Davies J. E. D. and Badwan A. A., *Journal of Pharmaceutical and Biomedical Analysis*, 2006, **41**, 857.

305. Krajczewski J., Kolataj K. and Kudelski A., *RSC Advances*, 2017, **7**, 17559.

306. Humbert C., Pluchery O., Lacaze E., Tadjeddine A. and Busson B., *Gold Bulletin*, 2013, **46**, 299.

307. Sachdeva R., Singh V. P., Saini G. S. S., Sinha M. M. and Verma S. S., *AIP Conference Proceedings*, 2015, **1675**, 030075.

308. Muehlethaler C., Lombardi J. R. and Leona M., *Journal of Raman Spectroscopy*, 2017, **48**, 647.

309. Chadha R., Maiti N. and Kapoor S., *Journal of Molecular Structure*, 2014, **1076**, 35.

310. Muehlethaler C., Lombardi John R. and Leona M., *Journal of Raman Spectroscopy*, 2017, **48**, 647.

311. Edwards H. G. M., Munshi T. and Page K., *Analytical and Bioanalytical Chemistry*, 2007, **389**, 2203.

312. Garrido C., Aguayo T., Clavijo E., Gómez-Jeria J. S. and Campos-Vallette M. M., *Journal of Raman Spectroscopy*, 2013, **44**, 1105.

313. Joshi B. D., Srivastava A., Tandon P. and Jain S., *Spectrochimica Acta Part A: Molecular and Biomolecular Spectroscopy*, 2011, **82**, 270.

314. Dinesh N. D., Nagaraja P., Made Gowda N. M. and Rangappa K. S., *Talanta*, 2002, **57**, 757.

315. Othman A. M., Rizk N. M. H. and El-Shahawi M. S., *Analytica Chimica Acta*, 2004, **515**, 303.

316. Berzas Nevado J . J., Rodríguez Flores J ., Castañeda Peñalvo G . and Rodríguez Fariñas N., *Journal of Chromatography A*, 2002, **953**, 279.

317. Magnusson B. and Örnemark U., *Eurachem Guide: The Fitness for Purpose of Analytical Methods - A Laboratory Guide to Method Validation and Related Topics*, 2nd edn., 2014.

318. Lanzarotta A., Lorenz L., Batson J. S. and Flurer C., *Journal of Pharmaceutical and Biomedical Analysis*, 2017, **146**, 420.

319. Lv M., Gu H., Yuan X., Gao J. and Cai T., *Journal of Molecular Structure*, 2012, **1029**, 75.

320. Hu X., Fang G., Han A., Fu Y., Tong R. and Wang S., *Journal of Separation Science*, 2017, **40**, 2506.

321. Yu S., Liu Z., Wang W., Jin L., Xu W. and Wu Y., *Talanta*, 2018, **178**, 498.

322. Zhao H., Hasi W., Bao L., Han S., Sha X., Sun J., Lou X., Lin D. and Lv Z., *Chinese Journal of Chemistry*, 2017, **35**, 1522.

323. Cheitlin M. D., Hutter A. M., Brindis R. G., Ganz P., Russell R. O. and Zusman R. M., *Circulation*, 1999, **99**, 168.

324. Chamsi-Pasha H., *Journal of Family & Community Medicine*, 2001, **8**, 63.

325. Guimarães A. C., Malachias M. V. B., Coelho O. R., Zilli E. C. and Luna R. L., *Arquivos Brasileiros de Cardiologia*, 1999, **73**, 521.

326. Vardi Y., Klein L., Nassar S., Sprecher E. and Gruenwald I., *Urology*, 2002, **59**, 747.

327. Webb D. J., Muirhead G. J., Wulff M., Sutton J. A., Levi R. and Dinsmore W. W., *Journal of the American College of Cardiology*, 2000, **36**, 25.

328. Kloner R. A., *The American Journal of Cardiology*, 2005, **96**, 42.

329. Govorov A. O., Bryant G. W., Zhang W., Skeini T., Lee J., Kotov N. A., Slocik J. M. and Naik R. R., *Nano Letters*, 2006, **6**, 984.

330. Chiu N.-F., Chen C.-C., Yang C.-D., Kao Y.-S. and Wu W.-R., *Nanoscale research letters*, 2018, **13**, 152.

331. Ye W., Long R., Huang H. and Xiong Y., *Journal of Materials Chemistry C*, 2017, **5**, 1008.

332. Wang X., Jian J., Diaz-Amaya S., Kumah C. E., Lu P., Huang J., Lim D. G., Pol V. G., Youngblood J. P., Boltasseva A., Stanciu L. A., O'Carroll D. M., Zhang X. and Wang H., *Nanoscale Advances*, 2019, **1**, 1045.

333. Petryayeva E. and Krull U. J., *Analytica Chimica Acta*, 2011, **706**, 8.

334. Njoki P. N., Lim I. I. S., Mott D., Park H.-Y., Khan B., Mishra S., Sujakumar R., Luo J. and Zhong C.-J., *The Journal of Physical Chemistry C*, 2007, **111**, 14664.

335. Jain P. K. and El-Sayed M. A., *The Journal of Physical Chemistry C*, 2007, **111**, 17451.

336. Gallinet B. and Martin O. J. F., *Opt. Express*, 2011, **19**, 22167.

337. Schatz G. C., *Accounts of Chemical Research*, 1984, **17**, 370.

338. Lange H., Juárez B. H., Carl A., Richter M., Bastús N. G., Weller H., Thomsen C., von Klitzing R. and Knorr A., *Langmuir*, 2012, **28**, 8862.

339. Tian X., Zhou Y., Thota S., Zou S. and Zhao J., *The Journal of Physical Chemistry C*, 2014, **118**, 13801.

340. Chadha R., Maiti N. and Kapoor S., *Chemical Physics Letters*, 2013, **579**, 68.

341. Nalawade P. and Kapoor S., *Spectrochimica Acta Part A: Molecular and Biomolecular Spectroscopy*, 2013, **116**, 132.

342. Tashkhourian J. and Afsharinejad M., *New Journal of Chemistry*, 2017, **41**, 13881.

343. Wu L. P., Li Y. F., Huang C. Z. and Zhang Q., *Analytical Chemistry*, 2006, **78**, 5570.

344. Hajizadeh S., Farhadi K., Forough M. and Sabzi R. E., *Analytical Methods*, 2011, **3**, 2599.

345. Hatamie A., Zargar B. and Jalali A., *Talanta*, 2014, **121**, 234.

346. Han Z., Liu H., Meng J., Yang L., Liu J. and Liu J., *Analytical Chemistry*, 2015, **87**, 9500.

347. Genov D. A., Sarychev A. K., Shalaev V. M. and Wei A., *Nano Letters*, 2004, **4**, 153.

348. Zhao Y., Zeng W., Tao Z., Xiong P., Qu Y. and Zhu Y., *Chemical Communications*, 2015, **51**, 866.

349. Kitahama Y., Itoh T., Pienpinijtham P., Ekgasit S., Han X. X. and Ozaki Y., 2012, Functional Nanoparticles for Bioanalysis, Nanomedicine, and Bioelectronic Devices Volume 2, American Chemical Society,p. 181-234.

350. Halvorson R. A. and Vikesland P. J., *Environmental Science & Technology*, 2010, **44**, 7749.

351. Yoon J. H., Selbach F., Langolf L. and Schlücker S., *Small*, 2018, **14**, 1702754.

352. Li X., Li J., Zhou X., Ma Y., Zheng Z., Duan X. and Qu Y., *Carbon*, 2014, **66**, 713.

353. Benítez–Martínez S., López-Lorente Á. I. and Valcárcel M., *Microchemical Journal*, 2015, **121**, 6.

354. Zalduendo M. M., Langer J., Giner-Casares J. J., Halac E. B., Soler-Illia G. J. A. A., Liz-Marzán L. M. and Angelomé P. C., *The Journal of Physical Chemistry C*, 2018, **122**, 13095.

355. Chen J., Su H., You X., Gao J., Lau W. M. and Zhang D., *Materials Research Bulletin*, 2014, **49**, 560.

356. Cheng C., Yan B., Wong S. M., Li X., Zhou W., Yu T., Shen Z., Yu H. and Fan H. J., *ACS Applied Materials & Interfaces*, 2010, **2**, 1824.

357. Picciolini S., Castagnetti N., Vanna R., Mehn D., Bedoni M., Gramatica F., Villani M., Calestani D., Pavesi M., Lazzarini L., Zappettini A. and Morasso C., *RSC Advances*, 2015, **5**, 93644.

358. Wang Y., Jin A., Quan B., Liu Z., Li Y., Xia X., Li W., Yang H., Gu C. and Li J., *Microelectronic Engineering*, 2017, **172**, 1.

359. Pradhan A. K., Konda R. B., Mustafa H., Mundle R., Bamiduro O., Roy U. N., Cui Y. and Burger A., *Opt. Express*, 2008, **16**, 6202.

360. Prakash V., Rodriguez R. D., Al-Hamry A., Lipovka A., Dorozhko E., Selyshchev O., Ma B., Sharma S., Mehta S. K., Dzhagan V., Mukherjee A., Zahn D. R. T., Kanoun O. and Sheremet E., *Analyst*, 2019, **144**, 3297.

361. Ben-Jaber S., Peveler W. J., Quesada-Cabrera R., Cortés E., Sotelo-Vazquez C., Abdul-Karim N., Maier S. A. and Parkin I. P., *Nature Communications*, 2016, **7**, 12189.

362. Glaus S. and Calzaferri G., *Photochemical & Photobiological Sciences*, 2003, **2**, 398.

363. Ke J., Niu C., Zhang J. and Zeng G., *Journal of Molecular Catalysis A: Chemical*, 2014, **395**, 276.

364. Zhang H., Fan X., Quan X., Chen S. and Yu H., *Environmental Science & Technology*, 2011, **45**, 5731.

365. Chen S., Carey J. L., Whitcomb D. R., Bühlmann P. and Penn R. L., *Crystal Growth & Design*, 2018, **18**, 324.

366. Zhao H., Hasi W., Bao L., Han S., Sha X., Sun J., Lou X., Lin D. and Lv Z., *Chinese Journal of Chemistry*, 2017, **35**, 1522.

367. Stafford U., Gray K. A. and Kamat P. V., *The Journal of Physical Chemistry*, 1994, **98**, 6343.

368. Kapoor S. and Varshney L., *The Journal of Physical Chemistry A*, 1997, **101**, 7778.

369. Spinks J. W. T. and Woods R. J., *An introduction to radiation chemistry*, John Wiley and Sons Inc, United States, 1990.

370. Creighton J. A., Blatchford C. G. and Albrecht M. G., *Journal*, 1979, **75**, 790-798.

371. Trummal A., Lipping L., Kaljurand I., Koppel I. A. and Leito I., *The Journal of Physical Chemistry A*, 2016, **120**, 3663.

372. Martínez L. L., Segarra M., Fernández M. and Espiell F., *Metallurgical Transactions B*, 1993, **24**, 827.

373. Ha H. and Payer J., *Electrochimica acta*, 2011, **56**, 2781.

374. Pfeiffer C., Rehbock C., Hühn D., Carrillo-Carrion C., de Aberasturi D. J., Merk V., Barcikowski S. and Parak W. J., *J R Soc Interface*, **11**, 20130931.

375. Šloufová I., Šišková K., Vlčková B. and Štěpánek J., *Physical Chemistry Chemical Physics*, 2008, **10**, 2233.

376. Scop P. M., *Physical Review*, 1965, **139**, A934.

377. Han C., Ge L., Chen C., Li Y., Zhao Z., Xiao X., Li Z. and Zhang J., *Journal of Materials Chemistry A*, 2014, **2**, 12594.

378. Ajitha B., Kumar Reddy Y. A., Reddy P. S., Jeon H.-J. and Ahn C. W., *RSC Advances*, 2016, **6**, 36171.

379. Anandalakshmi K., Venugobal J. and Ramasamy V., *Applied Nanoscience*, 2016, **6**, 399.

380. Li D., Ouyang L., Yao L., Zhu L., Jiang X. and Tang H., *ChemistrySelect*, 2018, **3**, 428.

381. Huang Y.-F., Wu D.-Y., Zhu H.-P., Zhao L.-B., Liu G.-K., Ren B. and Tian Z.-Q., *Physical Chemistry Chemical Physics*, 2012, **14**, 8485.

382. Rycenga M., Camargo P. H. C., Li W., Moran C. H. and Xia Y., *The Journal of Physical Chemistry Letters*, 2010, **1**, 696.

383. Gamage McEvoy J., Cui W. and Zhang Z., *Applied Catalysis B: Environmental*, 2014, **144**, 702.

384. Sriram S., Bhaskaran M., Chen S., Jayawardhana S., Stoddart P. R., Liu J. Z., Medhekar N. V., Kalantar-Zadeh K. and Mitchell A., *Journal of the American Chemical Society*, 2012, **134**, 4646.

385. D'Angelantonio M., Russo M., Kaloudis P., Mulazzani Q. G., Wardman P., Guerra M. and Chatgilialoglu C., *The Journal of Physical Chemistry B*, 2009, **113**, 2170.

386. Demircioğlu Z., Kaştaş Ç. A. and Büyükgüngör O., *Journal of Molecular Structure*, 2015, **1091**, 183.

387. A.J.B, *MOLSTR</cja:jid> Journal of Molecular Structure*, 1983, **101**, 344.

388. Moskovits M., *Reviews of Modern Physics*, 1985, **57**, 783.

389. Camden J. P., Dieringer J. A., Zhao J. and Van Duyne R. P., *Accounts of Chemical Research*, 2008, **41**, 1653.

390. Campion A. and Kambhampati P., *Chemical Society Reviews*, 1998, **27**, 241.

391. Lombardi J. R. and Birke R. L., *Accounts of Chemical Research*, 2009, **42**, 734.

392. Otto A., *Journal of Raman Spectroscopy*, 2005, **36**, 497.

393. Futamata M. and Maruyama Y., *Applied Physics B*, 2008, **93**, 117.

394. Fleischmann M., Hendra P. J. and McQuillan A. J., *Chemical Physics Letters*, 1974, **26**, 163.

395. Kneipp K., Kneipp H., Itzkan I., Dasari R. R. and Feld M. S., *Chemical Reviews*, 1999, **99**, 2957.

396. Cotton T. M., *Spectroscopy of surfaces*, Wiley, New York, 1988.

397. Pettinger B., *Adsorption of molecules at metal electrodes*, VCH Publishers, New York, 1992.

398. Bolboaca M., Iliescu T., Paizs C., Irimie F. D. and Kiefer W., *The Journal of Physical Chemistry A*, 2003, **107**, 1811.

399. Pergolese B., Muniz-Miranda M. and Bigotto A., *The Journal of Physical Chemistry B*, 2004, **108**, 5698.

400. SenGupta S., Maiti N., Chadha R. and Kapoor S., *Chemical Physics Letters*, 2015, **639**, 1.

401. Maiti N., Thomas S., Jacob J. A., Chadha R., Mukherjee T. and Kapoor S., *Journal of Colloid and Interface Science*, 2012, **380**, 141.

402. Thomas S., Maiti N., Mukherjee T. and Kapoor S., *Spectrochimica Acta Part A: Molecular and Biomolecular Spectroscopy*, 2013, **112**, 27.

403. Thomas S., Biswas N., Malkar V. V., Mukherjee T. and Kapoor S., *Chemical Physics Letters*, 2010, **491**, 59.

404. Biswas N., Thomas S., Sarkar A., Mukherjee T. and Kapoor S., *The Journal of Physical Chemistry C*, 2009, **113**, 7091.

405. Biswas N., Thomas S., Kapoor S., Mishra A., Wategaonkar S. and Mukherjee T., *The Journal of Chemical Physics*, 2008, **129**, 184702.

406. Biswas N., Kapoor S., Mahal H. S. and Mukherjee T., *Chemical Physics Letters*, 2007, **444**, 338.

407. Huang Y.-F., Zhang M., Zhao L.-B., Feng J.-M., Wu D.-Y., Ren B. and Tian Z.-Q., *Angewandte Chemie International Edition*, 2014, **53**, 2353.

408. Chadha R., Maiti N. and Kapoor S., *The Journal of Physical Chemistry C*, 2014, **118**, 26227.

409. Dhayagude A. C., Maiti N., Debnath A. K., Joshi S. S. and Kapoor S., *RSC Advances*, 2016, **6**, 17405.

410. Garrell R. L., *Analytical Chemistry*, 1989, **61**, 401A.

411. Schultz S., Smith D. R., Mock J. J. and Schultz D. A., *Proc Natl Acad Sci U S A*, 2000, **97**, 996.

412. Thorn G. D., *Canadian Journal of Chemistry*, 1960, **38**, 1439.

413. Zaidi S. A. A. and Siddiqi Z. A., *Journal of Inorganic and Nuclear Chemistry*, 1975, **37**, 1806.

414. Siddiqi K. S., Islam V., Khan P., Zaidi F. R., Siddiqi Z. A. and Zaidi S. A. A., *Synthesis and Reactivity in Inorganic and Metal-Organic Chemistry*, 1980, **10**, 41.

415. Huang L., Tang F., Hu B., Shen J., Yu T. and Meng Q., *The Journal of Physical Chemistry B*, 2001, **105**, 7984.

416. Singh G., Girdhar S., Singh A., Saroa A., Satija P., Verma V. and Singh J., *Silicon*, 2019, **11**, 2575.

417. Hu Y., Li C.-Y., Wang X.-M., Yang Y.-H. and Zhu H.-L., *Chemical Reviews*, 2014, **114**, 5572.

418. Szőke Á. F., Szabó G. S., Hórvölgyi Z., Albert E., Végh A. G., Zimányi L. and Muresan L. M., *International Journal of Biological Macromolecules*, 2020, **142**, 423.

419. Loto R. T., Loto C. A., Popoola A. P. and Fedotova T., *Journal of Central South University*, 2016, **23**, 258.

420. Fields E. K., *Ind. Eng. Chem.*, 1957, **49**, 1261.

421. Bhattacharya A., Singh T., Verma V. K. and Prasad N., *Tribology International*, 1995, **28**, 189.

422. Tianhui R., Qunji X. and Hanqing W., *Wear*, 1994, **172**, 59.

423. Zhang J. C., Luo Y. H. and Zhang B. Y., *Acta Petrol. Sin.*, 1997, 131.

424. Pillon L. Z., *Surface activity of petroleum derived lubricants*, CRC PRESS, [S.l.], 2018.

425. Robert F. O., *Rubber India*, 1997, **49**, 19.

426. Lawson E. E., Edwards H. G. M. and Johnson A. F., *Spectrochimica Acta Part A: Molecular and Biomolecular Spectroscopy*, 1997, **53**, 2571.

427. Kester J. J., Furtak T. E. and Bevolo A. J., *Journal of The Electrochemical Society*, 1982, **129**, 1716.

428. Thierry D. and Leygraf C., *Journal of The Electrochemical Society*, 1986, **133**, 2236.

429. Hashemi T. and Hogarth C. A., *Electrochimica Acta*, 1988, **33**, 1123.

430. Tatsuma T., Yokoyama Y., Buttry D. A. and Oyama N., *The Journal of Physical Chemistry B*, 1997, **101**, 7556.

431. Bats J., *Acta Crystallographica Section B*, 1976, **32**, 2866.

432. Joy V. T. and Srinivasan T. K. K., *Journal of Raman Spectroscopy*, 2001, **32**, 785.

433. Lawson E. E., Edwards H. G. M. and Johnson A. F., *Journal of Raman Spectroscopy*, 1995, **26**, 617.

434. Katritzky A. R. and Rees C. W., *Comprehensive heterocyclic chemistry : the structure, reactions, synthesis and use of heterocyclic compounds*, Pergamon, Oxford, 1984.

435. Millefiori S. and Millefiori A., *Journal of Molecular Structure: THEOCHEM*, 1987, **151**, 373.

436. Edwards H. G. M., Johnson A. F. and Lawson E. E., *Journal of Molecular Structure*, 1995, **351**, 51.

437. HUANG L., SHEN J., REN J., MENG Q. and YU T., *Chinese Science Bulletin*, 2001, **46**, 387.

438. Shouji E., Yokoyama Y., Pope J. M., Oyama N. and Buttry D. A., *The Journal of Physical Chemistry B*, 1997, **101**, 2861.

439. Huang L., Shen J., Yu C., Meng Q. and Yu T., *Vibrational Spectroscopy*, 2001, **25**, 1.

440. Kalimuthu P., Kalimuthu P. and John S. A., *The Journal of Physical Chemistry C*, 2009, **113**, 10176.

441. Creighton J. A., Blatchford C. G. and Albrecht M. G., *Journal of the Chemical Society, Faraday Transactions 2: Molecular and Chemical Physics*, 1979, **75**, 790.

442. Frisch Æ., Frisch M. J. and Trucks G. W., *Gaussian '03 : user's reference*, Gaussian, Wallingford, 2005.

443. Becke A. D., *The Journal of Chemical Physics*, 1993, **98**, 1372.

444. Chang R. K. and Furtak T. E., *Surface enhanced Raman scattering*, Plenum Press, New York, 1982.

445. Liang E. J., Engert C. and Kiefer W., *Vibrational Spectroscopy*, 1993, **6**, 79.

446. Sánchez-Cortés S., García-Ramos J. V., Morcillo G. and Tinti A., *Journal of Colloid and Interface Science*, 1995, **175**, 358.

447. Kiya Y., Hutchison G. R., Henderson J. C., Sarukawa T., Hatozaki O., Oyama N. and Abruña H. D., *Langmuir*, 2006, **22**, 10554.

448. Picart S. and Geniès E., *Journal of Electroanalytical Chemistry*, 1996, **408**, 53.

449. Drescher D., Büchner T., McNaughton D. and Kneipp J., *Physical Chemistry Chemical Physics*, 2013, **15**, 5364.

450. Moskovits M., *The Journal of Chemical Physics*, 1982, **77**, 4408.

451. Creighton J. A., *Surface Science*, 1983, **124**, 209.

452. Tripathi G. N. R., *Journal of the American Chemical Society*, 2003, **125**, 1178.

453. Maiti N., Kapoor S. and Mukherjee T., *Advanced Materials Letters*, 2013, **4**, 502.

454. Kulak A., Hall S. R. and Mann S., *Chemical Communications*, 2004, DOI: 10.1039/B314465H, 576.

455. Kinoshita T., Seino S., Okitsu K., Nakayama T., Nakagawa T. and Yamamoto T. A., *Journal of Alloys and Compounds*, 2003, **359**, 46.

456. Wolfe L. S., Calabrese M. F., Nath A., Blaho D. V., Miranker A. D. and Xiong Y., *Proceedings of the National Academy of Sciences*, 2010, **107**, 16863.

457. Reinke A. A. and Gestwicki J. E., *Chemical Biology & Drug Design*, 2011, **77**, 399.

458. KeliÉNyi G., *Journal of Histochemistry & Cytochemistry*, 1967, **15**, 172.

459. Sutharsan J., Lichlyter D., Wright N. E., Dakanali M., Haidekker M. A. and Theodorakis E. A., *Tetrahedron*, 2010, **66**, 2582.

460. Lopez-Tobar E., Antalik M., Jancura D., Cañamares M. V., García-Leis A., Fedunova D., Fabriciova G. and Sanchez-Cortes S., *The Journal of Physical Chemistry C*, 2013, **117**, 3996.

461. Biswas N., Thomas S., Sarkar A., Mukherjee T. and Kapoor S., *Chemical Physics Letters*, 2009, **479**, 248.